

2018 IEEE  
Nuclear and Space Radiation Effects Conference  
Short Course Notebook

July 16, 2018  
Kona, Hawaii

**Variability in Environments, Devices and  
Radiation Effects – from Average to Extreme**



**Sponsored by:**

IEEE/NPSS Radiation Effects Committee

**Supported by:**

Boeing | Cobham Semiconductor Solutions | Freebird Semiconductor | Harris  
IR HiRel, An Infineon Technologies Company | Jet Propulsion Laboratory | Renesas Electronics  
Southwest Research Institute | The Aerospace Corporation

Approved for public release: distribution is unlimited.

# **Table of Contents**

<b>Section I</b>	<b>A Brief History of Space Climatology: From the Big Bang to the Present Michael Xapsos</b>	<b>Page 9</b>
<b>Section II</b>	<b>Radiation Hardness Assurance: How Well Assured Do We Need to Be? Renaud Mangeret</b>	<b>Page 75</b>
<b>Section III</b>	<b>Process Variations and Radiation Effects in Advanced Transistors Marc Gaillardin</b>	<b>Page 139</b>
<b>Section IV</b>	<b>Addressing Device and Environment Variations in Single Event Rate Predictions Brian Sierawski</b>	<b>Page 194</b>

# Short Course Program

## VARIABILITY IN ENVIRONMENTS, DEVICES, AND RADIATION EFFECTS – FROM AVERAGE TO EXTREME

HILTON WAIKOLOA  
MONARCHY BALLROOM – MONDAY, JULY 16

8:00 AM	<b>SHORT COURSE INTRODUCTION</b> Prof. Simone Gerardin, <i>University of Padova Department of Information Engineering</i>
8:10 AM	<b>PART I - A BRIEF HISTORY OF SPACE CLIMATOLOGY: FROM THE BIG BANG TO THE PRESENT</b> Dr. Mike Xapsos, <i>NASA Goddard Space Flight Center</i>
9:40 AM	<b>BREAK (Grand Promenade)</b>
10:10 AM	<b>PART II - RADIATION HARDNESS ASSURANCE: HOW WELL ASSURED DO WE NEED TO BE?</b> Dr. Renaud Mangeret, <i>Airbus Defence and Space</i>
11:40 AM	<b>SHORT COURSE LUNCHEON</b> (Kona 4 and 5 Rooms)
1:20 PM	<b>PART III - PROCESS VARIATIONS AND RADIATION EFFECTS IN ADVANCED TRANSISTORS</b> Dr. Marc Gaillardin, <i>CEA</i>
2:50 PM	<b>BREAK (Grand Promenade)</b>
3:20 PM	<b>PART IV - ADDRESSING DEVICE AND ENVIRONMENT VARIATIONS IN SINGLE EVENT RATE PREDICTIONS</b> Dr. Brian Sierawski, <i>Vanderbilt University, Institute for Space and Defense Electronics</i>
4:50 PM	<b>WRAP-UP</b>
5:00 PM	<b>EXAM (only for students requesting CEU credit)</b>
5:30 PM	<b>END OF SHORT COURSE</b>

*Each Short Course attendee will receive the 1980-2018 Short Course Compendium*

# Short Course

## COURSE DESCRIPTION

A one-day short course, “*Variability in Environments, Devices, and Radiation Effects – from Average to Extreme*”, will be presented at the 2018 IEEE Nuclear and Space Radiation Effects Conference (NSREC). The course will discuss space weather and the effects of ionizing radiation in advanced electronic devices, with emphasis on variability and its main sources. Bounding and managing uncertainties is a key to mission success for space systems in harsh environments. The introduction of more scaled technologies, the growing interest towards using Commercial-Off-The-Shelf Components (COTS), and the push to reduce design margins and test time to decrease costs is making variability more challenging than ever. Accurate environmental modeling is therefore needed for a precise assessment of the radiation exposure during a mission. Average metrics may not fully capture the extent of radiation effects in modern devices and need to be replaced. Nanoscale components and sensitive volumes mandate the use of statistical or Monte Carlo techniques for evaluating and predicting failures in space.

This short course will benefit those new to the field by explaining in a clear and concise manner the basic concepts concerning the presence of ionizing radiation in space and its effects on electronic systems, while providing up-to-date material and insight into new phenomena and mechanisms for experienced engineers and scientists.

It is organized into four sections all featuring introductory material and advanced topics, with an emphasis on variability. The first one provides an overview of radiation environments. The second section of the course discusses hardness assurance methodologies. The third one focuses primarily on process variations and cumulative effects in MOSFETs. The final section addresses single event effects in scaled devices.

This short course is intended for system designers, radiation effects engineers, component specialists, and other technical and management personnel who are involved in developing reliable systems designed to operate in radiation environments. It provides a unique opportunity for IEEE NSREC attendees to benefit from the expertise of the instructors, along with a critical review of state-of-the-art knowledge in the field. Electronic copies of detailed course notes will be provided at registration.

## CONTINUING EDUCATION UNITS (CEUS)

For those interested in Continuing Education Units (CEUs), there will be an openbook exam at the end of the course. The course is valued at 0.6 CEUs and is endorsed by the IEEE and by the International Association for Continuing Education and Training (IACET).

## SHORT COURSE CHAIRMAN



Prof. Simone Gerardin  
University of Padova  
Department of Information Engineering  
Short Course Chairman

**Simone Gerardin** is an Associate Professor of Electronics at the University of Padova – Italy. He received the Laurea degree (cum laude) in Electronics Engineering in 2003, and a Ph.D. in Electronics and Telecommunications Engineering in 2007, both from the University of Padova. His research has been focused on ionizing radiation effects in advanced CMOS technologies and on their interplay with device aging and electrostatic discharges, in the space, terrestrial, and high-energy physics environments. Lately, his interests have been on innovative non-volatile memories for space and total ionizing dose effects at ultra-high levels. Simone has authored or co-authored more than 200 peer-reviewed journal articles, book chapters, and conference presentations, ten of which were recognized with international awards. He presented four tutorials at international conferences and co-edited a book. He has been an associate editor for the IEEE Transactions on Nuclear Science and member-at-large of the IEEE Radiation Effects Steering Group. He is currently a member of the RADECS Steering Group.

# Short Course Monday



**Mike Xapsos** joined the Radiation Effects and Analysis group at NASA Goddard Space Flight Center in 2001, where he oversees the group's space radiation environment work and supports space flight and research programs. Prior to that he worked in the Radiation Effects Branch of the Naval Research Laboratory as a research physicist, where his work involved device problems and the space radiation environment. He received the B.S. degree in physics and chemistry from Canisius College in 1978 and the Ph.D. degree in physics from the University of Notre Dame in 1985.

Mike led the development of the ESP/PSYCHIC solar particle event models that are widely used for spacecraft design requirements. He has presented prior Short Courses for the NSREC, Radiation Effects on Components and Systems (RADECS) Conference, and Hardened Electronics and Radiation Technology (HEART) Conference, and was lead author of an NSREC Outstanding Paper Award and a RADECS Outstanding Conference Oral Paper. He has been an editor of the IEEE Transactions on Nuclear Science NSREC issue and held various positions for the NSREC including conference chair in 2015. He has authored or co-authored approximately 100 technical publications.

## A BRIEF HISTORY OF SPACE CLIMATOLOGY: FROM THE BIG BANG TO THE PRESENT

Dr. Mike Xapsos  
*NASA Goddard Space Flight Center*

**Dr. Mike Xapsos**, NASA Goddard Space Flight Center, will discuss space climatology – the radiation environment observed over an extended period of time at a given location, corresponding to a space mission duration and orbit. It will begin with a unique introduction to the early universe and the origin of particles relevant for radiation effects – electrons, protons, neutrons, and heavy ions. A transitional period leading to modern times will be discussed involving the discovery of sunspots, the solar cycle and the sun's pervasive influence on space climatology. This leads to the main discussion about modern space climatology, with emphasis on galactic cosmic rays, solar particle events, and trapped particles. Metrics that describe the effects these radiations have on electronic devices and circuits will be introduced. Radiation properties such as elemental composition, fluxes, energies, and dependence on solar cycle phase and spacecraft orbit will be discussed, with emphasis on variability of these properties. Finally, current radiation models used for space system design along with example applications will be presented.

This will complete the attendee's journey along the space climatology time line ranging from the Big Bang to NSREC 2018!

### A top-level outline of the presentation is as follows:

- The early universe from a radiation effects perspective
  - Origin of electrons, protons, neutrons and heavy ions
- Transition to modern times
  - Sunspots and the solar activity cycle
- Modern times – the space radiation environment
  - Definition of space climatology and space weather
  - Galactic cosmic rays
    - Properties
    - Models
    - Current issue: elevated fluxes during prolonged solar minima
  - Solar particle events
    - Properties
    - Models
    - Current issue: use of statistical models vs. worst case observations
  - The Van Allen Belts
    - Properties
    - Models
    - Current issue: the case of the missing electrons
  - Example environments for total dose and single events
- Summary

# Short Course Monday



**Renaud Mangeret** received his PhD in electronics from the Paul Sabatier University, Toulouse (France) in the Materials and Components for Electronics Department in 1992. He then worked at the IBM Almaden Research Center, California, as a visiting scientist working on non-linear optics (NLO) polymers. From 1993-1995 Renaud worked at Giat Industries, Toulouse as a research and development engineer. Since 1995 Renaud has been the radiation specialist at Matra Marconi Space/EADS Astrium/Airbus Defence and Space, Toulouse, then in 2006 has been Astrium/Airbus Defence and Space's Radiation Expert and is now Transnational Radiation Senior Expert, still at Airbus Defence and Space in Toulouse. He is responsible for all aspects of radiation hardness assurance solutions for use of sensitive devices in space programs (telecommunications, Earth observation, interplanetary scientific and constellations). Renaud is a Member of the IEEE and currently serves as Treasurer for the RADECS Association Steering Committee.

## RADIATION HARDNESS ASSURANCE: HOW WELL ASSURED DO WE NEED TO BE?

Dr. Renaud Mangeret  
*Airbus Defence and Space*

**Dr. Renaud Mangeret**, Airbus Defence and Space, will discuss the intrinsic variability of numerous parameters within the Radiation Hardness Assurance (RHA) process. From the perspective of a space system provider, the need of supplying radiation robust products to multiple customers requires a cost/schedule effective approach of the RHA process. This results in a permanent trade-off between generic versus application specific approaches in several domains. After a short recap of the radiation environment (which is also quite variable), the presentation will address the variability issues in the radiation modelling and calculation process, in the area of radiation testing, in the electronic design domain and, finally, in the EEE parts themselves. This will cover a broad range of technical items which are to be put in perspective with the definition of a radiation design margin.

**A top-level outline of the presentation is as follows:**

- Introduction
- Radiation environment definition and potential impacts on RHA process
- Some parameters of influence on the RHA process
  - Customer
  - Normative system
  - Program nature
- Key parameters in the RHA process
  - TID/DD hardness assurance
    - Modelling activities
    - Device traceability
    - Test activities
    - Link with Worst Case Analysis
    - Margin policy
  - SEE hardness assurance
    - Device traceability
    - Test activities
    - Link with design tolerance (equipment, system)
    - SEE Rate calculation
- Conclusion

# Short Course Monday



**Marc Gaillardin** is an engineer at the Commissariat à l'Energie Atomique (CEA), in Arpajon, France. His primary research activities are focused on the radiation effects in innovative technologies including Ultra-thin SOI, FinFET and nanowire devices. He is involved in developing radiation-hardened technologies using modelling and experimental characterization assessment methodologies. He earned his M.S. in electronic engineering from University of Orsay (Paris-Saclay Univ.) and Polytech' Paris Sud (formerly FIUPSO), Orsay, France, and his PhD. in nanoelectronics from the Institut National Polytechnique de Grenoble, France.

## PROCESS VARIATIONS AND RADIATION EFFECTS IN ADVANCED TRANSISTORS

Dr. Marc Gaillardin  
CEA

**Dr. Marc Gaillardin**, CEA, will present radiation effects in advanced transistors with an emphasis on variability. This part of the short course will focus primarily on microelectronics technologies, transistor architectures, and their evolutions. Both Ultra-Thin SOI and FinFET architectures will be discussed, since they represent the best solutions to meet the requirements for nanometer scaled technology nodes. Then, process variability issues will be introduced to discuss their implications on devices and integrated circuits. The second half will review radiation effects in advanced devices. Total Ionizing Dose effects will be thoroughly investigated through the impact of geometry and device structure to discuss potential variability implications. A discussion about displacement damage dose effects in nano-scaled devices will be included as well. The end of the course will be dedicated to providing perspectives about the use of novel technologies in harsh environments.

### A top-level outline of the presentation is as follows:

- Introduction
- Microelectronic Technology: from micro to nanometer scaled transistors
  - Transistors architectures
  - MOSFET devices: evolutions and major breakthroughs
  - Variability issues
  - Summary of major keypoints on microelectronic technologies
- Radiation Effects in Ultra-Scaled MOSFETs
  - Basic mechanisms
  - Impact on MOSFET function
  - Nano-scaled MOSFETs TID response: Geometry and device structure dependence
  - Insights into process variability implications on TID response
- Perspectives of Radiation Effects in Ultra-Scaled Devices
- Conclusions

# Short Course Monday



**Brian Sierawski** is a Research Assistant Professor in Electrical Engineering with Vanderbilt's Institute for Space and Defense Electronics (ISDE). He received his B.S.E in Computer Engineering and M.S.E. in Computer Science and Engineering from the University of Michigan in 2002 and 2004, and his Ph.D. in Electrical Engineering from Vanderbilt University in 2011. He joined ISDE in 2005 where his research interests include the simulation of single event effects and error rate predictions in microelectronics. He developed the CRÈME website, investigated the contribution of low-energy proton and muon single event upsets in memories, and developed Vanderbilt's CubeSat program currently collecting telemetry from two radiation effects payloads. He is an IEEE senior member and served as the Finance Chair for the IEEE Nuclear and Space Radiation Effects Conference (NSREC) in 2016.

## ADDRESSING DEVICE AND ENVIRONMENT VARIATIONS IN SINGLE EVENT RATE PREDICTIONS

Dr. Brian Sierawski

*Vanderbilt University, Institute for Space and Defense Electronics*

**Dr. Brian Sierawski**, Vanderbilt University, Institute for Space and Defense Electronics, will review how proton and ion-induced single events are modeled, measured, and extrapolated into an on-orbit response. Limited resources for test and analysis favor minimal characterization and efficient models to estimate the rate of events in space. However, some event rates will not be well-predicted by the measured average device response and will require a greater level of attention. The second part of the course will discuss how variations in devices, events, and environments factor into single event error rates and the extent to which they should be accounted for in ground tests and on-orbit predictions. Notably, highly-scaled memories exhibit enhanced sensitivity to proton and electron upsets and radiation hard circuits can exhibit an ion species dependency. Understanding the limitations of data and models will direct test activities to account for the dominant mechanism for errors. Finally, the course will explore how tools have adapted to improve single event rate predictions.

A top-level outline of the presentation is as follows:

- Introduction
  - Basics of single events
  - Ground based tests and rate prediction methods
  - Factoring device and environment variations into rate predictions
- Variations in energy deposition
  - Nuclear reactions
  - LET fluctuations and concerns for small volumes
  - Proton and electron-induced events
- Predicting on-orbit rates
  - Application of Monte Carlo methods
  - Observed error rates in orbit
- Conclusions

# **A brief history of space climatology: from the big bang to the present**

Michael Xapsos,  
NASA Goddard Space Flight Center

## Table of Contents

1.	Background .....	3
2.	Introduction.....	7
3.	The Early Universe.....	7
A.	Big Bang Nucleosynthesis.....	8
B.	Stellar Nucleosynthesis.....	9
C.	Extreme Event Nucleosynthesis.....	10
D.	Abundances and Radiation Effects of the Elements.....	10
4.	Transition to Modern Times .....	13
5.	Modern Times – Space Climatology .....	15
A.	Definition of Space Climatology and Space Weather.....	16
B.	Galactic Cosmic Rays.....	17
1.	Properties.....	17
2.	Models.....	21
3.	Current Issue: Elevated Fluxes during “Deep” and Prolonged Solar Minima .....	23
C.	Solar Particle Events.....	24
1.	Properties.....	24
2.	Models.....	26
3.	Current Issue: Use of Statistical Models vs. Worst Case Observations .....	37
D.	The Van Allen Belts .....	38
1.	Trapped Particle Motion in the Magnetosphere .....	38
2.	Trapped Protons.....	41
3.	Trapped Electrons .....	48
E.	Example Environments Including Shielding.....	55
1.	Total Ionizing Dose.....	55
2.	Single Event Upset .....	58
6.	Summary .....	60
7.	Acknowledgments.....	61
8.	References .....	61

## 1. Background

This manuscript is focused on space climatology - the radiation environment observed over an extended period of time at a given location, corresponding to a space mission duration and orbit. Electronic devices and integrated circuits must be designed for this climatology in order to operate reliably. The main concerns covered are three categories of high-energy particle radiations. The first is galactic cosmic rays, a comparatively low-level flux of ions originating outside of our solar system. The second is solar particle events, bursts of radiation emitted by the sun characterized by high fluxes of protons and heavy ions. The third is the Van Allen Belts, primarily protons and electrons trapped by the Earth's magnetic field. The plasma environment and spacecraft charging effects will not be discussed here. However, an excellent Short Course presentation of this topic was given in 2015 [Ma15].

In order to have successful, cost-effective designs and implement new space technologies, the climatology must be understood and accurately modeled. Underestimating radiation levels leads to excessive risk and can result in degraded system performance and loss of mission lifetime. Overestimating radiation levels can lead to excessive shielding, reduced payloads, over-design and increased cost. The pervasive use of commercial-off-the-shelf (COTS) microelectronics in spacecraft to achieve increased system performance must be balanced by the need to accurately predict their complex responses in space, which begins by understanding the environment in which they function.

This section gives a top level description of the basic radiation effects and introduces the metrics that describe them. There are three categories of effects that are considered – single event effects (SEE), total ionizing dose (TID) and total non-ionizing dose (TNID) or displacement damage. The following manuscripts in this Short Course provide much greater detail of these effects on electronic devices and systems.

SEE can be defined as any measureable effect in a circuit caused by a single incident particle. It can be either non-destructive such as single event upset (SEU) and single event transients (SETs) or destructive such as single event latchup (SEL) and single event gate rupture (SEGR).

SEE can be caused by direct ionization as the incident particle passes through a sensitive region of a device, as shown in figure 1 [Ba13]. This is usually the case for incident heavy ions. The metric used to characterize the incident ion is Linear Energy Transfer (LET). LET is the ionizing energy lost by the ion per unit path length in the material of the sensitive region. One form LET units take is MeV/cm. However, it turns out that the general expression for LET is directly proportional to the material density. That dependence can be removed by dividing by the density in units of mg/cm<sup>3</sup>, giving LET units of MeV-cm<sup>2</sup>/mg. This is the form of LET most often used by the radiation effects community. This can also be viewed as the energy lost per unit path length, where path length is an areal density. The metric used to calculate single event rates in space is the charge collected at the sensitive volume junction,  $Q$ .

$$Q = C \cdot \text{LET} \cdot s \quad (1)$$

where  $s$  is the ion's path length through the sensitive volume and  $C$  is a unit conversion.

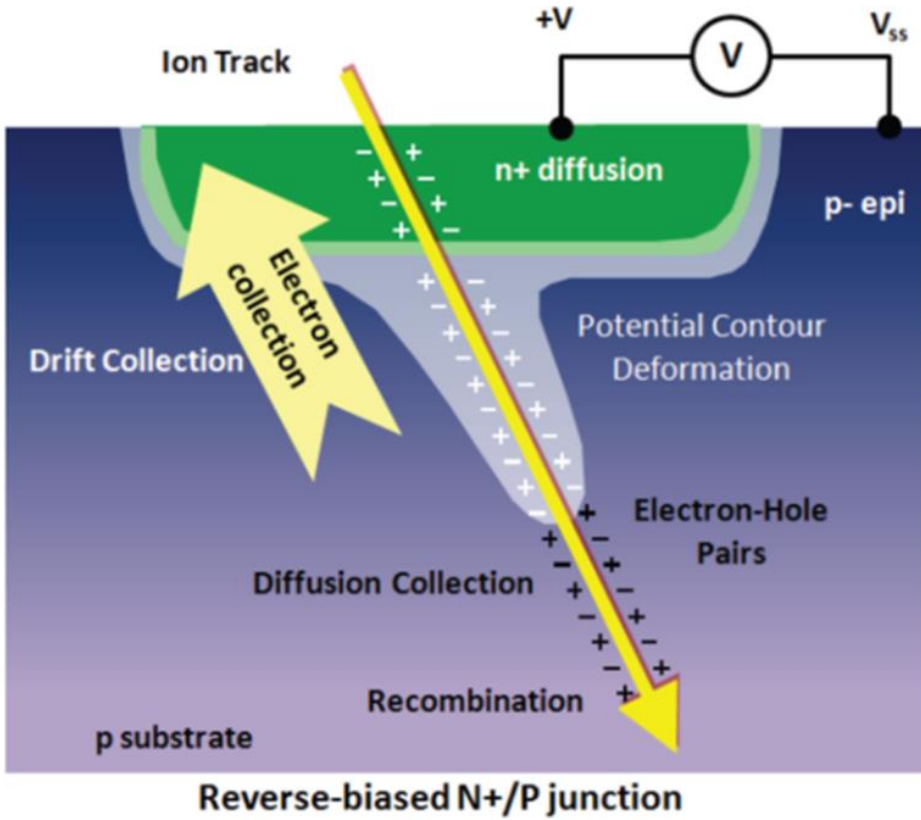


Figure 1. SEE caused by direct ionization [Ba13].

SEE can also be caused by nuclear reaction products from the interaction of the incident particle with a nucleus in the device material. This is usually the case for incident protons and always the case for incident neutrons. For this situation the relevant metric for single event rate calculation remains the charge collected in the sensitive volume but the calculation is more complex because there can be several emerging reaction products that deposit charge.

Total dose effects in electronic and photonic parts are cumulative, long-term degradation due to ionizing or non-ionizing radiation - mainly primary protons and electrons but secondary particles arising from interactions between these primary particles and spacecraft materials can also contribute. For the case of TID, the concern is mainly its effects in insulating regions of metal-oxide semiconductors (MOS) and bipolar devices, most commonly composed of SiO<sub>2</sub>. In MOS devices, ionizing radiation causes threshold voltage shifts due to exposure of gate oxides, shown in figure 2 [Sc02]. The effect first appears as parametric degradation and can eventually result in functional failure. Ionizing radiation can also cause leakage currents in MOS devices due to exposure of field oxide regions used for isolation and result in increased power consumption. Eventually the effect becomes so pronounced the transistor cannot be switched to the off state. For bipolar devices loss in performance is caused by gain degradation and increased leakage currents.

The TID metric is the ionizing energy deposited per unit mass of material in the sensitive volume. It is given by

$$TID = C \cdot LET \cdot \phi \quad (2)$$

where  $\phi$  is the incident particle fluence in  $\text{cm}^{-2}$  and  $C$  is a unit conversion. The MKS units for TID are the Gray (Gy), where  $1 \text{ Gy} = 1 \text{ J/kg}$ . The cgs units are the rad, where  $1 \text{ rad} = 100 \text{ erg/g}$ .

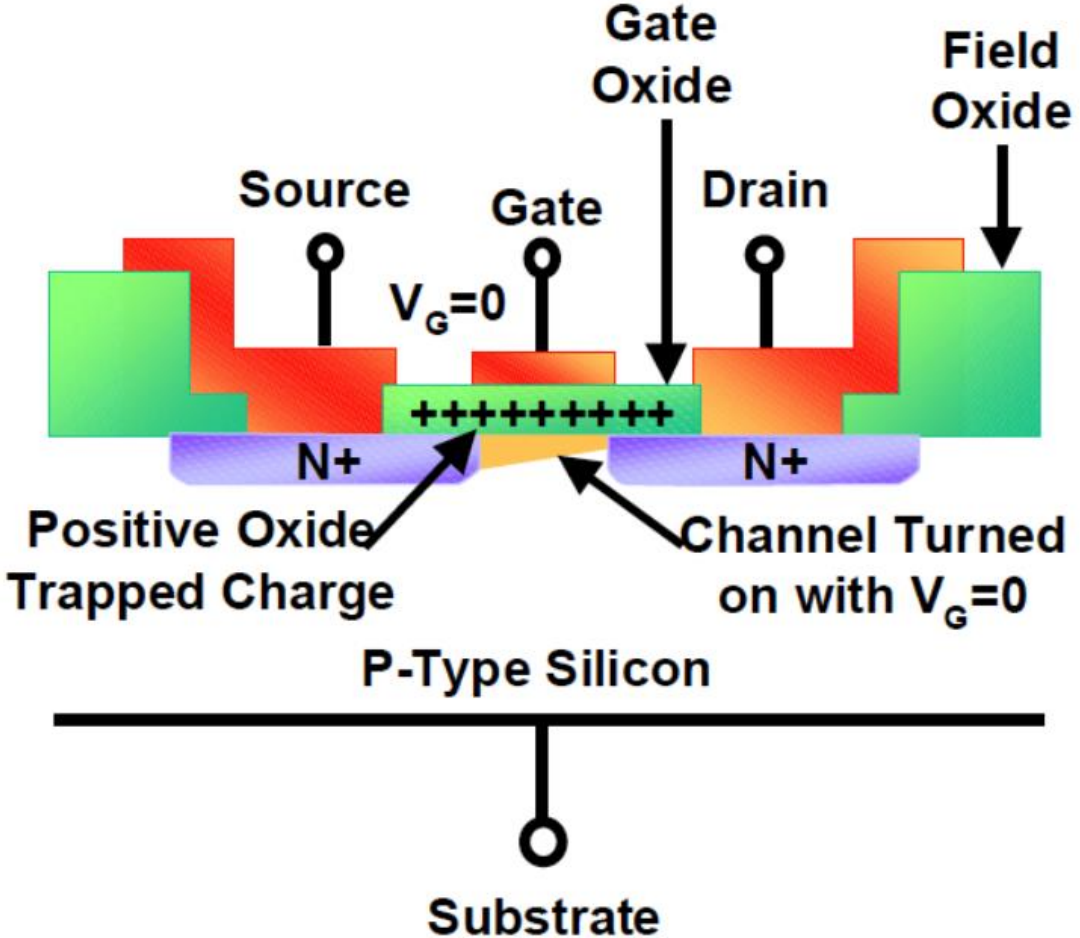


**Figure 2.** Illustration of the TID effect in the gate region of an MOS device [Sc02].

The effects of TNID or displacement damage dose are also cumulative effects caused when the incident radiation displaces atoms in a semiconductor lattice or optical material. TNID is the energy going into displaced atoms per unit mass of material in the sensitive volume. This is shown in figure 3, which illustrates defect production by a recoiling 50 keV silicon atom set in motion by an incident proton [Sr13]. Resulting defects can cause material property changes such as carrier lifetime shortening, mobility decreases and degradation of optical transmission. Displacement damage effects are commonly observed in solar cells, focal planes and optocouplers, which are often a component in power devices. There are two commonly used metrics for TNID. The first is completely analogous to the TID metric shown by equation (2).

$$TNID = C \cdot NIEL \cdot \phi \quad (3)$$

where NIEL, the Non-Ionizing Energy Loss [Su93], is the displacement damage analog of LET. It is the non-ionizing energy lost by the ion per unit path length in the material of the sensitive region. The second metric is to use an equivalent fluence of particles that causes an effect or is equivalent to the TNID value of interest. Equivalent fluences of 50 MeV protons are often used for space applications and in the case of solar cells 10 MeV protons and 1 MeV electrons are used.

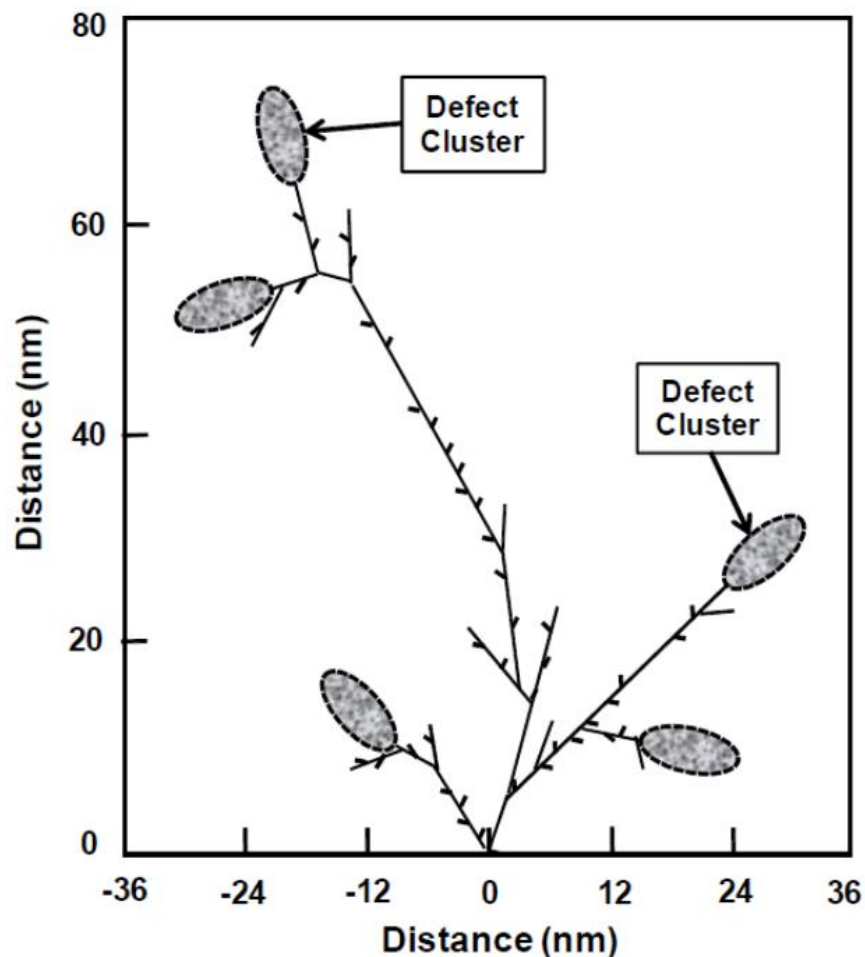


Figure 3. Illustration of the displacement damage produced by a 50-keV Si recoil [Sr13].

## **2. Introduction**

With the previous background information on basic radiation effects terminology, this section starts discussion of the history of space climatology. This will be developed by following a timeline starting with the Big Bang and ending at the present. A description of the early universe from a radiation effects perspective will be presented, featuring the origin and abundances of particles relevant for radiation effects – electrons, protons, neutrons and heavy ions. An interesting feature here is a recent development that is changing the view of the origin of ultra-heavy elements in the Periodic Table. It will be seen that the origin and abundances of these radiations are generally related to the radiation effects they cause in electronic devices and even some of the design requirements that are levied. A transitional period leading to modern times will then be discussed that involves the discovery of sunspots, the solar cycle and the sun's pervasive influence on space climatology. This leads to the main discussion about modern space climatology on galactic cosmic rays, solar particle events and trapped particles. Radiation properties such as elemental composition, fluxes, energies, and dependence on solar cycle phase and spacecraft orbit will be discussed, with emphasis on variability of these properties. Radiation models used for space system design will be presented along with a current issue associated with each of the three types of radiation. This will bring the reader up to date and complete the journey along the space climatology timeline.

## **3. The Early Universe**

It is now well established that the size of the universe is expanding with time. Therefore looking backward in time would reveal a universe that encompasses smaller and smaller volumes the farther back we go. Remarkably, scientists have been able to explain many phenomena by continuing to trace this contraction back to a time about 13.8 billion years ago, considered to be the age of the universe. At this point it is assumed to be a singularity of infinitesimal size and infinitely dense mass. This generally accepted Big Bang Theory of the birth and evolution of the universe is described in a number of interesting publications for a general audience [Ha88], [Ha05], [Li13], [Ma08]. Figure 4 shows an overall timeline beginning with the Big Bang and continuing through different eras to the present [after Li05].

The following discussion of the early universe is limited to the origin and abundances of radiations that are significant for radiation effects in electronic devices and circuits – electrons, protons, neutrons and heavy ions. It involves three types of nucleosynthesis processes – Big Bang, stellar and extreme event nucleosyntheses.

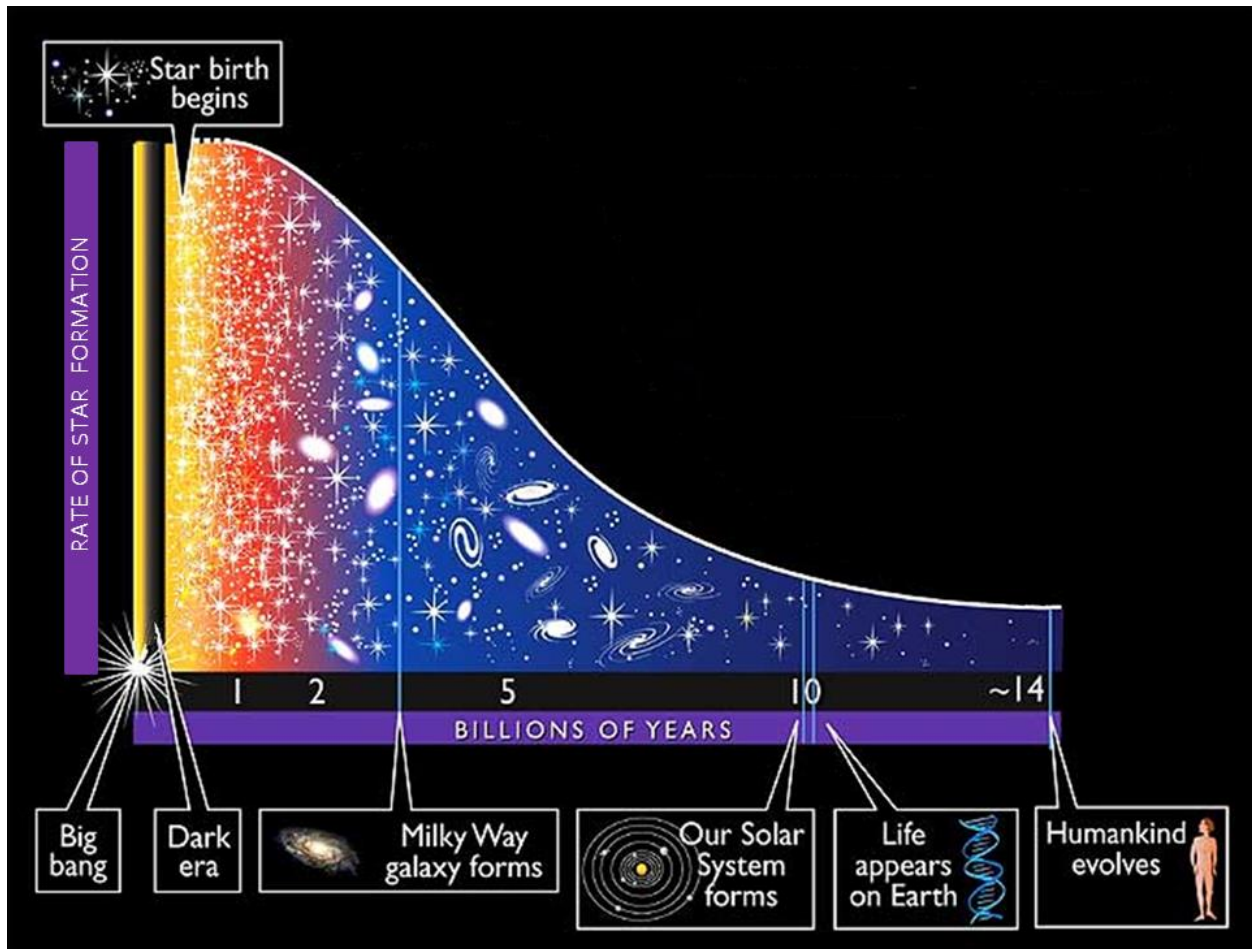


**Figure 4.** Timeline from the Big Bang to the present [after Li05].

#### A. Big Bang Nucleosynthesis

A tiny fraction of a second after the Big Bang it is theorized that elementary particles called quarks existed. There are 6 types of quarks – up, down, top, bottom, strange and charm. The most stable of these are the up and down quarks, which are the building blocks of nucleons. At times on the order of microseconds after the Big Bang the early universe had expanded and cooled enough to allow quarks to come together and form stable nucleons. Two up quarks and one down quark form a proton while two down and one up quark form a neutron. Electrons, which are known to be particles with no internal structure, also existed a tiny fraction of a second after the Big Bang. Continued expansion and cooling allowed protons and neutrons to coalesce into simple nuclei. At an age of about 380,000 years the universe had cooled enough to allow electrons to orbit nuclei and form simple atoms, mainly hydrogen and helium. This portion of the timeline is shown in figure 5.

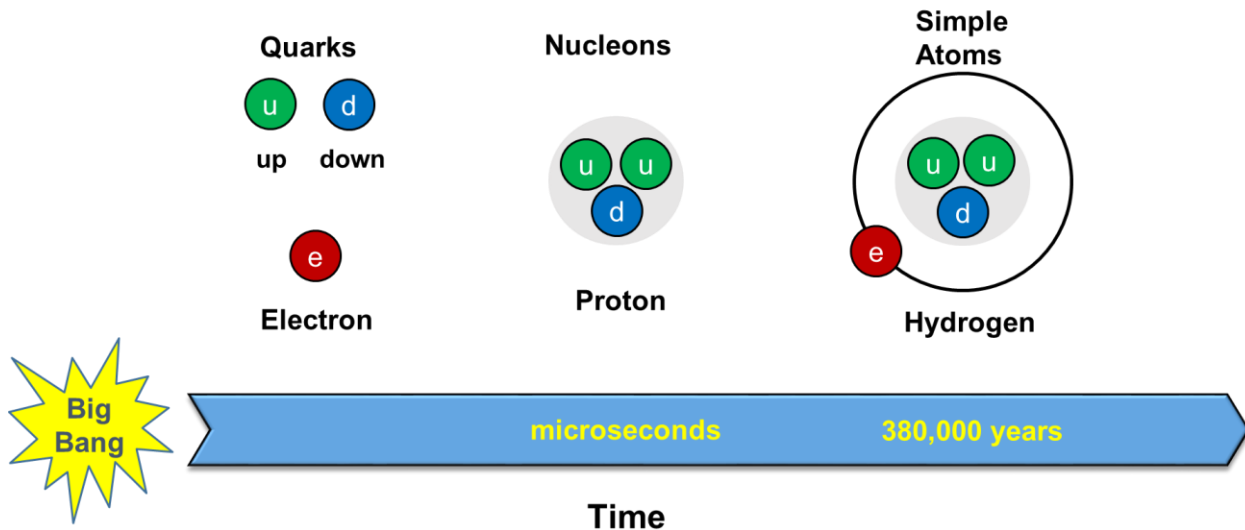


Figure 5. Timeline for the first 380,000 years after the Big Bang.

## B. Stellar Nucleosynthesis

The formation of the elements in the Periodic Table is a complex subject and there can be more than one pathway to the synthesis of an element. The purpose of the next two sections is not to exhaustively describe this for each element but to simply give a general description of elemental origins so they can ultimately be connected to the radiation effects they cause.

Over a long period of time on the order of hundreds of millions of years, the elements created after the Big Bang, primarily hydrogen, began accumulating into gaseous structures such as the iconic image shown in figure 6 taken by the Hubble Space Telescope and known as the "Pillars of Creation". These features of the Eagle Nebula are about 4 to 5 light years in their largest dimension. A star will be born when branches or portions of these structures separate and the hydrogen atoms are close enough to start fusing. It is believed this is how the first stars formed.

At this point in time stars would have consisted almost entirely of hydrogen and helium. The gravitational attraction of the star's enormous mass is balanced by the energy release of fusion reactions to form helium, and keeps the star from collapsing in on itself. When the hydrogen is mostly used up, the star begins to contract. This raises the temperature of the core and if the star is large enough (much larger than our sun) helium begins to fuse and additional energy is released to balance the gravitational force. Thus, during the lifetime of large stars a chain of nuclear fusion reactions starting with hydrogen and helium produce elements from carbon to iron in the star's core. Iron is the element with the highest binding energy in the Periodic Table and is therefore the most stable. When the star's core is entirely iron, fusion is no longer possible because the reaction requires energy to be provided rather than resulting in its release. The star's life is then over. It implodes and becomes a supernova as described in the next section. This production of the elements from C to Fe was first proposed by Hoyle [Ho46], [Li13].

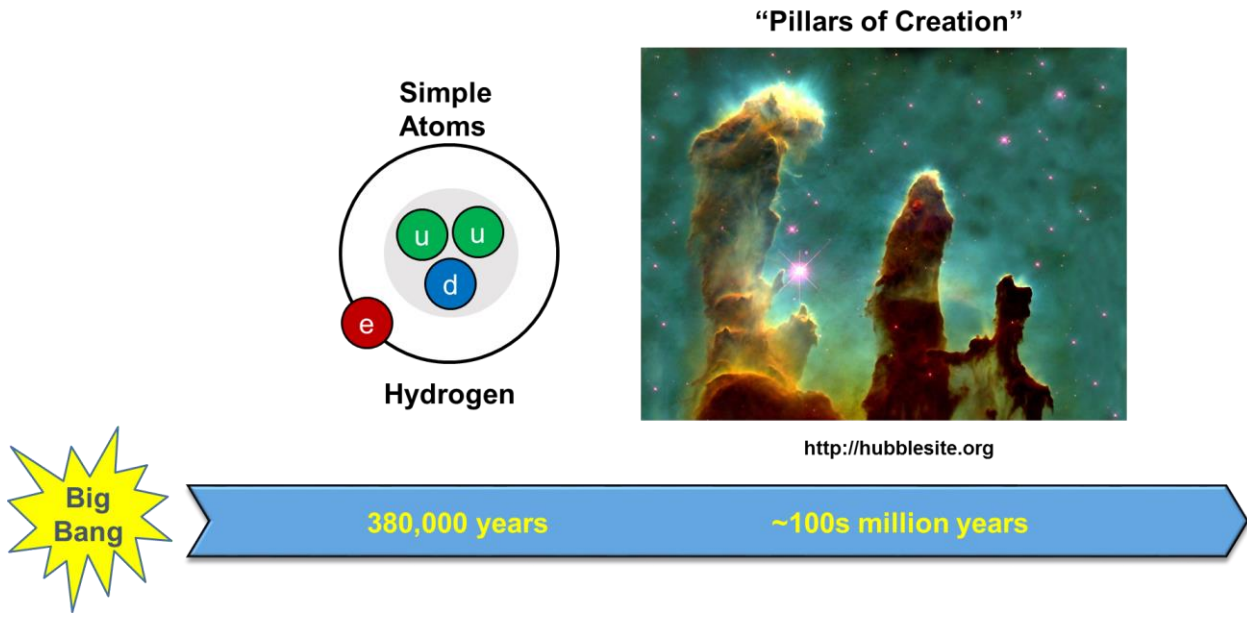


**Figure 6. Timeline for the formation of the first stars.**

### C. Extreme Event Nucleosynthesis

There are two basic conditions that are required for the production of ultra-heavy elements, i.e., those heavier than iron. The first is that there must be enormous energy available in order to overcome the unfavorable energetics of forming these ultra-heavy elements from lighter elements. The second is that there must be an abundance of neutrons available, which is seen by examining the excess of neutrons relative to protons in the nuclei of the ultra-heavy elements in the Periodic Table. There are few known processes in the universe where this could occur. The two most likely happen after the active lifetimes of large stars. One is due to a supernova explosion, which is initiated when a star's fuel is used up and the core consists entirely of iron. With no remaining energy to support itself against gravity, the star collapses. Protons and electrons are crushed together to form neutrons and there is a tremendous release of energy from the collapse making the production of the ultra-heavy elements possible. A second process is the collision/merger of two neutron stars, observed for the first time August 17, 2017 [Ka17]. A neutron star is the remnant of a large star after a supernova explosion that has collapsed to the density of nuclear material and consists mainly of neutrons. Visible light was detected from this event and gave evidence that ultra-heavy elements such as platinum and gold were formed in significant amounts. This led some scientists to postulate it could be the dominant process for formation of ultra-heavy elements.

### D. Abundances and Radiation Effects of the Elements

With that general background on the origin of elements, their abundances are now examined. Figure 7 presents the solar abundances of elements in the Periodic Table as a function of mass number. This generally represents the elemental abundances of the solar system [An89]. Protons and alpha particles existed shortly after the Big Bang so it is not surprising that the elements H and He are the most abundant. The elements ranging from C to Fe are synthesized in

stars larger than the sun in nuclear chain reactions. They are therefore less abundant than the lighter elements H and He. Since the sun ejects these heavy elements during solar particle events but cannot synthesize them, this has the interesting consequence that these heavy elements originated in previous generation stars. Finally, note the rapid decline of the elemental abundances beyond Fe. These ultra-heavy elements are likely only produced in the rare explosive processes discussed in section C.

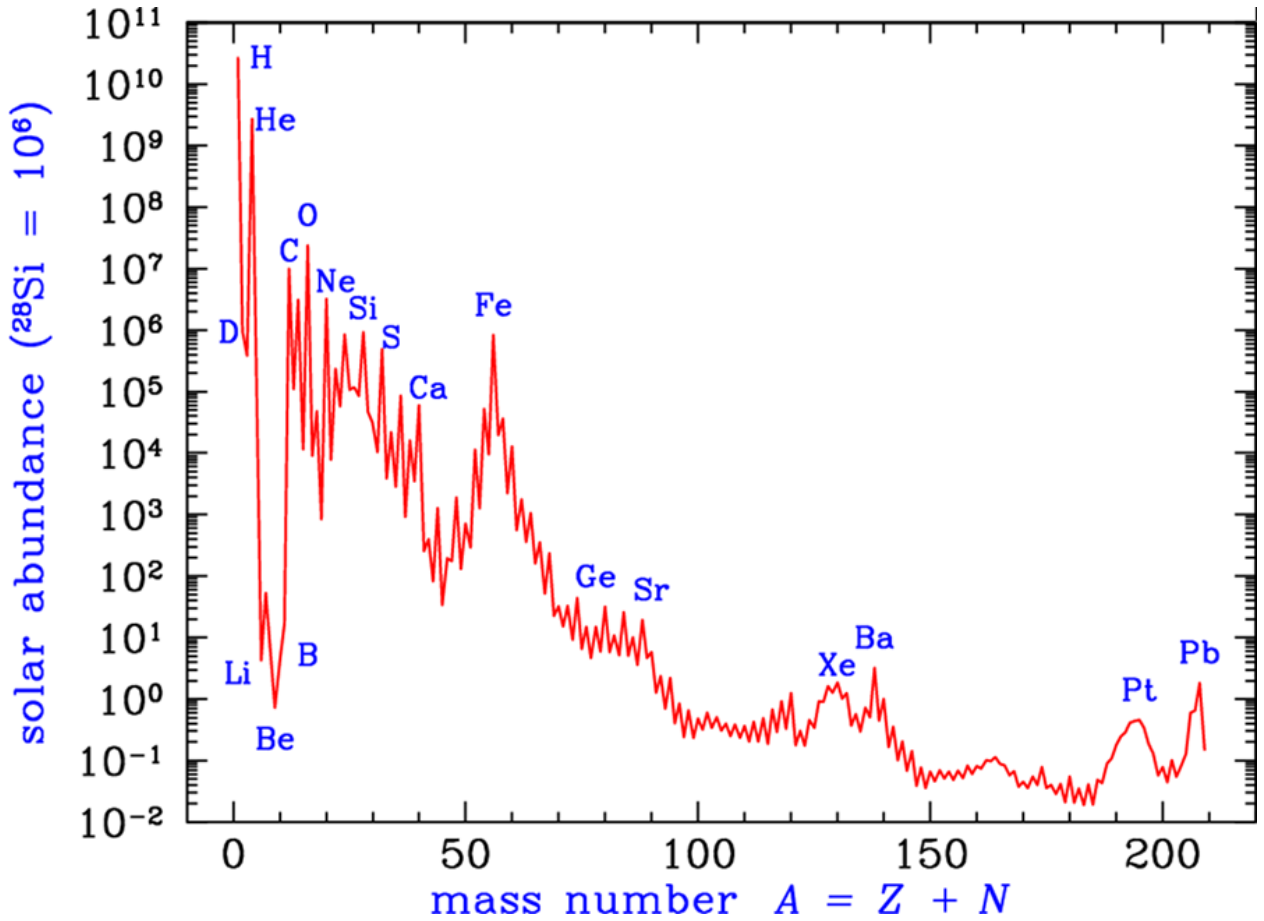


Figure 7. Solar abundances of the elements [An89].

A Periodic Table of Radiation Effects can now be constructed that shows the different effects these radiations produce. This is shown in figure 8 in which the effects are color coded. The blue color indicates that the radiation generally produces total dose effects, including both TID and TNID. A green color indicates SEE and the lavender color indicates charging effects. The table is geared toward radiation effects so electrons and neutrons are included alongside protons. The most abundant radiations, electrons and protons, are largely responsible for cumulative total dose effects that require large numbers of particle strikes in devices. The less abundant alpha particles can contribute to total dose effects to a limited extent as can neutrons. In space neutrons are produced primarily by interactions of protons with spacecraft materials, planetary atmospheres and planetary soils. Due to their large numbers, electrons are mainly responsible for charging, another cumulative effect. The heavy elements C through Fe are not abundant enough to contribute

significantly to these cumulative effects but they are important for SEE. Beyond the Fe, Co, Ni group the elemental abundances and therefore the particle radiation fluxes in space are very low. This is shown in the figure by shading only a small portion of the elemental box green. It can, however, be important to consider their effects for high confidence level applications such as destructive or critical SEE. The three remaining elements that have not yet been discussed, Li, Be and B are relatively rare and produced mainly by fragmentation of heavier galactic cosmic ray ions. This will be shown later in figure 13.

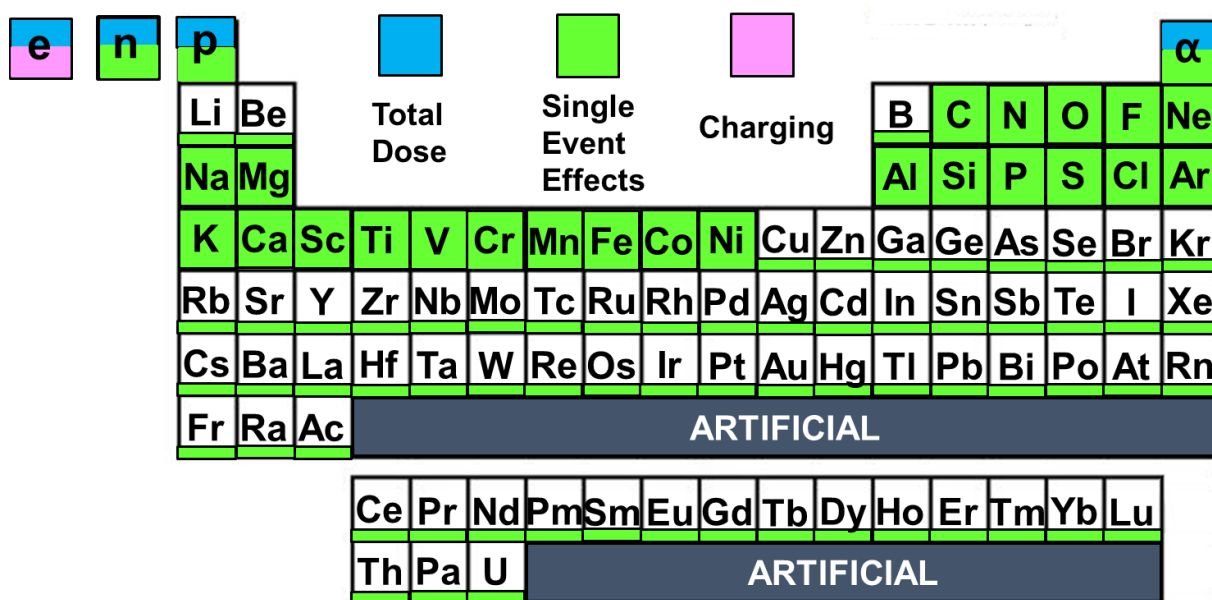
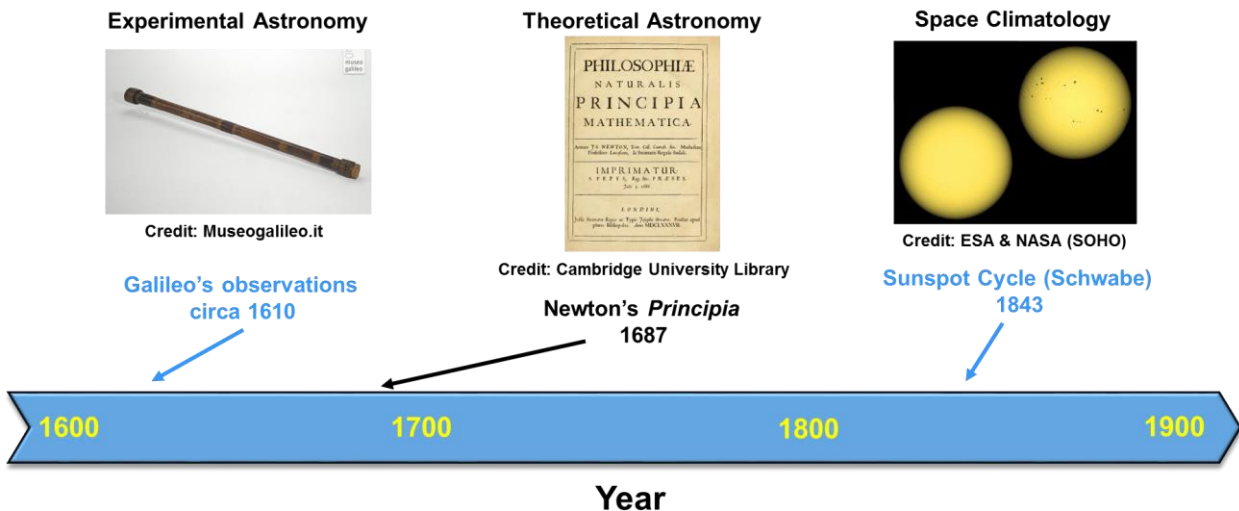


Figure 8. Periodic Table of Radiation Effects.

#### 4. Transition to Modern Times

Now that the origin of radiations in the early universe have been discussed along with their abundances and effects on electronic devices, let's move on to the transition period to modern times when the era of space climatology emerged. A timeline of this era is shown in figure 9.



**Figure 9. Timeline for the emergence of space climatology.**

The telescope was invented in 1608 by the Dutch lens maker Hans Lippershey. Shortly thereafter Galileo Galilei improved its magnification and was the first to use a telescope to study space. These studies could be regarded as the start of modern experimental astronomy. He was one of the first to observe sunspots through a telescope and hypothesized they were part of the solar surface as opposed to objects orbiting the sun.

Today sunspots are regarded as a proxy to solar activity. They are active regions having twisted magnetic fields that inhibit local convection. The region is therefore cooler than its surrounding and appears darker when viewed in visible light. The connection of sunspots to solar activity can be seen in figure 10, which compares two images taken at the same time, one in visible light and the other in ultraviolet (uv) light. The bright areas in the uv image indicate high activity and correspond almost exactly to the areas of sunspots, as seen in visible light.

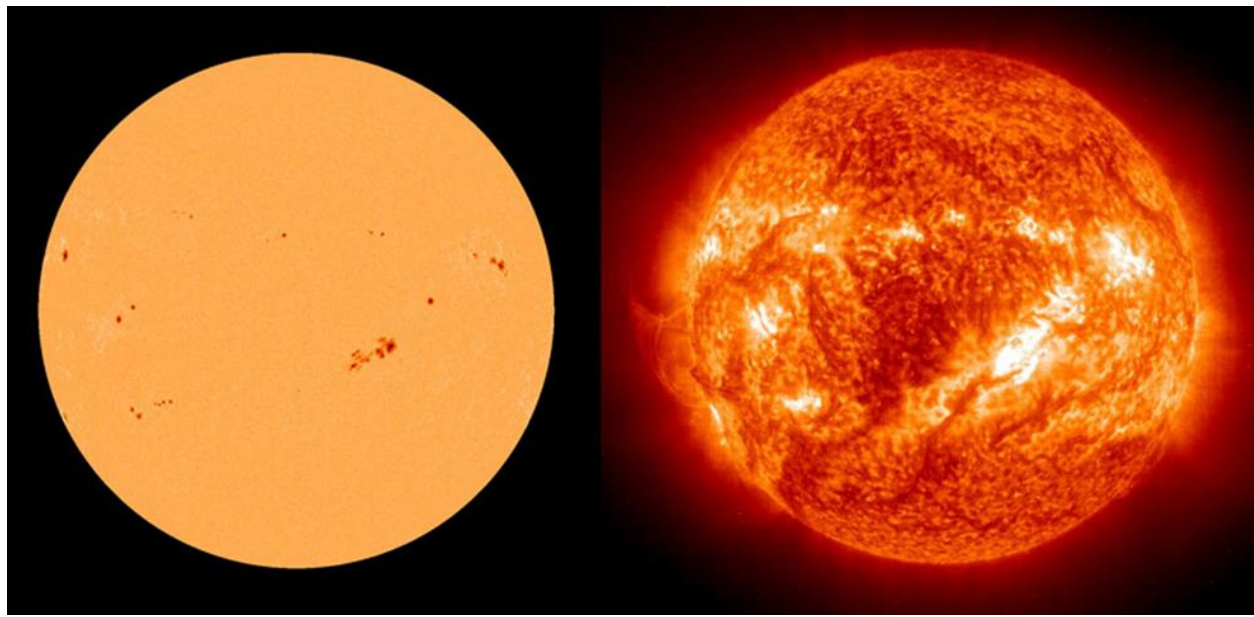


**Figure 10.** Images taken of the sun at the same time on February 3, 2002. The left image is in visible light and the right image is in ultraviolet light. Credit: ESA and NASA (SOHO)

Later in the century, in 1687, the first edition of Isaac Newton's monumental *Principia Mathematica* was published. This historical book mathematically described the laws of motion and the universal law of gravitation. Significantly, it showed that the law of gravitation could be used to derive Kepler's empirical laws of planetary motion. This could be viewed as the beginning of modern theoretical astronomy.

However, there was something troubling about the orbit of the planet Mercury that could not be entirely explained by Newton's law of gravitation. In particular the observed orbital precession did not exactly match the calculations. It was suspected that there may be an unknown planet inside of Mercury's orbit that was perturbing it and would be difficult to detect due to its proximity to the sun. In 1826 Heinrich Schwabe began a study in an attempt to understand this. It turned out the puzzle of Mercury's orbit would not be solved until Einstein applied his model of general relativity to it. However, Schwabe became interested in studying sunspots, and 17 years of meticulous studies later he published a paper describing the sunspot cycle. The era of modern space climatology began to take form in 1843 with this discovery.

Today it is recognized that understanding the sun's cyclical activity is an important aspect of modeling the space radiation environment. The record of sunspots dates back to the early 1600s, while numbering of sunspot cycles begins in 1749 with cycle number 1. Currently sunspot cycle 24 is nearly over. The sunspot cycle in recent times has been approximately  $11 \pm 1$  years long and can have significantly different levels of activity from one cycle to the next. This 11-year period is often considered to consist of 7 years of solar maximum when activity levels are high and 4 years of solar minimum when activity levels are low. In reality the transition between solar maximum and solar minimum is a continuous one but it is sometimes considered to be abrupt for convenience. The last 6 solar cycles of sunspot numbers are shown in figure 11 [WDC].

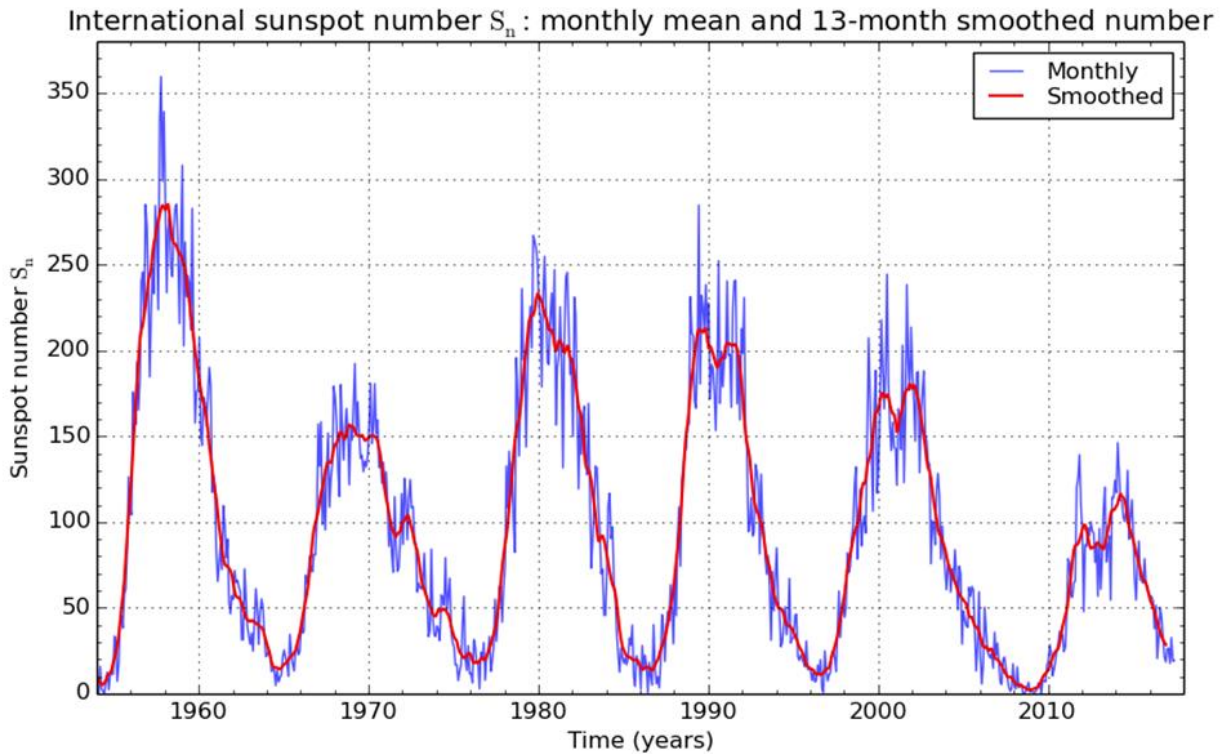


**Figure 11. Solar cycles 19 – 24.** Credit: WDC-SILSO, Royal Observatory of Belgium

Another common indicator of the approximately 11-year periodic solar activity is the solar 10.7 cm radio flux ( $F_{10.7}$ ). This closely tracks the sunspot cycle. The record of  $F_{10.7}$  began part way through solar cycle 18 in the year 1947.

The sun's influence on space climatology and space weather is pervasive. It is a source of solar protons and heavy ions, as well as trapped protons and electrons. Furthermore, it modulates these trapped particle fluxes as well as galactic cosmic ray fluxes entering our solar system. Galactic cosmic ray fluxes interact with the atmosphere and are the main source of atmospheric neutrons. These neutrons decay to protons and electrons and supply additional flux to the trapped particle population. The sun is either a source or a modulator of all energetic particle radiations in the near-Earth region. These radiations are discussed next in section V.

## 5. Modern Times – Space Climatology

The prior section brings us to the beginning of the era of space climatology. This modern era is shown by the timeline in figure 12. It is marked by the discovery of the space radiations and their impact on electronics that are used in spacecraft.

Galactic cosmic rays (GCR) were discovered in 1912 by Victor Hess using electroscopes in a balloon experiment [Ro64]. The penetrating power of this radiation was clear to Hess from these initial observations. It would turn out to be many orders of magnitude more energetic than particles emitted from radioactive materials, which were known at the time. Solar energetic particles were subsequently discovered by Scott Forbush in 1942 [Fo46]. It had been known for nearly 100 years prior that bursts of electromagnetic radiation could be emitted by the sun and

have an effect on Earth communications but this was the first indication that energetic particles could also be a problem. Shortly after that the transistor was invented at Bell Telephone Laboratories in William Shockley's group [Ga13]. The launch of the first satellites, Sputnik I and II, by the Soviet Union in 1957 was followed by the launch of Explorer I and III by the United States in 1958. The Explorer satellites led to the discovery of the Van Allen Belts by James Van Allen [Ro64]. Research began to analyze the effects of radiation on bipolar transistors, primarily for Department of Defense applications. With the beginning of this work the first Nuclear and Space Radiation Effects Conference (NSREC) was held at the University of Washington in 1964 [Ga13], [Pe13]. By 1975 SEU was reported to occur in spacecraft [Bi75], although it was apparently observed three years prior to this by the same group [Pe13a]. The NSREC was continuing to expand and held its first Short Course in 1980 [Pe13]. The Radiation and its Effects on Components and Systems (RADECS) Conference began in 1989. By 1991 the NSREC had recognized the importance of space environment research and began to include an environment session in the conference. Twenty-seven more years along the timeline brings us to the current conference in 2018.

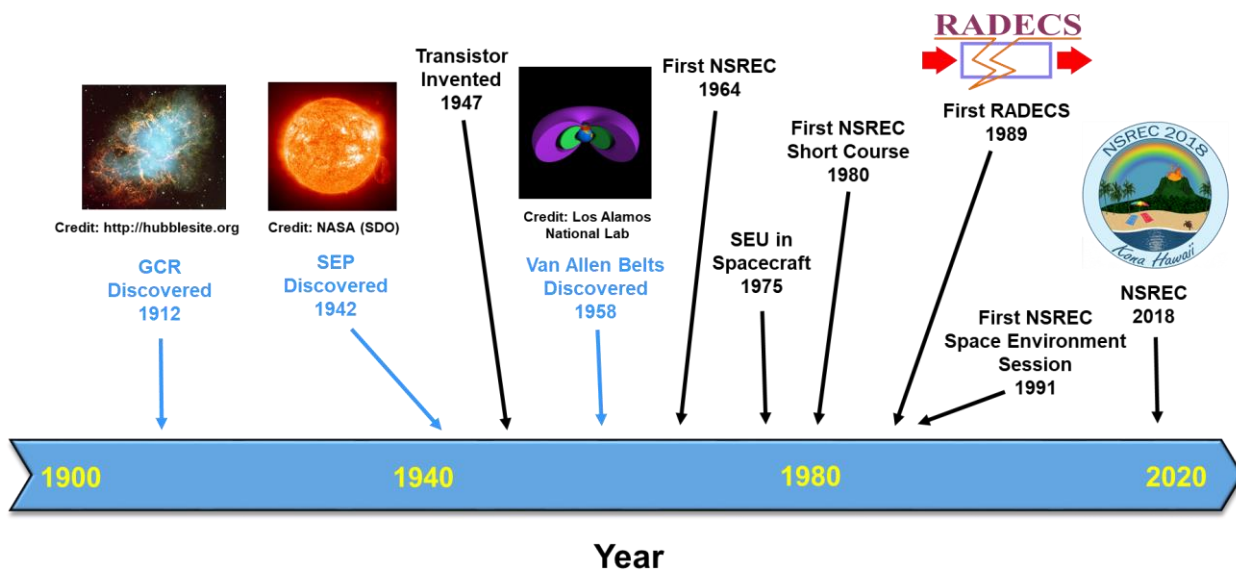


**Figure 12. Time line for modern space climatology from the year 1900 to the present and its relation to radiation effects conferences.**

With this perspective, the following discusses modern space climatology with emphasis on the items in figure 12 highlighted with blue arrows. Section A begins with a definition of space climatology and space weather. Sections B, C and D discuss properties, models and a current issue for each topic of galactic cosmic rays, solar particle events and the Van Allen Belts, respectively. Section E then applies the models discussed and shows examples of TID and SEU environments, including the effect of shielding.

#### A. Definition of Space Climatology and Space Weather

It is not difficult to find long and complex definitions of space climatology and space weather, especially the latter. These terms are generally defined here as the condition of the upper

atmosphere and beyond, more specifically the conditions of the space radiation environment for a given location or orbit. For space weather the time period of interest is the short term, e.g., daily conditions, whereas for space climatology the time period is an extended one such as a mission duration. This has implications for model use in the design and operation of spacecraft. Climatological models are used during the mission concept, planning and design phases of spacecraft in order to minimize mission risk. These are generally statistical models that allow risk projection well into the future over the mission duration. Space weather models are used during the launch and operation phases in order to manage residual risk. They are generally nowcast or short-term forecast models of the radiation environment. The following discussion deals mainly with the climatological aspects of the radiation environment.

## B. Galactic Cosmic Rays

### 1. Properties

Galactic cosmic rays (GCR) are high-energy charged particles that originate outside of our solar system. Some general characteristics are listed in Table 1. They are composed mainly of hadrons, the abundances of which are listed in the Table [Xa13]. A more detailed look at the relative abundances compared to solar abundances is shown in figure 13. The two abundance distributions are generally similar. The main differences result from fragmentation of GCR ions that tend to smooth out the GCR distribution relative to the solar abundances. This is particularly noticeable for the elements Li, Be and B ( $Z=3$  to  $5$ ), which are produced mainly from fragmentation of heavier GCR ions such as C and O in occasional collisions with interstellar hydrogen or helium. All naturally occurring elements in the Periodic Table (up through uranium) are present in GCR, although there is a steep drop-off for atomic numbers higher than iron ( $Z=26$ ).

**Table 1. Characteristics of Galactic Cosmic Rays.**

Hadron Composition	Energies	Flux	Radiation Effects	Metric
90% protons 9% alphas 1% heavier ions	Up to $\sim 10^{20}$ eV	1 to $10 \text{ cm}^{-2}\text{s}^{-1}$	SEE	LET

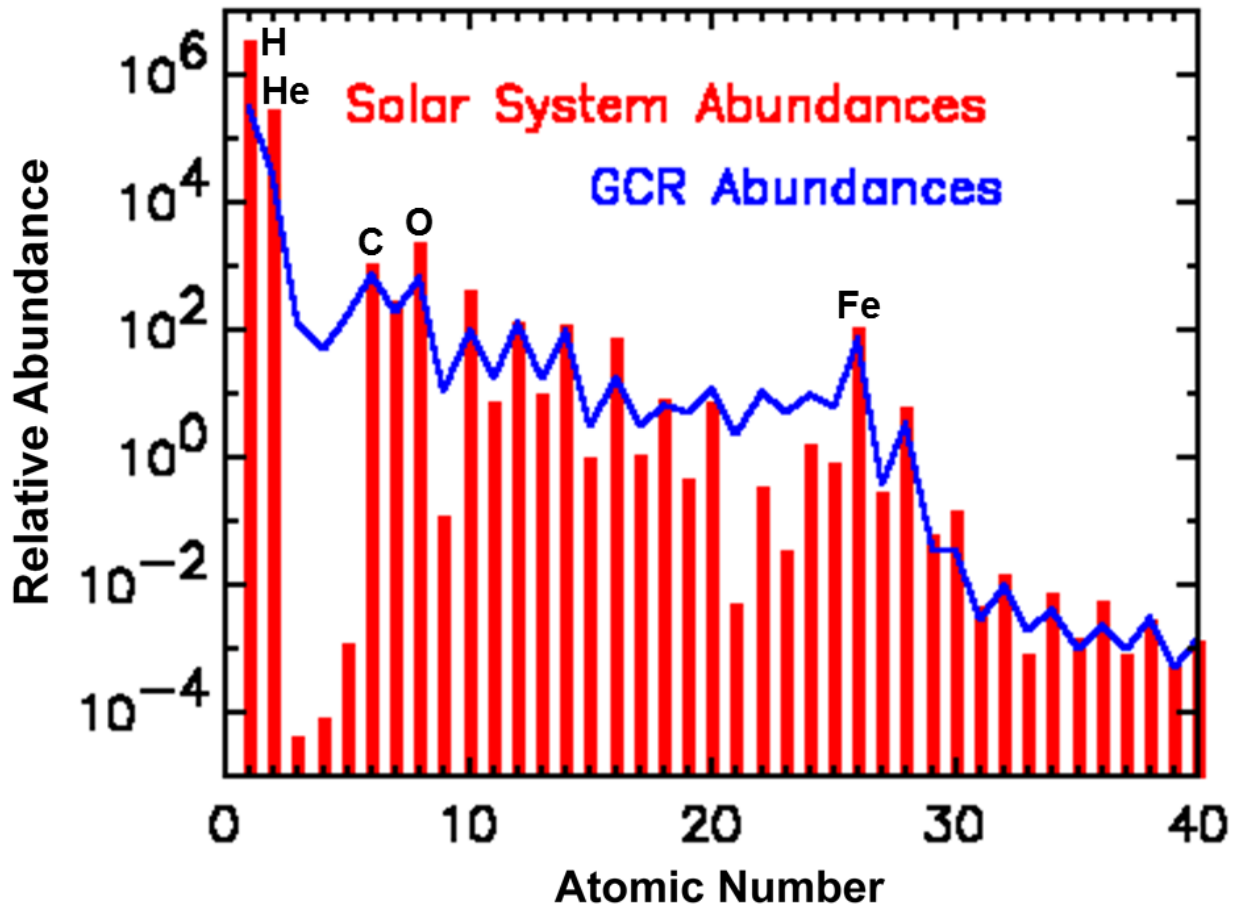


Figure 13. Comparison of the relative abundances of galactic cosmic ray and solar system ions. Credit: NASA (<https://imagine.gsfc.nasa.gov/>)

The amazing variation in energy range of GCRs is shown in figure 14 based on data compiled by Swordy [Sw01]. Energies can be up to the order of  $10^{20}$  eV, although the acceleration mechanisms to reach such extreme energies are not understood. GCR with energies less than about  $10^{15}$  eV are generally attributed to supernova explosions within the Milky Way galaxy and more recently neutron star collisions. These fluxes, on the order of a few ions  $\text{cm}^{-2}\text{s}^{-1}$ , are significant for SEE. On the other hand the origins of GCR with energies greater than about  $10^{15}$  eV are largely unknown. It is often stated that the origin of GCR with energies beyond  $10^{18}$  eV is extragalactic [Mr12]. A theoretical limit, the Greisen-Zatsepin-Kuzmin (GZK) limit [Gr66] shown in figure 14, is an upper limit in energy that a GCR proton cannot exceed if it travels a long distance as would occur if it originated in another galaxy. The reasoning is that the proton would interact with the omnipresent Cosmic Microwave Background (CMB) and lose energy to it. The CMB is residual electromagnetic radiation left from the Big Bang [Ma08]. However, this limit appears to have been exceeded many times and is a source of controversy. This illustrates how little is known about these ultra-high energy particles. Fortunately particle fluxes at these extreme energies are so low that they are not significant for SEE.

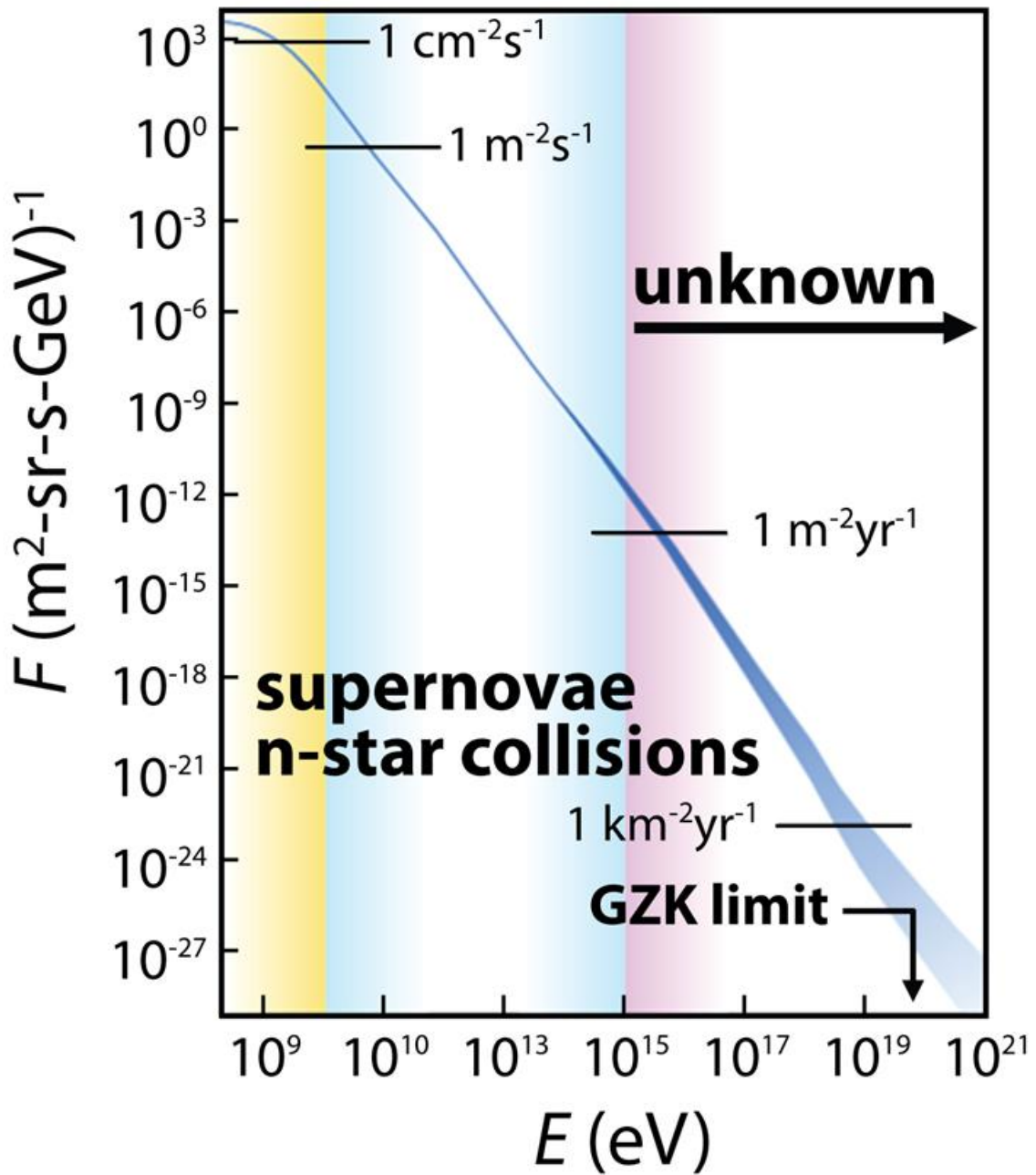
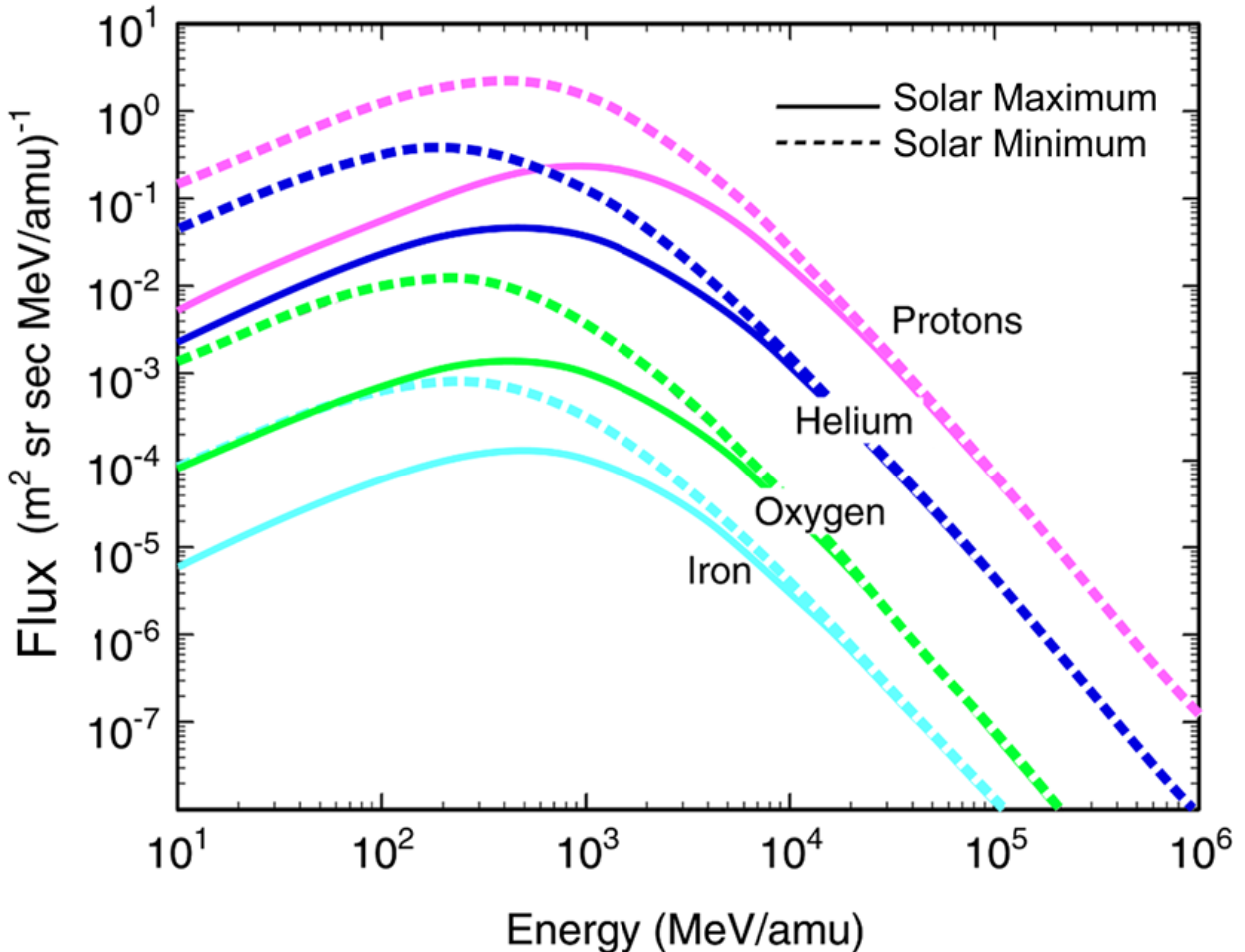


Figure 14. Differential flux vs. energy for GCRs [Sw01].

Typical GCR energy spectra for a few of the major elements during solar maximum and solar minimum are shown in figure 15 [Ba96]. The flux of the ions with energies less than about 20 GeV per nucleon is modulated by the magnetic field in the sun and solar wind. During the high activity solar maximum period there is significantly more attenuation of the flux, resulting in the spectral shapes shown in the figure.



**Figure 15. GCR energy spectra during solar maximum and solar minimum for some of the most abundant ions [Ba96].**

For SEE analyses energy spectra such as those shown in figure 15 are often converted to LET spectra. Integral LET spectra for solar maximum and solar minimum conditions are shown in figure 16. These spectra include all elements from protons up through uranium. The ordinate gives the flux of particles that have an LET greater than the corresponding value shown on the abscissa. Given the dimensions of the device sensitive volume this allows the flux of particles that deposit a given amount of charge or greater, and therefore an SEE rate, to be calculated in a simple approximation [Pe02]. The final manuscript in this Short Course by Brian Sierawski discusses the applicability and shortcomings of the LET parameter for calculating SEE rates in space.

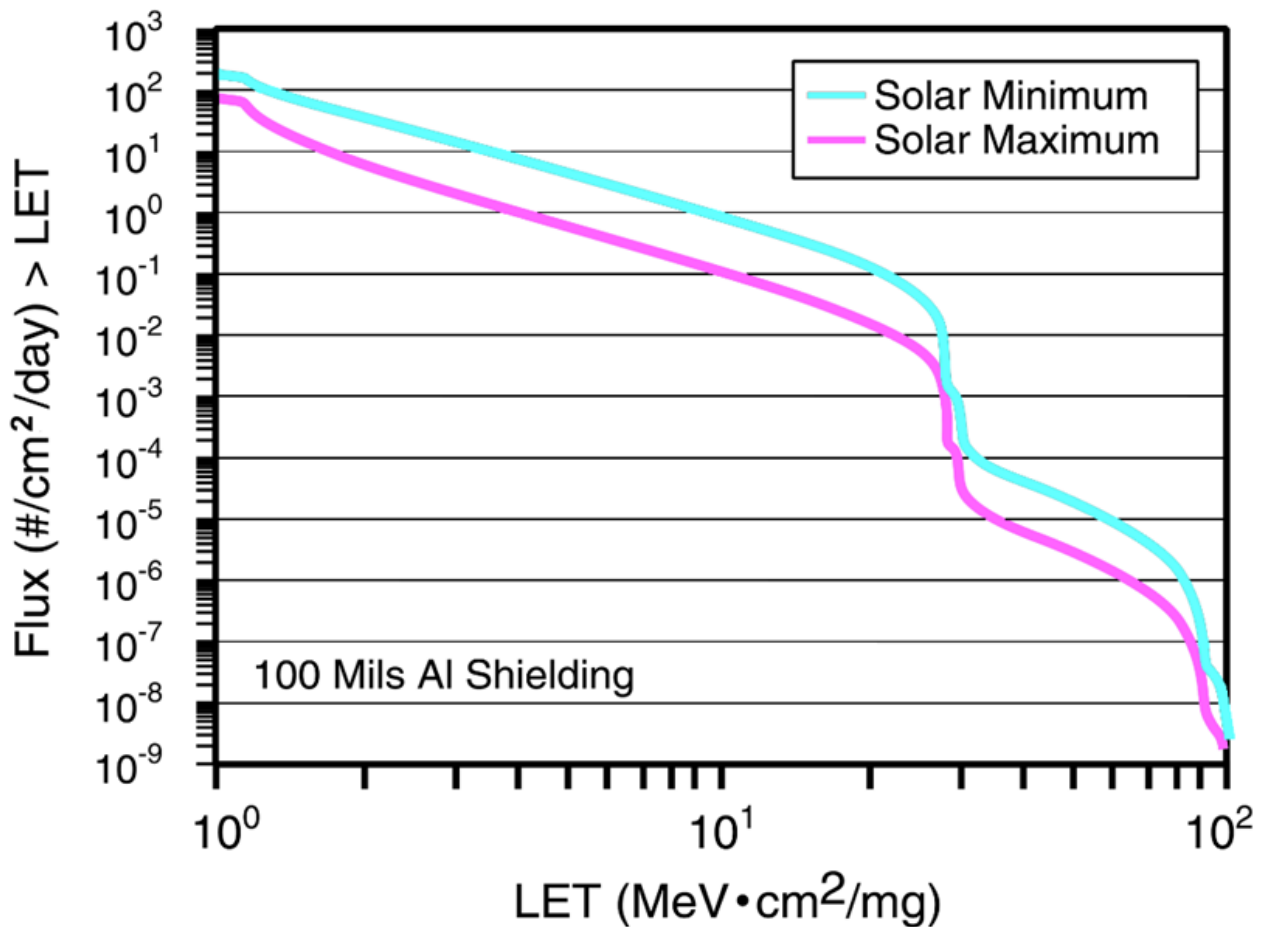


**Figure 16. GCR LET spectra for solar maximum and solar minimum conditions. From CREME96: <https://creme.isde.vanderbilt.edu>.**

The LET spectra shown in Figure 16 are applicable to geosynchronous missions where there is no significant geomagnetic attenuation. The Earth's magnetic field, however, needs to be accounted for at altitudes lower than geosynchronous. Due to the basic interaction of charged particles with a magnetic field, the particles tend to follow the geomagnetic field lines. Near the equator the field lines tend to be parallel to the Earth's surface. Thus all but the most energetic ions are deflected away. In the polar regions the field lines tend to point toward or away from the Earth's surface, which allows much deeper penetration of the incident ions. The effect of the geomagnetic field on incident GCR LET spectra is discussed for various orbits in the final manuscript of this Short Course and elsewhere [Ba97].

## 2. Models

There has been a long-time interest in developing models of GCR fluxes to aid in design of electronic systems, which began with James H. Adams' development of the GCR model in the Cosmic Ray Effects in Microelectronics 1986 (CREME86) code [Ad81], [Ad87]. This section focuses on two popular models used for calculating SEE rates in space, although there are other interesting models that are available [Da01], [Ku17], [Le06], [Ma13].

One model is that developed by R. Nymmik of Moscow State University (MSU) [Ny96]. It is currently used in CREME96 [Ty97], the updated version of the 1986 suite of codes hosted on the Vanderbilt University website, <https://creme.isde.vanderbilt.edu>. The other is the Badhwar-O'Neill model developed at the NASA Johnson Space Center [ON10], [ON15]. The two models are based on the idea that the energy spectra of GCR ions outside of the heliosphere is given by Local Interstellar Spectra (LIS). A diffusion-convection theory of solar modulation is used to describe the GCR penetration into the heliosphere and transport to near Earth at 1 Astronomical Unit (AU). This solar modulation is used as a basis to describe the variation of GCR energy spectra over the solar cycle, as shown in figure 17 for iron ions [ON15]. Both models currently use sunspot numbers as input for solar activity leading to solar modulation. The implementation, however, is different. The MSU model uses multi-parameter, semi-empirical fits to relate the sunspot numbers to GCR intensity. The Badhwar and O'Neill model solves the Fokker-Planck differential equation for the solar modulation parameter as a function of sunspot number. This implementation and various sources of GCR data are described by Pat O'Neill in [Xa13]. Figure 18 shows a comparison of the two models with data. Although both of these models are successfully used for SEE applications, the Badhwar-O'Neill model incorporates a broader and more recent data base and is used extensively by the medical community.

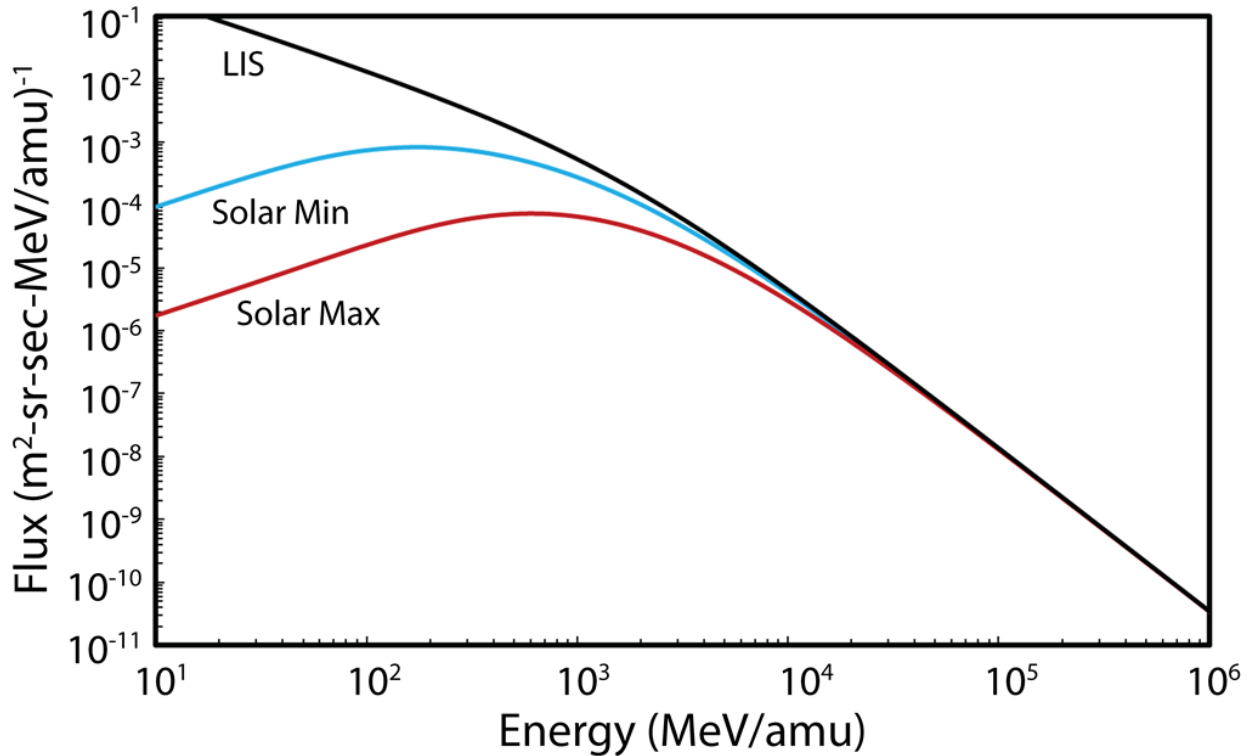


**Figure 17. Illustration of solar modulation for GCR iron ions [ON15].**

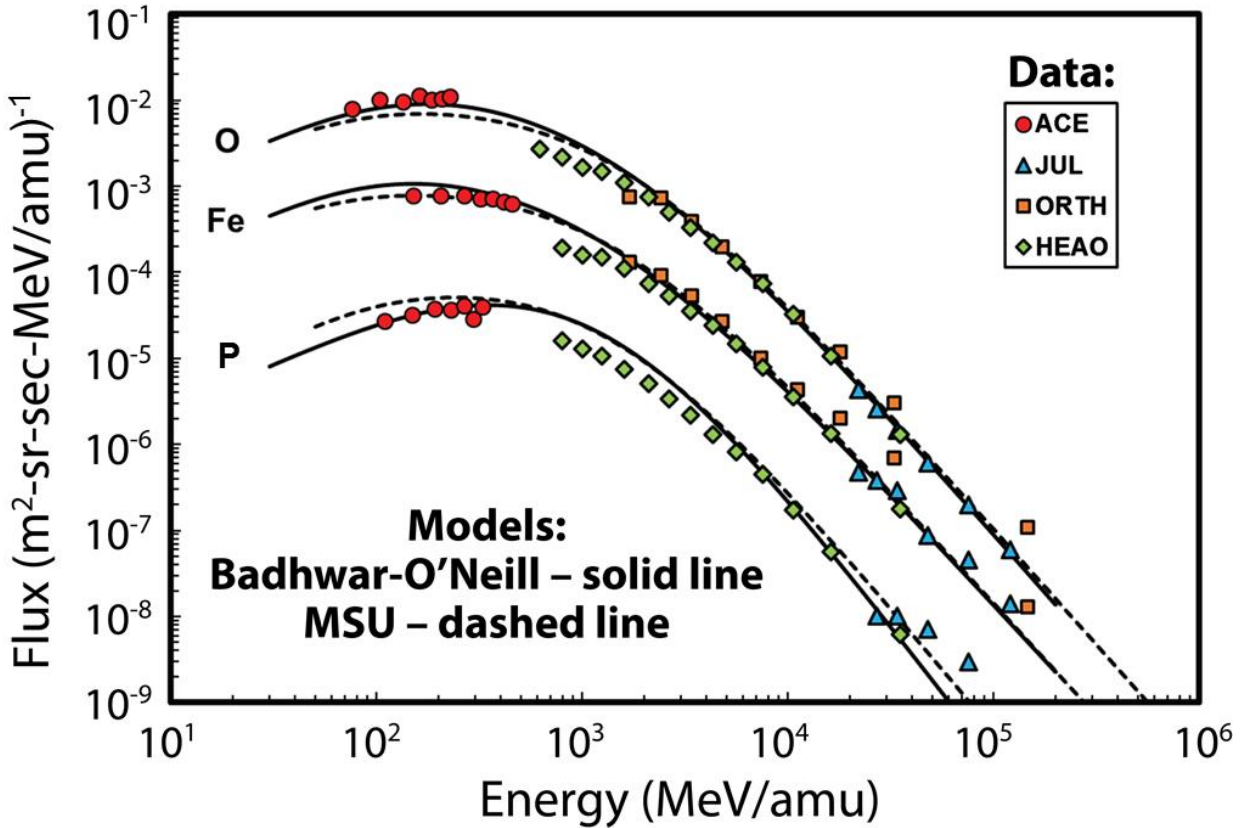


**Figure 18.** Comparison of the MSU [Ny96] and Badhwar-O'Neill 2014 [ON15] models with data from various sources.

### 3. Current Issue: Elevated Fluxes during “Deep” and Prolonged Solar Minima

In previous sections the solar modulation of GCR flux has been described. Lower solar activity levels result in higher GCR fluxes. As shown in figure 11, the most recent complete solar minimum period between cycles 23 and 24, approximately centered at the year 2009, was quite “deep” and prolonged. In fact it was the deepest solar minimum of the space era and resulted in the highest GCR fluxes observed in this era. This has raised concerns about solar cycles trending toward this behavior and how elevated the GCR fluxes could get in the future [Ma13].

One of the advantages of basing the solar modulation on sunspot numbers is that there is a continuous detailed record of sunspots dating back to 1749. This allows the GCR fluxes to be estimated over this period of time that covers 24 solar cycles. An example is shown in figure 19 for 80 MeV/amu oxygen [ON15]. It is seen that over this extended period of time the peak flux values for each solar minimum have not varied by more than about 30%. The recent deepest minimum of the space era in 2009 can be compared to the deepest since 1750, which occurred in 1810. It can also be compared to the 1977 solar minimum that is used in CREME96 as a typical minimum. The GCR models should be adequate for design of electronic systems as long as appropriate consideration is given to the recent trend in GCR fluxes.

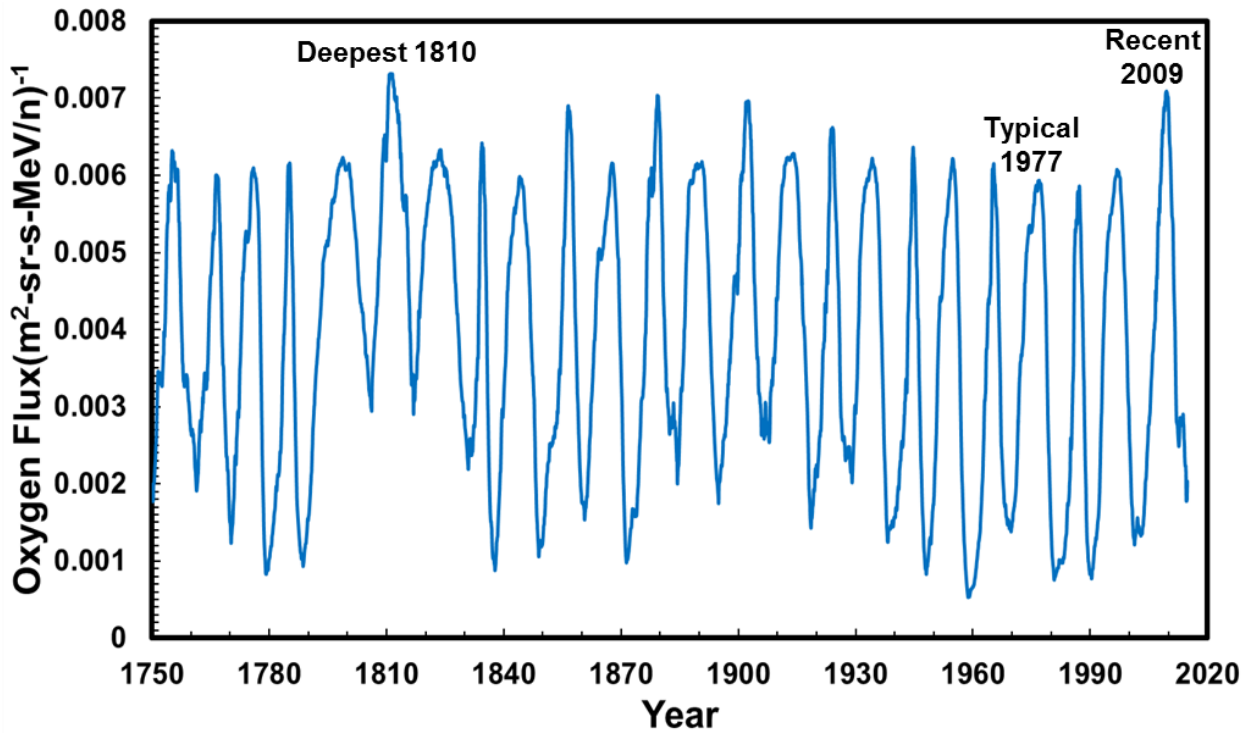


**Figure 19.** Fluxes for 80 MeV/amu GCR oxygen during solar cycles 1-24 [ON15].

### C. Solar Particle Events

#### 1. Properties

The terms solar flare, coronal mass ejection (CME) and solar particle event are often used colloquially and interchangeably. These terms actually have different meanings so this section begins by describing them. Figure 20 is a schematic showing solar energetic particle production. These particles are likely energized by magnetic reconnection, a process that converts stored magnetic energy to kinetic energy, thermal energy and particle acceleration.

One emission process of the sun is electromagnetic in nature. Irradiance is a comparatively low intensity emission that varies with the solar cycle. By contrast a solar flare is a burst of electromagnetic radiation characterized by a sudden brightening as shown on the right-hand side of figure 20. It turns out that solar flares are often, but not always, accompanied by solar energetic particles. The second general type of emission process of the sun is mass emission. The solar wind is a steady stream of plasma (a gas of free ions and electrons) consisting of protons, alpha particles and electrons in the eV to keV energy range and has an embedded magnetic field. A CME is a large eruption of plasma that carries an embedded magnetic field stronger than that of the solar wind. A CME image is shown on the left-hand side of figure 20. A CME that has a high enough speed will drive a shock wave that further accelerates particles. This is analogous to an airplane creating a shock wave if it exceeds the speed of sound. If the CME driven shock reaches Earth it can cause geomagnetic disturbances. CMEs are the second source of solar energetic particles, as shown in the

figure. Further properties of solar flares and CMEs are discussed in a review article by Reames giving a detailed account of the many observed differences [Re99].

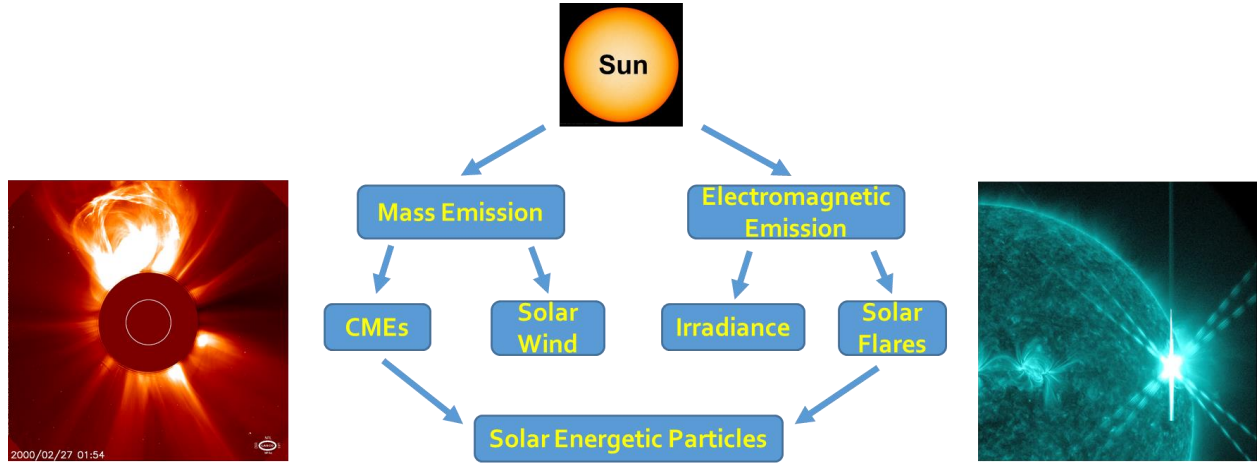


**Figure 20. Solar energetic particle production.** Image credits: NASA and ESA

CMEs are the type of solar particle events that are responsible for the major disturbances in interplanetary space and the major geomagnetic disturbances at Earth when they impact the magnetosphere. Therefore the focus here is mainly on CMEs. The mass of magnetized plasma ejected in an extreme CME can be on the order of  $10^{17}$  grams. CME speeds can vary from about 50 to 2500 km/s with an average speed of around 450 km/s. It can take anywhere from hours to a few days to reach the Earth. Table 2 lists some further general characteristics of CMEs.

**Table 2. Characteristics of CMEs.**

Hadron Composition	Energies	Integral Fluence ( $>10$ MeV/amu)	Peak Flux ( $>10$ MeV/amu)	Radiation Effects
96.4% protons 3.5% alphas ~0.1% heavier ions	Up to $\sim$ GeV/amu	Up to $\sim 10^{10}$ cm $^{-2}$	Up to $\sim 10^6$ cm $^{-2}$ s $^{-1}$	TID TNID SEE

All naturally occurring chemical elements ranging from protons to uranium are present in solar particle events. They can cause permanent damage such as TID and TNID that is due mainly to protons with a small contribution from alpha particles. Heavy ions are not abundant enough to significantly contribute to these cumulative effects. An extreme CME can deposit a few krad(Si) of dose behind 100 mils (2.5 mm) of aluminum shielding. Even though the heavy ion content is a small percentage of the total it cannot be ignored. Heavy ions, as well as protons and alpha particles in solar particle events, can cause both transient and permanent SEE.

The solar cycle dependence of both solar particle event and GCR fluxes is shown in figure 21 in which the differential flux of all carbon, nitrogen and oxygen ions in the 25 to 250 MeV/nucleon

range is shown during the time period 1974 to 1996 [Ba97]. Superimposed in blue are the sunspot numbers during that time period illustrating the activity of solar cycles 21 and 22. The solar particle event fluxes are seen as the sharp spikes in the figure, which indicate the statistical and periodic nature of these events. Note that the events occur with greater frequency during the solar maximum time periods. They are superimposed on the low level background flux of GCR approximately on the order of  $10^{-4}$  ( $\text{cm}^2\text{-s-sr-MeV/n}$ ) $^{-1}$  that slowly varies with the solar cycle as discussed in section V.B. The GCR fluxes are approximately anti-correlated with the solar cycle.

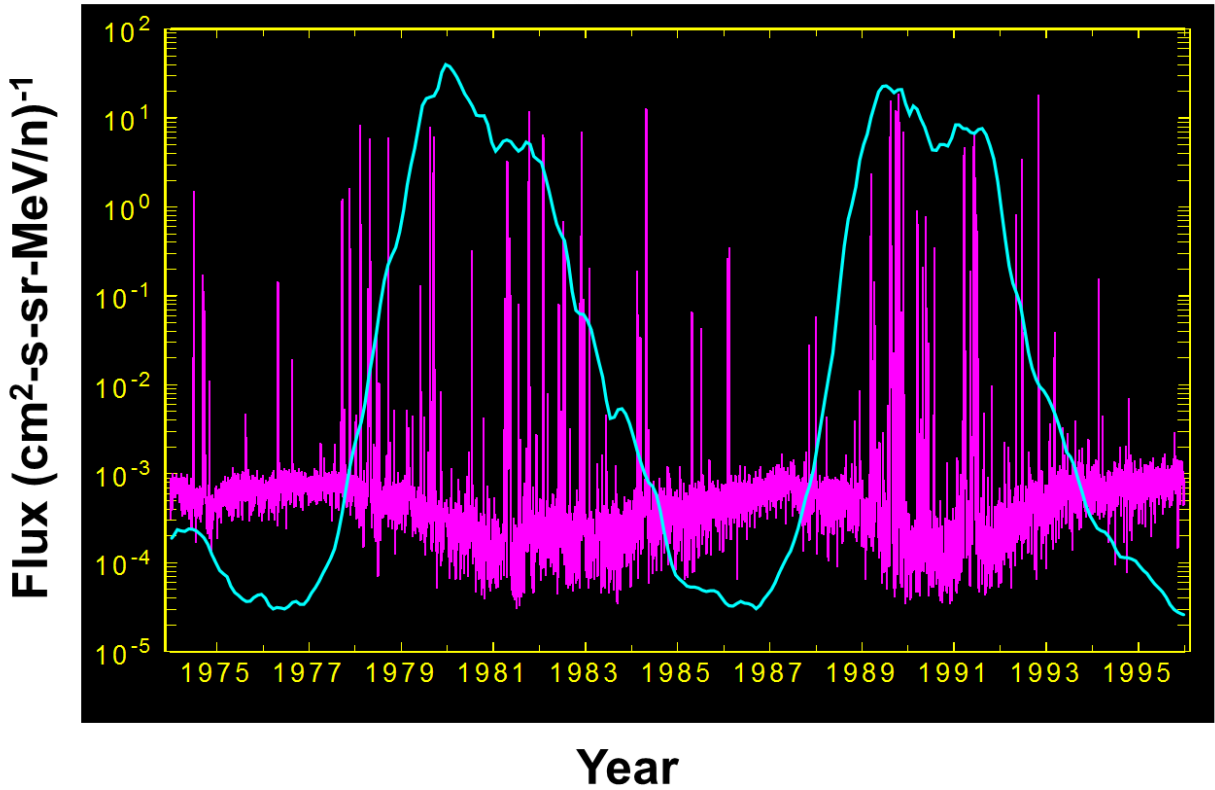


**Figure 21.** Differential flux of 25 – 250 MeV/nucleon C, N and O measured with IMP-8 spacecraft instrumentation between 1974 and 1996. Superimposed in blue are the sunspot numbers from solar cycles 21 and 22 [Ba97].

## 2. Models

There have been a number of climatological models for solar particle events developed over the years for spacecraft design. Due to the stochastic nature of events confidence level based approaches have often been used to allow the spacecraft designer to evaluate risk-cost-performance trades for electronic parts [Xa06]. The first such model was King's analysis of solar cycle 20 data [Ki74]. One "anomalously large" event, the well-known August 1972 event dominated the fluence of this cycle so the model was often used to predict the number of such events expected for a given

mission length at a specified confidence level [St74]. Using additional data a model from JPL emerged in which Feynman *et al.* showed the distribution of solar proton event magnitudes is continuous between small events and extremely large events such as that of August 1972 [Fe90]. The JPL model is a Monte Carlo based approach [Fe93]. Other probabilistic models followed based on more recent and extensive data. A model from Moscow State University introduced the full solar cycle dependence by assuming the event numbers are directly proportional to sunspot numbers [Ny99]. The NASA Emission of Solar Protons (ESP) and Prediction of Solar Particle Yields for Characterization of Integrated Circuits (PSYCHIC) models are based on Maximum Entropy Theory and Extreme Value Statistics [Xa99], [Xa00]. A summary of a number of statistical models is given in [Xa06a]. The European Space Agency (ESA) Solar Accumulated and Peak Proton and Heavy Ion Radiation Environment (SAPPHIRE) model using the Virtual Timelines method invokes a Levy waiting time distribution [Ji12] and continues to evolve [Ji18]. A new model is also under development that updated the data base of the ESP model [Ro18] and incorporates a new approach to solar cycle dependence of event numbers [Ad11].

### a) Cumulative Fluence Models

Models for cumulative solar proton fluence are useful for evaluating damage due to TID and TNID. They can also be used to determine long-term SEE rates for devices vulnerable to protons. This can be helpful for estimating the probability of a destructive SEE over the course of a mission.

The most straight forward cumulative solar proton fluence model is ESP/PSYCHIC. It is based on measured annual proton fluences during solar maximum. An advantage of this approach is that it is not necessary to know specific details about the time series of events such as the waiting time distribution, for which there are different approaches [Ju07], [Ji12]. It is implicit in the data. This is shown in figure 22 where total fluences from 21 solar maximum years are shown as points for 3 different energies [Xa00]. This graph is shown on lognormal probability paper on which a lognormal distribution appears as a straight line. The fitted distributions can then be used to obtain the lognormal parameters for N-year distributions. An example result is shown in figure 23 for 10 years in geostationary Earth orbit (GEO). Solar protons are not attenuated significantly by the geomagnetic field in GEO. As is the case for all the climatological models discussed above the output spectra are obtained at a user specified level of confidence for the mission duration. The confidence level represents the probability that the calculated spectrum will not be exceeded during the mission.

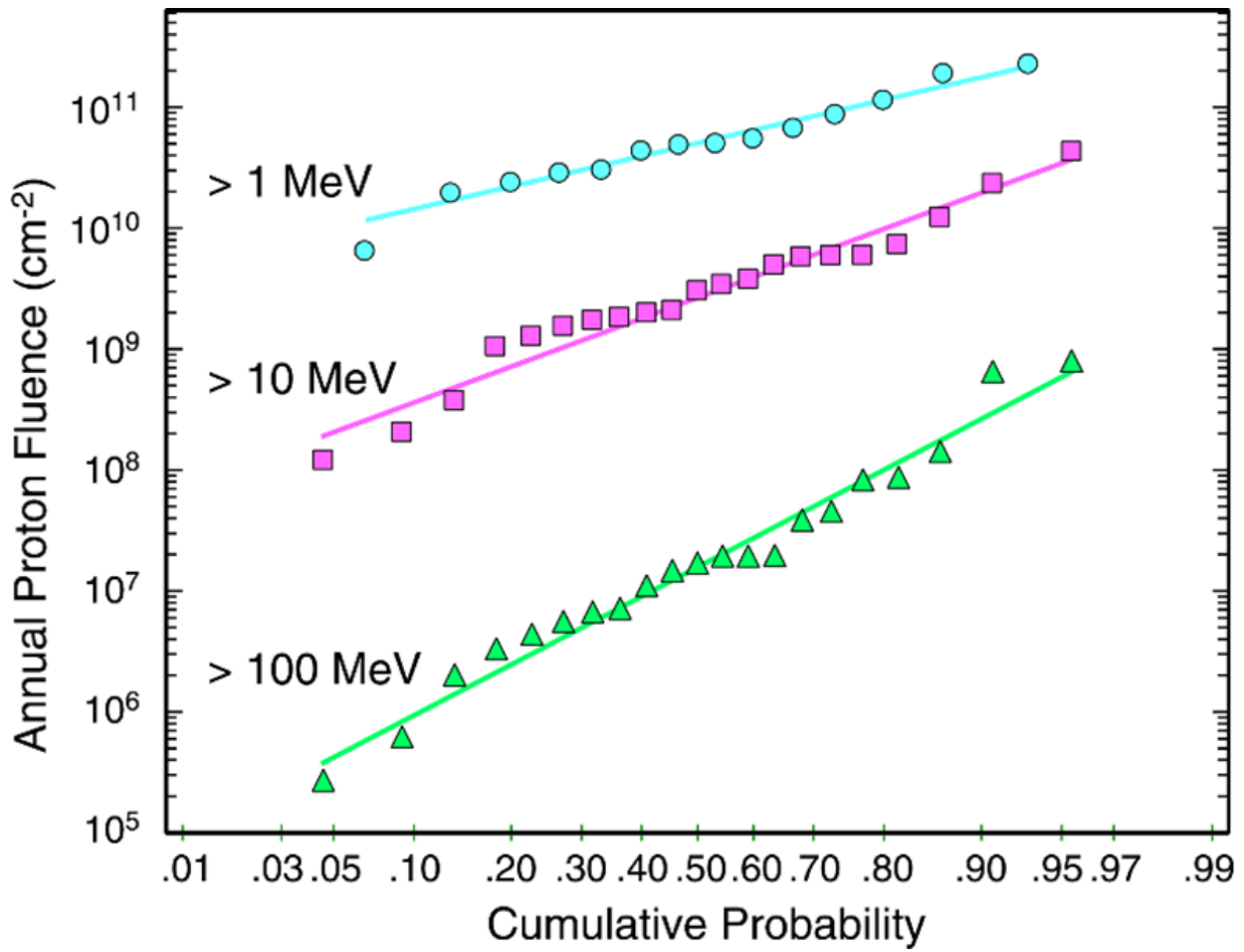
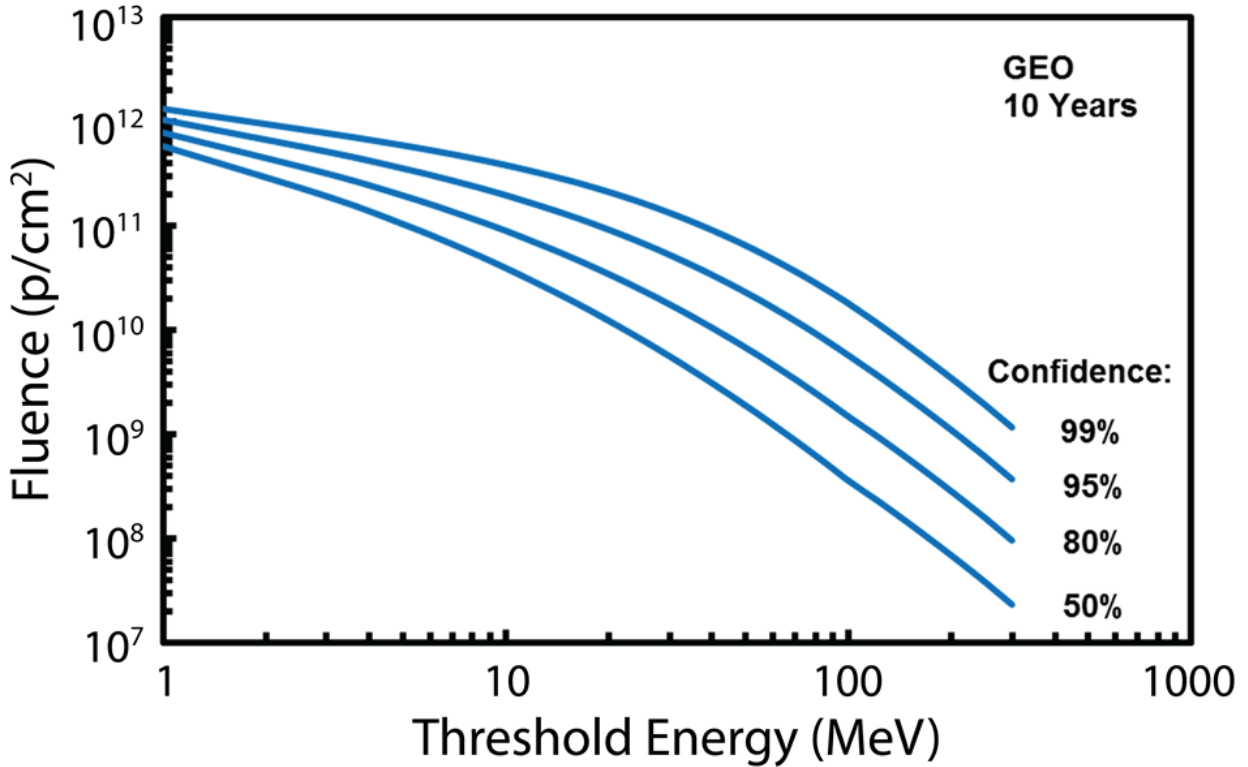


Figure 22. Cumulative annual solar proton event fluences during solar maximum periods for 3 solar cycles plotted on lognormal probability paper. The straight lines are fits to the data [Xa00].



**Figure 23.** ESP/PSYCHIC model results for cumulative fluence over a 10 year period including 7 years during solar maximum in GEO. Energy spectra are shown for confidence levels ranging from 50 to 99%.

Comparison of the JPL, ESP/PSYCHIC and SAPPHIRE models is shown in figure 24 for a 2-year solar maximum period at the 95% confidence level [Ji18]. The JPL and SAPPHIRE models are both Monte Carlo based approaches. It is seen that the largest differences between models occurs at high proton energies. A new statistical model, the Ground Level Enhancement (GLE) model, is also shown [Ra17]. It is based on randomly sampling parameters from fitted proton spectra based on neutron monitor data analyzed by Tylka [Ty09]. This model is expected to have its best accuracy at high proton energies, where it is seen to fall in the middle of predicted fluences by the other models.

During a space mission the solar particle event fluence that accumulates during the solar maximum time period is often the dominant contribution to the total fluence. A commonly used definition of the solar maximum period is the 7-year period that spans a starting point 2.5 years before and an ending point 4.5 years after a time defined by the maximum sunspot number in the cycle [Fe93]. The remainder of the cycle is considered solar minimum. Fluences that accumulate during solar minimum can be found in a number of publications [Ny99], [Xa04], [Ji12].

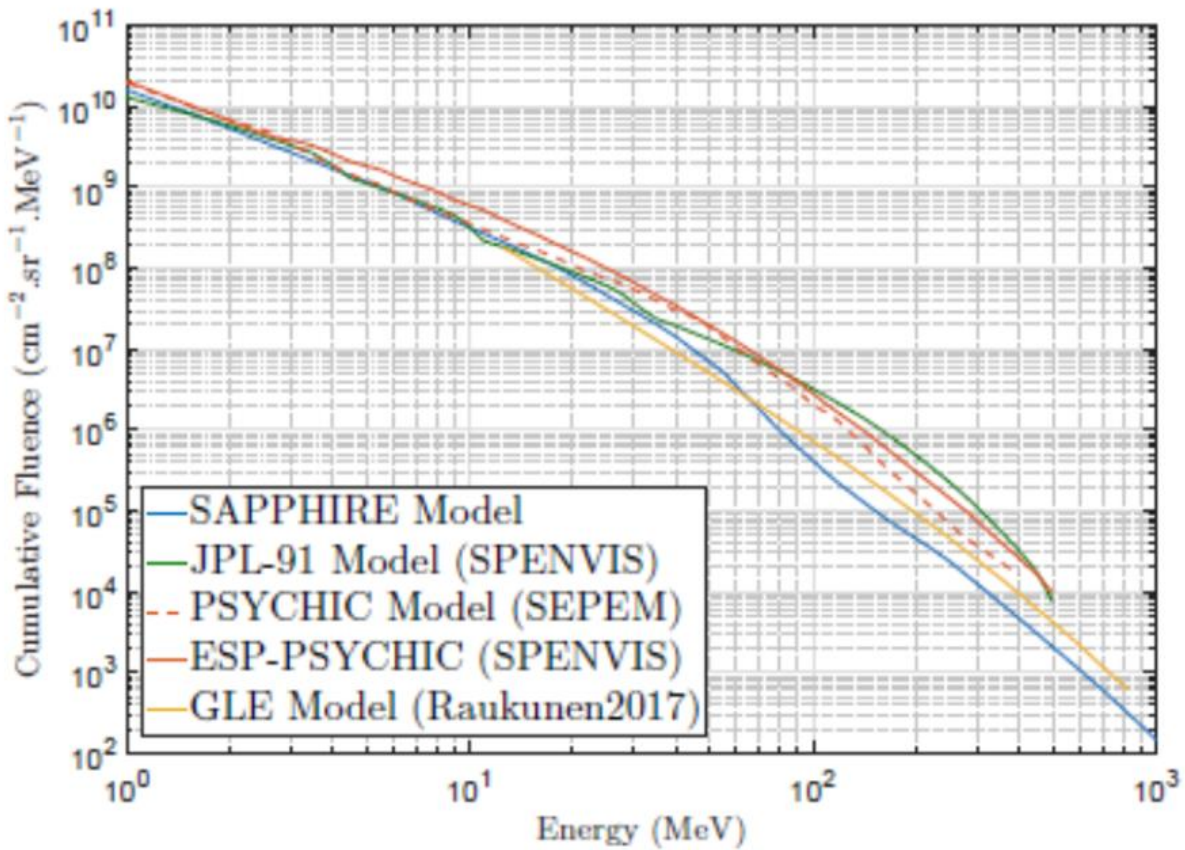


**Figure 24.** Comparison of cumulative fluences predicted by solar proton models for 2 years during solar maximum at the 95% confidence level [Ji18],

Solar heavy ion models are not as advanced as solar proton models primarily because the data are much more limited. For microelectronics applications they are needed to assess SEE. The ESP/PSYCHIC cumulative fluence model for solar heavy ions is described in [Xa07]. Due to the limited data available the probabilistic model is limited to long-term (approximately 1 year or more) cumulative fluences and not worst case events. The approach taken was to normalize the alpha particle fluxes relative to the proton fluxes based on measurements of the Interplanetary Monitoring Platform-8 (IMP-8) and Geostationary Operational Environmental Satellites (GOES) instrumentation during the time period 1973 to 2001. The energy spectra of remaining major heavy elements – C, N, O, Ne, Mg, Si, S and Fe – are normalized relative to the alpha particle energy spectra using measurements of the Solar Isotope Spectrometer (SIS) onboard the Advanced Composition Explorer (ACE) spacecraft for the 7 year solar maximum period of solar cycle 23. Remaining naturally occurring minor heavy elements in the Periodic Table are determined from measurements made by the International Sun-Earth Explorer-3 (ISEE-3) spacecraft or an abundance model. Example results for 2 years during solar maximum at the 50% (median) confidence level behind 100 mils of aluminum shielding are shown in figure 25.

LET spectra used for SEE analysis have a somewhat unusual shape. Figure 25 demonstrates that this shape is due to the elemental contributions. Interestingly, this can be related back to the

nucleosynthesis of elements in the Periodic Table described previously. The maximum LET that an ion can have in a material is called the Bragg Peak. Therefore on an LET plot such as figure 25, the fluence an ion contributes to the total LET spectrum drops sharply to zero at the Bragg Peak. For example, in silicon this occurs for protons at an LET less than 1. It is seen that protons and alphas produced in Big Bang nucleosynthesis contribute LET values to the total LET spectrum up to about 1 MeV-cm<sup>2</sup>/mg. Elements formed in stellar nucleosynthesis contribute up to an LET of about 29 MeV-cm<sup>2</sup>/mg, while elements formed from extreme event nucleosynthesis contribute over the full range of LET values.

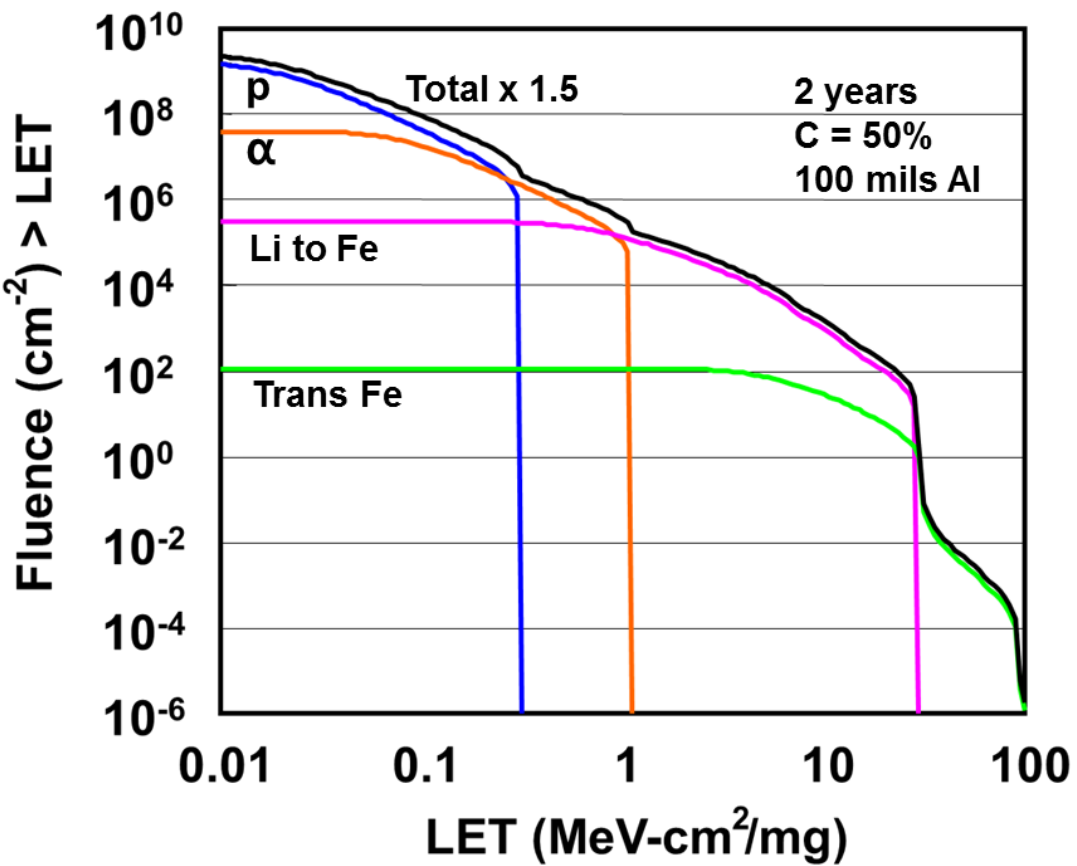


Figure 25. LET spectra for cumulative fluences of solar protons and heavy ions for 2 solar maximum years at the 50% confidence level behind 100 mils of aluminum shielding. The total fluence is multiplied by a factor of 1.5 for clarity. Also shown are the contributions to the total LET spectrum due to protons, alphas, Z = 3 (Li) to 26 (Fe), and Z = 27 to 92 (trans Fe) [Xa07].

### b) Worst Case Event Models

Another consideration for spacecraft design is the worst case solar particle event that occurs during a mission. It is important to know how high the SEE rate can get during such an event. The most straight forward approach is to design to a well-known large event. The radiation effects

community most often uses the October 1989 event while the medical community uses the August 1972 event. Hypothetical events such as a composite of the February 1956 and August 1972 events have been proposed [An94]. There are also event classification schemes in which the magnitudes range from “small” to “extremely large” that may be useful [Ny96a], [St96]. At one time the so-called Carrington Event of 1859 was widely quoted as being a worst case event over the last 400 years based on the nitrate record in polar ice cores [Mc01]. However, the glaciology and atmospheric communities disagreed with this interpretation, as the Carrington Event was not observed in most ice cores [Wo12]. Although this event resulted in a severe geomagnetic storm it is now recognized that the solar proton fluences for this event are not reliably known.

The commonly used October 1989 event is provided for use as a worst case scenario in the CREME96 suite of codes at three levels of solar particle event intensity [Ty97]. They are the “worst week”, “worst day” and “peak flux” models based on proton measurements from the GOES-6 and -7 satellites and heavy ion measurements from the University of Chicago Cosmic Ray Telescope on the IMP-8 satellite. The peak flux model covers the highest 5-minute intensity during the event. Comparisons of these models have been made with data taken by the Cosmic Radiation Environment Dosimetry (CREDO) Experiment onboard the Microelectronics and Photonics Test Bed (MPTB) during a very active period of solar cycle 23 [Dy02]. The data show that 3 major events during this time period approximately equaled the “worst day” model. An example of this is shown by the LET spectra in figure 26.

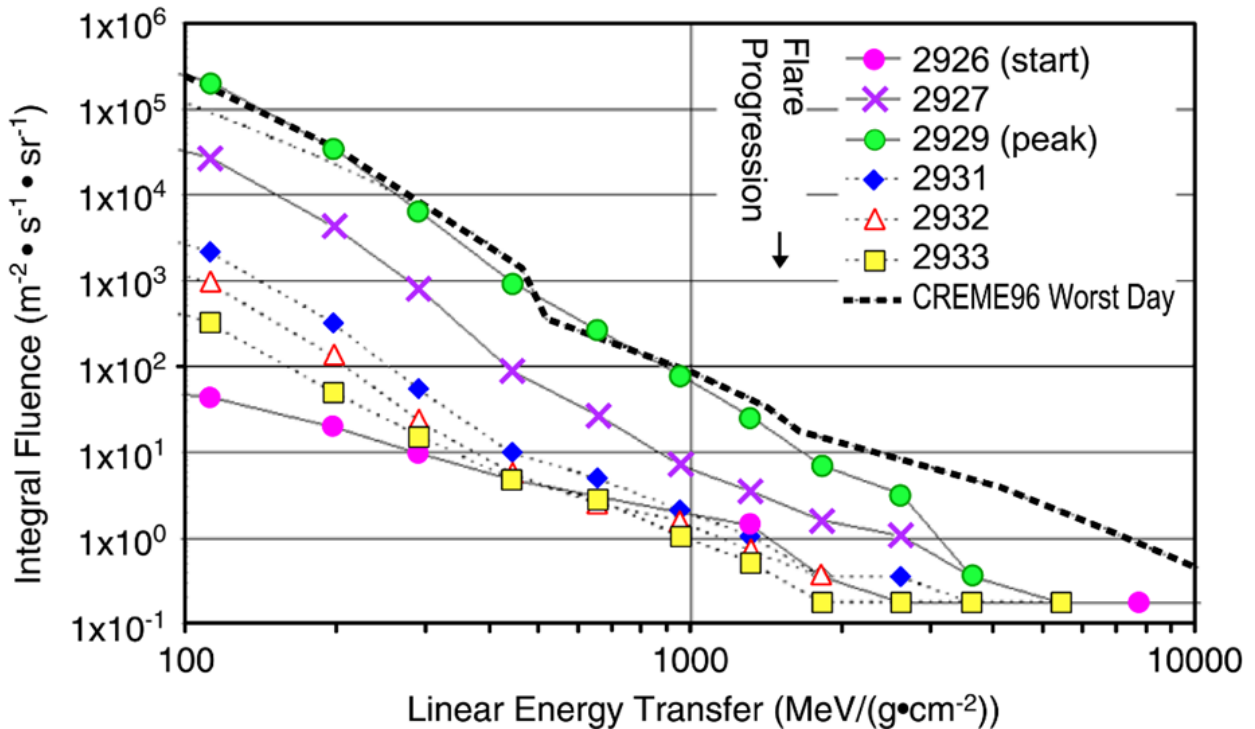


**Figure 26. Comparison of a major solar heavy ion event that occurred in November 2001 with the CREME96 “worst day” model. The progression of daily intensities is indicated with the peak intensity occurring on day 2929 of the mission [Dy02].**

Another approach to worst case event models is to use statistical methods. The idea is analogous to cumulative fluence models where a worst case event would be calculated for a given confidence level and mission duration. There have been several methods proposed for this including extreme value statistics [Xa98], [Xa99], semi-empirical approaches [Ny99], and Monte Carlo calculations [Ji12], [Ji18].

The field of extreme value statistics is one with both an extensive theoretical and applied history. It has frequently been used to describe extreme environmental phenomena such as floods, earthquakes, high wind gusts, and very appropriate for NSREC 2018, volcanoes [Gu58], [An85], [Ca88]! It has turned out to be a useful radiation effects tool when applied to large device arrays such as high density memories [Mc00], gate oxides [Va84], [Xa96], and sensors [Bu88], [Ma89].

Extreme value statistics focuses on the largest or smallest values taken on by a distribution. Thus, the “tails” of the distribution are the most significant. Here the focus is obtaining the extreme value distribution of a random process when information is known about the initial distribution.

Suppose that a random variable,  $x$ , is described by a probability density  $p(x)$  and corresponding cumulative distribution  $P(x)$ . These are referred to as the initial distributions. Figure 27 shows an initial probability density for a Gaussian distribution [Bu88]. If a number of observations,  $n$ , are made of this random variable there will be a largest value within the  $n$  observations. The largest value is also a random variable and therefore has its own probability distribution. This is called the extreme value distribution of largest or maximum values. Examples of these distributions are shown in the figure for  $n$ -values of 10 and 100. Note that as the number of observations increases the extreme value distribution shifts to larger values and becomes more sharply defined. The extreme value distributions can be calculated exactly for any initial distribution. The probability density for maximum values is

$$f_{max}(x;n) = n[P(x)]^{n-1} p(x) \quad (1)$$

The corresponding cumulative distribution of maximum values is

$$F_{max}(x;n) = [P(x)]^n \quad (2)$$

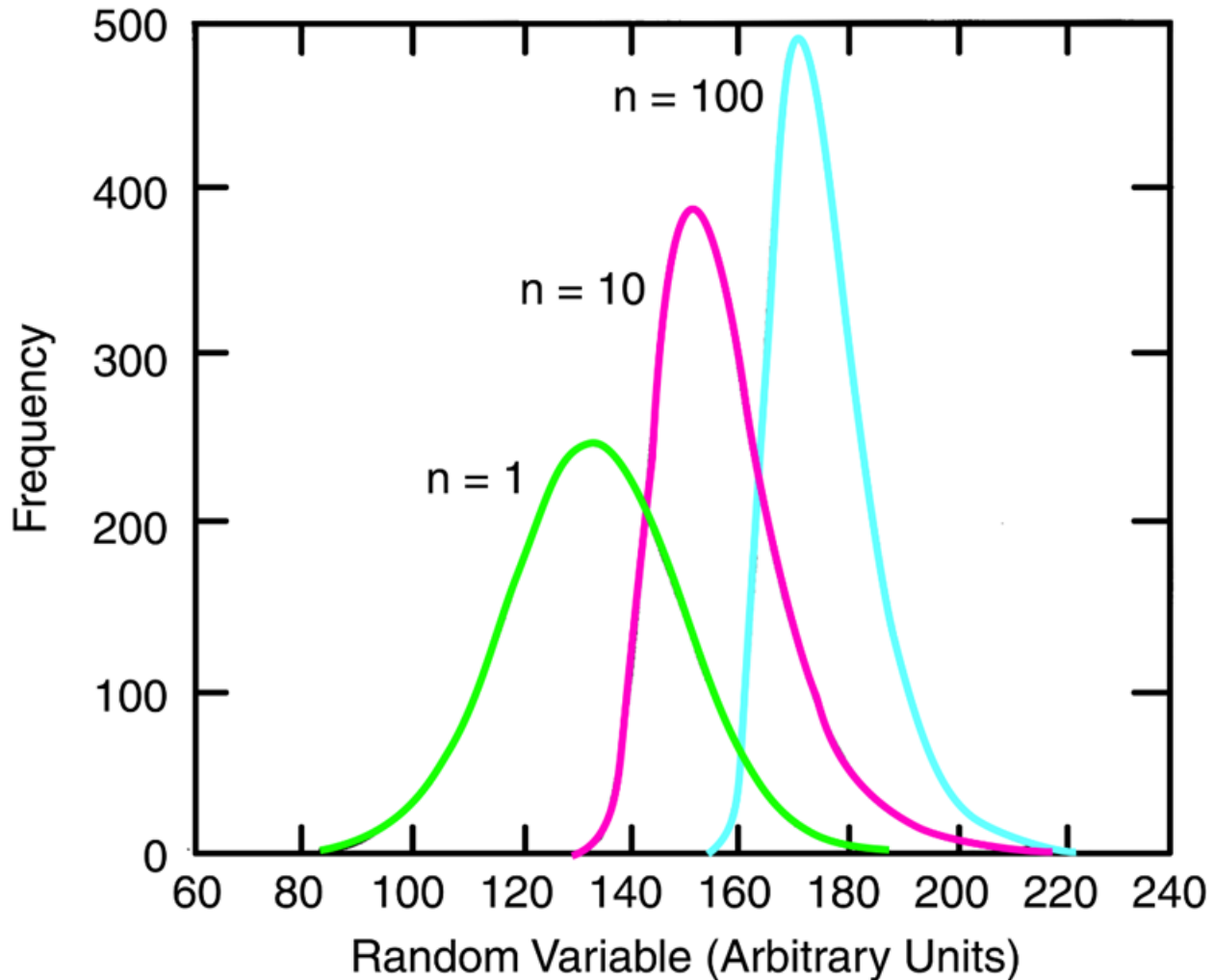


**Figure 27. Extreme value distributions for  $n$ -values of 10 and 100 compared to the initial Gaussian distribution [Bu88].**

As  $n$  becomes large, the exact distribution of extremes may approach a limiting form called the asymptotic extreme value distribution. If the form of the initial distribution is not known but sufficient experimental data are available, the data can be used to derive the asymptotic extreme value distribution. There are 3 types of asymptotic extreme value distributions of maximum values – the type I or Gumbel, type II and type III distributions [Gu58], [An85], [Ca88].

Next, an example will be shown that is directly related to the previous discussion of figure 27 before returning to the radiation environment. This is a problem about device processing distributions first identified as a radiation effects issue by Tim Oldham [Ol93]. It is also related to Marc Gaillardin's presentation on process variations and radiation effects in devices in this Short Course.

Suppose a threshold voltage adjust implant is used on an array of  $10^6$  NMOS transistors to tune the threshold voltage to the desired level. Post-implant measurements on a limited number of devices show threshold voltages with a Gaussian distribution having a mean of 700 mV and standard deviation of 5.1 mV. This is shown in figure 28. The problem is how to determine the

expected maximum and minimum threshold voltages in the array without making  $10^6$  measurements. This has significance for TID applications because the threshold voltage of an irradiated device can determine its radiation tolerance. The dose at which the array of transistors first begins to fail is more important than the dose at which the average transistor fails. Applying the methodology described above results in the extreme value distributions of maximum and minimum values for  $n = 10^6$  transistors, shown in the figure [Xa96]. Notice how far from the mean the extreme values appear for this large number of devices. The expected minimum and maximum threshold voltages in the array are 676 and 724 mV, respectively, close to 5 standard deviations from the mean value.

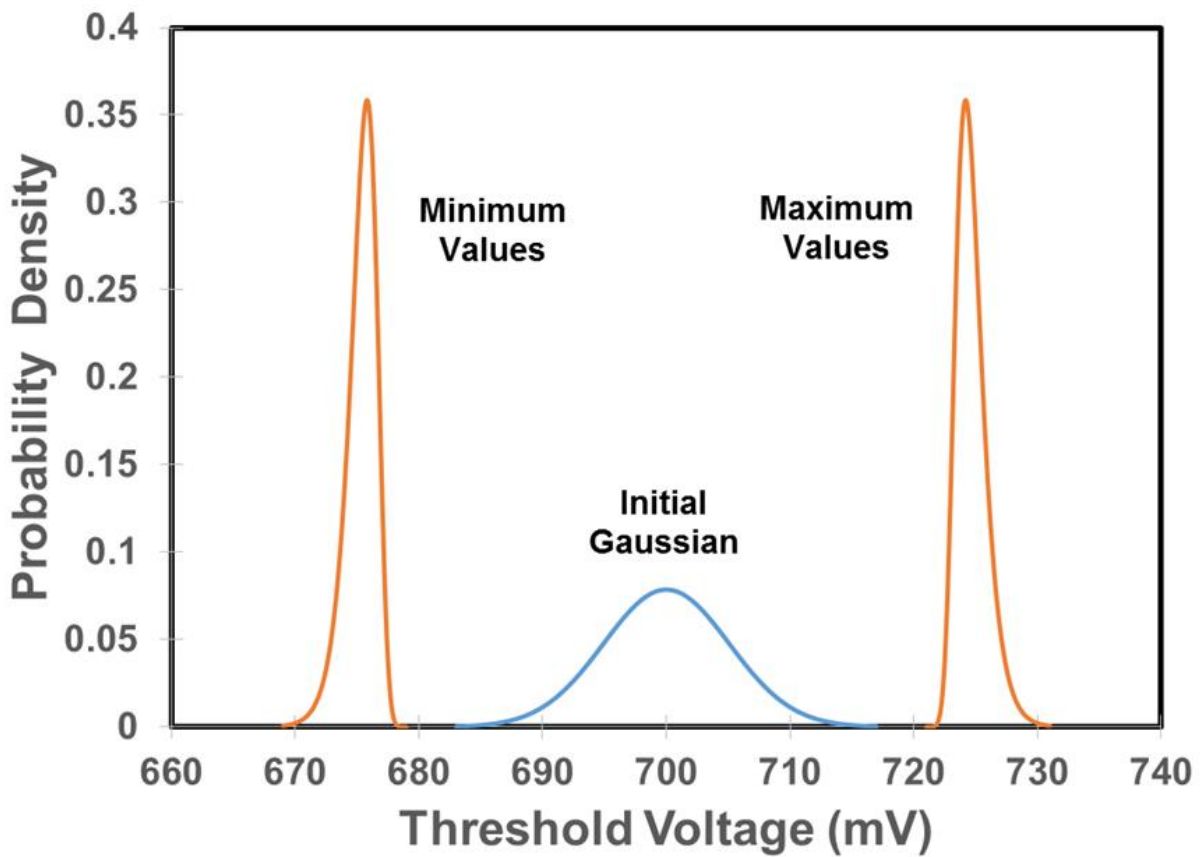


**Figure 28. Probability densities for the initial Gaussian distribution and extreme value distributions of maximum and minimum values of threshold voltage for  $10^6$  transistors after a threshold voltage adjust implant [Xa96].**

With this background the problem of worst case event models for solar particle events is now considered. In order to determine a worst case event probabilistically, either by extreme value theory or by Monte Carlo simulation, information about the initial distribution must be known. The first description of the complete initial distribution was determined using Maximum Entropy Theory [Xa99]. This is a mathematical procedure for making an optimal selection of a probability distribution when the data are incomplete by avoiding the arbitrary introduction or assumption of

information that is not available. It can therefore be argued that this is the best choice that can be made using the available data [Ja57], [Ka89]. The result is a truncated power law in the distribution of event magnitudes, shown in figure 29 for the case of  $> 30$  MeV proton event fluences. This describes the essential features of the distribution. The smaller event sizes follow a power law and there is a rapid falloff for very large magnitude events. Note that the figure also shows the October 1989 event used as a worst case event in CREME96. A variant of this distribution has subsequently been proposed [Ny07] but there is no significant improvement in the overall fit to data [Ji18], resulting in the use of both functional forms.

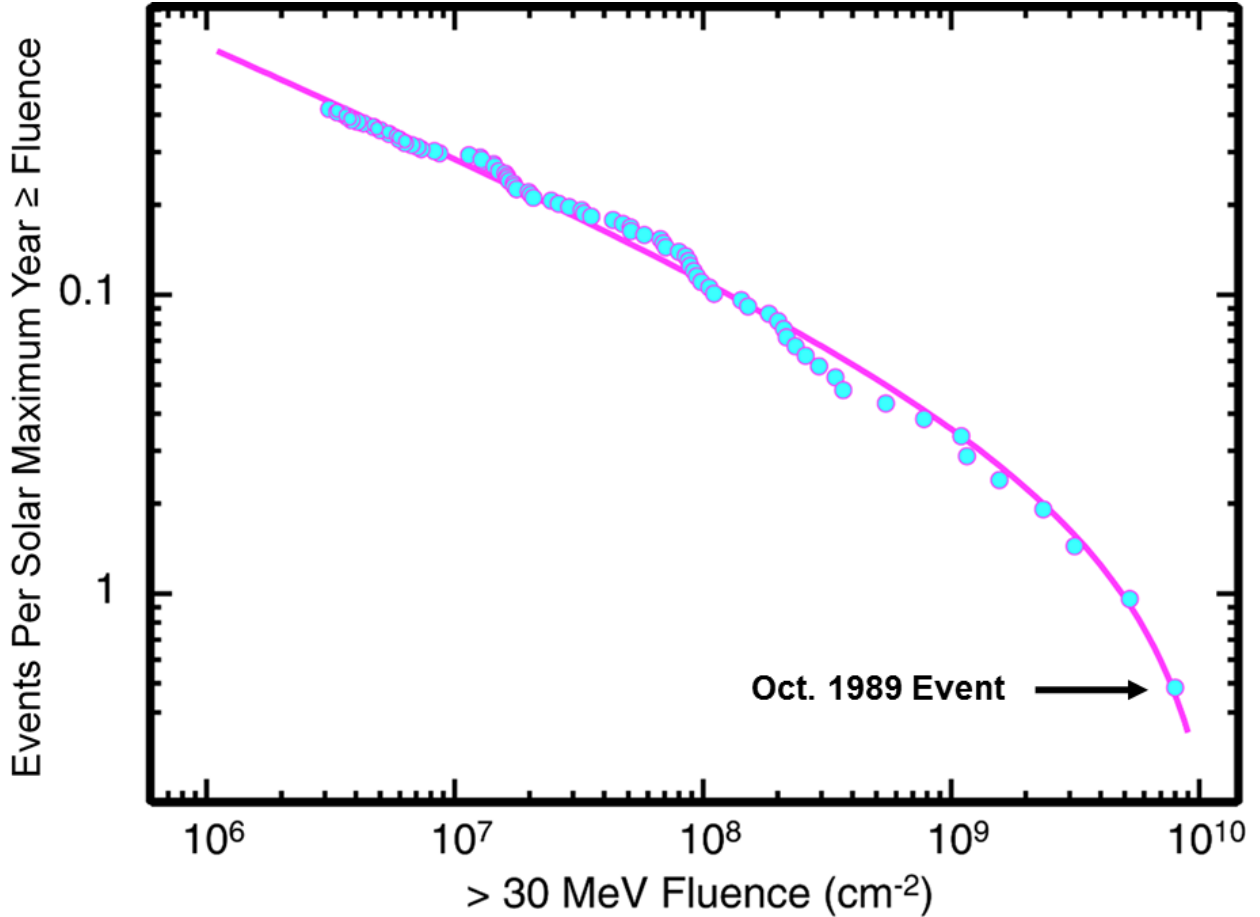


**Figure 29. Comparison of the truncated power law distribution to 3 solar cycles of data during solar maximum [Xa99].**

Given the initial distribution of event magnitudes such as the one shown in figure 29, the extreme value method can be applied to obtain a worst case event over the course of a mission. However, this situation is a little more complex. The number of events that occur during a mission is variable, so this must be taken into account. If it is assumed the event occurrence is a Poisson process [Fe93] the worst case distribution can be calculated according to [Xa98a], [Bo08]. Example results are shown in figure 30 for  $> 30$  MeV proton event fluences [Xa99]. The probability of exceeding the fluence shown on the y-axis equals one minus the confidence level.

An interesting feature of this model is the “design limit” shown in the figure. A reasonable interpretation is that it is the best value that can be determined for the largest possible event fluence, given limited data. It is not an absolute upper limit but is an objectively determined engineering guideline for use in limiting design costs.

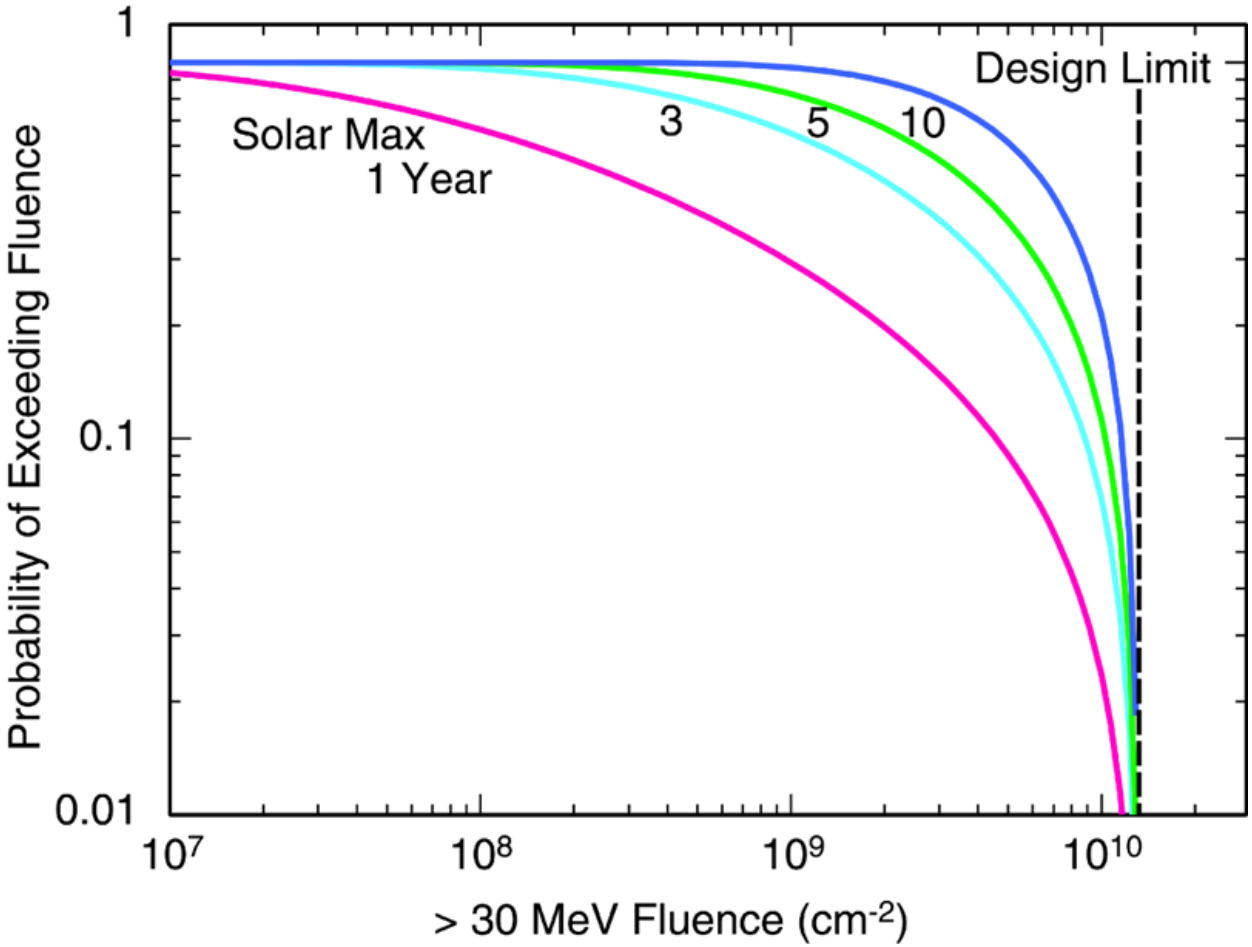


**Figure 30. Probability for worst-case event proton fluences expected during the indicated time periods during solar maximum [Xa99].**

Other worst case statistical models have been developed for both solar proton event fluences and peak fluxes [Xa98], [Xa98a], [Ny99], [Ji12], [Ji18]. There are worst case event statistical models for heavy ions but these are limited due to the lack of data [Ny99], [Ji18a]. There is also a probabilistic model for solar electrons that is part of an interplanetary electron model [Ta11].

### 3. Current Issue: Use of Statistical Models vs. Worst Case Observations

As seen in the last section there are two types of approaches for evaluating worst case solar particle events. One is to use a statistical model to calculate the worst case event that will occur

during the mission at a specified level of confidence. The other is to use a worst case observation such as the event that occurred in October 1989, as in CREME96. Figure 29 illustrates this difference. This section compares the approaches and discusses their advantages and disadvantages.

A statistical model uses the entire data base of events. There is much to consider as events can have very different characteristics in terms of magnitudes (fluence or peak flux), time duration, energy spectra and heavy ion content. On the other hand the worst case observation approach is straight forward and based on a single well characterized event. As a result the proton and heavy ion characterization of the event are self-consistent for a worst case observation. This is not necessarily true for the worst case statistical model in which the proton and heavy ion fluxes are analyzed independently. For example, proton and heavy ion fluxes can peak at different times, leaving open different approaches to what characterizes the worst case.

Another interesting comparison is that the statistical model allows the designer to make risk, cost, performance trades when selecting electronic parts. For example, a higher risk environment can be designed to in return for a higher performance or less expensive part. When using a worst case observation such as the October 1989 event there is little flexibility in the design environment. This can make requirements difficult to meet for high risk missions such as CubeSats. Thus, considering the type of mission can be important for deciding on an approach.

Lastly, it is worth noting the current state of development of these models. The worst case observation approach has a long history of successful use. Worst case statistical models for solar protons are also successfully used. However, heavy ion models are a developing area of research.

## D. The Van Allen Belts

### 1. Trapped Particle Motion in the Magnetosphere

The Earth's magnetosphere consists of both an external field due to the solar wind and an internal magnetic field. The internal or geomagnetic field originates primarily from within the Earth and is approximately a dipole field. The solar wind and its embedded magnetic field tends to compress the geomagnetic field. During moderate solar wind conditions, the magnetosphere terminates at roughly 10 Earth radii on the sunward side. During turbulent magnetic storm conditions it can be compressed to about 6 Earth radii. The solar wind generally flows around the geomagnetic field and consequently the magnetosphere stretches out to a distance of possibly 1000 Earth radii in the direction away from the sun.

Figure 31 shows the geomagnetic field, which is approximately dipolar for altitudes of up to about 4 or 5 Earth radii. It turns out that the trapped particle populations are conveniently mapped in terms of the dipole coordinates approximating the geomagnetic field. This dipole coordinate system is not aligned with the Earth's geographic coordinate system. The axis of the magnetic dipole field is tilted about 11.5 degrees with respect to the geographic North-South axis and its origin is displaced by a distance of more than 500 km from the Earth's geocenter. The standard method is to use McIlwain's ( $B, L$ ) coordinates [Mc61]. Within this dipole coordinate system,  $L$  represents the distance from the origin in the direction of the magnetic equator, expressed in Earth radii. One Earth radius is 6371 km.  $B$  is simply the magnetic field strength. It describes how far away from the magnetic equator a point is along a magnetic field line.  $B$ -values are a minimum at

the magnetic equator and increase as the magnetic poles are approached. Further background information on the magnetosphere and ( $B,L$ ) coordinates can be found in [Wa94], [Ba97], [Ma02], [Bo08].

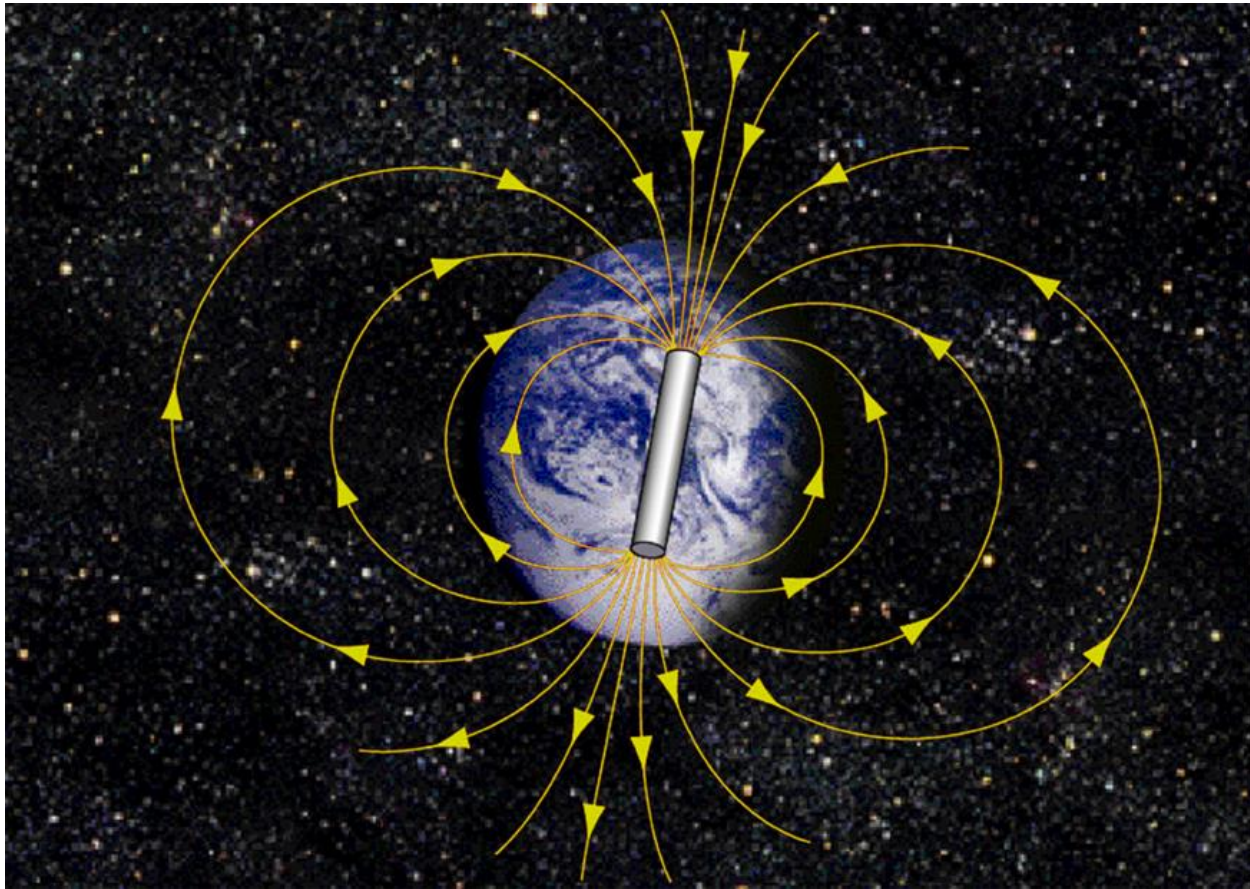


**Figure 31.** The Earth's internal magnetic field. Credit: ESA

Next the basic motion of a trapped charged particle in this approximately dipole field will be discussed. Charged particles become trapped because the magnetic field can constrain their motion. As shown in Figure 32 the motion a charged particle makes in this field is to spiral around and move along the magnetic field line. As the particle approaches the polar region the magnetic field strength increases and causes the spiral to tighten. Eventually the field strength is sufficient to force the particle to reverse direction. Thus, the particle is reflected between so called "mirror points" and "conjugate mirror points". Additionally there is a slower longitudinal drift of the path around the Earth that is westward for protons and eastward for electrons. This is caused by the radial gradient in the magnetic field. Once a complete azimuthal rotation is made around the Earth, the resulting toroidal surface that has been traced out is called a drift shell or  $L$ -shell. A schematic of  $L$ -shells is shown in Figure 33. The  $L$ -shell parameter indicates magnetic equatorial distance from Earth's center in number of Earth radii and represents the entire drift shell. It is important to understand because it provides a convenient global parameterization for a complex population of particles.

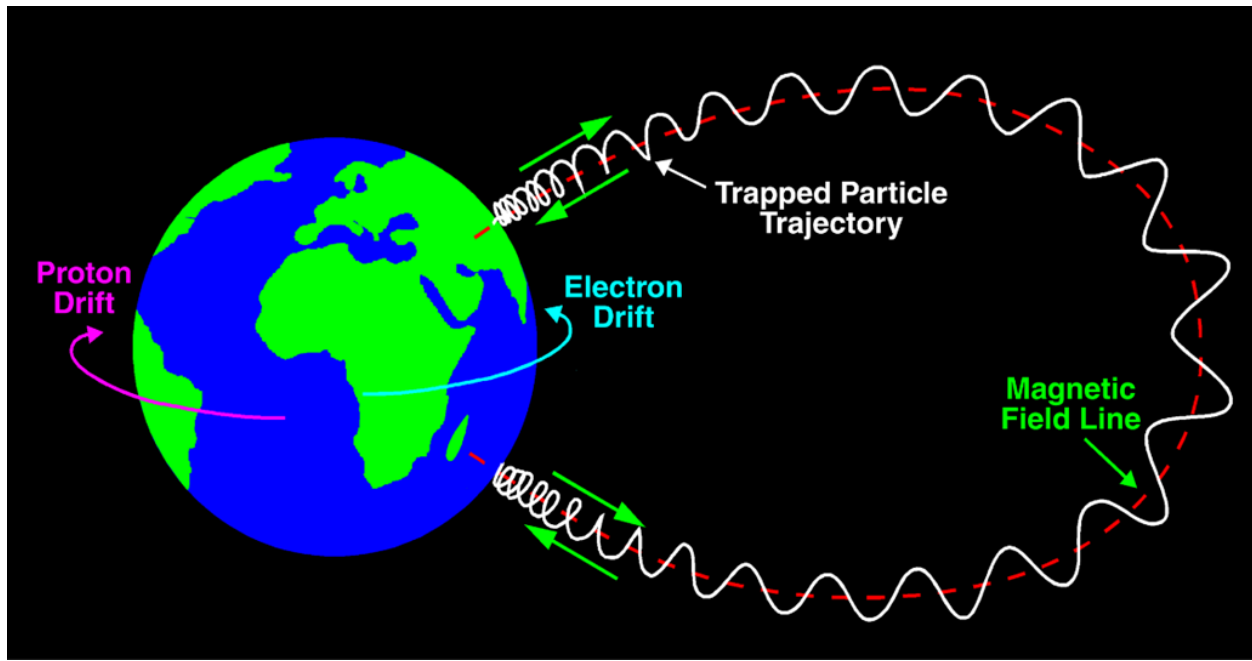


Figure 32. Motion of a charged trapped particle in the Earth's magnetic field. After E.G. Stassinopoulos [Ba97].

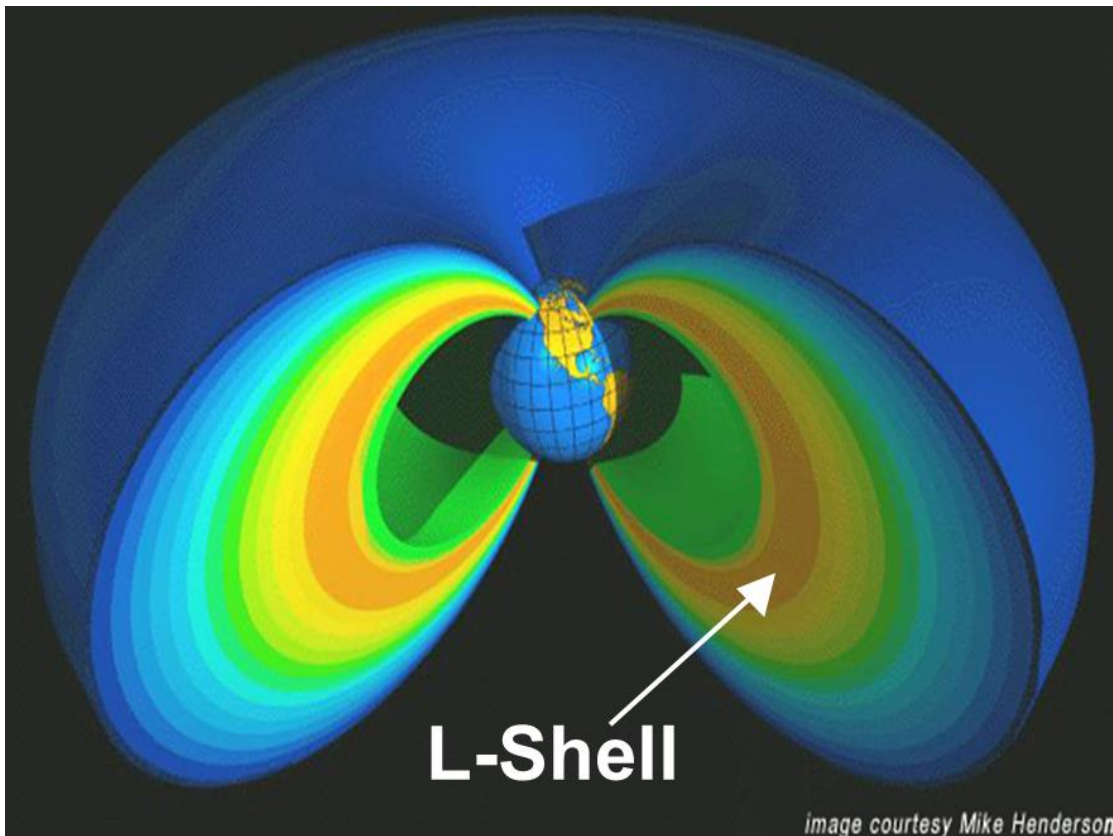


Figure 33. Illustration of the geometry of  $L$ -shells.

## 2. Trapped Protons

### a) Properties

Some of the characteristics of trapped protons and their radiation effects are summarized in Table 3 and shown in figure 34. The  $L$ -shell range is from about  $L = 1.14$  at the inner edge of the trapped environment out beyond geosynchronous orbits to an  $L$ -value of around 10. Trapped proton energies extend up to the GeV range. The energetic trapped proton population with energies  $> 10$  MeV is confined to altitudes below 20,000 km, while protons with energies of a few MeV or less are observed at geosynchronous altitudes and beyond. The maximum flux of  $> 10$  MeV protons occurs at an  $L$ -value around 1.7 and exceeds  $10^5 \text{ cm}^{-2}\text{s}^{-1}$ . The atmosphere limits the belt to altitudes above about 200 km. Trapped protons can cause TID, TNID and SEE.

**Table 3. Trapped Proton Characteristics.**

$L$ -Shell Values	Energies	Fluxes* ( $>10$ MeV)	Radiation Effects
1.14 – 10	Up to $\sim$ GeV	Up to $\sim 10^5 \text{ cm}^{-2}\text{s}^{-1}$	TID TNID SEE

\* long-term average

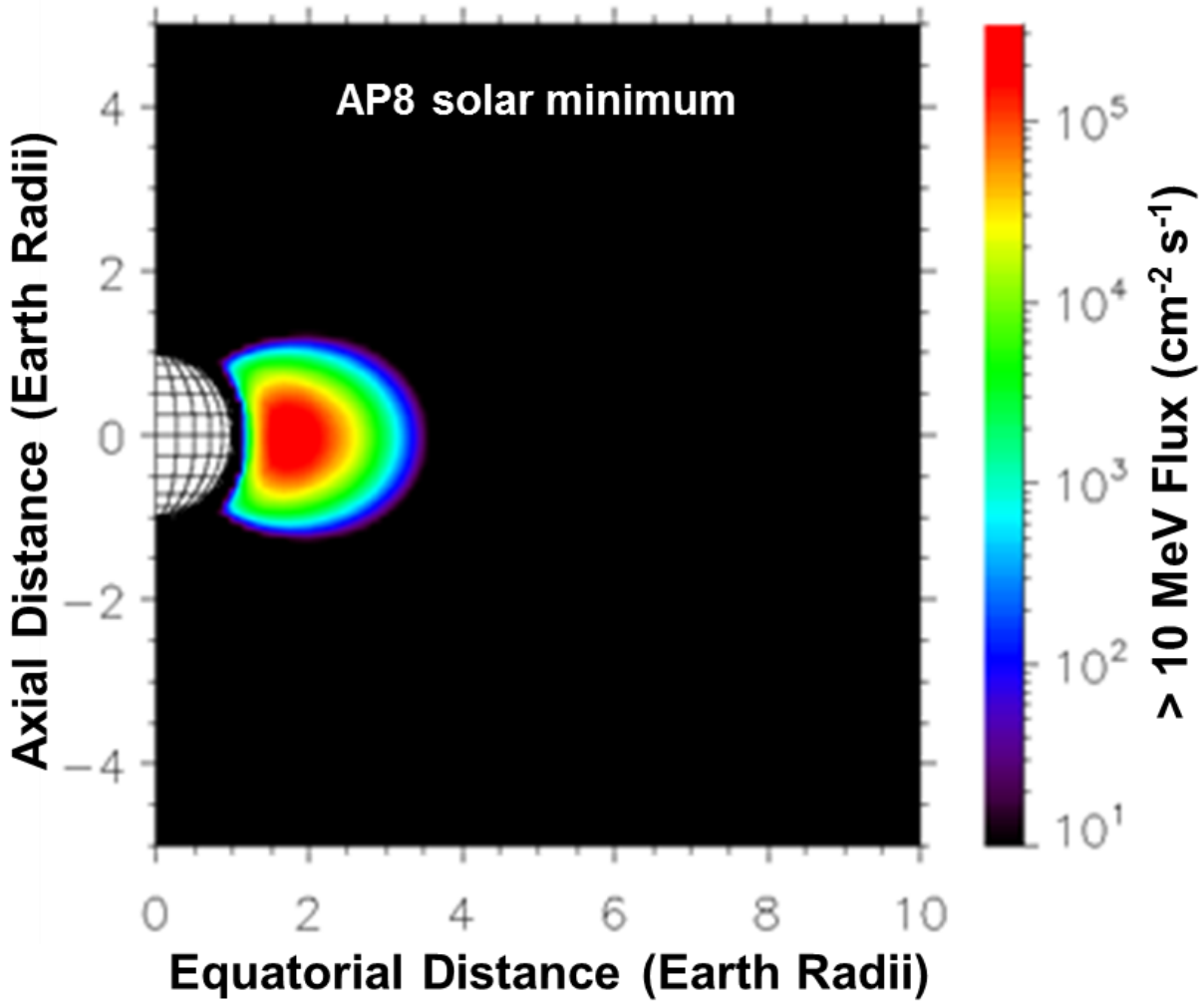


**Figure 34.** Trapped proton fluxes  $> 10$  MeV mapped in a dipole coordinate system [Bo08].

Figure 34 is a contour plot of the trapped proton population with energies  $> 10$  MeV shown in a dipole coordinate system. The x-axis is the radial distance along the geomagnetic equator in units of Earth-radii while the y-axis is the distance along the geodipole axis, also in units of Earth-radii. Thus, a y-value of zero represents the geomagnetic equator. A semi-circle with a radius of one centered at the point (0,0) represents the Earth's surface. It is seen that it is a particularly convenient way to reduce a large quantity of information and get an overview of the particle population on a single plot.

Trapped proton fluxes in Low Earth Orbit (LEO) are approximately anti-correlated with solar cycle activity. This is most pronounced near the belt's inner edge as shown in figure 35 [Hu98]. Here  $F_{10.7}$ , the solar 10.7 cm radio flux, is used as a proxy for solar activity. As solar activity increases the atmosphere expands and causes greater losses of protons to the atmosphere during solar maximum. In addition there is a decreased production of protons in the atmosphere during solar maximum coming from the Cosmic Ray Albedo Neutron Decay (CRAND) process. The CRAND process is the production of atmospheric neutrons from GCR that subsequently decay to protons

(and electrons) and can become trapped. As discussed previously, GCR fluxes are lower during solar maximum.

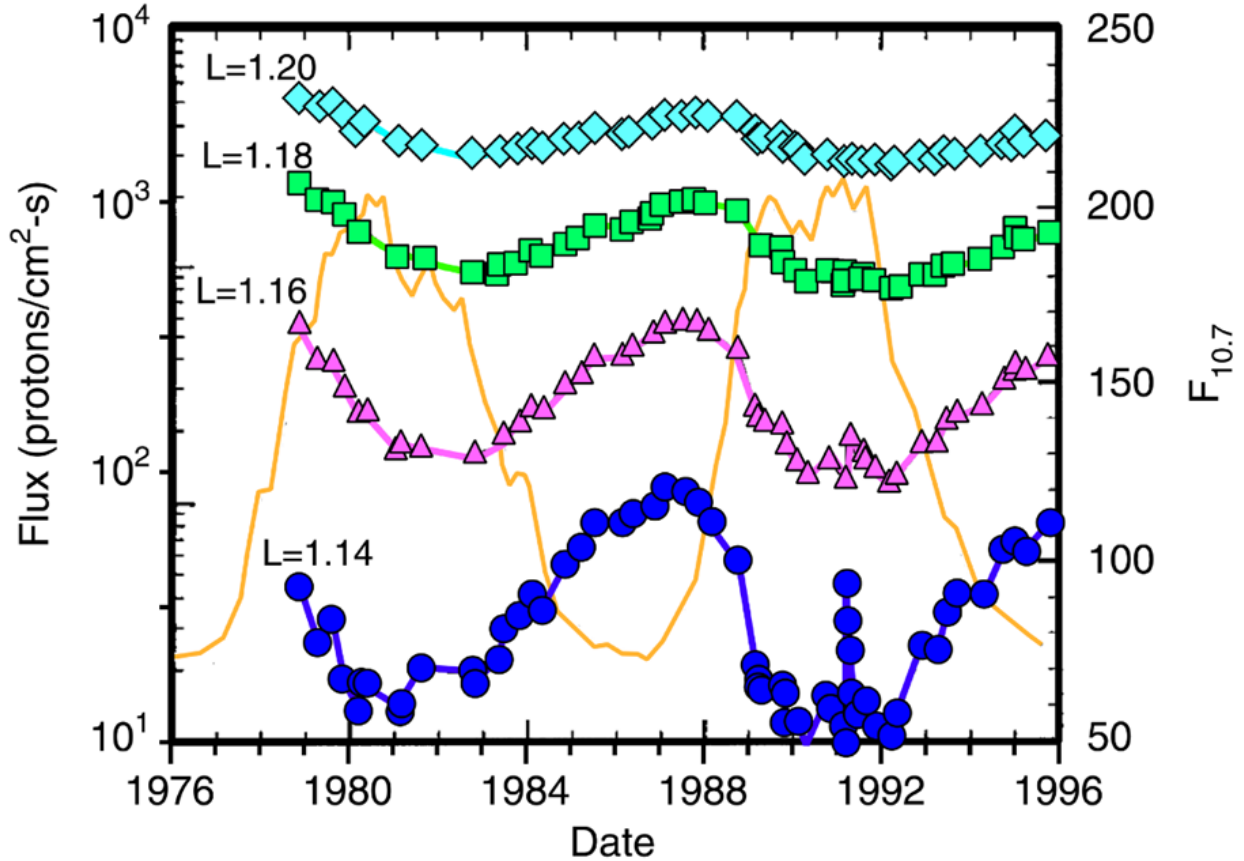


**Figure 35. Approximate anti-correlation of low altitude trapped proton flux (points) with  $F_{10.7}$  as an indicator of solar activity (gold curve) [Hu98].**

For spacecraft that have an orbit lower than about 1000 km the so-called “South Atlantic Anomaly” (SAA) dominates the radiation environment. This anomaly is due to the fact that the Earth’s geomagnetic and rotational axes are tilted and shifted relative to each other as discussed before. Thus, part of the proton belt’s inner edge is at lower altitudes as shown in figure 36. This occurs in the geographic region around South America. It is shown in figure 37 as a contour plot on geographic coordinates for > 35 MeV proton fluxes at an altitude of about 840 km [Jo15].

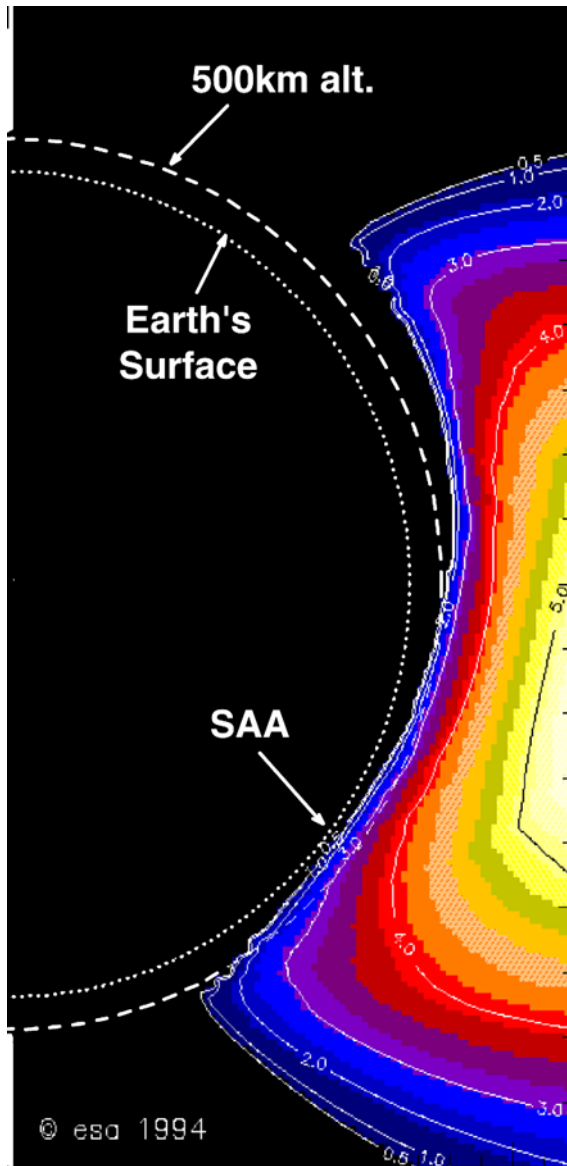
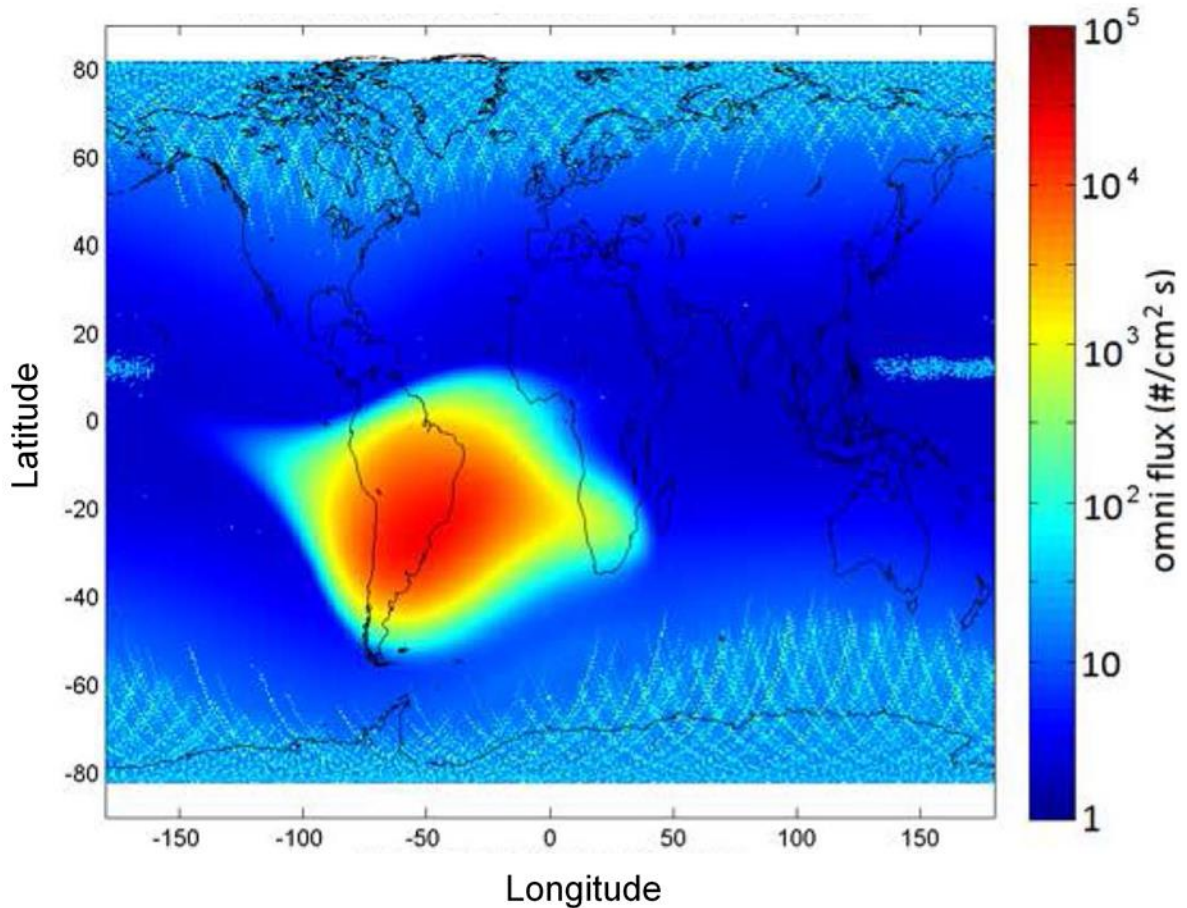
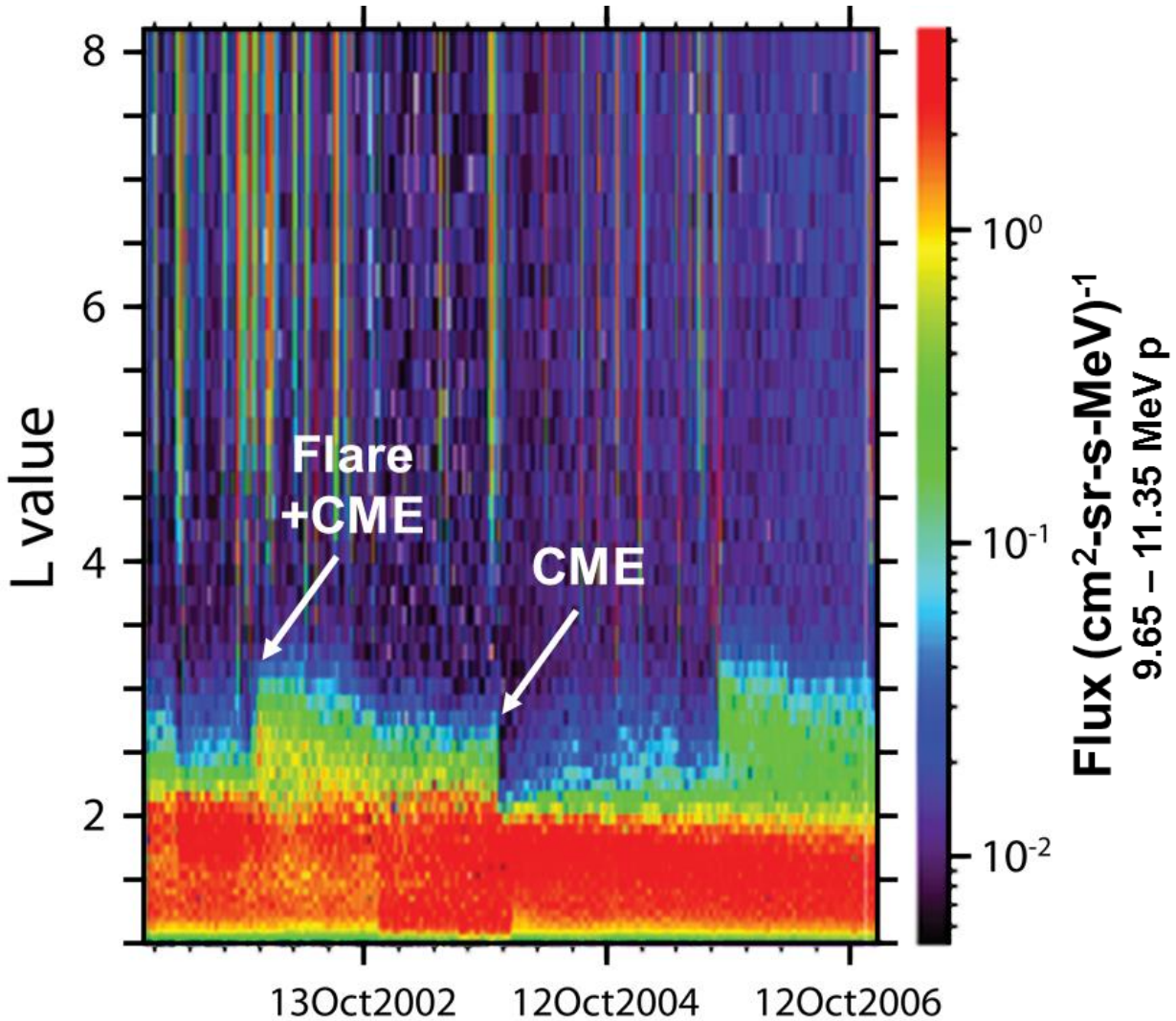


Figure 36. Illustration of the South Atlantic Anomaly (Da96).



**Figure 37.** Contour plot of proton fluxes  $> 35$  MeV in the SAA at an altitude of about 840 km measured by the Polar Orbiting Earth Satellite (POES) from July 1998 to December 2011 [Jo15].

Higher energy protons are generally fairly stable in the proton belt. However, during the 1990-1991 Combined Release and Radiation Effects Satellite (CRRES) mission the Air Force Research Laboratory (AFRL) discovered the formation of a transient proton belt in the  $L$ -shell 2 to 3 region [Gu96]. It is now known that CMEs can cause geomagnetic storms that suddenly reconfigure the belt. Figure 38 shows that enhanced fluxes can occur in the  $L$ -shell 2 to 3 region if a CME is immediately preceded by another event [Bo08]. Note that although the enhanced flux begins to decay immediately it can remain measurable for well over a year. The figure also shows that a CME can cause reduction of an enhanced flux. The details of these belt reconfigurations are not fully understood.



**Figure 38.** Sudden changes in 9.65 to 11.35 MeV trapped proton fluxes caused by solar particle events measured on the Satellite for Scientific Applications (SAC-C) [Bo08].

### b) Models

The general approach to a trapped particle model calculation is to first use an orbit generator to obtain the geographical coordinates of the spacecraft – latitude, longitude and altitude. Next the geographical coordinates are transformed to a dipole coordinate system in which the particle population is mapped. The trapped particle environment is then determined external to the spacecraft. The Space Environment Information System (SPENVIS) suite of programs has implemented a number of trapped particle models for unrestricted use at <http://www.spenvis.oma.be/>.

The well-known Aerospace Proton-8 (AP-8) trapped proton model is the eighth version of a model development effort led by James Vette. Over the years these empirical models have been indispensable for spacecraft designers and for the radiation effects community in general. The trapped particle models are static maps of the particle population during solar maximum and solar

minimum based on data from the 1960s and 1970s. Because these models provide the mean flux values of the environment, a Radiation Design Margin (RDM) is used for design specifications. Details of the AP-8 model and its predecessors can be found in [Sa76], [Ve91].

The shortcomings of AP-8 and the need for updates have been discussed [Da96]. Consequently there have been a number of notable efforts to develop new trapped proton models [Gu96], [Hu98], [He99], [Hu02], [Bo14]. Comparisons of these models with AP-8 and each other for different orbits are given by Lauenstein and Barth [La05].

Recently more comprehensive models have been developed. One such model was initially called AP-9 and is now undergoing a name change to the International Radiation Environment Near Earth (IRENE) model [Gi13], [Jo15]. AP9/IRENE allows 3 methods of calculation. There is a statistical model for the mean or percentile environment. There is a perturbed model that adds measurement uncertainty and data gap filling errors. Thirdly, there is a Monte Carlo capability that includes space weather variations. AP9/IRENE is based on data taken between 1976 and 2016. It does not include solar cycle variation, i.e., output is averaged over the solar cycle. As a result of its probabilistic approach and use of percentiles, confidence levels can be used for design specifications. The other recent comprehensive model is the Global Radiation Earth Environment model (GREEN) [Si18]. GREEN is an integration of AP-8 with other models that have been developed in order to expand the overall energy and orbital capabilities. Results for the GREEN model were not available at the time of this writing.

Figure 39 is a comparison of AP-8 and AP-9/IRENE for a polar LEO. The orbital parameters used were those of the Landsat-8 satellite. This provides a reasonable overall comparison as the spacecraft flies through varying portions of the proton belt multiple times each day. Although there are large differences between the models at energies less than 1 MeV, these energies are not significant for most applications. Over most of the remaining energy range the AP8 model shows higher fluxes during solar minimum compared to solar maximum, as expected, while AP9/IRENE generally results in the highest fluxes. AP9/IRENE also extends to higher energies, which is due to the incorporation of the NASA Van Allen Probes data.

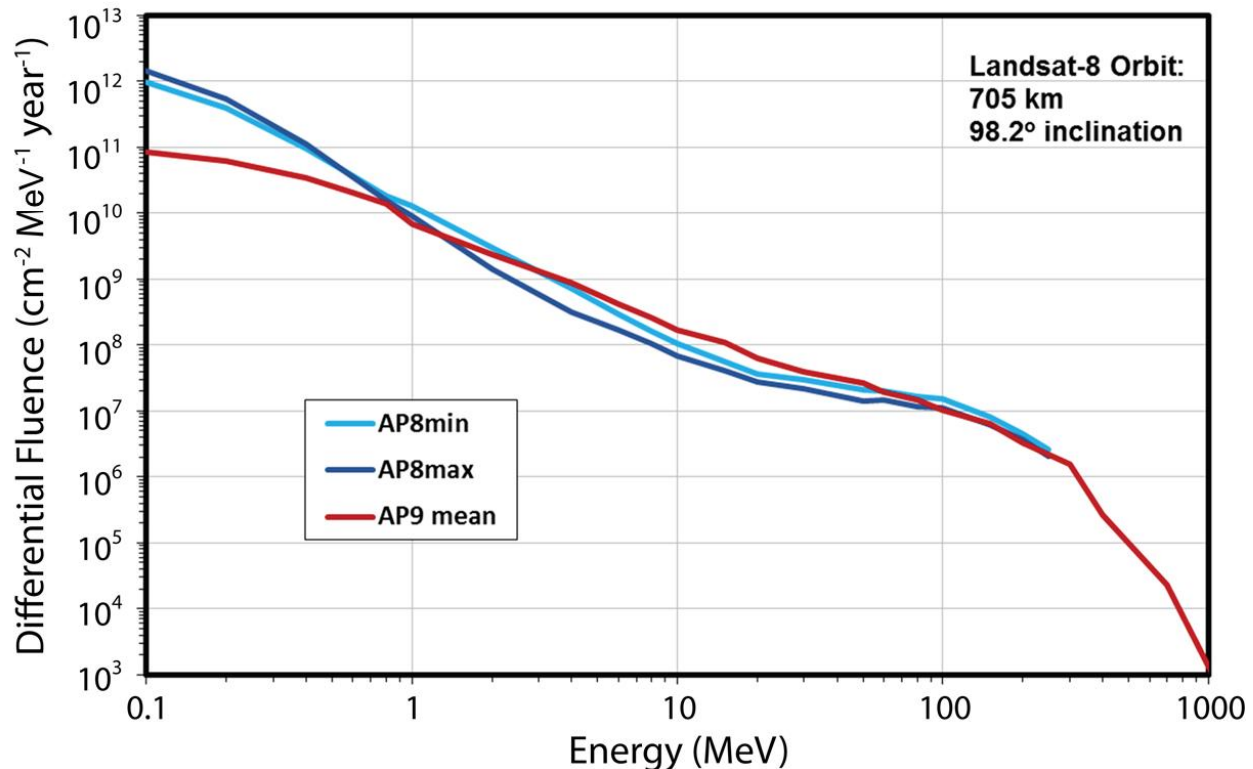
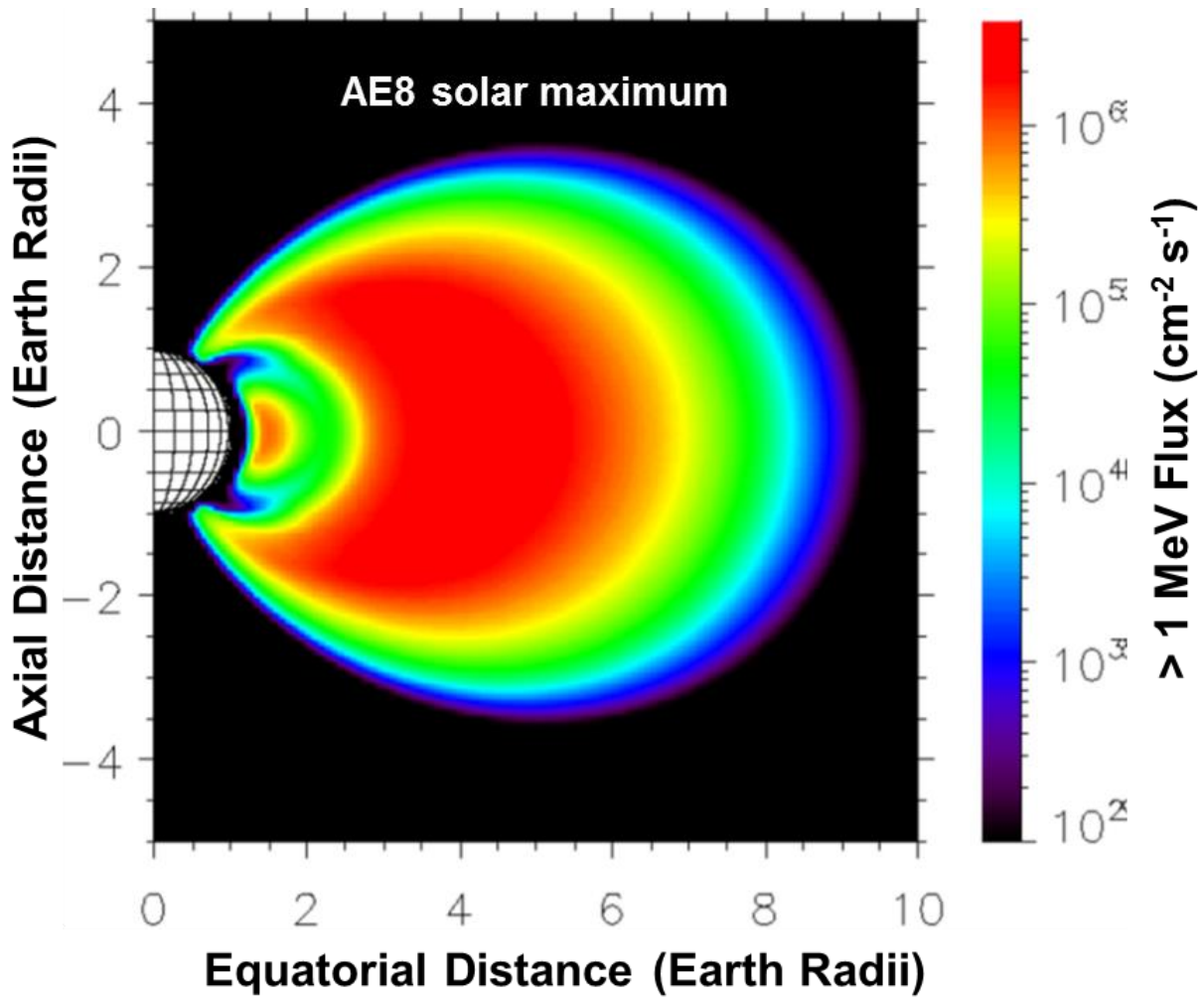


Figure 39. Comparison of the AP8 and AP9/IRENE (version 1.5) models for a polar LEO.

### 3. Trapped Electrons

#### a) Properties

Some of the characteristics of trapped electrons are summarized in Table 4 and shown in figure 40. There is both an inner and an outer zone or belt of trapped electrons. These two zones are very different so the characteristics are listed separately. As is also the case for trapped protons the boundaries of the zones are not sharp and they are to some extent dependent on particle energy. For the purposes of this discussion the inner zone is assumed to be between  $L$ -values of 1 and 2. It was originally thought that electron energies range up to approximately 5 MeV but that has not been observed recently. This electron population tends to remain relatively stable but a long-term average is difficult to ascertain as will be seen in section c). The outer zone has  $L$ -values ranging between about 3 and 10 with electron energies generally less than about 10 MeV. Here fluxes peak between  $L$ -values of 4.0 and 4.5 and the long-term average value for  $> 1$  MeV electrons is roughly  $3 \times 10^6 \text{ cm}^{-2}\text{s}^{-1}$ . This zone is very dynamic and the fluxes can vary by orders of magnitude from day to day. An interesting feature of the outer belt is that it extends down to low altitudes at high latitudes. Trapped electrons contribute to both TID and TNID effects.



**Figure 40.** Trapped electron fluxes  $> 1$  MeV according to the AE-8 model during solar maximum [Bo08].

Table 4. Trapped Electron Characteristics.

	L-Shell Values	Energies	Fluxes* ( $> 1$ MeV)	Radiation Effects
Inner Zone	1 - 2	Up to 5 MeV?	uncertain	TID TNID
Outer Zone	3 - 10	Up to 10 MeV	Up to $\sim 3 \times 10^6 \text{ cm}^{-2}\text{s}^{-1}$	

\* long-term average

The distribution of trapped particles is a continuous one throughout the inner and outer zones. However, between the two zones is a region where the fluxes are at a local minimum during quiet periods. However, the fluxes are quite variable. This is known as the slot region. The location of the slot region is assumed to be between  $L$ -values of 2 and 3 for this discussion. This is an attractive one for certain types of missions due to the increased spatial coverage compared to missions in LEO.

### b) Models

The long-time standard model for trapped electrons has been the Aerospace Electron-8 (AE-8) model [Ve91], [Ve91a]. It consists of two static flux maps of trapped electrons – one for solar maximum and one for solar minimum conditions (see figure 40). Due to the variability of the outer zone electron population, the AE-8 model is valid only for long periods of time. A conservative rule of thumb is that it should not be applied to a period shorter than 6 months.

A feature of the outer zone is its high degree of volatility and dynamic behavior. This results from geomagnetic storms and substorms, which cause major perturbations of the geomagnetic field. Measurements from the Upper Atmosphere Research Satellite (UARS) illustrate the high degree of variability of electron flux levels prior to and after such storms. Figure 41 shows the electron energy spectra for  $3.25 < L \leq 3.5$  after long-term decay from a prior storm (day 235) and two days after a large storm (day 244) compared to the average flux level over a 1000 day period [Pe01]. It is seen for example, at 1 MeV, that the difference in the one-day averaged differential fluxes over a 9-day period is about 3 orders of magnitude. This illustrates the difference between the long-term average space climate and the short-term space weather in the outer zone.

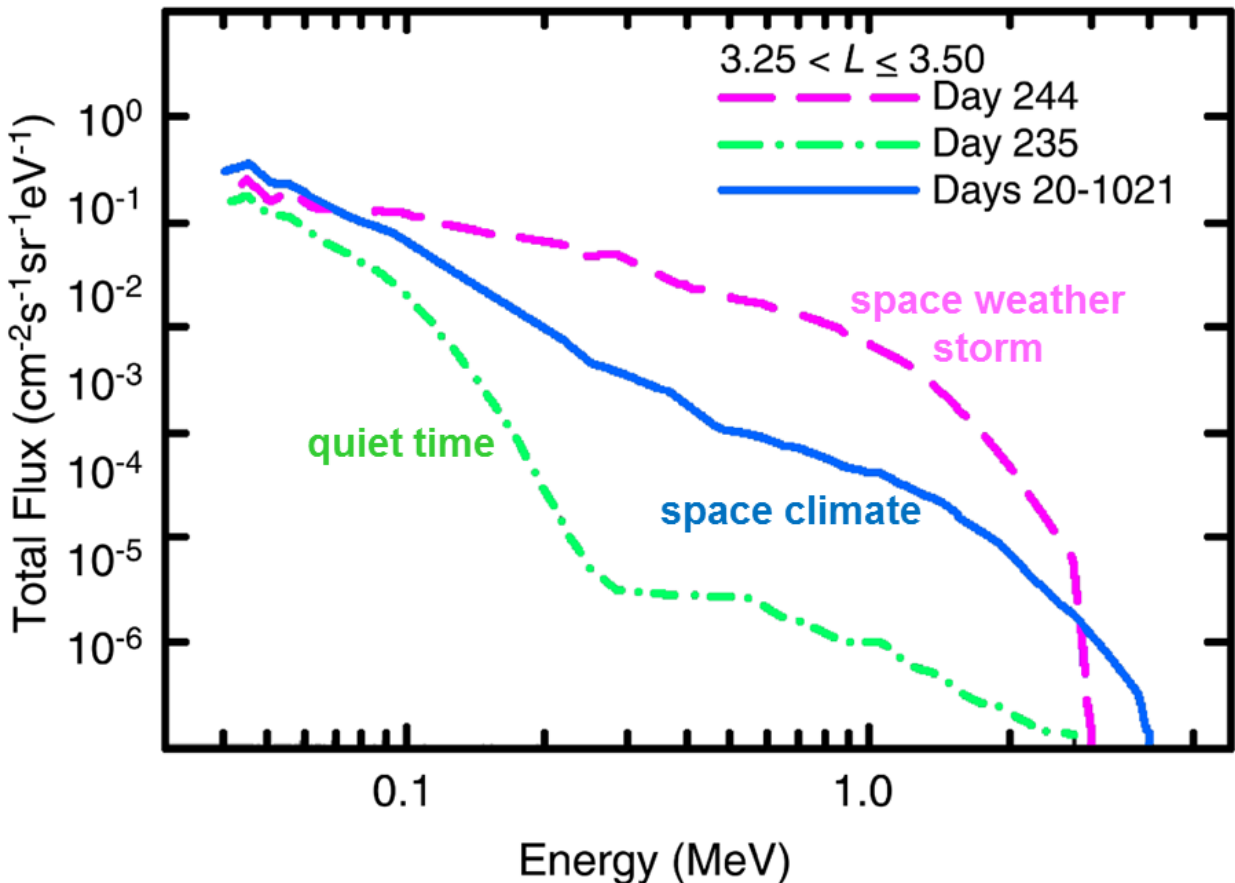


**Figure 41.** Total electron flux before and after a geomagnetic storm compared to a long-term average as measured onboard the UARS [Pe01].

Due to the volatile nature of the outer zone, it seems natural to resort to probabilistic methods. This is the case for the new AE-9/IRENE trapped electron model [Gi13], [Jo15], which uses the same methodology as described before in the discussion on trapped protons. Other statistical analyses have also been used for both the outer zone and slot region [Wr00], [Ko01], [Pe01], [Br04]. Another approach used to describe outer zone fluxes has been to relate them to the level of disturbance of the geomagnetic field by using geomagnetic activity indices such as  $A_p$  [Br92] and  $K_p$  [Va96].

An important orbit in the outer zone that is widely used for telecommunications satellites is GEO. Figure 42 shows a comparison between the AE8 and AE9/IRENE mean values. AE8 has no solar cycle dependence in GEO so there is no distinction between solar maximum and solar minimum, as was the case in figure 39. It is seen that AE8 gives more conservative fluxes over most of the energy range. The group at ONERA, the French National Aerospace Research Center, has also done considerable work on trapped electron models for GEO. Their most recent model is IGE-2006 [Si06], which gives the option of a maximum (worst case), mean or minimum (best case) flux output. When calculation of the mean flux is done in SPENVIS and compared to figure 42, results show lower fluxes than both AE8 and AE9/IRENE except at energies approximately less than 0.1

MeV. However, the IGE-2006 model has been incorporated into the group's new comprehensive GREEN model for trapped electrons so more detailed comparisons are deferred until GREEN becomes available for use.

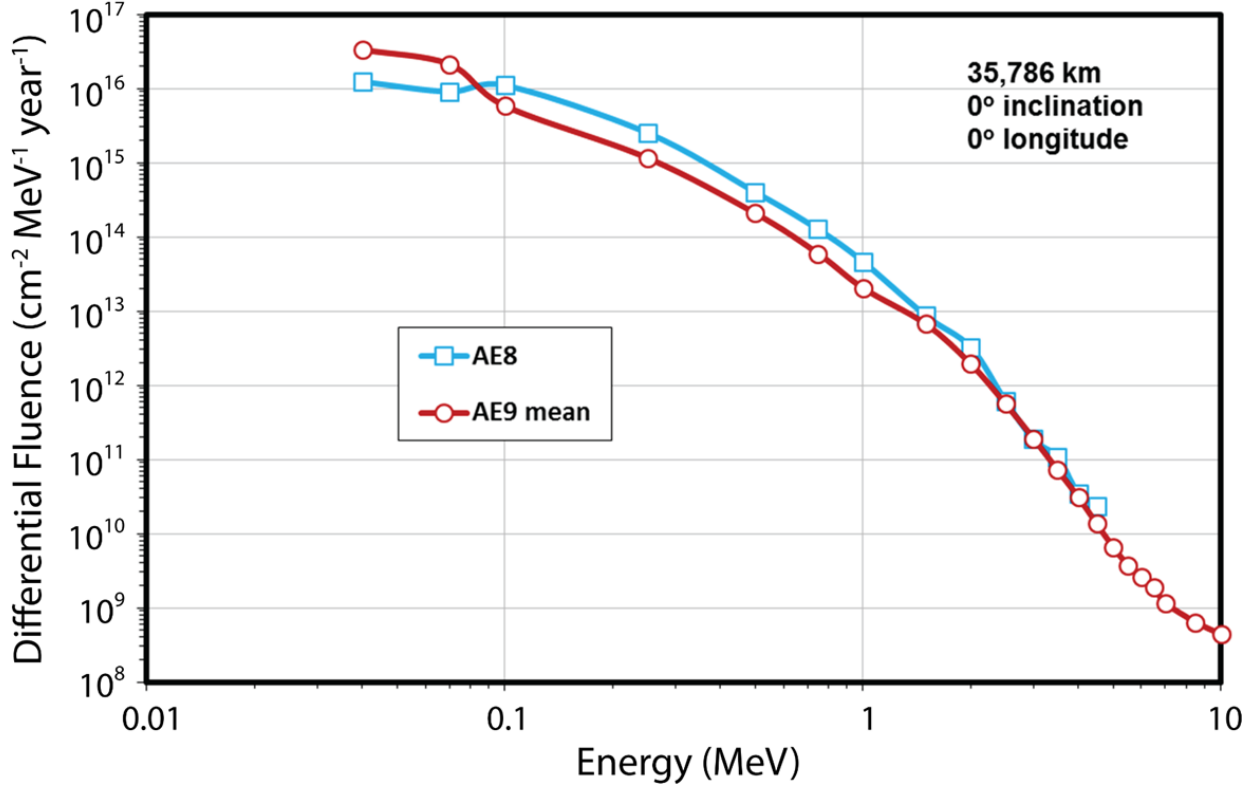


**Figure 42. Comparison of the AE8 and AE9/IRENE (version 1.5) models for GEO.**

Figure 43 gives a good overall view of the dynamic behavior of trapped electrons for about a 3.5 year period as measured by Van Allen Probes instrumentation [Cl17]. Fluxes of 0.75 MeV electrons are mapped out according to  $L$ -shell values as a function of time. Color coding of electron intensities are shown along the top of the graph. The 2 boxed areas indicate the most severe storm periods. The figure shows the volatile nature of the outer zone ( $L > 3$ ). During storm periods electrons can be injected into the slot region ( $2 < L < 3$ ). Here they are fairly short-lived as the decay period is about 10 days. During severe storms electrons can also be injected into the inner zone ( $1 < L < 2$ ). Note the stability of the inner zone as the injected electrons decay away very slowly and persist strongly more than a year after the storm.

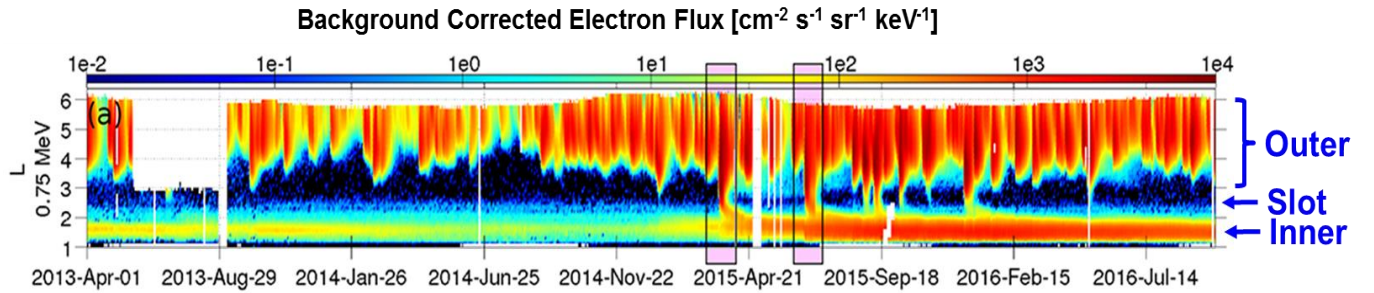


**Figure 43.** Fluxes of 0.75 MeV electrons mapped according to  $L$ -shell as a function of time for approximately 3.5 years. Fluxes are background corrected [Cl17].

### c) Current Issue: The Case of the Missing Electrons

Figure 43 is a good indicator of the behavior of the electron belts in recent times for energies up to about 0.75 MeV. The inner zone is fairly stable for long periods of time, as evidenced in the figure. When high energy ( $> 1.5$  MeV) electron data are similarly examined as shown in the top portion of figure 44 [Cl17], nothing looks out of the ordinary. The outer belt looks volatile and the inner belt appears stable. While inner zone fluxes predicted by models in current use such as AE8 and AE9/IRENE are not large for energies between 1.5 MeV and a maximum of about 5 MeV, they are ordinarily accounted for in radiation effects analysis. However, the top portion of the figure has not been corrected for background contamination, which is mainly due to high energy protons. The Van Allen Probes instrumentation has improved capability in this regard and when background contamination is removed the result is shown in the bottom portion of figure 44. The high energy electrons of the inner zone are almost completely gone! In fact there is no evidence of  $> 1.5$  MeV electrons in the inner zone since the Van Allen Probes were launched in 2012. This is the case of the missing electrons.

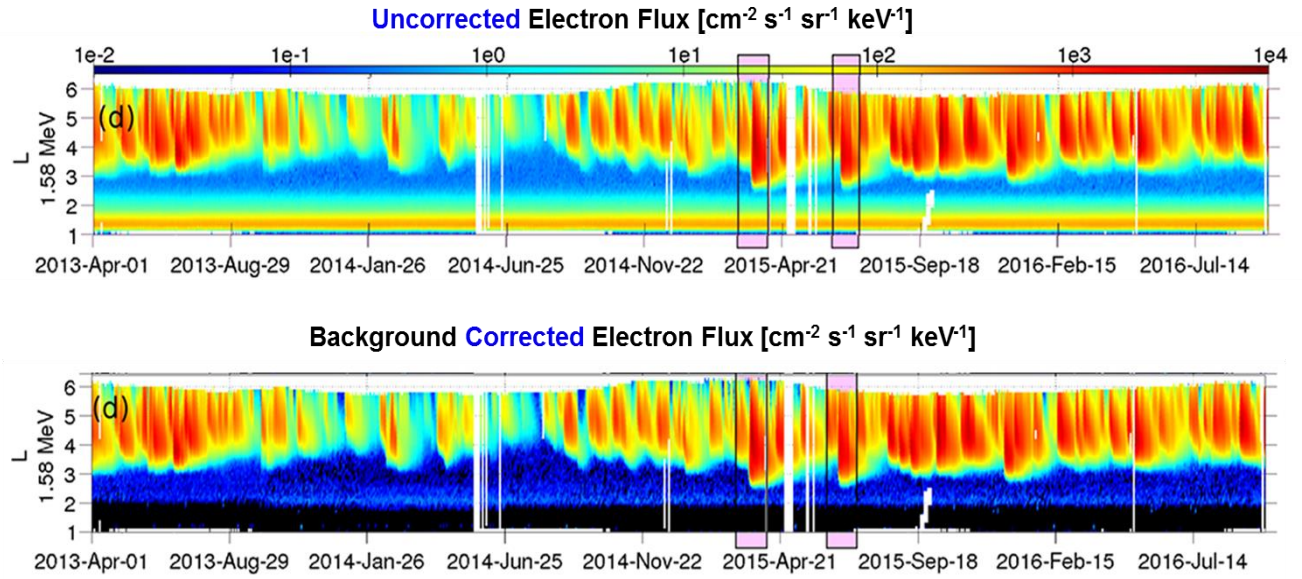


**Figure 44.** Fluxes of 1.58 MeV electrons mapped according to  $L$ -shell as a function of time for approximately 3.5 years. The top graph is uncorrected for background contamination and the bottom graph is corrected. Note the difference in the inner zone ( $1 < L < 2$ ) [Cl17].

The question of what happened to this portion of the inner zone remains. Instrumentation prior to the Van Allen Probes has not had the same capability for analyzing background contamination. It therefore seems fairly certain that some of the older data reported as trapped electrons were actually due to high energy proton contamination. In addition the situation may also reflect a difference in time periods. The injection of  $> 1.5$  MeV electrons into the inner zone may require extreme magnetic storms while the storms during the Van Allen Probes era have been fairly mild.

Finally in this section the question of how this affects TID requirements is addressed. As an example the LEO corresponding to the Hubble Space Telescope is examined and presented in figure 45. Electron fluence-energy spectra are shown calculated with 2 models. The first is the AE8 model, which consists of older data from the 1960s and 1970s. The other is AE9/Irene, which is based on Van Allen Probes data and CRRES data for the inner zone. The CRRES data includes the severe storm of March 1991. It is seen that the models agree well out to about 1 MeV. Above energies of 1 MeV it is not surprising from the above discussion that the AE8 model shows higher fluxes. Analysis of TID behind 2.5 mm of aluminum shielding for the Hubble orbit shows that if AP8/AE8 is used electrons contribute less than 20% of the TID. If AP9/AE9/Irene is used electrons contribute less than 2% of the TID. Thus, although inner belt electrons present an interesting scientific challenge they are unlikely to drive radiation effects problems except possibly surface effects.

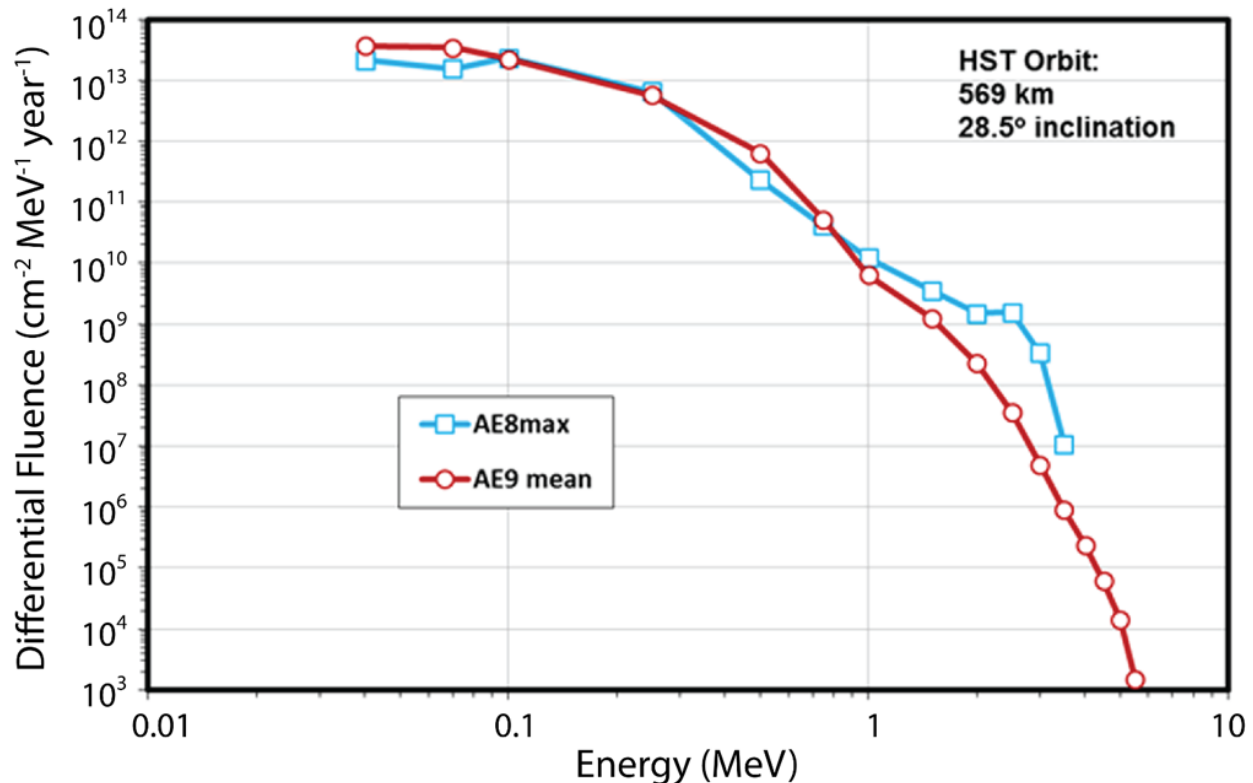


Figure 45. Comparison of the AE8 and AE9/IRENE (version 1.5) models for the LEO of the Hubble Space Telescope.

## E. Example Environments Including Shielding

### 1. Total Ionizing Dose

In this example a total ionizing dose vs. shielding depth curve will be obtained. A highly elliptical orbit is chosen because it is exposed to all particle populations that contribute significantly to TID – trapped protons, trapped electrons and solar protons. The orbital parameters used were those of the first portion of the NASA Magnetic MultiScale (MMS) mission. Shielding calculations were done for a solid aluminum sphere geometry with dose in silicon calculated at the center of the sphere. In a later presentation of this Short Course by Renaud Mangeret, discussion of more complex shielding at the box level will be presented.

There are now 2 basic options for methods of design specification. The first is the traditional margin-based approach. In this case the dose-depth curve is calculated and a margin is applied to that. Although different margins are used for different applications, government organizations use a margin of times 2 for many situations. This is shown by the red curve in figure 46 where the AP8, AE8 and ESP/PSYCHIC models were used. The newer method is a confidence level based approach, where the dose-depth curve is calculated for a given level of confidence. This necessitates the use of the AP9/IRENE and AE9/IRENE models because they are the only trapped particle models with this capability. The blue curve in figure 46 shows results using the newer trapped particle models along with the ESP/PSYCHIC model to calculate the dose-depth curve at the 95% confidence level. No margin is applied to this. It is seen that the results agree well out to about

6 mm of aluminum shielding. Beyond this the difference is primarily due to higher proton flux levels predicted by AP9/IRENE and secondarily the fact that the newer models extend to higher proton and electron energies. For those readers interested in transitioning to the confidence level based approach, dose-depth curves at the 95% confidence level are fairly consistent with using a mean environment with times 2 margin for various orbits.

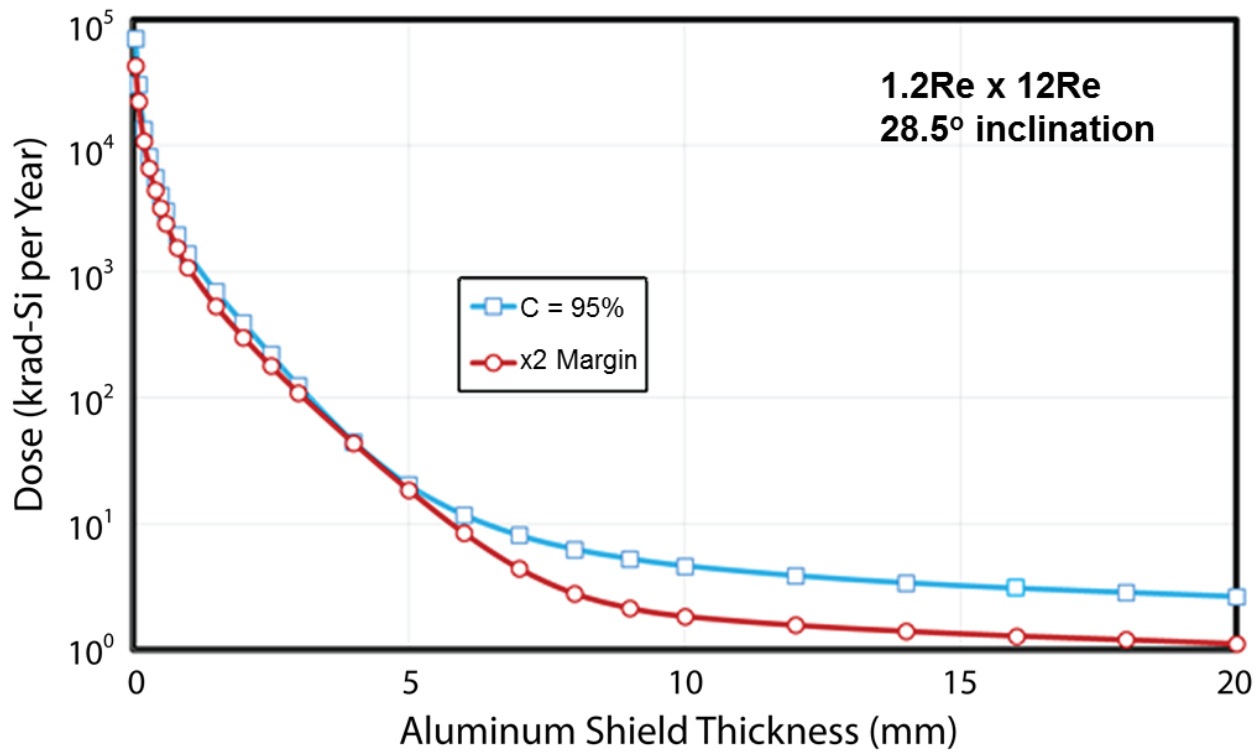


**Figure 46.** Dose-depth curves for a highly elliptical orbit using 2 specification methods. The orbit of 1.2 x 12 Earth radii (1274 km perigee x 70.080 km apogee) at a 28.5 degree inclination includes trapped protons, trapped electrons and solar protons contributing to TID.

Figure 47 shows the different radiation contributions to the dose-depth curve in figure 46. The results show the 95% confidence level but the situation is similar for the case of times 2 margin for the same orbit. For lightly shielded electronics the trapped electron component dominates TID. However, electrons can be effectively shielded against and at higher levels of shielding the trapped proton contribution is the major contributor. Solar protons and bremsstrahlung radiation contribute at a low TID level for the range of shielding shown. The latter is photon emission due to the slowing down of electrons in material. It should be noted that these results are particular to the spacecraft orbit considered.

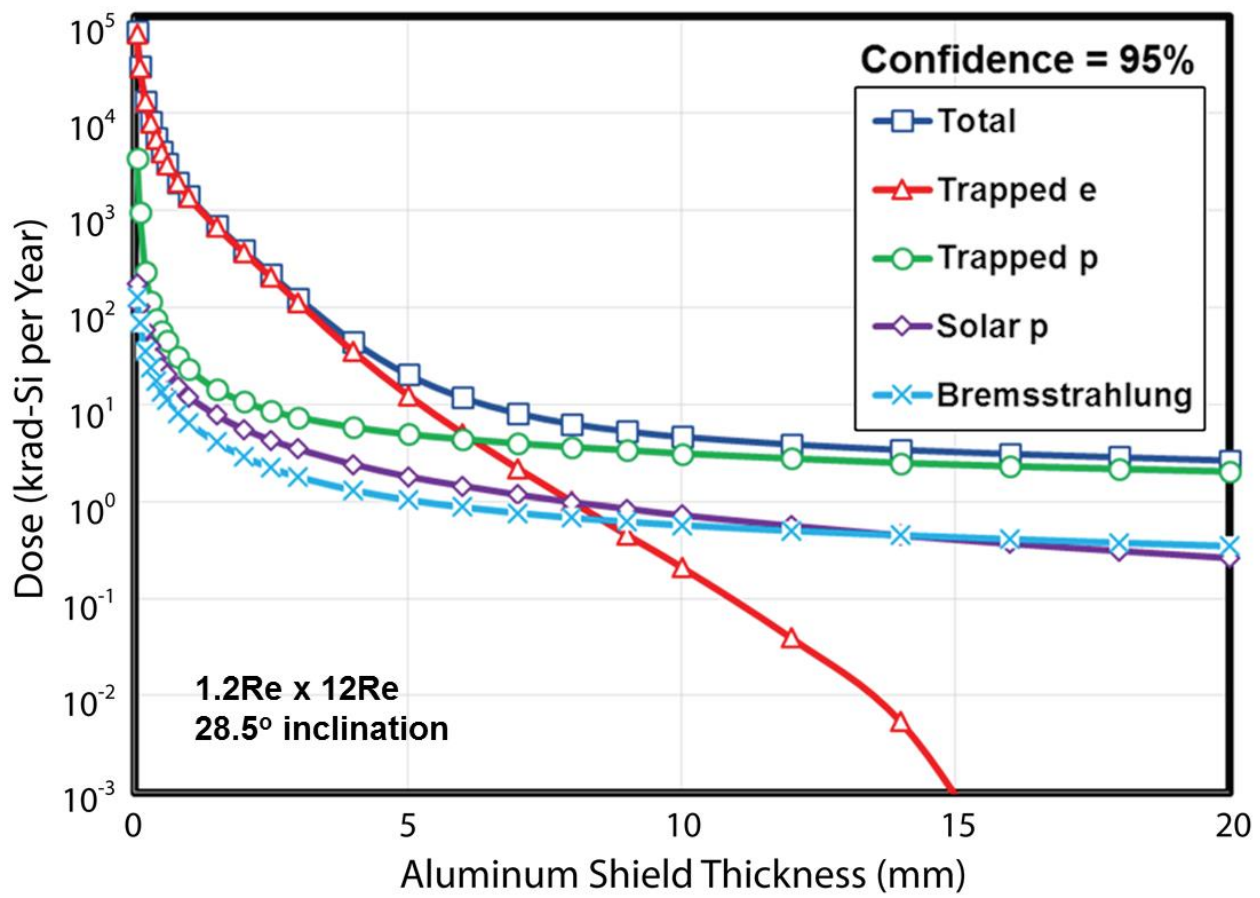


**Figure 47. Contributions of trapped electrons and protons, solar protons and bremsstrahlung radiation to the 95% confidence level dose-depth curve shown in figure 46.**

The confidence level based TID approach has several advantages over the traditional margin based approach. When convolved with laboratory test data it allows the device TID failure probability to be calculated for a mission at the desired level of shielding [Xa17]. An example of this is shown in figure 48 for bipolar transistors used for high speed, low power applications for several orbits. This is a better characterization of a device radiation performance in space. It allows more systematic trades during the design process. It is also amenable to reliability analyses, which is not possible if only a TID margin is known.

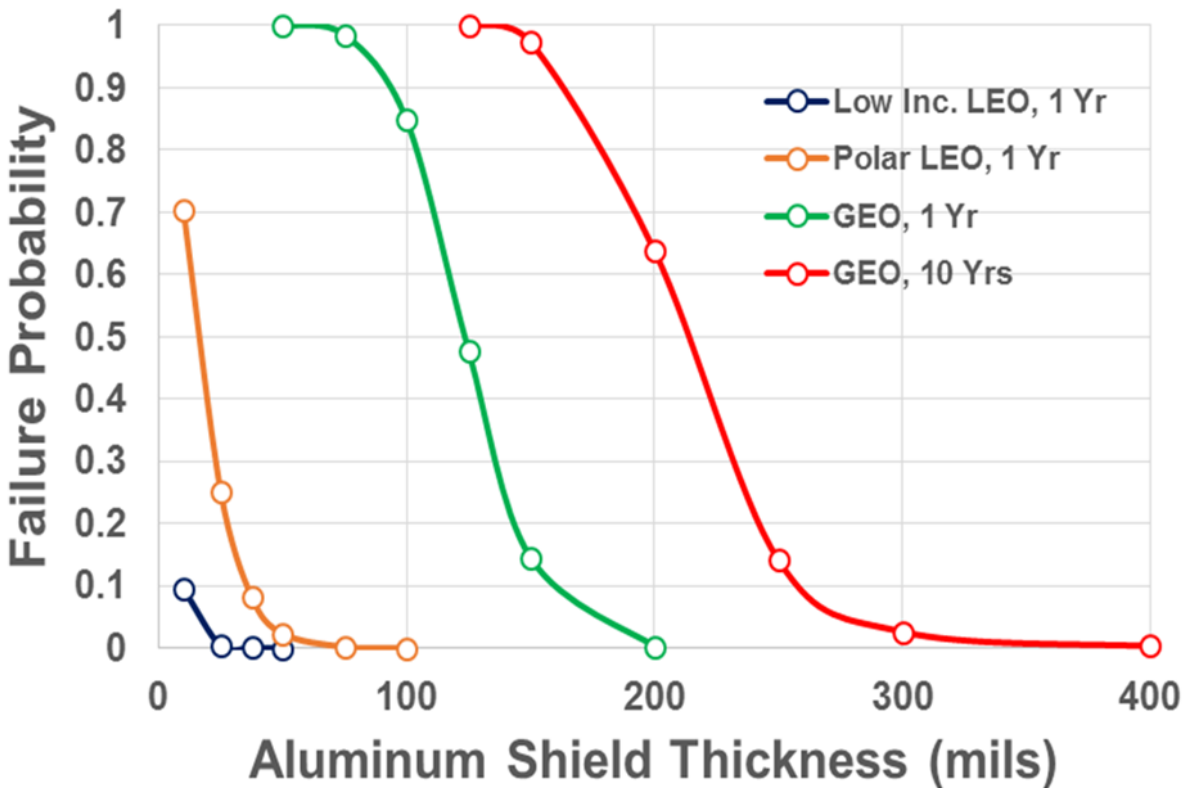
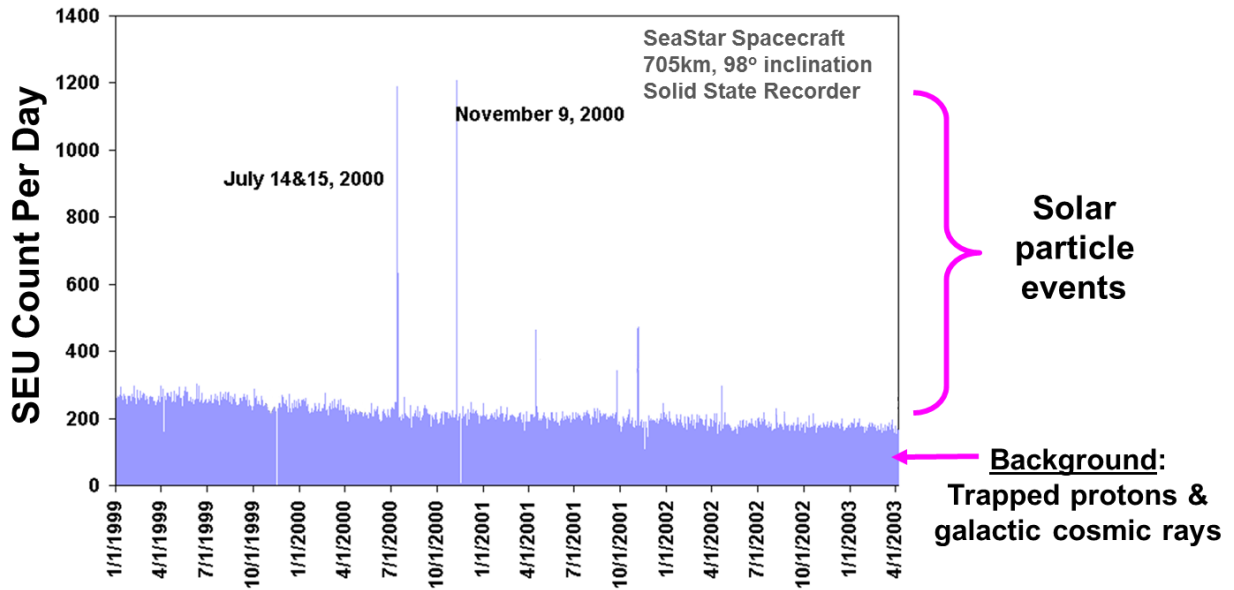


Figure 48. Failure probability for Solid State Devices, Inc., SFT2907A bipolar transistors as a function of shielding level for various orbits [Xa17].

## 2. Single Event Upset

Next SEE environments are considered. The examples presented here are restricted to single event upset (SEU) data and calculations. Figure 49 shows SEU data from the Air Force Research Laboratory SeaStar spacecraft detected on a solid state recorder for more than 4 years [Po02]. The spacecraft was in a polar LEO. The SEU count per day is shown on the y-axis. There is a slowly varying background of upsets due to trapped protons and GCR. In this case it is believed most of these SEU were due to trapped protons. Superimposed on this background are sharp increases in the upset rate due to radiation bursts from solar particle events. The largest event spikes were due to the July 14-15, 2000 and November 9, 2000 events. In addition rate spikes due to subsequent smaller events are also seen. Although the environment here is different than what is observed in figure 21, note the general similarity in that the effects are due to background radiation that varies slowly with solar cycle superimposed with solar particle events.



**Figure 49.** SEU count per day for a solid state recorder on AFRL's SeaStar spacecraft in a polar LEO. Data were obtained for more than 4 years beginning in January 1999. Upsets due to the solar particle events of July and November 2000 are identified [Po02].

Finally, calculated SEU rates are shown for the same highly elliptical orbit considered previously for figures 46 and 47. In this orbit the calculations must account for GCR and solar heavy ions. Additionally if the device is sensitive to proton-induced upset, solar protons and trapped protons must also be considered. SEU rates are shown in figure 50 that were calculated for a 4 Gbit NAND flash memory [Pe10]. The sensitive volume was obtained from process reverse engineering and publicly available data. It is seen that increased shielding reduces SEU rates for the worst case solar particle event, the October 1989 event, used in the CREME96 suite of programs. Proton-induced upsets, both those caused by solar protons and trapped protons, can also be reduced with increased shielding. However, the GCR rates are fairly constant with increased shielding. Thus, the GCR rate provides a lower limit for the SEU rate that is not practical to reduce significantly. The rates provided here for heavy ions do not include fragmentation processes in shielding. For discussion of this the reader is referred to [ON15a].

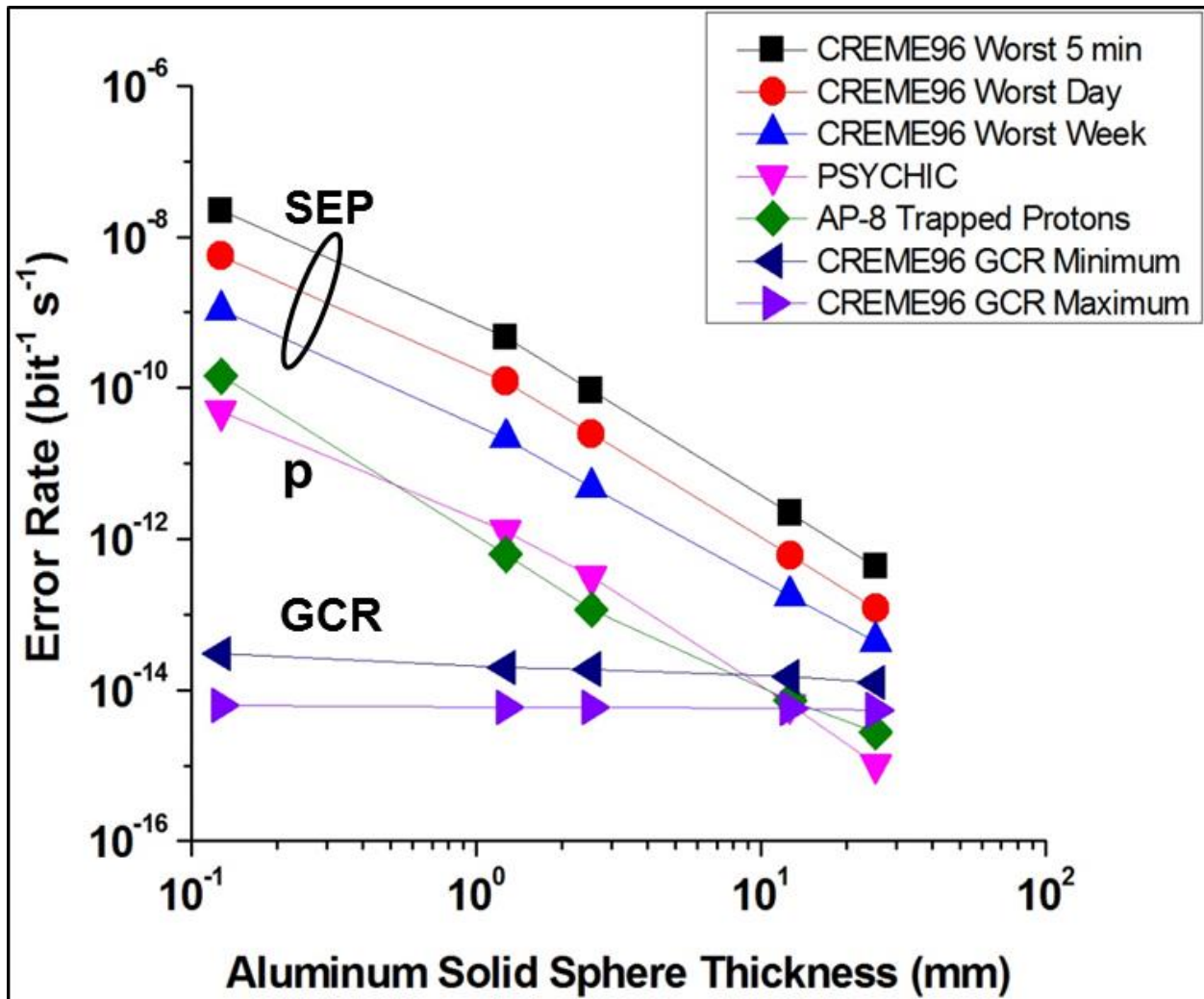


**Figure 50.** SEU rates calculated for a 4 Gbit NAND flash memory for a worst case solar particle event, solar protons, trapped protons and GCR during solar minimum and solar maximum as a function of shielding [Pe10].

## 6. Summary

This work presented a space climatology timeline ranging from the Big Bang to NSREC 2018. It began with a description of the early universe including the origin and abundances of particles significant for radiation effects. It continued to a transition period to modern times when the era of modern space climatology began to emerge due to discoveries of sunspots and the solar activity cycle, along with development of early astronomical methods. The timeline concluded in the modern era with a description of the radiation environments of galactic cosmic rays, solar particle events and the Van Allen Belts.

A general theme is that the space radiation environment is highly variable and must be understood to produce reliable, cost-effective designs for successful space missions. This includes both long-term variations of space climate and short-term variations of space weather.

## 7. Acknowledgments

The author thanks Pat O'Neill of Johnson Space Center for providing the calculations and data for figures 17 – 19. He further thanks Craig Stauffer of AS&D, Inc. for assistance with calculations and Martha O'Bryan of AS&D, Inc. for assistance with graphics.

## 8. References

- [Ad81] J.H. Adams, Jr., R. Silberberg and C.H. Tao, *Cosmic Ray Effects on Microelectronics, Part I: The Near-Earth Particle Environment*, NRL Memorandum Report 4506, Naval Research Laboratory, Washington DC, Aug. 1981.
- [Ad87] J.H. Adams, Jr., *Cosmic Ray Effects on Microelectronics, Part IV*, NRL Memorandum Report 5901, Naval Research Laboratory, Washington DC, Dec. 1987.
- [Ad11] J.H. Adams, Jr., W.F. Dietrich and M.A. Xapsos, "Probabilistic Solar Energetic Particle Models", Proc. 32<sup>nd</sup> Int. Cosmic Ray Conf., Beijing (2011).
- [An85] A.H-S. Ang and W.H. Tang, *Probability Concepts in Engineering Planning and Design, Vol. II*, Wiley, NY, 1985.
- [An89] E. Anders and N. Grevesse, "Abundances of the Elements: Meteoritic and Solar", *Geochimica et Cosmochimica Acta*, Vol. 53, 197-214 (Jan. 1989).
- [An94] B.J. Anderson and R.E. Smith, *Natural Orbital Environment Guidelines for Use in Aerospace Vehicle Development*, NASA Technical Memorandum 4527, Marshall Space Flight Center, Alabama, June 1994.
- [Ba96] G.D. Badhwar and P.M. O'Neill, "Galactic Cosmic Radiation Model and Its Applications", *Adv. Space Res.*, Vol. 17, No. 2, (2)7-(2)17 (1996).
- [Ba97] J.L. Barth, "Modeling Space Radiation Environments" in *1997 IEEE NSREC Short Course*, IEEE Publishing Services, Piscataway, NJ.
- [Ba13] R. Baumann, "Landmarks in Terrestrial Single Event Effects" in *2013 IEEE NSREC Short Course*, IEEE Publishing Services, Piscataway, NJ.
- [Bi75] D. Binder, E.C. Smith and A.B. Holman, "Satellite Anomalies from Galactic Cosmic Rays", *IEEE Trans. Nucl. Sci.*, Vol. 22, No. 6, 2675-2680 (Dec. 1975).
- [Bo08] S. Bourdarie and M. Xapsos, "The Near-Earth Space Radiation Environment", *IEEE Trans. Nucl. Sci.*, Vol. 55, No. 4, 1810-1832 (Aug. 2008).
- [Bo14] D. Boscher *et al.*, "A New Proton Model for Low Altitude High Energy Specification", *IEEE Trans. Nucl. Sci.*, Vol. 61, 3401-3407 (Dec. 2014).
- [Br92] D.H. Brautigam, M.S. Gussenhoven and E.G. Mullen, "Quasi-Static Model of Outer Zone Electrons", *IEEE Trans. Nucl. Sci.*, Vol. 39, 1797-1803 (Dec. 1992).
- [Br04] D.H. Brautigam, K.P. Ray, G.P. Ginnet and D. Madden, "Specification of the Radiation Belt Slot Region: Comparison of the NASA AE8 Model with TSX5/CEASE Data", *IEEE Trans. Nucl. Sci.*, Vol. 51, 3375-3380 (Dec. 2004).
- [Bu88] E.A. Burke, G.E. Bender, J.K. Pimbley, G.P. Summers, C.J. Dale, M.A. Xapsos and P.W. Marshall, "Gamma Induced Dose Fluctuations in a Charge Injection Device", *IEEE Trans. Nucl. Sci.*, Vol. 35, 1302-1306 (1988).
- [Ca88] E. Castillo, *Extreme Value Theory in Engineering*, Academic Press, Boston, 1988.
- [Cl17] S.G. Claudepierre *et al.*, *J. Geophys. Res.: Space Phys.*, Vol. 122, Issue 3, 3127-3144 (March 2017).

- [Da96] E.J. Daly, J. Lemaire, D. Heynderickx and D.J. Rodgers, "Problems with Models of the Radiation Belts", IEEE Trans. Nucl. Sci., Vol. 43, No. 2, 403-414 (April 1996).
- [Da01] A.J. Davis, et al., "Solar Minimum Spectra of Galactic Cosmic Rays and Their Implications for Models of the Near-Earth Radiation Environment", J. Geophys. Res., Vol. 106, No. A12, 29,979-29,987 (Dec. 2001).
- [Dy02] C.S. Dyer, K. Hunter, S. Clucas, D. Rodgers, A. Campbell and S. Buchner, "Observation of Solar Particle Events from CREDO and MPTB During the Current Solar Maximum", IEEE Trans. Nucl. Sci., Vol. 49, 2771-2775 (2002).
- [Fe90] J. Feynman, T.P. Armstrong, L. Dao-Gibner and S.M. Silverman, "New Interplanetary Proton Fluence Model", J. Spacecraft, Vol. 27, 403-410 (1990).
- [Fe93] J. Feynman, G. Spitale, J. Wang and S. Gabriel, "Interplanetary Fluence Model: JPL 1991", J. Geophys. Res., Vol. 98, 13281-13294 (1993).
- [Fo46] S.E. Forbush, "Three Unusual Cosmic-Ray Increases Possibly Due to Charged Particles from the Sun", Phys. Rev., Vol. 70, 771-772 (1946).
- [Ga13] K.F. Galloway, "From Displacement Damage to ELDRS: Fifty Years of Bipolar Transistor Radiation Effects at the NSREC", IEEE Trans. Nucl. Sci., Vol. 60, No. 3, 1731-1739 (June 2013).
- [Gi13] G. Ginet *et al.*, "The AE9, AP9 and SPM: New Models for Specifying the Trapped Energetic Particle and Space Plasma Environment", Space Sci. Rev., Vol. 179, Issue 1-4, 579-615 (Nov. 2013).
- [Gr66] K. Greisen, "End to the Cosmic Ray Spectrum?", Phys. Rev. Lett., Vol. 16, 748-750 (April 1966).
- [Gu58] E. Gumbel, *Statistics of Extremes*, Columbia University Press, NY, 1958.
- [Gu96] M.S. Gussenhoven, E.G. Mullen and D.H. Brautigam, "Improved Understanding of the Earth's Radiation Belts from the CRRES Satellite", IEEE Trans. Nucl. Sci., Vol. 43, No. 2, 353-368 (April 1996).
- [Ha88] S.W. Hawking, *A Brief History of Time*, Bantam Books, NY, 1988.
- [Ha05] S.W. Hawking, *A Briefer History of Time*, Bantam Dell, NY, 2005.
- [He99] D. Heynderickx, M. Kruglanski, V. Pierrard, J. Lemaire, M.D. Looper and J.B. Blake, "A Low Altitude Trapped Proton Model for Solar Minimum Conditions Based on SAMPEX/PET Data", IEEE Trans. Nucl. Sci., Vol. 46, 1475-1480 (Dec. 1999).
- [Ho46] F. Hoyle, "The Synthesis of the Elements from Hydrogen", Monthly Notices Royal Astronomical Soc., Vol. 106, Issue 5, 343-383 (Oct. 1946).
- [Hu98] S.L. Huston and K.A. Pfitzer, "A New Model for the Low Altitude Trapped Proton Environment", IEEE Trans. Nucl. Sci., Vol. 45, 2972-2978 (Dec. 1998).
- [Hu02] S.L. Huston, *Space Environments and Effects: Trapped Proton Model*, Boeing Final Report NAS8-98218, Huntington Beach, CA, Jan. 2002.
- [Ja57] E.T. Jaynes, "Information Theory and Statistical Mechanics", Phys. Rev., Vol. 106, 620-630 (1957).
- [Ji12] P. Jiggens *et al.*, "ESA SEPEM Project: Peak Flux and Fluence Model", IEEE Trans. Nucl. Sci., Vol. 59, No. 4, 1066-1077 (Aug. 2012).
- [Ji18] P. Jiggens et al., "Updated Model of the Solar Energetic Proton Environment in Space", J. Space Weather Space Clim., submitted 2018.
- [Ji18a] P. Jiggens *et al.*, "The Solar Accumulated and Peak Proton and Heavy Ion Radiation Environment (SAPPHIRE) Model", IEEE Trans. Nucl. Sci., Vol. 65, No. 2, 698-711 (Feb. 2018).

- [Jo15] W.R. Johnston *et al.*, "Recent Updates to AE9/AP9/SPM Radiation Belt and Space Plasma Specification Model", IEEE Trans. Nucl. Sci., Vol. 62, 2760-2766 (Dec. 2015).
- [Ju07] I. Jun et al., "Statistics of Solar Particle Events: Fluences, Durations and Time Intervals", Adv. Space Res., Vol. 40, 304-312 (2007).
- [Ka89] J.N. Kapur, *Maximum Entropy Models in Science and Engineering*, John Wiley & Sons, Inc., NY, 1989.
- [Ka17] D. Kasen et al., "Origin of the Heavy Elements in Binary Neutron-Star Mergers from a Gravitational Wave Event", Nature, <http://dx.doi.org/10.1038/nature24453> (2017).
- [Ki74] J.H. King, "Solar Proton Fluences for 1977-1983 Space Missions", J. Spacecraft, Vol. 11, 401-408 (1974).
- [Ko01] H.C. Koons, "Statistical Analysis of Extreme Values in Space Science", J. Geophys. Res., Vol. 106, No. A6, 10915-10921 (June 2001).
- [Ku17] N.V. Kuznetsov, H. Popova and M.I. Panasyuk, "Empirical Model of Long-Time Variations of Galactic Cosmic Ray Particle Fluxes", J. Geophys. Res. Space Physics, Vol. 122, 1463-1472 (Feb. 2017).
- [La05] J-M. Lauenstein and J.L. Barth, "Radiation Belt Modeling for Spacecraft Design: Model Comparisons for Common Orbits", 2005 IEEE Radiation Effects Data Workshop Proceedings, pp. 102-109, IEEE Operations Center, Piscataway, NJ, 2005.
- [Le06] F. Lei, A. Hands, S. Clucas C. Dyer and P. Truscott, "Improvements to and Validations of the QinetiQ Atmospheric Radiation Model (QARM)", IEEE Trans. Nucl. Sci., Vol. 53, No. 4, 1851-1858, (Aug. 2006).
- [Li05] M. Livio, "Hubble's Top Ten Scientific Discoveries", Invited Presentation at IEEE Nuclear & Space Radiation Effects Conference, Seattle, WA, July 2005.
- [Li13] M. Livio, *Brilliant Blunders*, Simon & Schuster, NY, 2013.
- [Ma89] P.W. Marshall, C.J. Dale, E.A. Burke, G.P. Summers and G.E. Bender, "Displacement Damage Extremes in Silicon Depletion Regions", IEEE Trans. Nucl. Sci., Vol. 36, 1831-1839 (1989).
- [Ma02] J. Mazur, "The Radiation Environment Outside and Inside a Spacecraft" in *2002 IEEE NSREC Short Course*, IEEE Publishing Services, Piscataway, NJ.
- [Ma08] J.C. Mather and J. Boslough, *The Very First Light*, Basic Books, NY 2008.
- [Ma13] D. Matthia, T. Berger, A.I. Mrigakshi and G. Reitz, "A Ready-to-Use Galactic Cosmic Ray Model", Adv. Space Res., Vol. 51, 329-338 (2013).
- [Ma15] J. Mazur, "No Charge Left Behind: A Review of the Charging Phenomenon and Associated Hazards" in *2015 IEEE NSREC Short Course*, IEEE Publishing Services, Piscataway, NJ.
- [Mc61] C.E. McIlwain, "Coordinates for Mapping the Distribution of Magnetically Trapped Particles", J. Geophys. Res., Vol. 66, 3681-3691 (1961).
- [Mc01] K.G. McCracken, G.A.M. Dreschoff, E.J. Zeller, D.F. Smart and M.A. Shea, "Solar Cosmic Ray Events for the Period 1561 – 1994 1. Identification in Polar Ice", J. Geophys. Res., Vol. 106, 21585-21598 (2001).
- [Mc00] P.J. McNulty, L.Z. Scheick, D.R. Roth, M.G. Davis and M.R.S. Tortora, "First Failure Predictions for EPROMs of the Type Flown on the MPTB Satellite", IEEE Trans. Nucl. Sci., Vol. 47, 2237-2243 (2000).
- [Mr12] A.I. Mrigakshi, D. Matthia, T. Berger, G. Reitz and R.F. Wimmer-Schweingruber, "Assessment of Galactic Cosmic Ray Models", J. Geophys. Res., Vol. 117, A08109 (Aug. 2012).
- [Ny96] R.A. Nymmik, M.I. Panasyuk and A.A. Suslov, "Galactic Cosmic Ray Flux Simulation and Prediction", Adv. Space Res., Vol. 17, No. 2, (2)19-(2)30 (1996).

- [Ny96a] R.A. Nymmik, "Models Describing Solar Cosmic Ray Events", Radiat. Meas., Vol. 26, 417-420 (1996).
- [Ny99] R.A. Nymmik, "Probabilistic Model for Fluences and Peak Fluxes of Solar Energetic Particles", Radiation Measurements, Vol.30, 287-296 (1999).
- [Ny07] R.A. Nymmik, "Improved Environment Radiation Models", Adv. Space Res., Vol. 40, 313-320 (2007).
- [Ol93] T.R. Oldham et al., "Total Dose Failures in Advanced Electronics from Single Ions", IEEE Trans. Nucl. Sci., Vol. 40, 1820-1830 (Dec. 1993).
- [ON10] P.M. O'Neill, "Badhwar-O'Neill 2010 Galactic Cosmic Ray Flux Model; Revised" IEEE Trans. Nucl. Sci., Vol. 57, 3148-3153 (Dec. 2010).
- [ON15] P.M. O'Neill, *Badhwar-O'Neill 2014 Galactic Cosmic Ray Flux Model Description*, NASA/TP-2015-218569, NASA Johnson Space Center, Houston, March 2015.
- [ON15a] P.M. O'Neill, "Ionizing Radiation Environment Inside Spacecraft" in *2015 IEEE NSREC Short Course*, IEEE Publishing Services, Piscataway, NJ.
- [Pe01] W.D. Pesnell, "Fluxes of Relativistic Electrons in Low Earth Orbit During the Decline of Solar Cycle 22", IEEE Trans. Nucl. Sci., Vol. 48, 2016-2021 (Dec. 2001).
- [Pe02] E.L. Petersen, J.C. Pickel, J.H. Adams, Jr. and E.C. Smith, "Rate Prediction for Single Event Effects – A Critique", IEEE Trans. Nucl. Sci., Vol. 39, 1577-1599 (Dec. 1992).
- [Pe10] J.A. Pellish, *et al.*, "Impact of Spacecraft Shielding on Direct Ionization Soft Error Rates for Sub-130 nm Technologies", IEEE Trans. Nucl. Sci., Vol. 57, 3183-3189 (Dec. 2010).
- [Pe13] R.L. Pease, "A Brief History of the NSREC", IEEE Trans. Nucl. Sci., Vol. 60, No. 3, 1668-1673, (June 2013).
- [Pe13a] E.L. Petersen, "The Single Event Revolution", IEEE Trans. Nucl. Sci., Vol. 60, No. 3, 1824-1835, June 2013).
- [Po02] C. Poivey *et al.*, "Single Event Upset (SEU) Study of SeaStar, and the MAP Anomaly", 2002 Single Event Effects Symposium, Los Angeles, CA (April 2002).
- [Ra17] O. Raukunen et al., "Two Solar Proton Fluence Models Based on Ground Level Enhancement Observations", J. Space Weather Space Clim., submitted 2017.
- [Re99] D.V. Reames, "Particle Acceleration at the Sun and in the Heliosphere", Space Sci. Rev., Vol. 90, 413-491 (1999).
- [Ro64] B. Rossi, *Cosmic Rays*, McGraw-Hill, Inc., NY, 1964.
- [Ro18] Z.D. Robinson, J.H. Adams, Jr., M.A. Xapsos and C.A. Stauffer, "Database of Episode-Integrated Solar Energetic Proton Fluences", J. Space Weather Space Clim., Vol. 8: A24 (Jan. 2018).
- [Sa76] D.M. Sawyer and J.I. Vette, *AP-8 Trapped Proton Environment for Solar Maximum and Solar Minimum*, NSSDC/WDC-A-R&S, 76-06, NASA Goddard Space Flight Center, Greenbelt, MD, Dec. 1976.
- [Sc02] J.R. Schwank, "Total Dose Effects in MOS Devices" in *2002 IEEE NSREC Short Course*, IEEE Publishing Services, Piscataway, NJ.
- [Si06] A. Sicard-Piet, *et al.*, "A New International Geostationary Electron Model: IGE-2006, from 1 keV to 5.2 MeV", Space Weather, Vol. 6, Issue 7, 1-13 (July 2008).
- [Si18] A. Sicard-Piet *et al.*, "GREEN: A New Global Radiation Earth Environment Model", J. Ann. Geophys., submitted March 2018.
- [Sr13] J.R. Srour and J.W. Palko, "Displacement Damage Effects in Devices" in *2013 IEEE NSREC Short Course*, IEEE Publishing Services, Piscataway, NJ.
- [St74] E. G. Stassinopoulos and J.H. King, "Empirical Solar Proton Models for Orbiting Spacecraft Applications", IEEE Trans. Aerospace and Elect. Sys., Vol. 10, 442-450 (1974).

- [St96] E.G. Stassinopoulos, G.J. Brucker, D.W. Nakamura, C.A. Stauffer, G.B. Gee and J.L. Barth, "Solar Flare Proton Evaluation at Geostationary Orbits for Engineering Applications", IEEE Trans. Nucl. Sci., Vol. 43, 369-382 (April 1996).
- [Su93] G.P. Summers, E.A. Burke, P. Shapiro, S.R. Messenger and R.J. Walters, "Damage Correlations in Semiconductors Exposed to Gamma, Electron and Proton Radiations", IEEE Trans. Nucl. Sci., Vol. 40, 1372-1379, Dec. 1993.
- [Sw01] S. Swordy, "The Energy Spectra and Anisotropies of Cosmic Rays", Space Sci. Rev., Vol. 99, 85-94 (Feb. 2001).
- [Ta11] B. Taylor, G. Vacanti, E. Maddox and C.I. Underwood, "The Interplanetary Electron Model (IEM)", IEEE Trans. Nucl. Sci., Vol. 58, 2785-2792 (Dec. 2011).
- [Ty97] A.J. Tylka et al., "CREME96: A Revision of the Cosmic Ray Effects on Microelectronics Code", IEEE Trans. Nucl. Sci., Vol. 44, 2150-2160 (1997).
- [Ty09] A.J. Tylka and W.F. Dietrich, "A New and Comprehensive Analysis of Proton Spectra in Ground-Level Enhanced (GLE) Solar Particle Events", 31<sup>st</sup> International Cosmic Ray Conference, Lódź, Poland (2009).
- [Va84] P.J. Vail and E.A. Burke, "Fundamental Limits Imposed by Gamma Dose Fluctuations in Scaled MOS Gate Insulators", IEEE Trans. Nucl. Sci., Vol. 31, 1411-1416 (1984).
- [Va96] A.L. Vampola, *Outer Zone Energetic Electron Environment Update*, European Space Agency Contract Report, Dec. 1996; [http://space-env.esa.int/R\\_and\\_D/vampola/text.html](http://space-env.esa.int/R_and_D/vampola/text.html).
- [Ve91] J.I. Vette, *The NASA/National Space Science Data Center Trapped Radiation Environment Program (1964-1991)*, NSSDC 91-29, NASA/Goddard Space Flight Center, National Space Science Data Center, Greenbelt, MD, Nov. 1991.
- [Ve91a] J.I. Vette, *The AE-8 Trapped Electron Environment*, NSSDC/WDC-A-R&S 91-24, NASA Goddard Space Flight Center, Greenbelt, MD, Nov. 1991.
- [Wa94] M. Walt, *Introduction to Geomagnetically Trapped Radiation*, University Press, Cambridge, 1994.
- [WDC] WDC-SILSO, World Data Center - Sunspot Number and Long-term Solar Observations, Royal Observatory of Belgium, on-line Sunspot Number catalogue: <http://www.sidc.be/SILSO/>.
- [Wo12] E.W. Wolff et al., "The Carrington Event not Observed in Most Ice Core Records", Geophys. Res. Lett., Vol. 39, No. L08503, (Apr. 2012).W
- [Wr00] G.L. Wrenn, D.J. Rodgers and P. Buehler, "Modeling the Outer Belt Enhancements of Penetrating Electrons", J. Spacecraft and Rockets, Vol. 37, No. 3, 408-415 (May-June 2000).
- [Xa96] M.A. Xapsos, "Hard Error Dose Distributions of Gate Oxide Arrays in the Laboratory and Space Environments", IEEE Trans. Nucl. Sci., Vol. 43, 3139-3144 (1996).
- [Xa98] M.A. Xapsos, G.P. Summers and E.A. Burke, "Probability Model for Peak Fluxes of Solar Proton Events", IEEE Trans. Nucl. Sci., Vol. 45, 2948-2953 (1998).
- [Xa98a] M.A. Xapsos, G.P. Summers and E.A. Burke, "Extreme Value Analysis of Solar Energetic Proton Peak Fluxes", Solar Phys., Vol. 183, 157-164 (1998).
- [Xa99] M.A. Xapsos, G. P. Summers, J.L. Barth, E.G. Stassinopoulos and E.A. Burke, "Probability Model for Worst Case Solar Proton Event Fluences", IEEE Trans. Nucl. Sci., Vol. 46, 1481-1485 (1999).
- [Xa00] M.A. Xapsos, G.P. Summers, J.L. Barth, E.G. Stassinopoulos and E.A. Burke, "Probability Model for Cumulative Solar Proton Event Fluences", IEEE Trans. Nucl. Sci., Vol. 47, No. 3, 486-490 (June 2000).

- [Xa04] M.A. Xapsos, C. Stauffer, G.B. Gee, J.L. Barth, E.G. Stassinopoulos and R.E. McGuire, "Model for Solar Proton Risk Assessment", IEEE Trans. Nucl. Sci., Vol. 51, 3394-3398 (2004).
- [Xa06] M.A. Xapsos, C. Stauffer, J.L. Barth and E.A. Burke, "Solar Particle Events and Self-Organized Criticality: Are Deterministic Predictions of Events Possible?", IEEE Trans. Nucl. Sci., Vol. 53, No. 4, 1839-1843 (Aug. 2006).
- [Xa06a] M.A. Xapsos, "Modeling the Space Radiation Environment" in *2006 IEEE NSREC Short Course*, IEEE Publishing Services, Piscataway, NJ.
- [Xa07] M.A. Xapsos, C. Stauffer, T. Jordan, J.L. Barth and R.A. Mewaldt, "Model for Cumulative Solar Heavy Ion and Linear Energy Transfer Spectra", IEEE Trans. Nucl. Sci., Vol. 54, 1985-1989 (Dec. 2007).
- [Xa13] M.A. Xapsos, P.M. O'Neill and T.P. O'Brien, "Near-Earth Space Radiation Models", IEEE Trans. Nucl. Sci., Vol. 60, No. 3, 1691-1705 (June 2013).
- [Xa17] M.A. Xapsos *et al.*, "Inclusion of Radiation Environment Variability in Total Dose Hardness Assurance Methodology", IEEE Trans. Nucl. Sci., Vol. 64, No. 1, 325-331 (Jan. 2017).

# **Radiation hardness assurance: how well assured do we need to be?**

Renaud Mangeret,  
Airbus Defence and Space

## Table of Contents

1.	Introduction.....	4
2.	Radiation Hardness Assurance – A Definition.....	5
3.	Radiation Environment Definition and Potential Impacts on RHA Process .....	7
3.1	Introduction.....	7
3.2	Galactic Cosmic Rays (GCR).....	7
3.3	Solar Particle Events (SPE).....	9
3.4	Trapped Particles .....	12
3.4.1	Trapped Electrons.....	13
3.4.2	Trapped Protons .....	14
3.5	Derived Quantities .....	16
4.	Radiation Effects on Electronics – Cumulative Phenomena.....	18
4.1	Total Ionizing Dose (TID) - Basics .....	18
4.2	Total Non Ionizing Dose (TNID) – Displacement Damage (DD) - Basics.....	19
4.3	TID/DD Calculation Methods .....	20
4.4	TID testing .....	21
4.4.1	General .....	21
4.4.2	TID Testing – Sources.....	22
4.4.3	TID Testing – Application Conditions.....	23
4.4.4	TID testing – Enhanced Low Dose Rate Sensitivity (ELDRS).....	26
4.4.5	TID testing – traceability .....	27
4.4.6	TID testing – test results analysis .....	28
4.4.7	TID testing – normative documents.....	29
4.5	DD Testing .....	31
4.6	TID/DD Testing at Board Level .....	34
4.7	TID/DD: Link with the Worst Case Analysis .....	36
4.8	TID – Margin Policy.....	37
4.9	DD – Margin Policy.....	38
5.	Radiation Effects on Electronics – Single Event Effects (SEE).....	40
5.1	SEE from Heavy Ions and Protons - Basics .....	40
5.2	SEE Testing.....	41
5.2.1	SEE testing - general .....	41
5.2.2	SEE testing – traceability .....	42
5.2.3	SEE testing – influence of the application condition .....	42
5.2.4	SEE testing – critical parameters.....	44

5.2.5	SEE testing – normative documents .....	47
5.3	SEE Rate Calculation Method.....	49
5.4	SEE – Radiation Hardness Assurance .....	52
5.5	SEE – link with design engineering.....	53
5.5.1	SEE Inputs.....	53
5.5.2	SEE Mitigation – Part/Equipment/Subsystem Level.....	55
5.5.3	SEE Mitigation – System Level.....	56
6.	Conclusion .....	57
7.	References .....	58

## **1. Introduction**

As exhibited in the previous part of this course, the space radiation environment can lead to extremely harsh operating conditions for the on-board electronic equipment and systems and, to some extent, to poorly shielded materials.

On top of it, space systems providers, like Airbus, are willing to develop space products fitting the need of multiple potential customers in a cost effective manner. This results in a continuous trade-off between a generic versus an application/product specific approach, and, in the consideration of the intrinsic variability of numerous parameters within the radiation assurance process.

In particular, this part of the course will address the following items:

Variability in the radiation environment

- The use of static models versus dynamic environment
- The impact of changing a radiation model within a radiation specification
- The product development for multi-mission/multi-orbit purposes

Variability in the radiation modelling and calculation process

- Product line: the platform is similar however some changes are required from time to time: what is the best to use: a generic worst case model? No model at all? A specific model for each program?
- Also valid at sub-system/equipment level

Variability in radiation testing

- A device type is usually used in multiple application conditions. What approach is the best: generic worst case application (maybe difficult to find)? Specific application means one test per application
- TID testing: what dose rate to select: do we really need such a high confidence level that we shall test for 15 years in case of a 15 years mission?
- What kind of statistics to apply for the coverage of part to part, wafer to wafer, lot to lot variability?

Intrinsic variability of EEE parts

- Traceability: how far do we need to go?

Variability in the consideration of radiation degradation in the design

- One single method to perform a Worst Case Analysis (WCA)?
- Worst case approach versus specific approach (example of SET)

This has of course to be put in perspective with Radiation Design Margin (RDM).

Ultimately, the proper RHA process is the one which allows fulfilling the mission, whatever the mission is, according to the mission definition (which not only contains technical elements).

## 2. Radiation Hardness Assurance – A Definition

The Radiation Hardness Assurance (RHA) process consists in deploying all activities needed to insure that all the potentially radiation sensitive units of a space system, including the space system itself, will meet their design specifications up to the end of the targeted mission. A top level description of its content is presented in Figure 1.

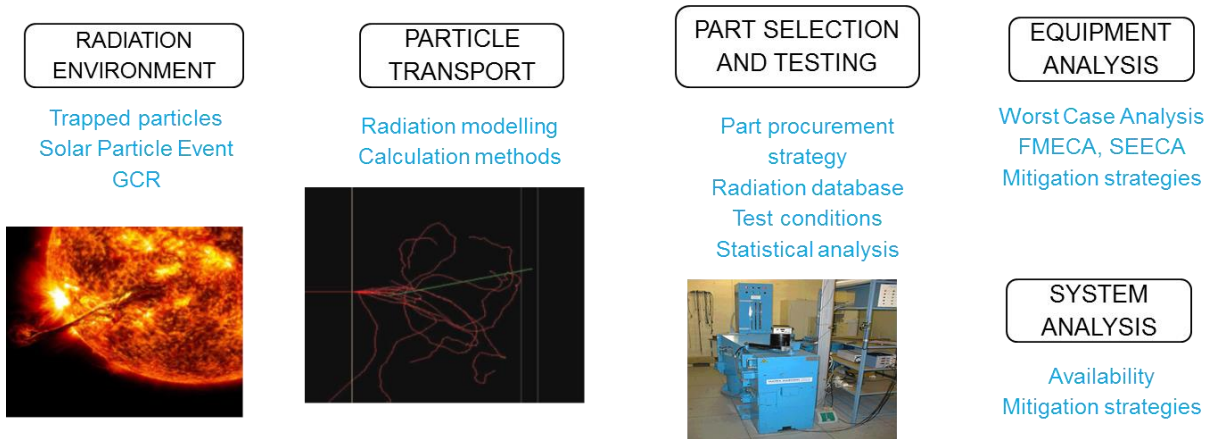


Figure 1: top level description of the Radiation Hardness Assurance coverage

This process is iterative. It starts first with top-level estimations of the radiation environment (provided in the mission radiation environment specification), then the radiation levels are transported at sensitive element levels and the electronic designs analyzed in order to validate the most sensitive parts:

- The mission radiation environment specification provides the radiation inputs outside the spacecraft: the particle spectra (heavy ion Linear Energy Transfer (LET) spectra, proton and electron energy spectra and dose-depth curves). This will be used later on for the definition of the radiation levels within spacecraft and/or the radiation specification levels.
- Assessment on parts radiation sensitivity: The radiation hardness of the parts is estimated on the basis of part selection, radiation databases relevant radiation tests, Radiation Design Margin, etc...
- Radiation aspects in Worst Case Analysis (WCA, Failure Mode, Effects and Criticality Analysis FMECA) of circuit, equipment and system design. The overall equipment and spacecraft worst case performance over the mission length, taking into account radiation effects, aging and other causes of degradation is estimated.
- System or equipment level countermeasure: Countermeasures can be implemented to either increase the acceptable sensitivity level of the part or reduce the radiation environment level: additional shielding at component level (spot shielding) or at box level (additional thickness of box cover), switching of redundant component or function, error correction system, specific memory organization, latch-up protection circuitry, etc.

As introduced earlier, the main goal of the RHA process is to ensure that the radiation sensitive elements of a space system perform to their design specifications after exposure to the space radiation environment. This means that the RHA process to deploy will be customized considering system robustness and redundancy.

Therefore, the RHA process itself would by nature be variable; the point for the space industry is to find the proper compromise between state of the art scientific radiation knowledge, industrial strategy and individual customer needs.

Numerous courses and presentation have been delivered in the past at NSREC of RADECS conferences (and elsewhere!), the reader will find references to these documents all along this course.

### **3. Radiation Environment Definition and Potential Impacts on RHA Process**

#### **3.1 Introduction**

In depth description of the space radiation environment can be found in the first part of this course or in older reviews [see for example 1 to 7]; we are more interested here in the necessary inputs required in the radiation environment requirement specification of a given space program [8 - 9]. In particular, we will focus on the variability sources which are behind the various entries of such environmental specification.

In the space industry, it is of foremost importance to describe the space radiation environment with regard to radiation sensitive elements and spacecraft mission. This will allow estimation of the kind of constraints that the spacecraft will experience during a mission, to compare it with sensitive element radiation tolerance and finally, to perform a risk assessment at elementary/subsystem/system level. As a matter of fact, the space radiation environment is one of the major inputs of the Radiation Hardness Assurance (RHA) process.

Regardless of the nature of a space program, radiation constraints apply. As an example, a launcher, which lifetime is considerably shorter than any satellite mission, has to deal with Single Event Effects on integrated circuits. Thus, the heavy ion and proton environment has to be described as precisely as possible. In a word, the description and the associated radiation environment specification have to be targeted regarding the nature of both the space system and mission.

At European level, the information that should be provided with such specification is specified in ECSS-E-ST-10-04C [10].

We need then to model the kind of particles that are capable of degrading the sensitive elements used in space systems. Thus, we will present today's available models for solar ions and GCR, trapped particles and solar protons. Most of the models presented here are available in different toolkits like OMERE [13 - 14] or SPENVIS (SPace ENVironment Information System) [11 - 12].

We'll show that there may exist several models which describes the same particle type, or, that most of the model can be tuned according to a confidence level. Also, some models are updated with new set of in-flight measurements, or, are refurbished according to the state of the art. At the end, this provides the user with the possibility of finding several representations of the same particle type, for the same mission.

#### **3.2 Galactic Cosmic Rays (GCR)**

Galactic Cosmic Ray are highly energetic and particularly penetrating particles. They are described by a spectrum representing the particle flux as a function of the Linear Energy Transfer (LET). LET is the amount of energy deposited by a gradually slowing particle per unit of length. It is material dependant and also a function of particle energy.

Today's most used models are Badhwar – O'Neill 2014 Model [15 to 19] and MSU (Nyrmik) model used in CREME96 [20 to 22]. The GCR ISO 15390:2004 model [23] is also based on the semi-empirical GCR models of the Moscow State University (MSU). To account for solar-cycle variations in the GCR

intensities, 12 month averages of the Wolf(sunspot) number are used. The model does not include anomalous cosmic rays. It is the one (specified in [10]) used at Airbus DS, through the OMERE software.

In the following, we have compared the GCR LET spectra in two different aspects; the first is to investigate the influence of the shielding (material and geomagnetic) and second to investigate the influence of the solar activity.

The Figure 2 illustrates that the shielding has very little influence on the GCR spectrum; therefore, the variability of this parameter will be negligible compared to all other elements needed in calculating a Single Event Effect (SEE) rate.

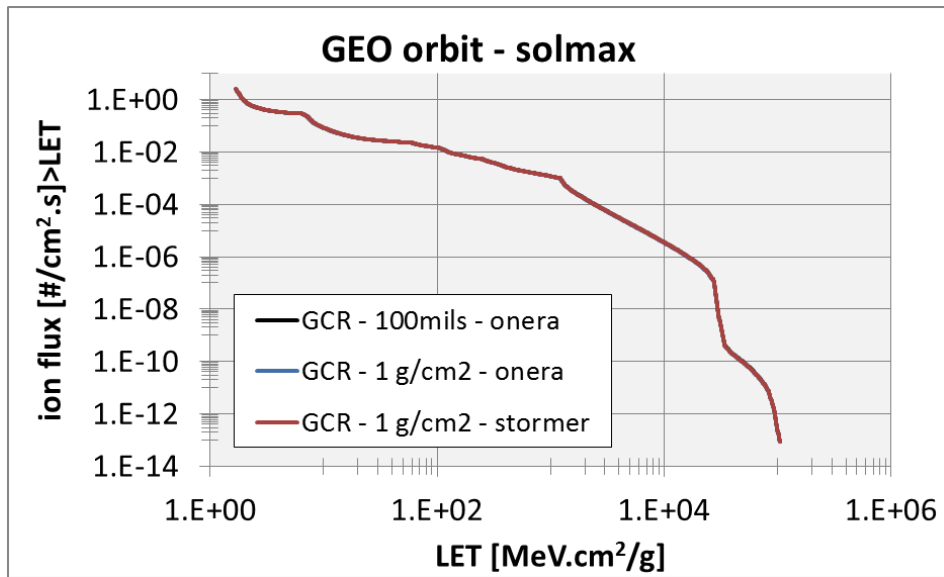


**Figure 2: comparison of GCR spectra for various shielding hypotheses**

Figure 3 compares GCR spectra in solar minimum and solar maximum conditions, with ISO 15390 model. This figure exhibits that the GCR flux will be worse in solar minimum than in solar maximum, by a non-negligible amount. Therefore, the standard Airbus DS approach in terms of specification is to consider the solar minimum activity for GCR in order to cover the worst case launch date scenario for product lines.

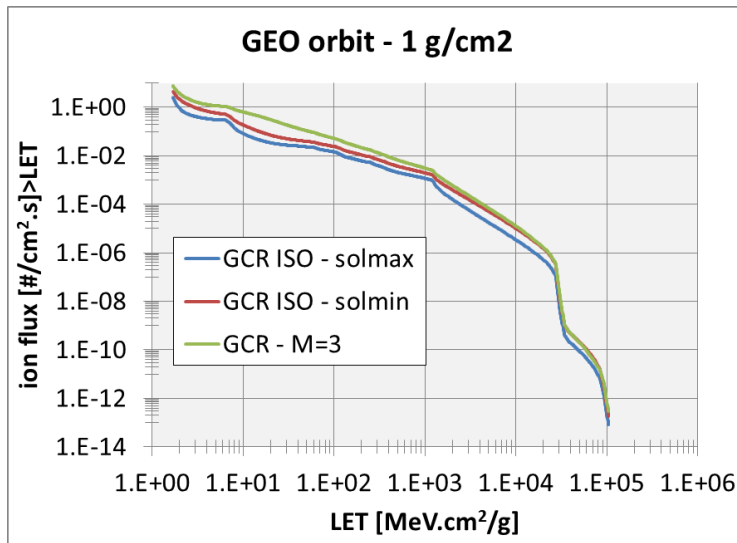


**Figure 3: comparison of GCR spectra for various solar activities; comparison with older CREME86 model, interplanetary weather index M=3**

The figure also compares the ISO 13390 model to the older CREME 86 [24] model.

CREME 86 offered different models of the GCR environment as well as the solar flare environment. For GCR, the proposed options go from M=1 (mean flux) to M=4 (singly ionised anomalous component) but M=2 (fully ionised anomalous component) is not been recommended for use [25]. For comparison purpose, the graph uses the M=3 (90% worst case environment) option even though M=1 and M=4 were recommended standards for GCR description [25 ], M=3 is applicable only for short duration satellite missions.

CREME 86 M=3 can still be found in some documents, we can see from Figure 3 that it gives a conservative estimate of the GCR flux.

### 3.3 Solar Particle Events (SPE)

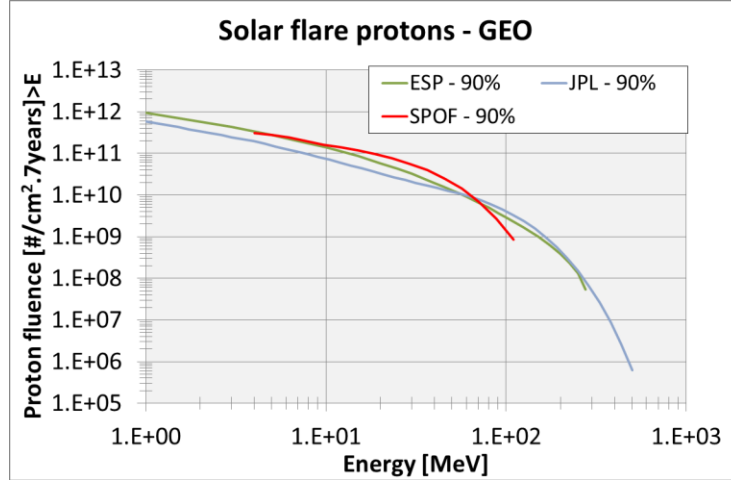
The development of an accurate model for Solar Particle Events is made more difficult by the nature of their infrequent occurrence. Some of the currently available models are for example: CREME96, ESP/PSYCHIC [26], IOFLAR [27] and SAPPHIRE (Solar Accumulated and Peak Proton and Heavy Ion Radiation Environment, [29]).

Protons traversing electronic components are responsible for a number of radiation degradation mechanisms. These are identified as total ionising, non-ionising dose deposition and SEE phenomena. Additionally, solar flares generating protons are not of constant amplitude (so called "ordinary events" and "Anomalously Large Events"). Thus, it is important to employ models for the averaged as well as peak (or worst case) environment conditions.

The approach of JPL91 (also known as the Feynman model) [30] and SPOF (Solar Proton ONERA Fluence) models is to predict total proton fluence for a given period with a given confidence level.

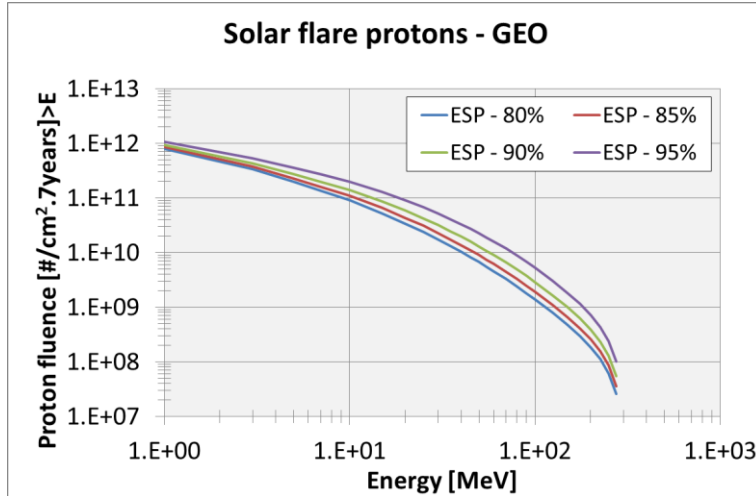
Note that Emission of Solar Protons (ESP) model, may be used for worst case as well as cumulative purpose [26, 31].

Figure 4 illustrates that for a given confidence level, spectra obtained with ESP, JPL91 or SPOF models are not rigorously identical. This means that the calculation of derived quantities (TID, TNID/DDEF) or Single Event Effect rate will result in different results.



**Figure 4: solar proton from SPE, different averaged models**

On the other hand, the selection of a given confidence level will also impact the solar proton spectrum. This is illustrated in Figure 5, with ESP model using confidence levels varying from 80 to 95%.



**Figure 5: solar proton spectra with ESP model and different confidence levels**

One can see from this figure that a large discrepancy exists for spectra in the 10 to 200 MeV energy range. This discrepancy will also be reflected in the calculation of the derived quantities.

The European space environment specification [10] requires use of the ESP model however it does not provide guidelines for the selection of a confidence level. As a consequence, the different customers may have a different approach in the selection of this parameter, making the product line approach difficult for the space industry. As of today, the Airbus DS approach is to use ESP model with a confidence level of 85%.

The particle composition of solar flares changes from events to events. The composition and quantities are similar to sun composition: Hydrogen ions (corresponding to protons) and Helium ions are more abundant than Oxygen, Carbon, Nitrogen, Magnesium, Silicon and Iron. IOFLAR model takes into account 28 types of heavy ions (from Z=1 to Z=28). It has been made using heavy ions fluxes measured in flight on IMP-7 and 8, Voyager and ISEE-3. The model is relying on Chenette analysis based on a law to express the heavy ions abundance versus Z. The IOFLAR model is based on data from a single flare of 1977. Consequently, this model is not to be considered as a generic model but as an example of a major heavy ion flare, in the same manner as the August 1972 or the October 1989 events may be considered as examples of major proton flares.

A worst case Solar Particle Event is an input of any radiation environment specification. It will serve for the validation of the electronics robustness toward SEE. The variability of this input, depending on the event which has been selected is illustrated in Figure 6.

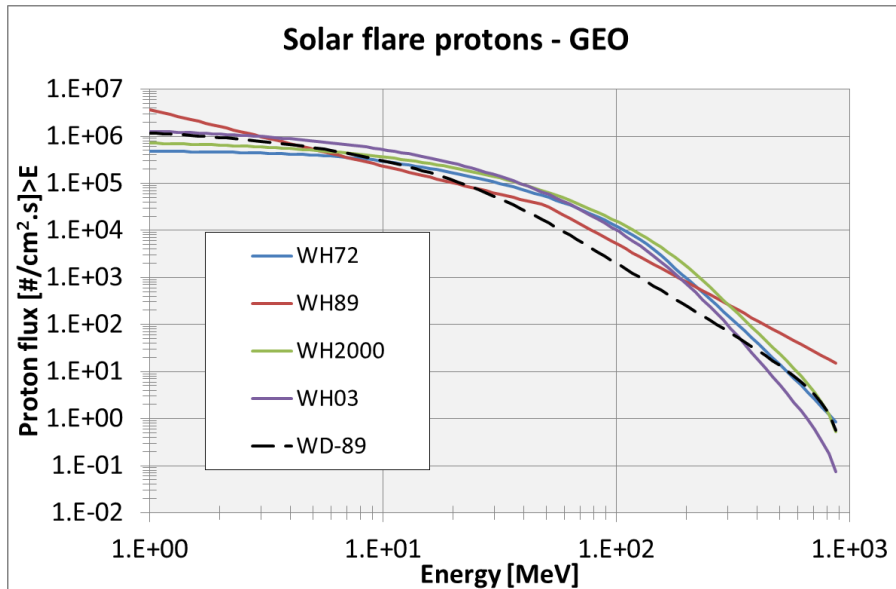


**Figure 6: worst hour proton spectrum for different events, with reference to worst day spectrum**

Besides the differences in the major events which occurred in the past, the duration selected for the particle flux evaluation is a key parameter. A first illustration has been given in Figure 6, it is further presented in the Figure 7.

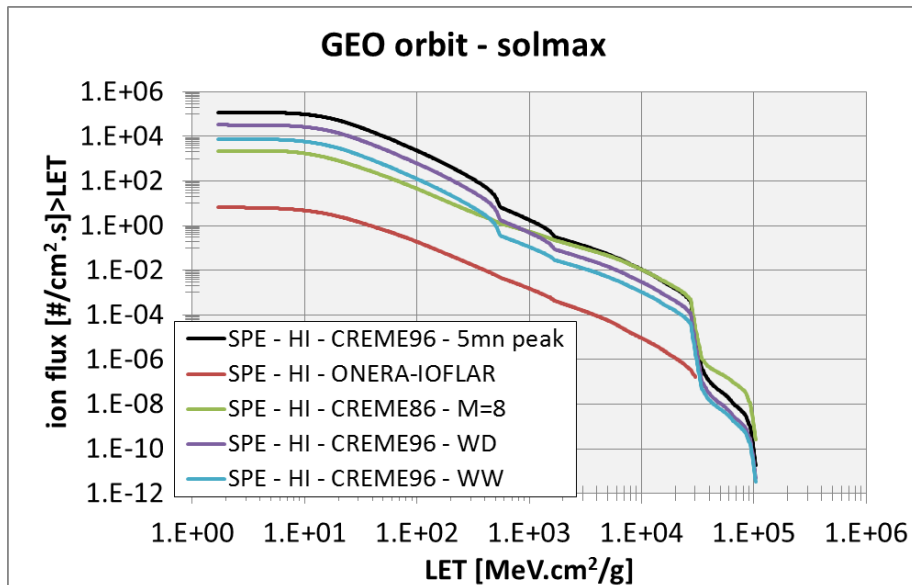


**Figure 7: Solar Particle Event – heavy ions**

This figure compares various inputs:

- spectra from the same event, but corresponding to different durations (worst 5 min, worst day, worst week)
- spectra computed with CREME96, CREME86 and IOFLAR models.

Regarding the first item, naturally, the shorter the duration is, the more stringent the flux will be. Figure 7 illustrates that there is about one order of magnitude in the heavy ion flux between the five minutes peak and the worst week. This order of magnitude will be transferred in the calculated SEE rate and therefore can easily make the difference between an acceptable and a rejected design.

Similarly to the confidence level applied to statistical SPE proton models, there is usually no specific recommendation in terms of duration to be selected in the normative documents. The duration to be selected shall for example consider the risk of having a SEE mitigation strategy defeated due to the successive SEE during a solar particle event.

For the second aspect, this figure clearly shows that (in the chosen conditions) predictions made by all the worst case models are still far more conservative than the 1977 eruption employed as a reference by the IOFLAR model.

### 3.4 Trapped Particles

The Earth's radiation belts contain electrons and protons: two electrons belts, the innermost of which is centred at  $L=1.4$  and extends to a distance of  $L=2.8$  and contains electrons whose energies are limited to about 5 MeV and the outermost centred at  $L=5$  and extends over a distance from  $L=2.8$  to  $L=12$ . The outer electron belt is more dynamic than the inner one and electron energies as high as 7 MeV are encountered. Trapped electrons are particularly a concern for MEO and GEO orbits.

The altitude corresponding to the maximum proton flux varies with the proton energy: it ranges from L=1.3 for the highest energies (400 MeV) to L=3 for the lowest energies (< 1 MeV). Trapped protons are more a concern for LEO and GTO orbits (including Electrical Orbit Rising, EOR), at least as far as electronic devices are concerned.

Finally, one should mention the South Atlantic Anomaly (SAA), a zone where the radiation belts drop in altitude, due to a 515 km/11° offset between the rotational axis and the Earth's magnetic dipole.

### 3.4.1 Trapped Electrons

Currently, the most frequently used model for trapped electrons remains the NASA AE8 model [32] but as for trapped protons, studies have been performed [e.g. 35] or are still in progress in order to improve our understanding of the trapped electron modelling. AE8 model has two main options related to the solar activity.

An electron model for the geostationary orbit has been developed by DESP-ONERA, mainly relying on data provided by Los Alamos National Laboratory (LANL); it has been presented for the first time during NSREC2003 [33] and his now the so-called IGE 2006 model [34, 36]. It proposes three different options: lower/average/upper case which also varies with the solar activity. It is now used as the standard model by numerous organization and is the ECSS-E-ST-10-04C reference for the geostationary orbit.

Finally, a set of new models, AE9/AP9/IRENE, for energetic electrons, energetic protons and space plasma [37], has been developed to fully replace AE8/AP8. It proposes an approach through confidence level definition (similar to what is actually proposed by ESP or JPL models for solar protons) and also the possibility to use several calculation methods. This set of models is still experiencing major updates which are reflected in Figure 8. This figure compares the electron spectra delivered by AE8, IGE-2006 and several revisions of AE9.

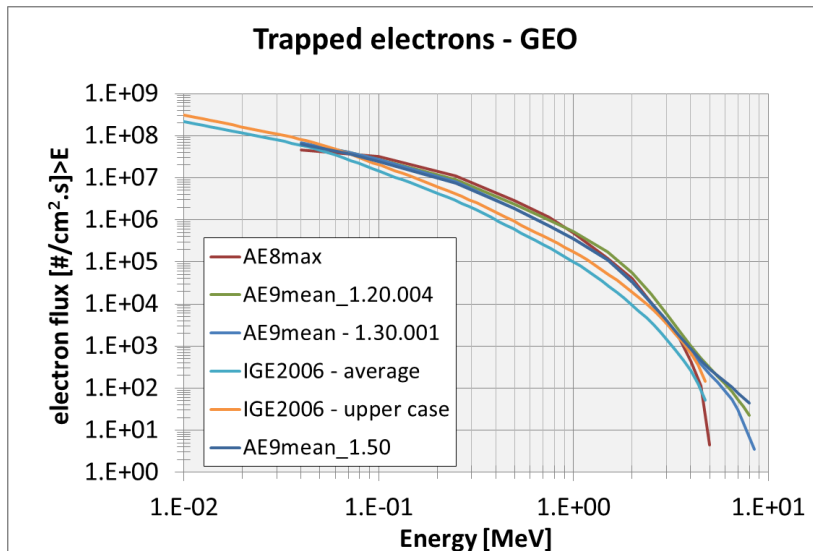
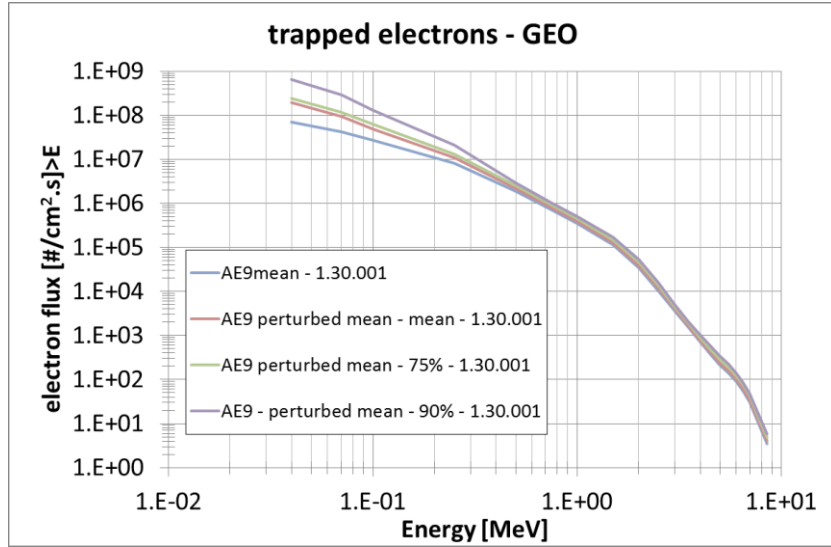


Figure 8: electron fluxes in GEO orbit, several models

This figure illustrates once again that models deliver outputs which experiences some variability, and that this variability may be of different nature depending on the particle energy range.

The next figure illustrates the influence of the confidence level on the electron spectrum, when using the AE9 model.



**Figure 9: electron flux in GEO orbit described by help of AE9 model**

This figure shows that for electrons whose energy is above 500 keV, the outputs are very similar. Oppositely, for the lowest electron energy, there is almost one order of magnitude of difference, which may be an issue for the calculation of TID levels for external surfaces.

### 3.4.2 Trapped Protons

Similarly to the trapped electron population, NASA AP8 [38] model is in fact the standard used for trapped proton modelling, even if, like for electrons, work has been performed and is still in progress to improve the estimation of the trapped protons environment [39, 40, 41, 42].

Like for electrons, the AP-9 trapped radiation models has been recently made available in order to improve the AE-8/AP-8 models. It uses the same approach as for electrons, mentioned in the previous section.

The following graph presents a comparison between AP8 model in solar minimum activity condition and the successive releases of the AP9 model, with the mean option. It illustrates the variability of the outputs in the course of the evolution of this model.

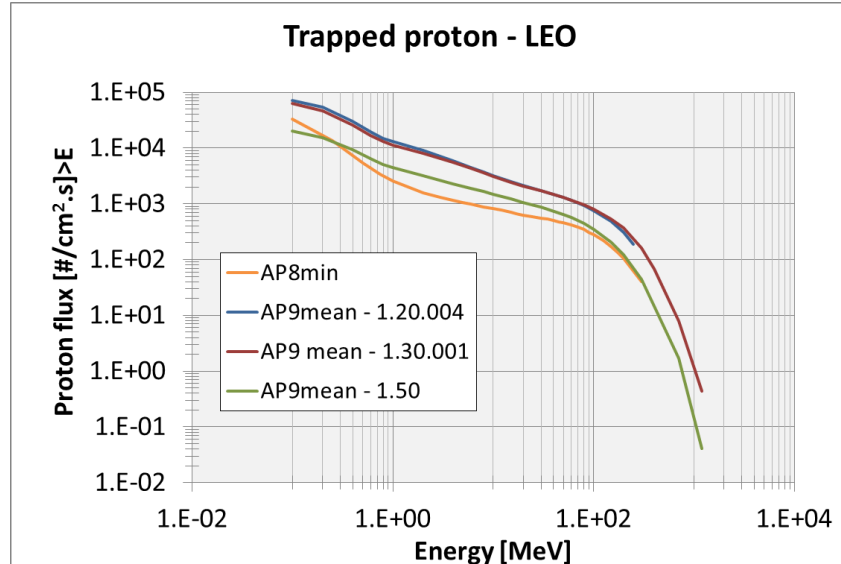


**Figure 10: AP8/AP9 comparison for LEO orbit**

One can note a major evolution between version 1.30.001 and version 1.50 which illustrates the difficulty for space industry to dimension their spacecraft with a model which is still experiencing regular updates. The next figure presents the influence of the confidence level on the spectrum nature; in this case, the influence of the confidence level between the mean value and 90% is limited among the whole energy range.

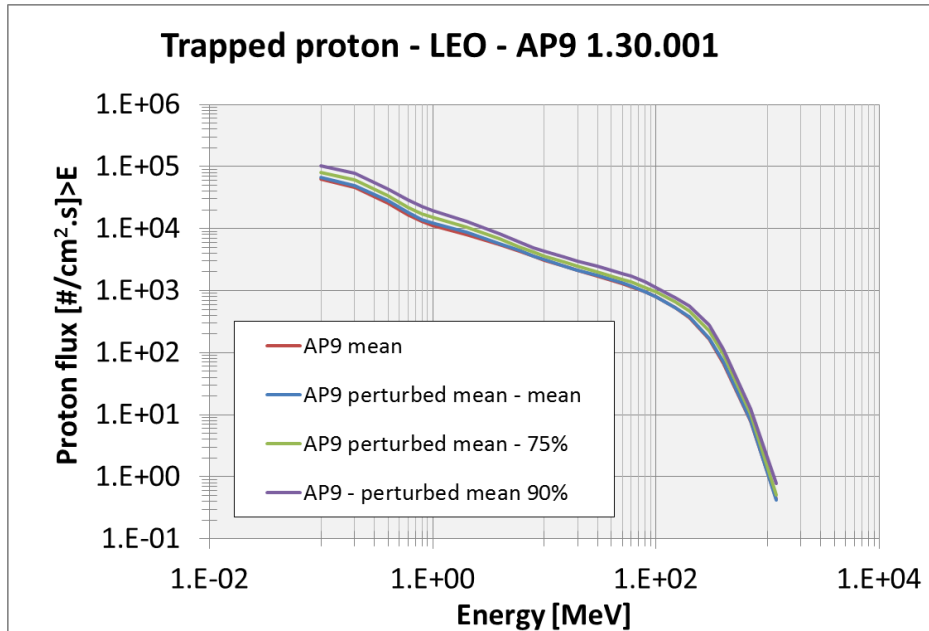


**Figure 11: trapped proton energy spectra in LEO modelled with AP9 model**

### 3.5 Derived Quantities

In order to avoid total dose induced failures during a mission, total dose levels to be received at component die level shall be calculated for all sensitive parts. This task is not so easy since typical material thickness encountered in a spacecraft partially shields the radiations, and makes exact calculation rather complicated. Specific tools are available to take into account the overall shielding given by the complex structure of spacecraft including equipment.

Total dose simulations can be performed either using 3D sector based codes or 3 D Monte Carlo transport codes. Sector based codes are simple to use and provide results with low CPU time while Monte Carlo codes are CPU time consuming but much more accurate.

Sector based analysis needs as input :

- 1-D dose depth curve
- 3-D structural model of materials surrounding the sensitive components : structural model of satellite and equipment where sensitive parts are located.

Sector based analysis output is the total dose to be received at the sensitive component die level.

The Dose/Depth curve gives the total dose received  $D(r)$  inside a specific 1-D normalised shielding geometry, for a shielding thickness  $r$ , for a given radiative environment. The dose/depth curve is the result of Monte Carlo calculation on a 1-dimension geometry, while dose calculations within a specific equipment require a 3-dimension treatment.

As an example, Figure 12 illustrates a typical 1-D normalised geometry : the so called "Solid Sphere model" and "Shell sphere model" for GEO orbit.

The dose/depth curve is established using the radiative environment specified at satellite level.

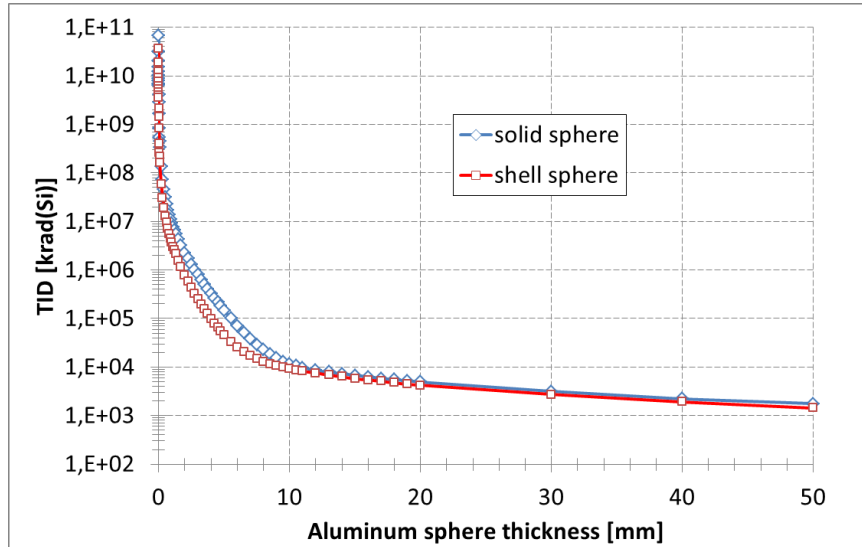
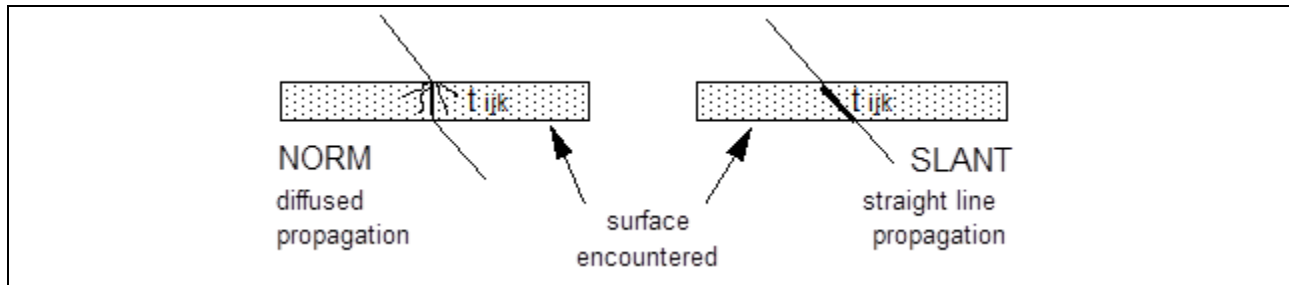


Figure 12: solid and shell sphere dose depth curve in GEO orbit

For first order estimations, sector based codes are preferred. The procedure uses tabulated attenuation data for simple geometrical shields. The analysis is performed using a numerical solid angle integration around a detector point. For each solid angle sector, a ray is traced from the detector to the outside of the geometry model. The total mass thickness along the ray is then used to calculate the dose received within the elemental solid angle from the tabulated dose/depth curve. Integration over all solid angles allows an estimate of the total dose level at die location. For example available sector based codes are FASTRAD [46], NOVICE/SIGMA [43, 44] and SYSTEMA/DOSRAD [45].

Two techniques are typically used to determine the thickness for each elemental sector: the NORM technique and the SLANT technique described in Figure 13.



**Figure 13 : So-called NORM and SLANT techniques for sector based analysis.**

Both techniques lead to significantly different estimate of shielding thicknesses along ray. Comparison between sector based analysis and Monte Carlo simulations shows there is a limited range of application for each of these techniques.

Such techniques have to be used in conjunction with a TID-depth curve for determination of the TID at target level. Some studies have been conducted in the past [47, 48, 49] in order to determine the adequacy or the accuracy of the ray tracing methodology with respect to Monte Carlo calculations. As a conclusion regarding TID level calculation methodology, it turns out that:

- The accuracy of ray tracing methods is strongly linked to the geometrical configuration surrounding the targets.
- Shell sphere + NORM and Solid sphere + SLANT ray tracing methods are both acceptable once you know that they provide an estimate of the TID level within about 30% compared to Monte Carlo calculation.
- Shell sphere + SLANT sectoring analysis method may lead to TID level underestimation of about 80% and should not to be used.

## 4. Radiation Effects on Electronics – Cumulative Phenomena

### 4.1 Total Ionizing Dose (TID) - Basics

Total Ionising Dose (TID) effects are due to energetic light particles such as electrons and protons of the natural space radiation environment impinging on materials. The interaction between particles and atoms may be of various nature, however, a large fraction of the energy loss generates electron/hole pairs in materials. In this process, called ionisation, the valence band electrons in the solid are excited to higher energy levels (trapping levels) in the bandgap and are highly mobile if an electric field is applied. The positively charged holes are also mobile, but to a lower degree. As a consequence, some of these electron/hole pairs will recombine, but a fraction will remain trapped as charges in solid layers. These charges may cause Total Ionising Dose damage in materials and electronic devices. TID damage is progressive and cumulates for the time the device or material is exposed to the radiation environment.

Regarding electronic (and opto-electronic) devices, TID degradation may lead to irreversible parametric drifts (see for example Figure 14 ) and eventually functional failures at component level. Exposure to ionising radiation at high doses can also degrade polymers and optical materials. In the case of the former, radiolytic reactions occur in which the bonds in the polymer chains are broken and formed with other reactive fragments. The result can be degradation of mechanical and dielectric properties, coloration, and production of gasses that can contaminate and corrode nearby materials. Other optical materials such as silica glasses can also suffer coloration and therefore degradation of their optical properties, de-pending upon the purity of the material.

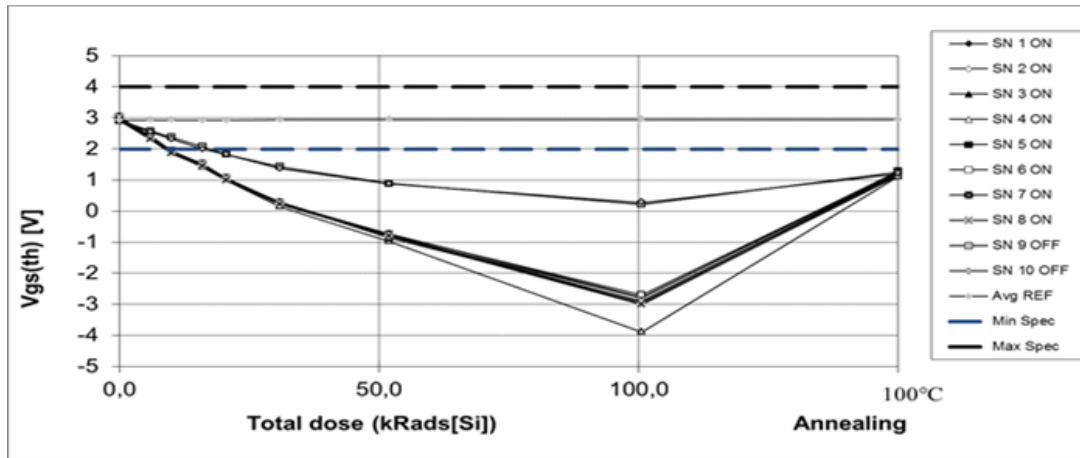


Figure 14: parametric drift of a MOS transistor under TID irradiation

Further details in this area can be found in numerous courses and publications, for example in NSREC and RADECS short courses (see for example 50, 51 and 52 for the recent ones).

#### 4.2 Total Non Ionizing Dose (TNID) – Displacement Damage (DD) - Basics

Energetic incident particles lose their energy through ionizing and non-ionizing processes as they travel through a given target material. The non-ionizing energy deposited by particle irradiation displaces atoms and creates electronic defect levels in the semiconductor bandgap. These radiation-induced electrically active defects can give rise to several processes [53], including generation, recombination, trapping, compensation, scattering..., etc. For example, a defect level near midgap can enhance the carrier thermal generation rate. Other defects can act as recombination centres and cause both the minority carrier lifetimes and diffusion lengths to decrease. This is the dominant mechanism for gain degradation due to displacement damage in bipolar transistors. Charge carriers can also be trapped temporarily at some typically shallow defect levels which can increase the transfer inefficiency in charge-coupled devices. Radiation-induced defects can also act as scattering centers and cause the carrier mobility to decrease. A common parameter to scale degradations is the Non-Ionizing Energy Loss (NIEL). The NIEL is the energy deposited in a material per unit of length that leads to displacement damage.

Displacement Damage leads to irreversible parametric drifts (e.g. in opto-coupler in ) and eventually functional failures at component level. The component drift must be considered in the equipment WCA, with drifts due to TID, ageing and other relevant effects.

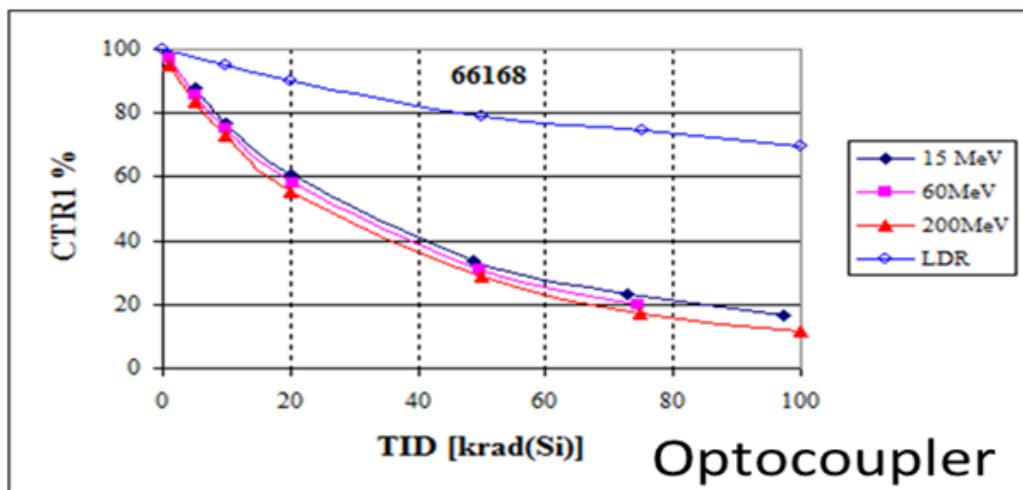


Figure 15: parametric drift of an under proton and Cobalt 60 irradiation

It is also not the purpose of this course to go further in details in this area, numerous courses and publications are available, for example in NSREC and RADECS short courses (see 54, 55 for the most recent).

### 4.3 TID/DD Calculation Methods

As mentioned in §3.5, there are two main techniques that allow calculation of the mission TID/DD levels. The first uses the input particle spectra and calculates each interaction of each particle with any material placed between the space and the target (target being the die of an electronic device or any material of interest). This may be done by tracking the particle from the source to the target (direct Monte Carlo: GEANT4 [56], ETRAN [57], MCNPX [58, 62]) or backward from the target to the source (reverse Monte Carlo: e.g. ITS5.0 [61], GEANT4 [59, 60], MCNP [63], NOVICE, FASTRAD). These methods are the most accurate for calculating a TID level in a complex geometrical structure using numerous materials of different nature [64] (device packaging + equipment geometry + spacecraft geometry). However, processing time may be prohibitive when hundreds of targets are concerned. The second method for TID level calculation is the ray tracing (or sectoring analysis) methodology. Such methodology is performed using numerical solid angle integration around a target point. For each solid angle sector, a ray is traced from the target to the outside of the geometry model. The total mass thickness encountered by the ray is then used to determine the corresponding TID level, using the dose-depth curve. The dose depth curve generally gives the dose levels at the centre of an Aluminium solid or shell sphere versus the shield thickness that is the radius of the sphere.

In a Space industrial program, this calculation process is in most of the cases separated in two phases. The first one is implemented at satellite/system level. Since the Large System Integrators in general don't share the layout of the satellite (and the equipment suppliers don't share the equipment layout as well), the first calculation step aims at determining the equivalent shielding brought by the satellite to the equipment under study. This output is in general a box, whose walls thickness represents the satellite shielding. Of course, depending on the equipment location and surrounding, this simplified figure may be more or less accurate.

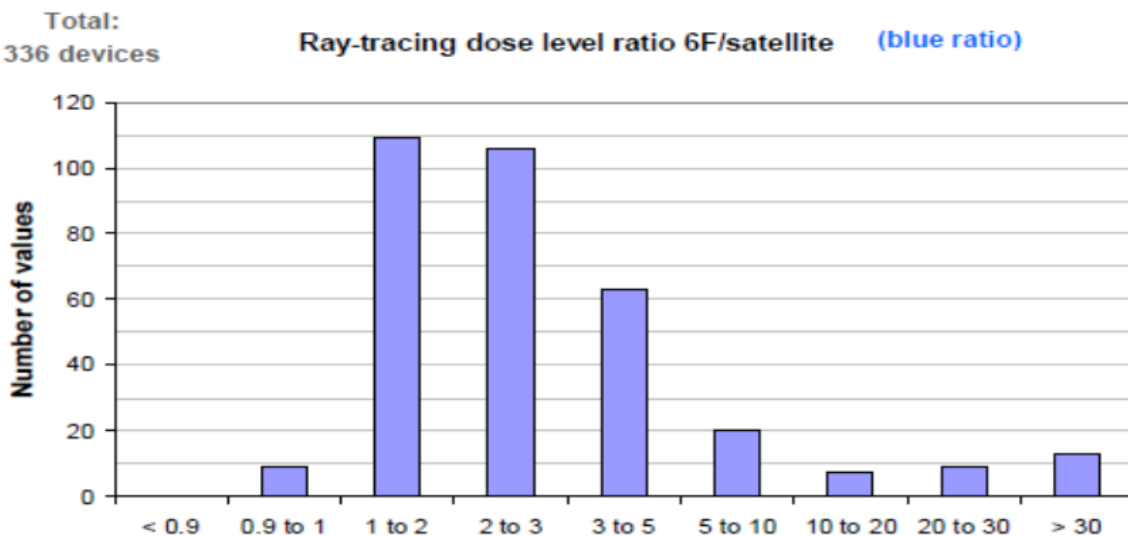


**Figure 16: comparison of calculated TID levels on devices based on real or simplified shielding shape**

Figure 16 [49] presents the result of calculations performed with ray tracing, for 336 devices distributed in several pieces of equipment, protected by a real or 6-faces equivalent shielding shape

for the satellite. We can see the variability of the outputs: with a simplified geometry, the calculated levels are conservative in the large majority of the cases, with a few cases underestimating the real figure by a very limited factor.

The next step is performed by the equipment supplier, who receives the equivalent shielding figures by the prime contractor and shall compute the TID/DD levels at sensitive die level. Then, the variability of the results may come from the selected calculation method - ray tracing (solid sphere / SLANT or shell sphere / NORM) vs reverse Monte Carlo. This is illustrated in Figure 17 and is further detailed in [65]. This figures exhibit that in this case, ray tracing outputs are likely conservative, except if the option shell sphere / SLANT method is used (which is not usable in the modern radiation tools, and is anyway forbidden in the Radiation Hardness Assurance standards).

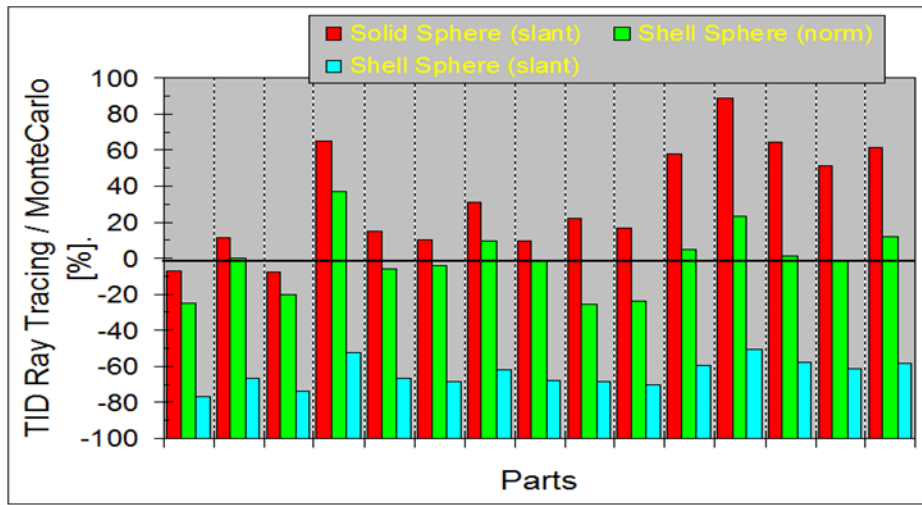


**Figure 17: TID results at equipment level, with different calculation methods**

Also large differences in the results may appear depending on the level of details that the geometrical model of the equipment/satellite contains.

## 4.4 TID TESTING

### 4.4.1 General

For the space industry, the goal at the evaluation phase is simply to assess the robustness of the device towards TID, to identify the parameters drifting under irradiation at the pre-selected levels, and also whether the device remains functional until the end of the irradiation. This is why the irradiation is generally pursued up to quite a high level (typically 100 krad(Si) for a standard space mission) in order to cover as many missions as possible with a single test.

Whatever test conditions are selected, one should keep in mind that such ground testing will only mimic, or at least bound the flight usage, since it is not possible to reproduce the space conditions at ground level, as illustrated in Figure 18.

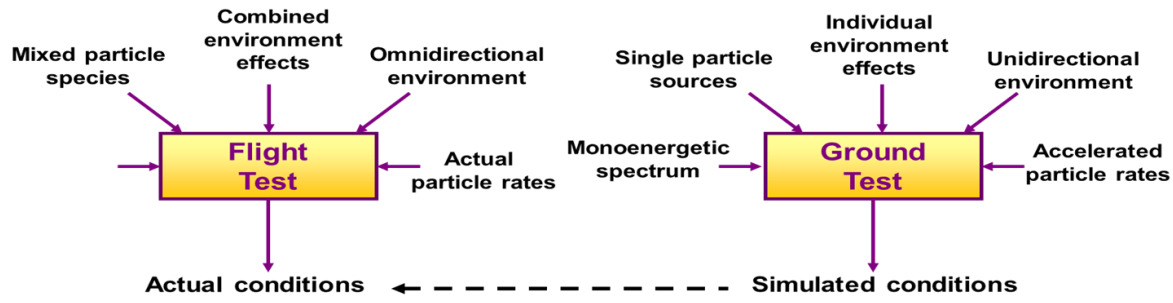


**Figure 18: differences between flight and ground test conditions**

#### 4.4.2 TID Testing – Sources

Total dose radiation tests are designed to characterise changes in device performance due to TID deposition.  $^{60}\text{Co}$  is the most commonly used source for simulating ionisation effects in components and materials. It emits photons of energy 1.173 and 1.332 MeV and has a half-life of 5.27 years. X-rays irradiation, provided they can be introduced into the active region of a device and the doses correctly estimated, may also be used. X-rays are generated when a beam of electrons bombards a target, usually a high-Z metal such as tungsten or copper, producing bremsstrahlung X-rays.



**Figure 19: Cobalt 60 source formerly used at Matra Marconi Space (now Airbus DS)**

These sources (an example of a cobalt 60 source is illustrated in Figure 19) allow use of a standard dose rate range (from some  $\text{rad}(\text{Si})/\text{h}$  to several  $\text{krad}(\text{Si})/\text{h}$ ) which are compatible with RHA requirements. They are also known to provide a conservative estimate of the space radiation environment [66, 67] as pointed out in Figure 20.

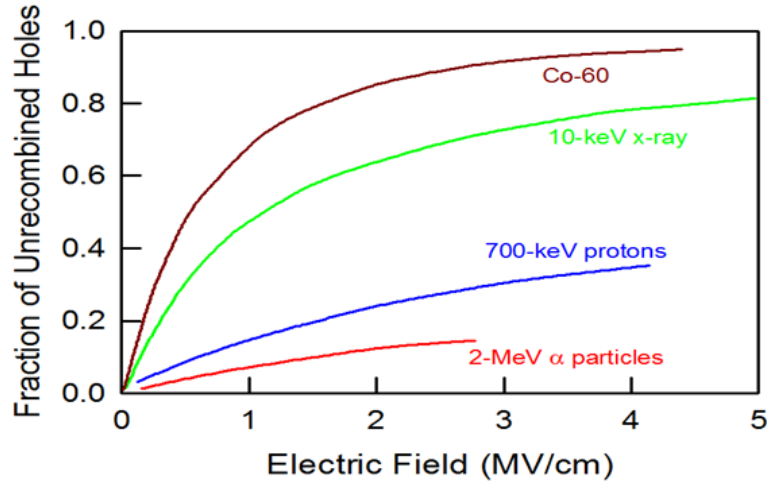


**Figure 20: measure of charge yield with different ionization source**

For some specific space radiation environment (typically electron rich Jupiter missions), it has been investigated whether Cobalt 60 testing remained a good source for TID testing [68] and it has been showed to be pretty much the case. This is illustrated in Figure 21.

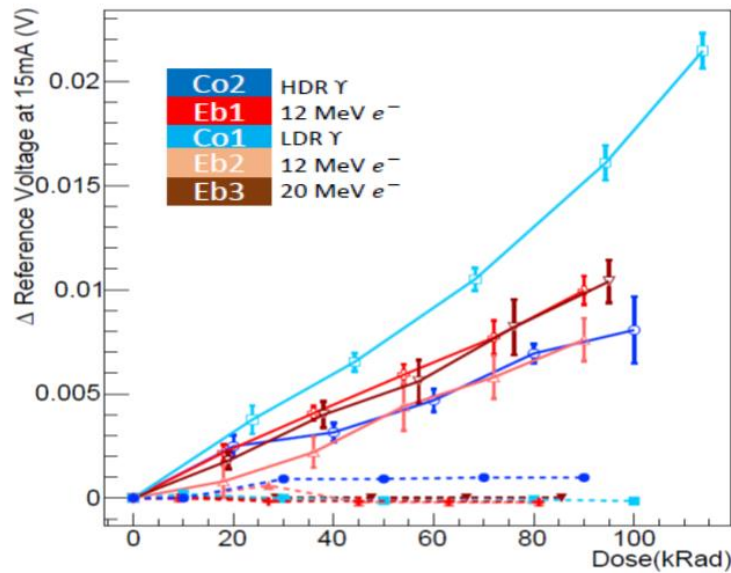


**Figure 21: outputs of TID testing with Cobalt 60 and electrons**

#### 4.4.3 TID Testing – Application Conditions

Among all the parameters indicated in the device specification (or data sheet), some of them may be critical for normal applications. Therefore, they have to be considered for the evaluation. Also the biasing conditions may vary from application to application, as will the way the device itself is used

(as an example there are several ways to use an operational amplifier in electronic designs). This is why TID testing is not an area restricted to radiation engineering, it should also be linked to electronic design engineering in order to ensure that testing will meet the needs in terms of further design analysis (WCA). As an example, at evaluation phase, biased and unbiased states have to be investigated since for some bipolar devices, and for some of their electrical parameters, devices irradiated unbiased may degrade much more than the ones irradiated biased. Figure 22 presents the drift of an OP470 positive bias current as a function of the total dose level for both biased (N°2 to N°6) and unbiased (N°7 to N°11, "OFF") samples.

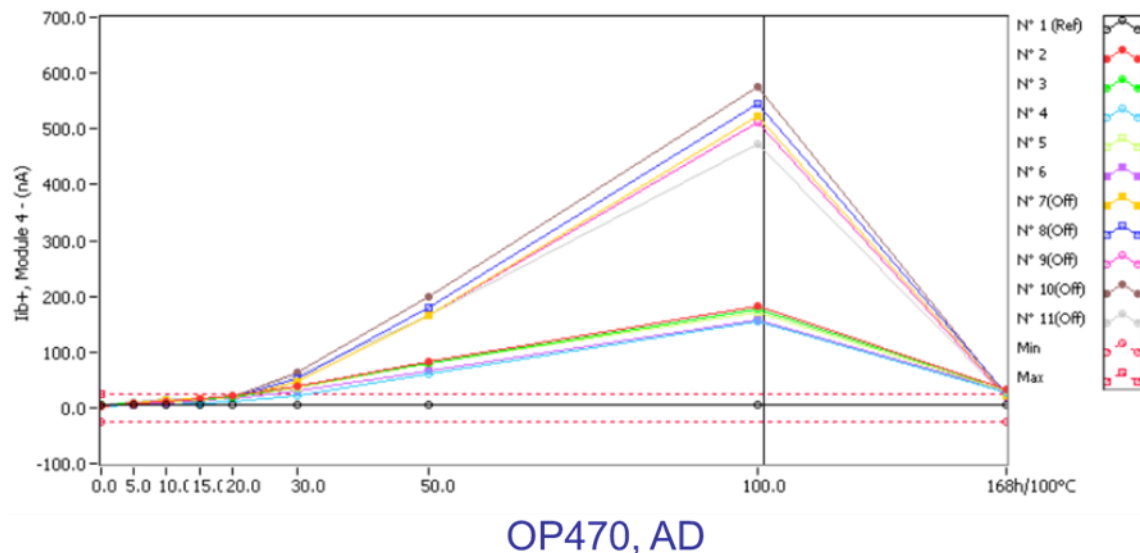


**Figure 22: Influence of biasing on TID tolerance**

In addition, the Figure 23 and Figure 24 presents the difference in TID behaviour that the same device may experience in two different usage conditions. Up to 30 krad(Si) the behaviour is very similar however if the dose to account for the Worst Case Analysis is 50 krad(Si), the parametric drift exhibits a strong difference between circuit n°1 and circuit n°2.

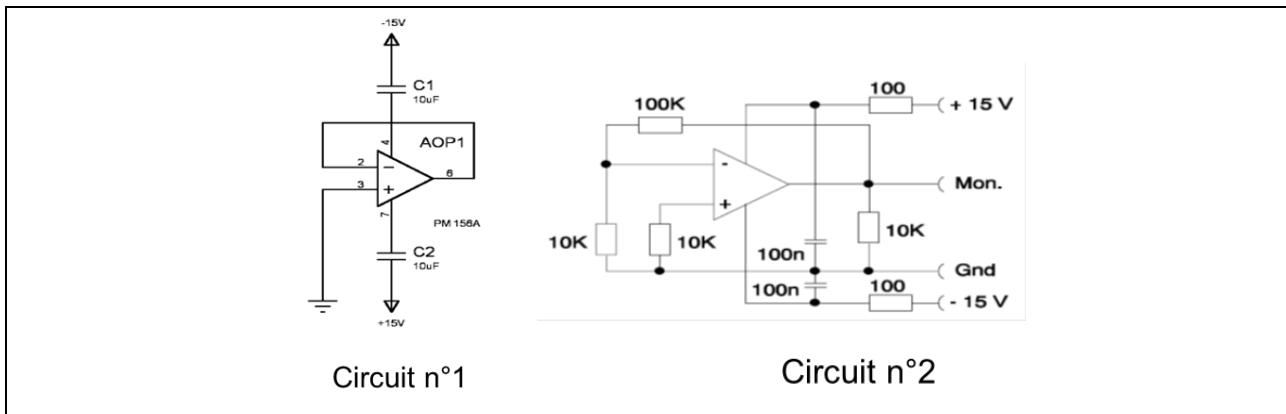


Figure 23: operational amplifier used in application n°1 and application n°2

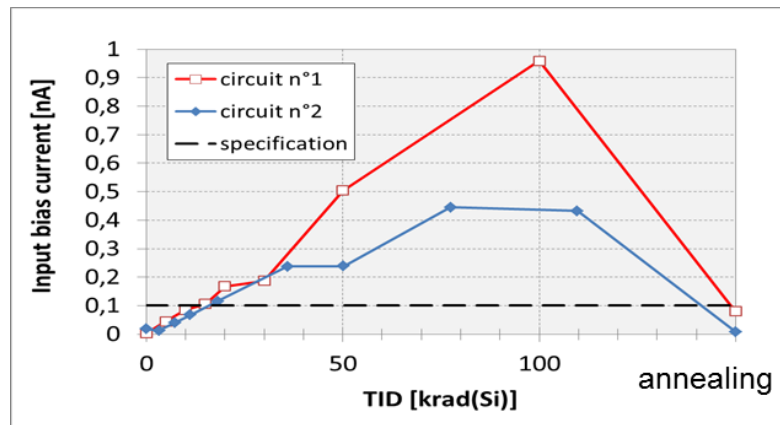


Figure 24: parametric evolution of the AOP under irradiation for application n°1 and n°2

Another example is provided in Figure 25 with the current transfer ratio drift of an opto-coupler.

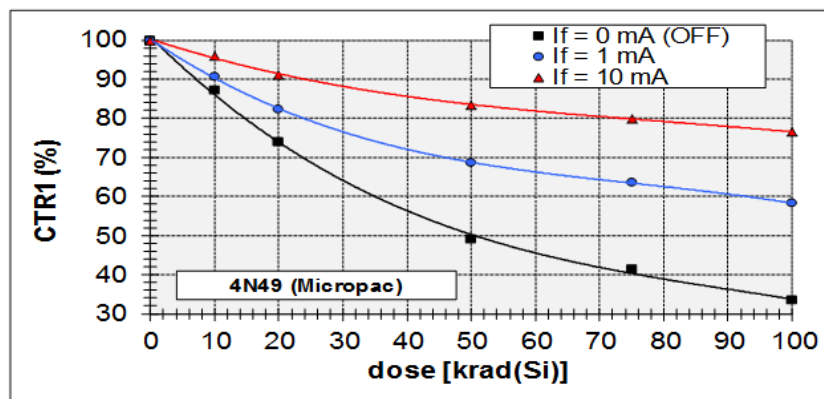


Figure 25: parametric evolution of the opto-coupler under irradiation for several forward current values

#### 4.4.4 TID testing – Enhanced Low Dose Rate Sensitivity (ELDRS)

ELDRS effect has been firstly reported in [69]. It was found that in some bipolar devices, the amount of TID gain degradation is greater at a given TID level when the TID is accumulated at a low rate. This has been confirmed later on by numerous papers (see for example [70, 71, 72]. An illustration of ELDRS is provided in Figure 26.

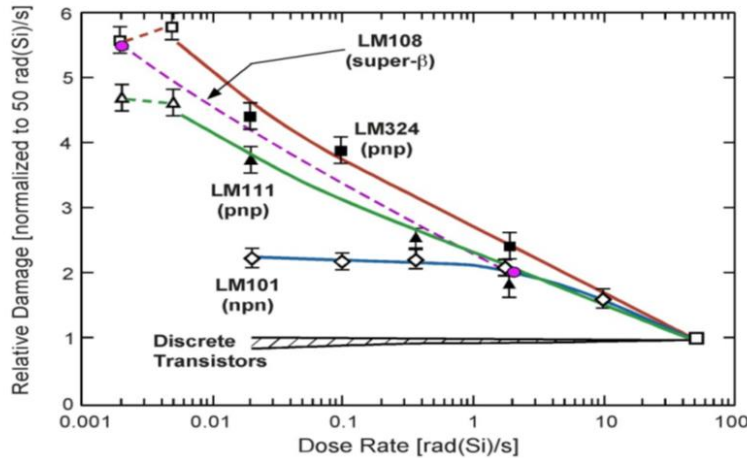


Figure 26: Effect of dose rate on total dose damage for various technologies - 72

Furthermore, despite the numerous attempts to simulate the phenomena by other means (see for example [73 to 77]) the low dose rate behaviour of bipolar devices remains unpredictable in the majority of the cases. Then, up to now, ELDRS remains a particular concern to tackle in the RHA process: as a matter of fact, the worst case situation for bipolar device may not be at the lowest dose rate; there are several results where extreme low dose rate (e.g.  $< 0.01$  rad(Si)/s) has been demonstrated as optimistic compared to low dose rate ( $0.1$  rad(Si)/h) [78, 79].

#### OP27 plots examples

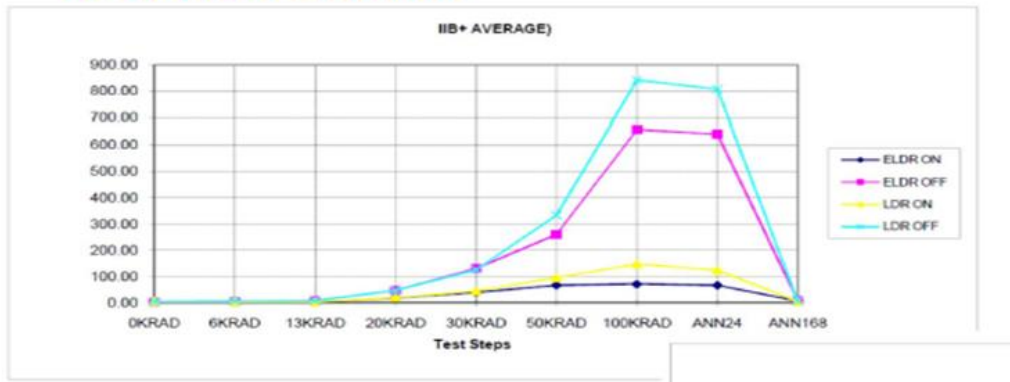
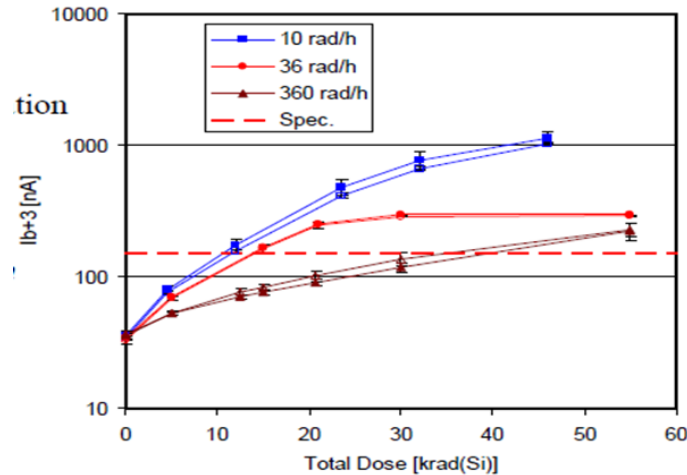


Figure 27: OP27 TID testing with two different low dose rates – [78]

In other cases, the lower the dose rate is, the worst the device behaviour is (Figure 28). Therefore, in terms of RHA, the need to statistically spot the risk versus the dose rate value remains valid.



**Figure 28: test of a bipolar integrated circuit at three different dose rates – [80]**

#### 4.4.5 TID testing – traceability

A general definition of traceability is the ability to verify the history, location, or application of an item by means of a documented recorded identification. This idea is fully applicable to an electronic device and represents a typical record of device “pedigree” that would benefit consideration of any further use of the same device (see Figure 29).

PART PEDIGREE AS-BUILT			
EEE Component			
Item		Type	
Manufacturer		Manufacturer Reference	
General Information			
Astrium Electrical Function		Package	
Die Manufacturer (if different of manufacturer part)			
Detail Specification			
Technology		Quality Level	
Part Traceability : PAD Requirement			
Diffusion Lot Number or Manufacturer Lot		Wafer Plant	
Die Marking			
Part Marking			
Date Code			
Comments			

**Figure 29: device pedigree**

Device traceability must be fully representative of flight parts. Therefore, they must be of the same quality level, have experienced the same ground process (including Pre-irradiation Elevated Temperature Stress (PETS)), and must benefit from all necessary traceability information, as illustrated in Figure 29. Die and package pictures are systematically recorded as additional traceability information (Figure 30).

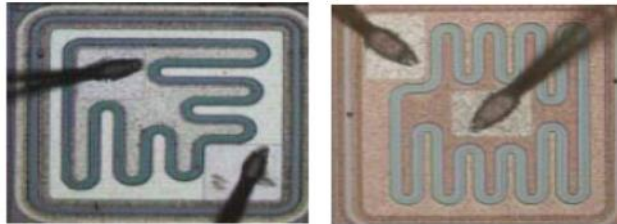


**Figure 30: die picture of a bipolar transistor, same reference**

It is important to note that traceability is the key information to insure that the tested device will behave in a similar way to the flight device. This represents in particular a major issue for COTS, where traceability is difficult to access.

#### 4.4.6 TID testing – test results analysis

Sampling size for TID testing shall be determined depending upon the kind of analysis that will be required for the test results. Most RHA specifications link sampling size to statistics: since there is some dispersion between devices, even though they belong to the same wafer lot, it is important to make use of statistical tools for test data analysis in order to provide robust values to integrate into the design WCA. RHA usually sets the statistical requirements in identifying a desired probability of survival ( $P_s$ ) and a confidence level ( $C$ ). Then, the most commonly used method for statistical analysis to determine the change in a parameter ( $\Delta P$ ) and is to assume a normal distribution with one sided tolerance limits ( $K_{TL}$ ):

$$\Delta P_{rad} = \Delta P_{av} + K_{TL} \times \sigma$$

Where  $\Delta P_{av}$  is the average parameter delta at a given test level,  $K_{TL}$  is the one sided tolerance factor based on sample size and  $\sigma$  the standard deviation of the parameter deltas.  $K_{TL}$  varies with the confidence level, with the required probability of survival and with the sampling size. It should be noted that below a sampling size of 5 parts, the KTL value dramatically increases. More details about statistical methods can be found in [81].

The point is that the selection of both probability of survival and confidence level will heavily impact the determination of the parameter value to use for the WCA, as illustrated in Figure 31 and in Figure 32. Depending on the nature of the intra-lot dispersion, the impact may be moderate (Figure 31) or major (Figure 32).

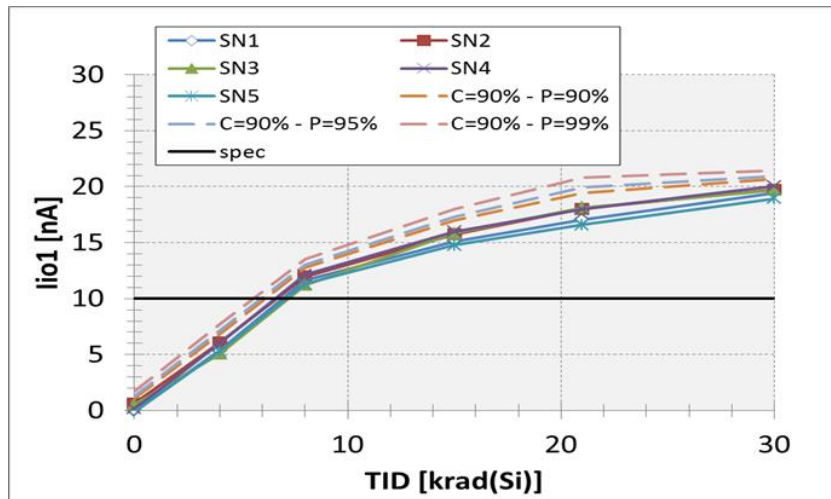


**Figure 31: variability of statistical analysis for TID test results**

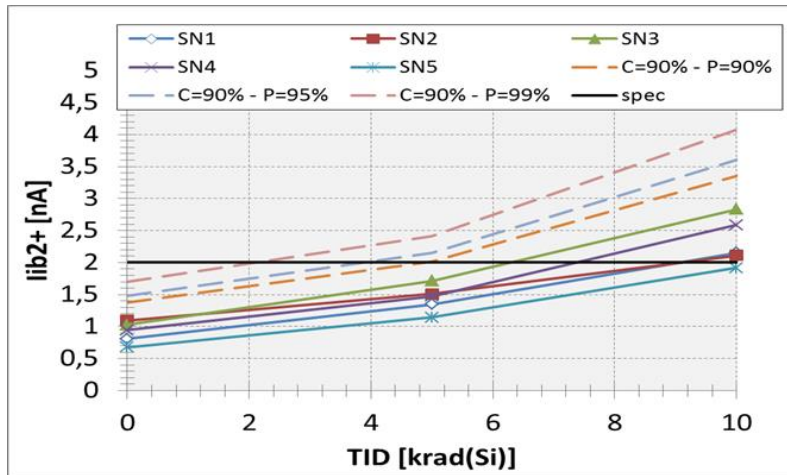


**Figure 32: variability of statistical analysis for TID test results, another example**

Usual practice from the European space industry is to use both parameters set at 90% however, as for ELDRS, the value to select, corresponding to an acceptable risk, is still subject of debate (see for example [82]).

#### 4.4.7 TID testing – normative documents

In order to ensure reproducibility of test conditions, comparison of test results and test adequacy with respect to flight conditions, normative specifications based on the technical state of the art exists for TID testing. If we focus on microcircuits, the following norms are applicable:

- For Europe: "Total Dose Steady State Irradiation Test method", ESCC 22900 issue 5 [83].

- For US: MIL-STD-883/Test method 1019.9 [84] for integrated circuits and MIL-STD-750, Test Method 1019 [85] for discrete devices.

When comparing ESCC 22900 and MIL-STD-883/Test method 1019.9, both documents are of similar nature, nevertheless we can also note some variability from specification to specification in the following areas, as shown in Figure 33:



- |  |  |   |
|--|--|---|
| <ul style="list-style-type: none"> <li>▪ <b>radiation source:</b></li> <li>▪ <b>Dose rate:</b></li> <li>▪ <b>Annealing</b></li> <li>...</li> </ul> | <ul style="list-style-type: none"> <li>▪ Cobalt 60 gamma source or electron accelerator beam.</li> <li>▪ Window 1 ("Standard Rate"): 0.36 to 180 krad(Si)/hour</li> <li>▪ Window 2 ("Low Rate"): 36 to 360 rad(Si)/hour</li> <li>▪ Room T° 24h and 100°C 168h, all device types</li> </ul> | <ul style="list-style-type: none"> <li>▪ uniform field of a 60Co gamma ray source</li> <li>▪ Condition A. to E. various DR conditions between <math>\leq 10</math> mrad(Si)/h and 300 rad(Si)/s possibly with accelerated test.</li> <li>▪ Room T° (all devices), duration may be extended</li> <li>▪ Accelerated (MOS only) at 100°C, variable duration</li> </ul> |
|--|--|---|

**Figure 33: differences between ESCC and MIL specifications for TID testing**

On top of it, the structure of both documents is different: in the European Space Components Coordination (ESCC) standard, there are two separate paragraphs providing the requirements to apply in case the user is or is not in the frame of an ESCC context. So in summary, there are requirements for part manufacturer wishing to achieve an ESCC qualification and other requirements for users who are not in this context (like equipment suppliers or prime contractors from the space industry). This does not exist in the MIL standard.

From a technical point of view, if some of the deltas may be insignificant in some cases (for example Cobalt 60 TID testing is widely used), they may represent a challenge in other areas. In particular, the requirements in terms of Dose Rate are different in the two specifications.

Let's consider the case of being outside an ESCC evaluation/qualification context.

In the ESCC 22900, the requirement will be:

The dose rate shall be:

- Within the Standard or Low Dose Rate window (as defined in Figure 33) for MOS and CMOS devices,
- Within the Low Dose Rate window for devices containing bipolar transistors, or
- As justified by application and/or mission conditions.

In the MIL standard, the requirement will be:

Radiation dose rate. The radiation dose rate for bipolar and BiCMOS linear or mixed-signal parts used in applications where the maximum dose rate is below 50 rad(Si)/s shall be determined as described in paragraph 3.13 below. Parts used in low dose rate applications, unless they have been demonstrated to not exhibit an ELDRS response shall use Condition C, Condition D, or Condition E.

NOTE: Devices that contain both MOS and bipolar devices may require qualification to multiple subconditions to ensure that both ELDRS and traditional MOS effects are evaluated.

With:

- Condition C For condition C, (as an alternative) the test may be performed at the dose rate agreed to by the parties to the test. Where the final user is not known, the test conditions and results shall be made available in the test report with each purchase order.
- Condition D For condition D, for bipolar or BiCMOS linear or mixed-signal devices only, the parts shall be irradiated at  $\leq$  10 mrad(Si)/s.
- Condition E For condition E, for bipolar or BiCMOS linear or mixed-signal devices only, the parts shall be irradiated with the accelerated test conditions determined by characterization testing as discussed in paragraph 3.13.2. The accelerated test may include irradiation at an elevated temperature.

As a result, in case your equipment/system addresses both European and US customers, it shall be developed in accordance with the worst case condition of the above specifications.

#### 4.5 DD Testing

TID, which involves interactions between high energy particles and atomic electrons is usually the main concern for cumulative damage from electrons and protons in the natural space environment. On the other hand, displacement damage involves interactions between an incident particle and the nucleus of an atom within a material, in contrast with direct ionization, which is produced by interactions between an incoming particle and loosely bound electrons. It may be of importance for various types of electronic and optoelectronic parts (see examples given in Figure 34 and in Figure 35) although most of them are only affected by displacement effects at fluence levels which are not reached in most of the standard near-Earth space missions. As a result, displacement damage evaluation is for most of the time restricted to optoelectronic parts [86, 88, 90, 91], and, to a lesser extent, to bipolar integrated circuits [87, 89] in the context of some low Earth or elliptical orbit missions, where the population of trapped protons may be of importance.

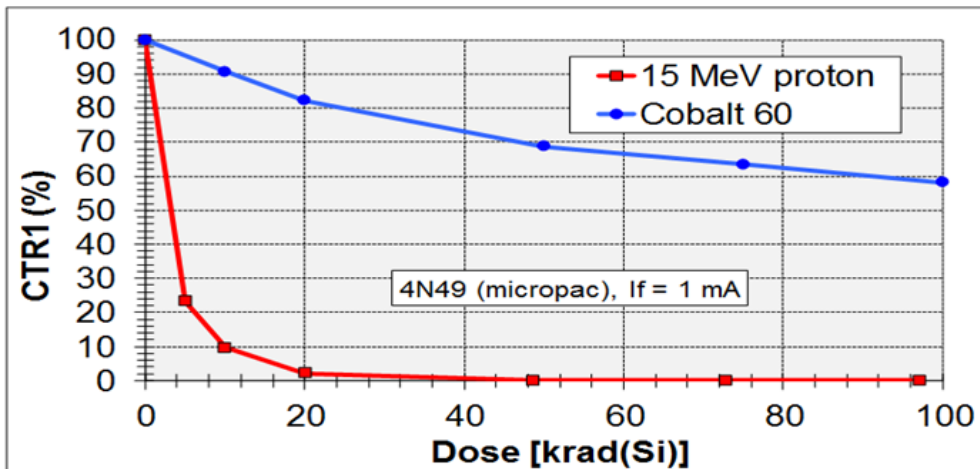


Figure 34: CTR degradation of an optocoupler when irradiated with Cobalt 60 or protons of various energies -91

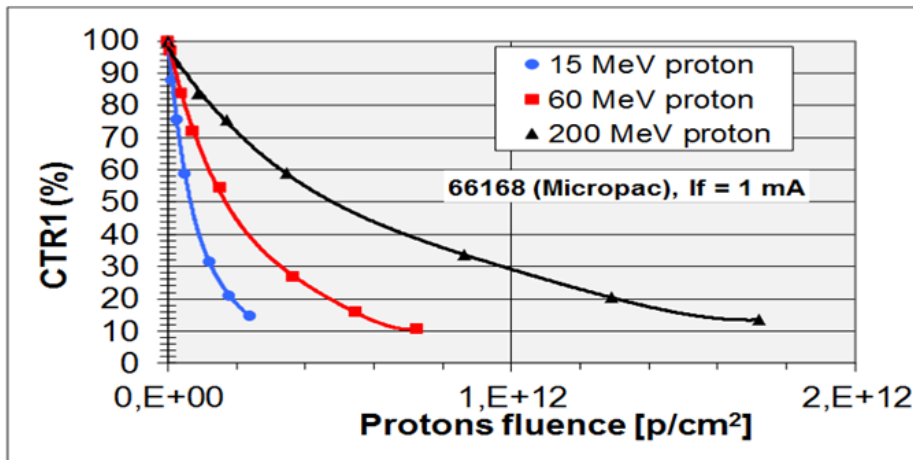


Figure 35: CTR degradation of an optocoupler when irradiated with protons of various energies -91

Most of the items mentioned for TID testing are also valid for DD, nevertheless, there are a few particular items for DD testing:

1. No normative documentation exists at present (although an ESCC document is actually under preparation) which makes the general framework of DD testing quite vague and a validity assessment of each DD testing mandatory. DD testing guidelines can be found in [89, 92 and 93].
2. Particle sources to be used for DD testing: most of the time, DD testing is performed using proton accelerators with proton energies varying from a few MeV to some hundreds of MeV. Neutrons can also be used. Neutron damage is typically specified in terms of “1 MeV equivalent neutrons”. However, this equivalence is not always known very accurately, and may be affected by the presence of moderating material around the detector. Another

disadvantage is that neutrons tend to activate packages and leads (even though this may also be the case with protons at elevated fluences). For protons, the energy is usually chosen in the 50 MeV range since this allows irradiation of devices without removing their lids.

3. When performing proton irradiation, some TID will also be deposited. Devices tested for DD are most of the time sensitive to TID as well. One must estimate the amount of the TID deposited (which usually does not match with the TID level expected during the mission) and consider it when performing the WCA. This implies that a device sensitive to DD will also have to be characterized for TID. Both characterizations may then be performed in parallel or sequentially. Each approach has advantages and drawbacks. Doing the TID and DD testing separately is less representative of the flight environment. However several steps can be performed and the degradation considered at various levels (for several different application and/or radiation levels). When TID and DD testing are sequential, the annealing between the two tests must be considered. The overall testing can only be unambiguous for the first test which is performed (usually the DD testing). So at the evaluation stage, unless a firm application and mission are identified, it is rather advisable to perform separate testing even though this may not be fully accurate.
4. Testing with a particle accelerator implies that testing will be performed with high flux and therefore at an elevated dose rate even though the resulting TID deposition may need to be considered for bipolar circuits (which might be sensitive to low dose rate effects).
5. Computing fluence levels for DD testing necessitates the use of the Non Ionizing Energy Loss (NIEL) as a function of energy for the semiconductor of concern, in order to convert the space radiation environment energy spectra into an “equivalent” fluence of a unique particle and energy (the displacement damage equivalent fluence, DDEF). As an example, NIEL values are provided for silicon in Figure 36. Also note from this figure that several sets of values exist for each semiconductor material. In the absence of agreement on the one to consider as the standard, this may lead to confusion in terms of DDEF computation.

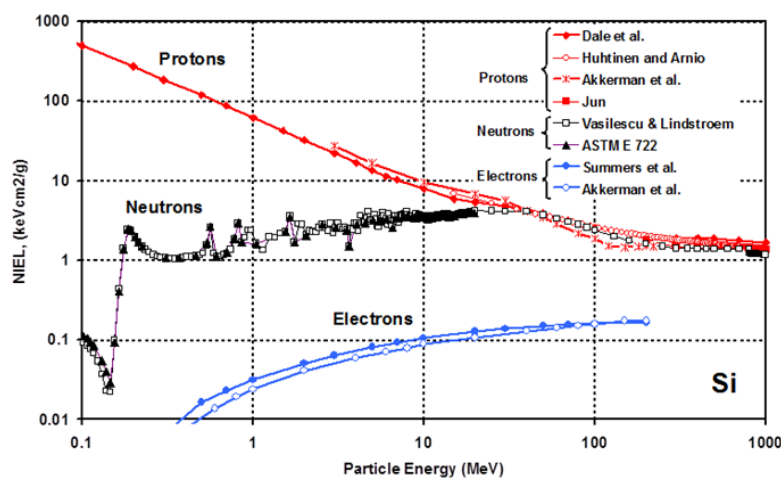
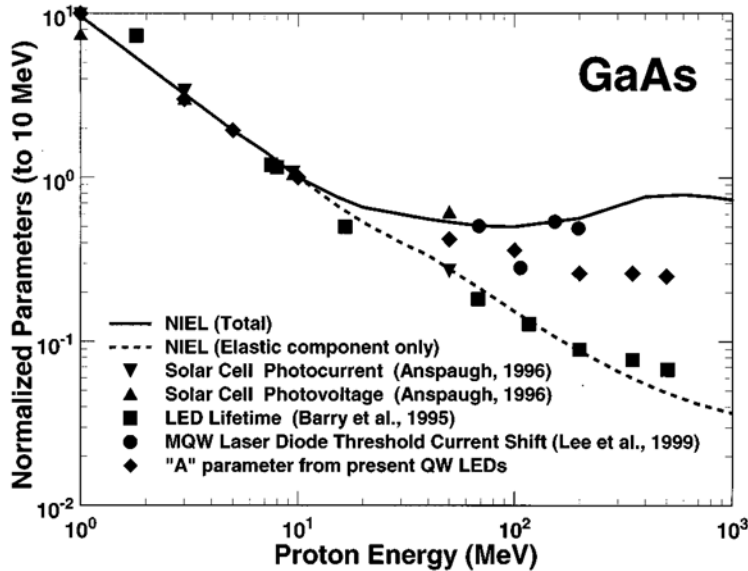


Figure 36: NIEL values for silicon [94]

A potential issue is that NIEL is constituted by both elastic and inelastic components and the importance of the degradation may preferentially be due to one or the other component, depending on the device nature and technology. Figure 37 shows for example the NIEL components for GaAs, along with measurements. As a consequence, this may result in erroneous computation of the DDEF and it is always best to test at several energies. This is not always practical, for example for funding reasons.



**Figure 37: NIEL in GaAs [95]**

For solar cells, the shielding from the cover glass or array structure is relatively small and most of the damage comes from low energy protons and electrons. Therefore, testing with 1-3 MeV electrons and 3-10 MeV protons is common. Another point is that since the dependence on NIEL is different for electrons and protons, it is advisable to do separate tests.

As a summary, there are inherent difficulties in DD testing because of the wide range of particle energies, along with the cost of typical facilities. On top of this, the interpretation of damage measured for one type of particle and energy in the broader context of the particle spectra in the real space environment is still a problematic. This is partially solved (or addressed) by the use of NIEL although this creates a potential source of variability in DDEF computation.

#### 4.6 TID/DD Testing at Board Level

The increasing sophistication of next generation space systems will necessitate new, higher performance components. In comparison to military or space-grade components, commercial-of-the-shelf (COTS) electronics can offer increased performance and reductions in size, power and cost. Although, COTS components performance capabilities may outperform traditional space qualified components, there are limitations strongly complicating their use for space applications. Limitations

concern lack of traceability, packaging constraints, radiation sensitivity and questions regarding board level and component level testing. The main issue with COTS remains to be able to qualify these components in a cost-effective way for a given application with a Radiation Hardness Assurance (RHA) process targeting the risk level authorized for the mission.

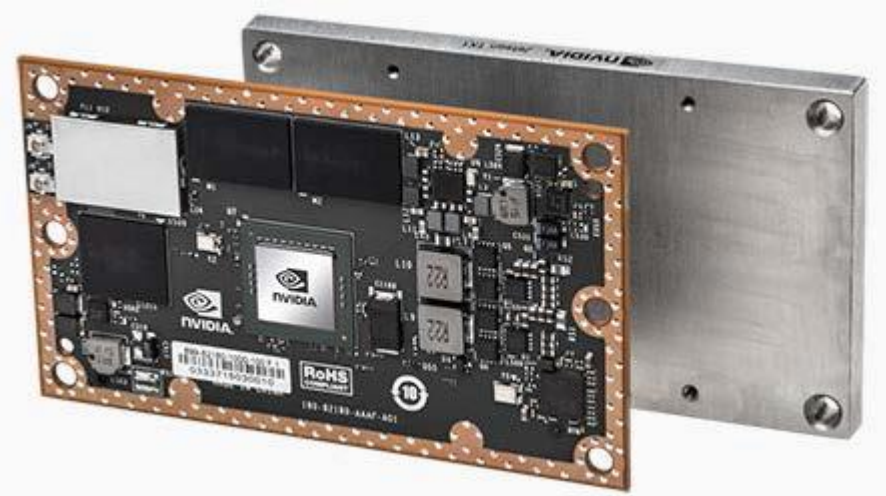


**Figure 38: Nvidia Jetson TX1 System on Module [96]**

The investigation whether testing at board instead of device level would represent a benefit started years ago [99] and is still being debated now [82, 97, 98, 100, 101]. The main objective is to reduce the cost compared to traditional device testing level. However, testing at board level has several drawbacks which appear to be difficult to overcome as soon as the program has a significant requirement in terms of risk tolerance. In particular, for cumulative phenomena, the following items (non-exhaustive list) shall be looked at with great caution:

- Board testing means limited information about device parametric degradation; therefore, the approach which consists in injecting the parametric drifts into the Worst Case Analysis is not possible.
- Since the measurements are performed at board level, only functionality can be monitored: it works or it doesn't. In case the function is not working after test, investigation shall be led to understand which device could be responsible of the failure and eventually restart a new series of test.
- Traceability of COTS in general is a challenge. How to insure all devices present on tested board(s) will have the same traceability than the ones embarked on the flight boards?
- Testing the board once with a single particle source (e.g. protons) for both TID and DD purpose (and eventually SEE on top of the rest) requires to have access to device technology, since particle accelerator fluxes aren't compatible to ELDRS test conditions.

- Some devices may drift during testing, without being noticed, therefore not resulting in test failure, however reliability of adjacent part may be affected and failure may occur later on in the course of the mission.
- In case lot testing is necessary (because Radiation Design Margin is not high enough, see the following sections), this needs to be re-performed at board level, with the traceability issue highlighted above
- How many boards to be tested? Does statistical analysis apply?

As a conclusion, the acceptability of board testing approach is once again a matter of project risk acceptance, and also a matter of potential impact from the radiation degradation mechanism under test (TID, TNID).

#### 4.7 TID/DD: Link with the Worst Case Analysis

A TID test report is unlikely to be the most useful document used by designers to complete their WCA. One needs a synthesis document gathering together the drifts of the critical parameters in a simple way, so that the designer can easily integrate radiation degradation in his WCA (see Figure 39), together with other sources of degradation like temperature and aging. Such a document should account for device dispersion in a batch ("intra-lot") and also for batch-to-batch variation, since the objective is to avoid re-doing the WCA each time a new device batch is ordered. Therefore, each time TID testing is performed on a given device type, the test data are added to previous ones in order to construct a so-called "TID template" included in the device "radiation sheet". An illustration of an Airbus DS TID template is given in Figure 40.

Component Type	Parameter	Initial Tolerance	Temp. effects	Ageing Effect	Radiation Effects 37Krad	Total BoL	Total EoL
AOP	Voffset (mV)	$\pm 0.5\text{mV}$	$\pm 0.5\text{mV}$	$\pm 0.2\text{mV}$	$\pm 4\text{mV}$	$\pm 1\text{mV}$	$\pm 5.2\text{mV}$
	Source	5962-98637	5962-98637	AD1	HRX/TID/0481		
	Ioffset (nA)	$\pm 0.2\text{nA}$	$\pm 2.5\text{pA}/^\circ\text{C}$ $\pm 0.15\text{nA}$	$\pm 9\%$ 0.032nA	$\pm 10\text{nA}$	$\pm 0.35\text{nA}$	$\pm 10.4\text{nA}$
	Source	5962-98637	5962-98637	AD1	HRX/TID/0481		
	Ibias (nA)	$\pm 2\text{nA}$	$\pm 1\text{nA}$	$+1.8\%$ 0.033nA	$\pm 10\text{nA}$	$\pm 3\text{nA}$	$\pm 13\text{nA}$
	Source	5962-98637	5962-98637	AD1	HRX/TID/0481		

Figure 39: example of parametric degradation (incl. radiation) accounted in a given electronic application

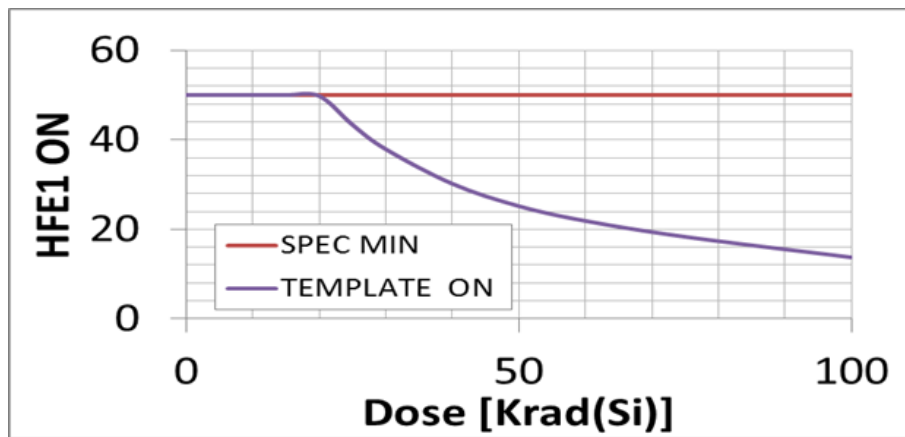


Figure 40: Airbus DS TID template from transistor radiation sheet

Since the template shall be robust to device batch variability, it shall be ruled in a way that the probability of being defeated is minimum; nevertheless, it shall not be too conservative in order to optimize the possibility of using the device in the biggest amount of applications/designs.

#### 4.8 TID – Margin Policy

A definition of Radiation Design Margin (RDM) may be found in [102]: RDM is often used in relation to electronic components, and is defined as:

$$RDM = D_f / D_D$$

Where  $D_f$  is the mean dose (for the sampled devices, it may also be called Total Ionizing Dose Sensitivity - TIDS) resulting in the violation of operating conditions or failure of a device resulting in a malfunction of the system, and  $D_D$  is the specified environmental dose (may also be called Total Ionizing Dose Level – TIDL).

As examples, particle spectra of the radiation environment specification will be used to compute Total Ionizing Dose Levels (TIDL). The higher TIDL is, the lower the RDM is and the more likely the need for testing (or device rejection) will be. One should also note that need for testing does not only represent a source of cost and an element to be inserted in the program planning. It is also possible that the test fails and therefore an alternative solution is required, potentially leading up to a design change, which then could jeopardize the good progression of the program.

The RDM aims at covering the various sources of variability at each step of the RHA process implementation (even though in most of the cases, worst cases have been chosen as the standard approach): radiation environment definition, radiation modelling, radiation testing, etc...

Besides the RDM value itself, it is of foremost importance to validate that both TIDS and TIDL have been obtained according to applicable RHA requirements. We have seen in the previous chapters of the present course that all steps of the RHA process intrinsically contain some variability, due to the uncertain nature of the inputs and/or the discrepancies between ground and flight conditions.

One key element within a space industry is to harmonize the RHA practices along the different programs of the company; this is why the major European space industry players have in many cases developed their own RHA standards at a time European ECSS-Q-ST-15C [103] and ECSS-E-ST-10-12C [104] standards did not yet exist. These industrial standards were pretty similar, even though adapted to each industrial organization. It may also happen that several prime contractors end up with the same set of standard (RHA and radiation environment), like Airbus DS and TAS in the frame of the NEOSAT program [105, 106].

On top of it, for competitiveness reason, most of the space industry players are promoting the use of product lines (valid at satellite and equipment levels). This is for example the case in the commercial telecommunication market, and also in the Earth observation commercial market, however this approach may be expanded further, with systems/sub systems or equipment being developed in one of these frame being reused in other kinds of programs.

For the reasons presented here above, space industry puts a lot of attention into all aspects which could generate a deviation from their product line standards, just because a deviation from these requirements, even minor, may trigger additional radiation testing, device/design changes or more generally a change which is not expected in a product line approach and may generate large over-cost.

At Airbus DS, the applied policy is based on the categorization approach and is roughly based on:

- The minimum Radiation Design Margin (RDM) for TID shall be 1.2.
- Radiation verification testing (RVT/RADLAT) on flight lot shall be performed if the component meets following condition:  $1.2 \times TIDL < \text{component type TIDS} < 2 \times TIDL$

It is worth noting that some exceptions may apply for this latter category (e.g. Detectors).

Previous chapters pointed out the variability of each individual assessments in the RHA process; nevertheless, it has also been shown that most of the best practices intrinsically contain some conservatism, and that on top of it some hidden margins also exists (e.g. within the Worst Case Analysis, which combines several sources of degradation) even though their value is for sure highly variable, and in any case unknown.

As a consequence, it is key to consider the RDM policy globally, and not try to multiply RDM corresponding to each stage of the process, which will lead to over-conservative figures.

## 4.9 DD – Margin Policy

Most of what has been presented for TID also applies for DD. Requiring the RDM to exceed a minimum value ensures that allowance is made for the uncertainties in the prediction of the radiation environment and DD damage effects, such as:

- Uncertainties in the models and data used to predict the environment;
- The potential for stochastic enhancements over the average environment (such as enhancements of the outer electron radiation belt);

- Systematic and statistical errors in models used to assess the influence of shielding, and determine radiation parameters (e.g. TID, TNID, particle fluence) at components' locations;
- Uncertainties in the radiation tolerance of components, established by irradiation tests, due to systematic testing errors;
- Uncertainties as a result of relating test data to the actual parts procured, and variability of measured radiation tolerance within the population of parts.

The key message concerning devices which are sensitive to DD is that they are likely sensitive to TID as well and therefore drifts due to both DD and TID shall be accounted in the Worst Case Analysis.

At Airbus DS, the applied policy is based on the categorization approach and is roughly based on:

- The minimum Radiation Design Margin (RDM) for TNID/DD shall be 1.2.
- Radiation verification testing (RVT/RADLAT) on flight lot shall be performed if the component meets following condition:  $1,2 \times \text{TNIDL} < \text{component type TNIDS} < 2 \times \text{TNIDL}$

It is important to note that some exceptions may apply for this latter category (e.g. Detectors).

## 5. Radiation Effects on Electronics – Single Event Effects (SEE)

### 5.1 SEE from Heavy Ions and Protons - Basics

Heavy ions transfer their energy to the material by ionization and when stopping, by structural defects creation. The electron hole pairs are created in a very dense plasma so that a very large fraction will recombine (95-99%). When an ion path crosses a depleted junction, the remaining pairs will be separated by the junction electric field and a current spike can be observed. The induced current has two components: a prompt component and a delayed one. The prompt component of collected charges consists of drift ( $Q_d$ ) and funnelling ( $Q_f$ ) and lasts in the order of hundreds of picoseconds. The delayed component may last hundreds of nanoseconds and consists of charges collected by diffusion ( $Q_{df}$ ). Figure 41 [107] gives a schematic view of these two contributions.

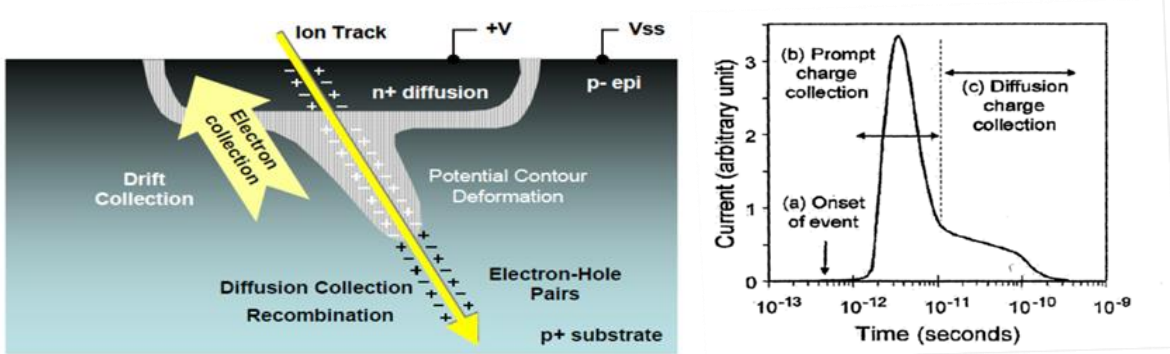


Figure 41: Ion track and current pulse induced by passage of a heavy ion through a depletion region of IC [107]

High energy protons can also generate Single Event Phenomena (SEP). They act in general in a more complex way than heavy ions. Two different effects can occur:

- In the first one, protons interact with device atoms to create secondary ions with much higher LET than incident protons (up to 8-15 MeV cm<sup>2</sup>/mg, considering only interactions with silicon). Devices atoms involved in the reaction are mainly the bulk atoms, but can also be metallization line atoms, which can be much heavier. For a device which exhibits a SEE sensitivity induced by protons, its indirect contribution to SEP cannot be ignored in most of the cases since proton fluxes are in general far above heavy ion ones.
- In the second case, protons directly induce SEP in a similar way as heavy ion. Due to the low LET of protons (below 1MeV cm<sup>2</sup>/mg), the direct contribution to SEP is low or negligible for most of the older technologies. However in bulk Si and SOI circuits from the 20-90 nm technology nodes range, SEE induced by low energy protons have been recorded [108, 109].

SEE can occur randomly in time and space, depending on ion flux contrarily to total dose damage, which is a progressive degradation. It is a probabilistic phenomenon.

Some SEEs are non-destructive, as in the case of Single Event Upset (SEU), Single Event Transient (SET), Multiple Cell Upset (MCU), and Single Event Functional Interrupt (SEFI) (non-exhaustive list). Single event effects can also be destructive as in the case of single event SEL, SEGR, and SEB (non-exhaustive list). The severity of the effect can range from noisy data to loss of the mission, depending on the type of effect and the criticality of the system in which it occurs.

For further see the last part of this short course or the bibliography in [111 and 112]

## 5.2 SEE Testing

### 5.2.1 SEE testing - general

SEE testing has been described in various short courses [see for example 113 to 117]. The trend in semiconductor manufacturing continues to be the decrease in feature size. Knowing that the rate of charge generated by an ionized particle will remain invariant, it is obvious that if the critical charge required to produce an event is reduced, the sensitivity to this event will increase.

In addition to device technology evolution, it is still useful to recall that SEE testing (as for others radiation effects) is only an approximation of the real flight environment (see Figure 18) and therefore test outputs may differ from what will be observed in flight. This has to be considered in both the specification and SEE analysis: the functional specification of a space system, sub-system or equipment specifies the reliability threshold (if any), accounting for uncertainty in the ground prediction delivered by the SEE analysis.

Industry's objectives when performing SEE testing are first to identify the sensitivity to any kind of SEE and also whenever the device turns out to be SEE sensitive, to produce the cross section curve (see Figure 2) in order to perform SEE rate calculation.

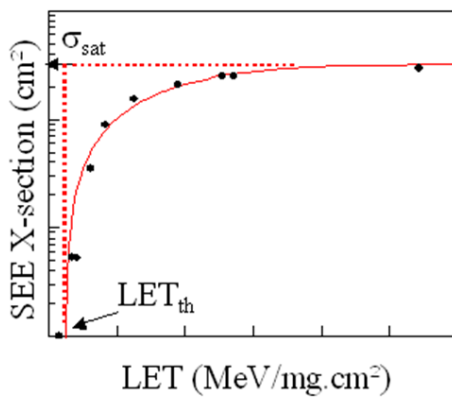


Figure 42: Typical cross section curve for SEE

In some cases, the main goal is to determine the suitability of the device for one or several applications and the SEE rate calculation may be difficult to be implemented: this is for example the case of SEB/SEGR sensitivity for power MOSFETs. In this area, testing may be performed according to the definition of the Safe Operating Area (SOA) where ion LET is set to a value which may allow one to consider that if no events are seen, the probability of experiencing a failure in flight is negligible. This

is a method used by most of the MOSFET manufacturers, which usually provides such a SOA with various LET values so the user may choose the most appropriate one (example given in Figure 43).

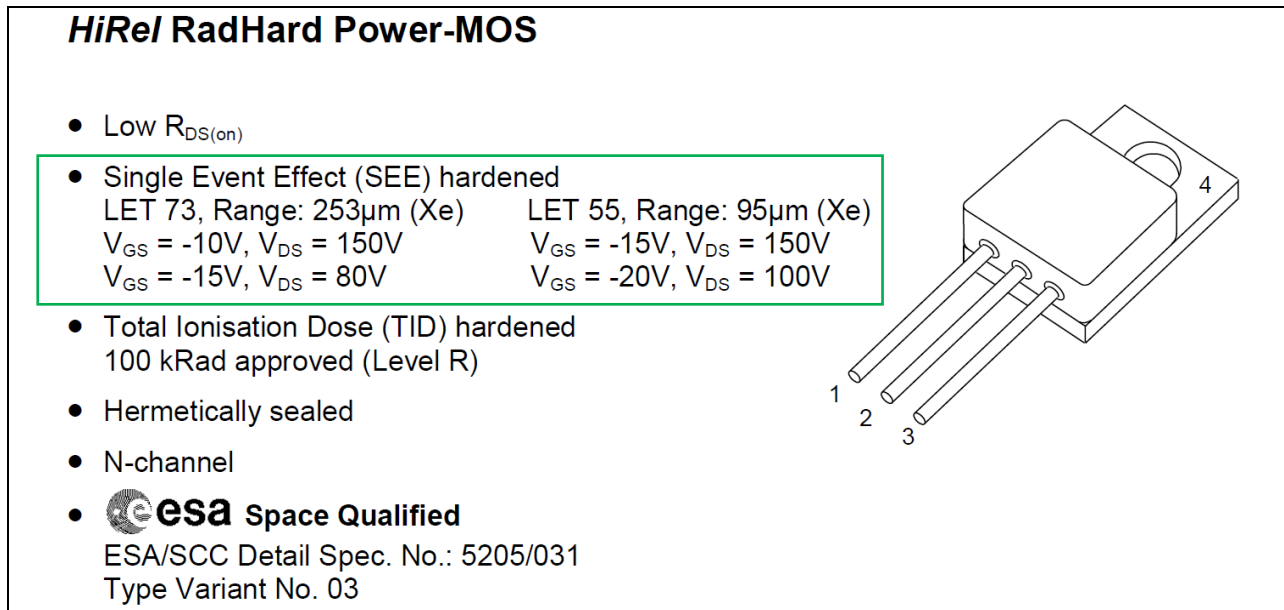


Figure 43: SOA for a MOSFET [118]

### 5.2.2 SEE testing – traceability

RHA assesses the conditions where SEE test data may be reused. Of course, in the space business, industry must optimize cost while keeping the reliability at the level required by the customer. As a consequence, the reuse of SEE test data will be encouraged as much as possible. This means that any time SEE testing is performed one must keep precise records of both testing conditions and device traceability. General definition of traceability is the ability to verify the history, location, or application of an item by means of documented recorded identification. This is fully applicable to an electronic device and Figure 29 presents a typical record of device “pedigree” that would benefit consideration of any further use of the same device. Requirement in terms of traceability is the same for all radiation effects. This can be of foremost importance, in particular in view of destructive SEE.

### 5.2.3 SEE testing – influence of the application condition

Within the course of the SEE test preparation, the relevant application conditions shall be exhaustively collected. At Airbus DS, the collection of all use cases is performed at transnational level to take into account all the supplier sites. This is a pragmatic approach to avoid redundant testing among the sites and to optimize the test plan by defining worst-case test conditions (whenever

possible) and to be time and cost-effective. One must bear in mind that more than 6 months can pass from the test definition to its achievement at the SEE facility (due to long booking delays in some cases associated to more restrictive access to HI and proton facilities). In addition, the cost associated with the radiation tests can be relatively important with respect to the mission costs and hence needs to be justified and documented. Test preparation documents are a good way to capitalize all the documentation related to the test preparation between the radiation and design engineering teams. They need to be validated by both parties.

The test conditions are derived from the application conditions and the datasheets and /or application notes on the device (when necessary). During this operation it is ascertained whether the test conditions defined are representative or worst-case compared to the final flight conditions in an exhaustive way.

SET in analog parts has been evidenced in various works [119 to 125]. In this section, we will take the SET on analog Integrated circuits as an example of the impact of application conditions (even though this phenomenon is also of concern for digital devices, as illustrated for example in [126, 127]). It remains a concern for space industry, in particular because the nature of SET in terms of shape, amplitude and duration is application dependent, as illustrated in Figure 44, extracted from [119]. In this work, four different applications have been investigated for the LM124: voltage comparator, non-inverting gain (x101), non-inverting gain (x11), and voltage follower. Three of them are presented.

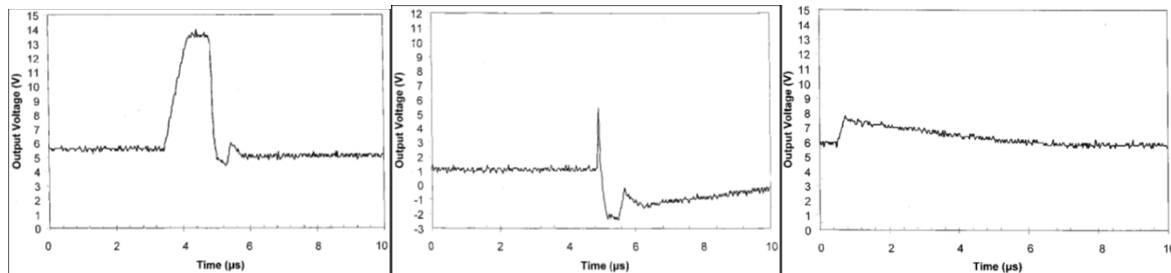


**Figure 44: SET in LM124 tested in various application conditions [119]**

Since many analog circuits are used in particular for the protection function of electronic equipment, an un-adapted consideration of the SET not linked to the application (consideration of erroneous transient shape/duration in designing the electronics filtering for example) can lead to significant impact at space system level.

To overcome the fact that a single device type may be used in more than 10 different application conditions and therefore performing SET testing with heavy ion beams in all configurations may become really expensive, the way to handle it is to use as far as possible worst case SET templates, as specified in RHA specifications (see Table 1 here below).

Device type	SET nature at device output (*)
OP-amps	$\Delta V_{\max} = +/- V_{CC}$ & $\Delta t_{\max} = 15 \mu s$
Comparators	$\Delta V_{\max} = +/- V_{CC}$ & $\Delta t_{\max} = 10 \mu s$
Voltage Regul.	$\Delta V_{\max} = +/- V_{IN}$ & $\Delta t_{\max} = 10 \mu s$
Voltage Ref.	$\Delta V_{\max} = +/- V_{CC}$ & $\Delta t_{\max} = 10 \mu s$

Table 1: SET template for some families of analog integrated circuits

However, in some cases, handling SET at design level is not possible and then more precise data are needed. Using data coming from testing performed in “similar” or “worst case” conditions will be very challenging: the key parameter is to determine the nature of the event which triggers a problem at design level. If the considered SET is too extreme, then the prediction will be totally unrealistic. This is a complex issue since sometimes the circuit design is quite complicated and so knowing the exact estimation of the SET shape and duration which will cause an issue is very difficult. In this case, besides use of simulation tools (like SPICE, ensuring that the tool is properly used), the best approach is to perform the test in strictly the same application as in flight.

One efficient way to avoid multiple heavy ion testing is to make use of laser testing [128 to 131]. One needs a test reference obtained with heavy ions in order to calibrate the laser experiment with the heavy ion one. Once this is done, the other applications are tested and cross section characteristics obtained by comparison with the reference. Laser testing can be extremely useful, when properly used.

Application conditions are of course not only of importance for analog circuits, but also for the most complex Systems on Chips (SoC), where an exhaustive SEE characterization turns out to be nearly impossible, as illustrated in [131 to 135]. As an example, functional tests in dynamic mode must be implemented to detect any anomaly occurring prior to SEL or during no-detectable low current Single Event Latchup (SEL) [136]. This testing condition is sometimes difficult to apply as the device operating current may vary significantly. The precise determination of critical limits of current and shutdown time is important to further ensure the mitigation circuitry efficiency [113]. This is why it is mandatory to record in real-time during the irradiation runs the current consumption in order to discriminate and avoid any artefact due to the device normal current fluctuation.

#### 5.2.4 SEE testing – critical parameters

A SEE test must be organized into three main sections: before, during and after the test, as illustrated in Figure 45. At each step of this process, applied process has a chance to influence the final SEE test results; we are going to spot some areas of influence to be considered in order to validate that the obtained set of data match the requirements.

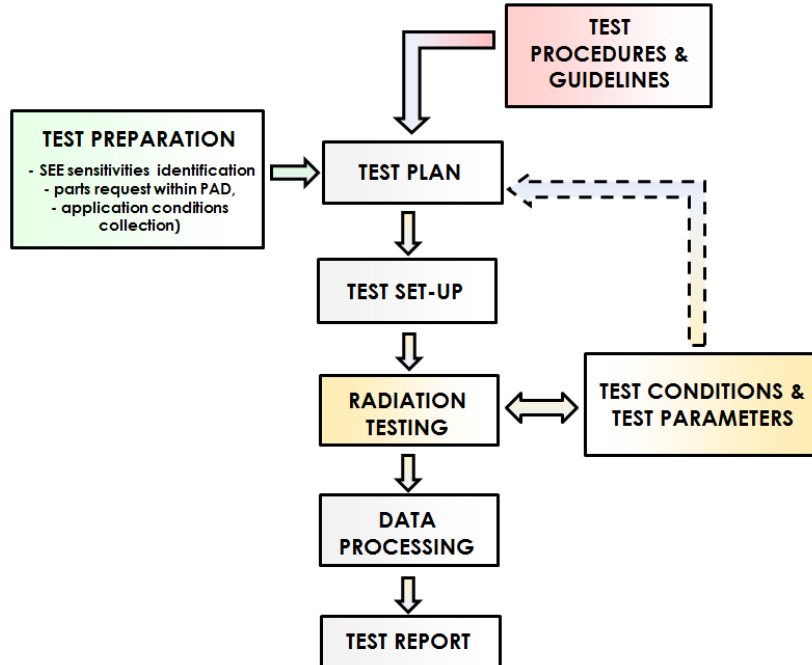
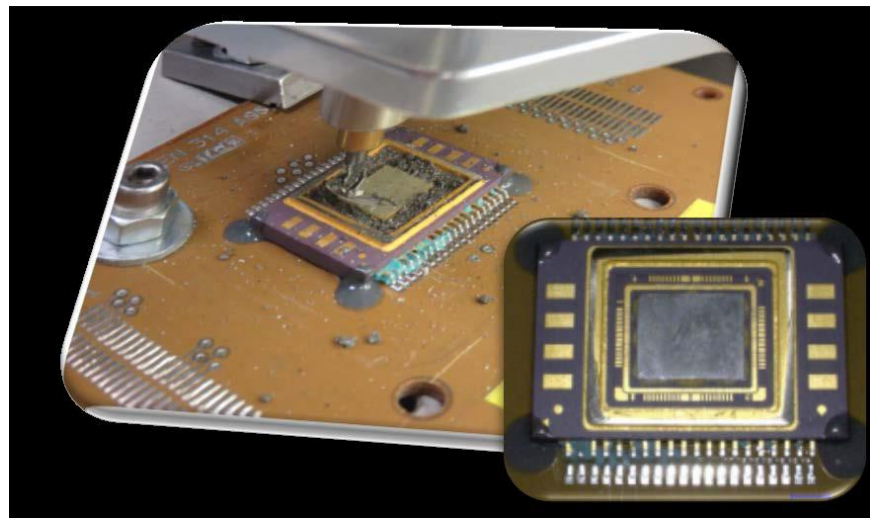


Figure 45: Typical SEE test flow chart [112]

- Most of the heavy ion irradiations are generally performed in vacuum since air limits the range and energy of the available ion beams. Experiments are performed then in a vacuum chamber with long cable feedthroughs for transmission of signals. Vacuum conditions may result in overheating leading to unwanted temperature increase at die level [137]. In addition, the long cables may lead to increased circuit noise with possible signal capture problems.
- The accelerator facility is an electrically noisy environment. To avoid interferences on measurements the test bench must be optimized by grounding and shielding techniques.
- Sample preparation is required, and turns out to be vital before testing for SEE. Due to the limited particle range at the accelerator facilities, delidding the samples is generally required to expose the bare die to the heavy ions beam. For complex device technologies and COTS technologies that often use lead-on-chip, flip-chip constructions and plastic packages, the preparation of samples may be complex and challenging and one can face severe opening issues [138]. Special skills and techniques may be required to cope with the broad packages and dice variety and specifics. At Airbus Defence & Space such specific tasks are handled by a dedicated technology lab with well-skilled engineers and specialists (see Figure 46).



**Figure 46: Snapshot of the coating removal of the over layer for a complex device during the sample preparation for SEE testing (Airbus Defence & Space technology laboratory, Elancourt, France) [112]**

- For proton-induced SEE testing, delidding is not necessary since high energies are generally used. However, the control circuitry and the surrounding test apparatus may be unwantedly exposed unless well protected by efficient shielding.
- The bond wires may sometimes shadow the die resulting in non-negligible variations of particle ranges [139]. Disassembling and re-bonding may be necessary in some cases since the bonds are very fragile and may even be broken-down during the delidding process (chemical etching with hot acid or during mechanical opening).
- For complex devices, micro latch-up may sometimes be observed. It consists of many latch-up paths that can occur leading to a wide range of SEL currents. This necessitates the use of accurate current limiting circuits with the threshold currents set very close to the steady state consumption of the device.
- With the fast evolution of new technologies associated to the increasing technology integration levels, devices are getting more and more complex and consequently more and more SEE-sensitive with new failure modes. Testing for SEE such very complex devices (last generations of FPGAs or processors for example) is accordingly more and more challenging.
- Heavy ion accelerators used for SEE testing are different and do not use ions of the same nature and energies, therefore, not all of them are suitable for testing all SEE phenomena, especially when the single event effect results from long range charge collection mechanisms (SEB for example, [140, 141, 142]). As an illustration, Figure 6 presents the characteristics of the various ions available at JYFL (Finland [143]). This shows that different heavy ion energies lead to very different charge deposition characteristics.

### LET curves for RADEF's ion cocktail elements

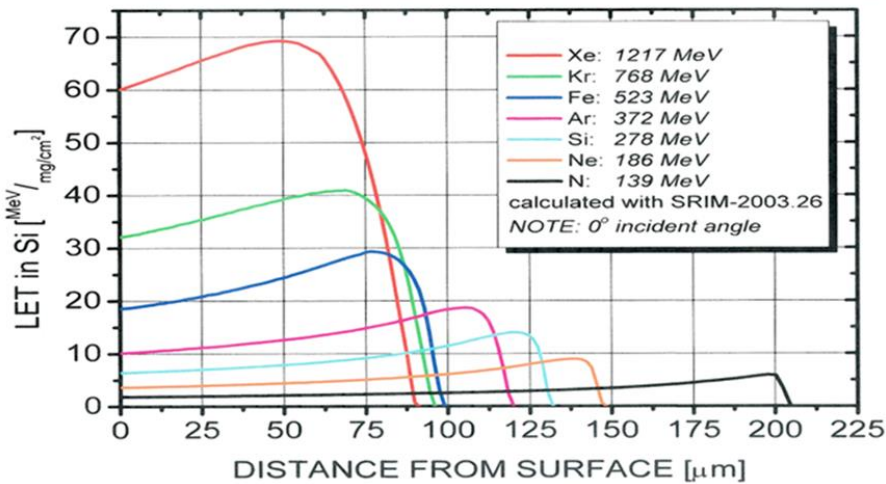


**Figure 47: Ion characteristics for RADEF accelerator**

#### 5.2.5 SEE testing – normative documents

Performing SEE tests in adequate test conditions (bias levels, operating modes, test pattern, frequency, duty cycle,...) and with a well-defined procedure (facility selection, particles, energy, fluence, fluxes,...) is of prime importance in order to minimize the risk associated to the different uncertainties related to ground testing and to minimize and bound systematic and random errors (e.g. effect of the omni-directional particles in space, range of the ions used in testing, dosimetry...).

SEE test standards and guidelines for testing have been developed in the US namely the JEDEC Test Standards, the JESD57 [144] and the JESD234 [145], the MIL-STD-750-1 method 1080 [146] or the US ATM F1192-90 [147]) and in Europe (the ESA/SCC 25100 [182]). Didactic by nature, these norms aim at ensuring that SEE tests are performed following best practices and that results from different vendors/testers are comparable [148, 149].

The JEDEC JESD57 standard is only valid for heavy ions (HI) with  $Z>2$ . It must be complemented by the JEDEC JESD234 which deals with proton-induced SEE test. The ESA/SCC 25100 is applicable for both HI and protons testing. Both methods are similar in the principle but present discrepancies. The main points are:

- The ESA/SCC requires HI with sufficient energy to deliver a particle range in silicon (Si) greater than 40  $\mu\text{m}$  for SEU, SET, SEFI testing of CMOS logic devices, while for SEL testing a minimum range of 60  $\mu\text{m}$  is required. No specific value is specified in the JESD57 procedure which requires a range greater than the depth of the charge collection region of the device. Range requirements are important because some modern microcircuits have multiple layers of metallization and in addition charge collection lengths (epitaxial thickness layer) may range up to 150  $\mu\text{m}$  for a 1000V-rated power MOSFET [150, 151].

- For HI testing, the maximum LET (Linear Energy Transfer) recommended in the JEDEC JESD57 for determining “robust” parts, is  $120 \text{ MeV.cm}^2/\text{mg}$ . If no event is observed at the LET, the device can be declared as “non-sensitive”.
- A minimum fluence is required in the JESD57 ( $5 \times 10^5 \text{ ions/cm}^2$  for discrete parts and  $10^7 \text{ ions/cm}^2$  for integrated circuits) whereas for the ESA/SCC 25100 a fluence in the range  $10^5$  to  $10^7 \text{ ions/cm}^2$  or at least 100 events is recommended; a fluence of  $10^{10} \text{ protons/cm}^2$  for protons testing at the energy threshold for the event of concern is required. Also one shall consider that if the test is pursued up to high fluence values, TID influence will not be negligible.
- A minimum sampling size of 3 parts (same datecode, DC) is required for destructive SEE tests by the ESA/SCC 25100 and also the MIL-STD-750-1. Whereas no minimum sampling size was specified in the JEDEC but a minimum of 4 parts is recommended in the last draft version of the JESD57.

To illustrate this, Figure 48, extracted from [112] compares the main features of the MIL-STD-750, method 1080, the ESA/SCC 25100 and the JEDEC JESD57 test methods for the case of SEB and SEGR testing of POWER MOSFETs.

		
<b>MIL-STD-750, Method 1080</b> Single Event Burnout and Single Event Gate Rupture. - 2014 <hr/> <b>Range:</b> > Epitaxial layer thickness <b>Flux:</b> $10^5 \leq \text{Flux} \leq 10^8 \text{ ions/cm}^2/\text{s}$ however die dependant <b>Fluence:</b> $10^5$ to $10^7 \text{ ions/cm}^2$ <b>LET:</b> Not specified; effective LET invalid <b>Sampling:</b> 3 samples minimum for destructive tests <b>Ion species:</b> Influencing the SEGR response but no specific ion specie recommended <b>Angle of incidence:</b> Need to be characterized (some stripFET technologies exhibit a sensitivity) <b>Device operating conditions:</b> OFF-state bias for SEB/SEGR. SEGR may be tested ON-state if $V_{DS}$ bias @ 0V. Increment $V_{GS}$ steps < 10% of rated $V_{GS}$ Increment $V_{GS}$ steps < 25% of rated $V_{GS}$ <b>Measurement during irradiation:</b> $I_{DS}$ and $I_{GSR}$ for SEB and SEGR <b>Temperature:</b> Higher temperature considered as worst case for SEB and SEGR. To be considered on a case-by-case basis (note 19)	<b>ESA/SCC 25100 issue 2</b> Single Event effects test methods and guidelines. - 2014 <hr/> <b>Range:</b> > Epitaxial layer thickness <b>Flux:</b> $10^4 \leq \text{Flux} \leq 10^8 \text{ ions/cm}^2/\text{s}$ <b>Fluence:</b> $10^5$ to $10^7 \text{ ions/cm}^2$ as per MIL-STD-750, Method 1080 <b>LET:</b> Not specified; LET up to $60 \text{ MeV}/(\text{cm}^2/\text{mg})$ ; effective LET invalid <b>Sampling (per test condition):</b> 3 samples minimum <b>Ion species:</b> Not specified; <b>Angle of incidence:</b> No need for planar technologies (normal incidence is worst case). Other technologies (trench, lateral-diffusion MOS, ... to be characterized under tilt/roll angles) <b>Device operating conditions:</b> SEB: destructive or non-destructive mode SEGR: destructive mode only; PIGST to perform with $V_{DS}$ bias @ 0V while $V_{GS}$ is swept up to the maximum rated voltage ( $\pm 10\%$ ) during 1s minimum. <b>Measurement during irradiation:</b> $I_{DS}$ and $I_{GSR}$ for SEB and SEGR <b>Temperature:</b> Low operating temperature. Room temperature usually considered as acceptable	<b>JESD57 (last draft revision)</b> Test procedures for the measurement of Single-Event Effects In semiconductor devices from heavy ion irradiation. - 2017 <hr/> <b>Range:</b> > depth of charge collection region: maximum energy deposited in the epi-layer(s) <b>Flux:</b> $10^4 \leq \text{Flux} \leq 10^8 \text{ ions/cm}^2/\text{s}$ <b>Fluence:</b> $3 \times 10^5 \text{ ions/cm}^2$ for discrete $10^6 \text{ ions/cm}^2$ for integrated devices <b>LET:</b> Not to be used as the single metric <b>Sampling (per test condition):</b> 4 samples minimum <b>Ion species:</b> Not specified; <b>Angle of incidence:</b> In VDMOS normal incidence is worst case for SEB and SEGR for planar technologies (but cut-off angle may differ with the device topology) <b>Device operating conditions:</b> OFF-state bias Increment $V_{DS}$ steps < 10% of rated $V_{DS}$ starting @ $V_{DS} = 0\text{V}$ Increment $V_{GS}$ steps < 25% of rated $V_{GS}$ <b>Measurement during irradiation:</b> $I_{DS}$ and $I_{GSR}$ for SEB and SEGR <b>Temperature:</b> For SEGR, the temperature is not a primary factor. For SEB, minor effective cases. Not a real concern

Figure 48: Comparative chart of 3 test standards for SEB/SEGR testing of power MOSFETs [112]

The presented SEE test standards propose guidelines to give a frame to devices testing for SEE. However, no complete consensus exists between these test specifications and it is therefore

extremely difficult to comply with all of them, unless systematically using the worst requirement of each standard.

### 5.3 SEE Rate Calculation Method

SEE test data post-processing and formatting must enable constructive use of the information to determine:

- The signature of the SEE (e.g. the SET envelope as the amplitude versus duration curve of the perturbation for a given electrical configuration);
- The SEE cross-section ( $X$ -section  $\sigma$ ) curve as a function of the LET for HI and energy for protons of the tested configuration
  - o SEE cross section curves are usually fitted using a Weibull function; the choice of the fitting function influences the final in-orbit event rate as highlighted later on in this chapter.
- The parameters for event rates calculation purposes, to be considered in the design analysis together with the design inputs (for example for the implementation of protection schemes such as EDAC for SEU, or majority voter, use as is, power cycling or, reset in case of SEFI,...);
- In the case of Power MOSFETs testing (and potentially HV-Diodes [152, 153, 154]), the SOA i.e. the domain with respect to the drain to source voltage  $V_{DS}$  as a function of OFF-state gate to source voltage  $V_{GS}$  into which the MOSFET will be able to operate safely without experiencing SEB or SEGR. In this latter case, no further calculation is needed since the nature of the test insures that the probability of experiencing an event when being within the SOA (incl. derating factor) is negligible.

Prediction of SEE rates involves a combination of experimental data, assumptions about the device, fitting functions, and knowledge of the energetic particle environment. SEE rate prediction models typically use ground test data to extract information about the device sensitivity, measured in terms of cross section ( $\sigma$ ) and critical charge ( $Q_c$ ), as a function of LET and/or proton energy. Once the cross section versus LET or proton energy data have been experimentally acquired, there are established techniques for using the data to predict SEE rates in a given space environment. Of course, the quality of the predictions is a function of the quality and representativeness of the test data, of the reliability of the environment description, and the skill of the modeler, taking into account the assumptions and limitations of the models. More details may be found in the last part of this short course or in [155, 156].

To a first order, the Linear Energy Transfer (LET) i.e. the energy deposition per unit of length drives the effects. This allows simplification of the prediction problem through the use of LET spectra, as first developed by Heinrich [157]. All the ion types and distributions of energy in the space environment can be reduced to their LET, and deposited energy can be estimated as LET times the chord-length through the sensitive volume. With this simplification, the problem to be solved is to identify the size of the sensitive volume, calculate the rate of ion hits and the consequent energy depositions, and determine the subset of total ion hits that cause SEE. The problem is complicated by

the angular dependence since the amount of energy deposited in the sensitive volume depends on chord-length, which in turn depends on angle of incidence.

Several rate prediction methodologies and codes are discussed in the literature, but they all fall into one of these general categories: Chord-length model [158], Effective Flux Model [159], Figure of Merit Approximation [160, 161].

While the test methods and rate prediction approaches described above have been proven to sufficiently estimate the observed on-orbit SEE rate (see, for example, [162]) for pre-2000 technologies, these methods do have limitations.

- The concept of effective LET [158] is based on the fact that the sensitive volumes are thin Rectangular Parallelepipeds (RPPs). However, not all devices have thin sensitive volumes (some are not RPPs at all). When the heavy ion beam is rotated at some off normal angle, the ions have a path length distribution that is much more complicated than simple cosine law, i.e., effective LET concept may not valid in thick sensitive volumes and in complex modern devices.
- The current rate prediction models assume that the line of charge created as the ion passes through the material is very thin compared to the collection volume dimensions which is not the case anymore as technology scales to much smaller sizes. The technological integration led to modified collection mechanisms occurring at circuit level (multiple collection nodes).

In order to improve the RPP model, several concepts were proposed, whose objective is to take into account a more realistic charge transport nature [163, 164, 165, 166, 167].

However, most of the proposed approaches need detailed information about the device technology under study, which nature is not available to users, or are not accessible in engineering tools like OMERE [168] or CRÈME [169].

This is why the RPP/IRPP approaches remain widely used in the space business, even though its use may be questionable in particular for the most recent devices.

Besides the nature of the sensitive volume definition, there are other areas which may heavily influence the values of the predicted SEE rates. We may cite, as illustrated in [168]:

- Influence of LET threshold, and more generally the quality of the test data set (in particular the amount of LET values during the test sequence)
- the impact of Weibull parameters fitting; The "elbow" region of the cross section curve must be well described as it directly impacts the LET values involved in the SER.

In order to limit the potential variability of the Weibull fit determination, several methods have been proposed; Figure 49: Weibull function examples presents the fits obtained with the maximum likelihood method [170] and with the least squares approach.

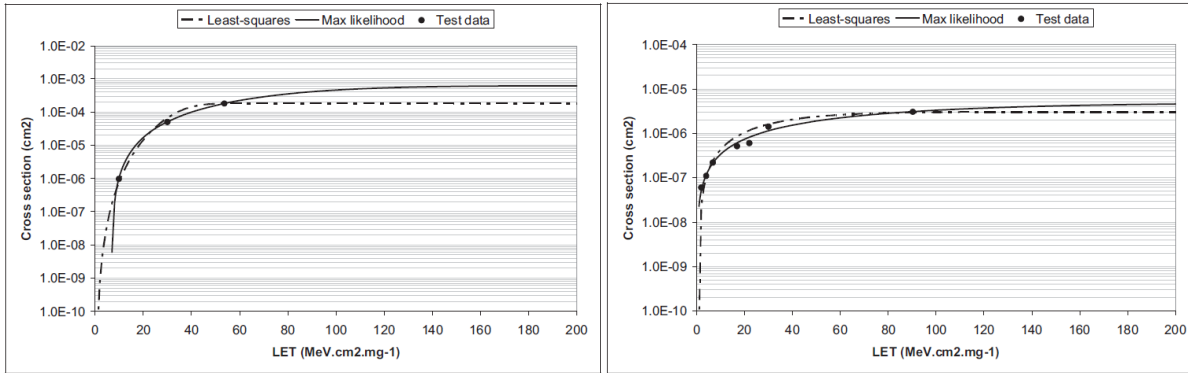


**Figure 49: Weibull function examples**

For the SEE induced by protons, we have to distinguish whether the SEE is created through the secondary mechanism (with proton induced nuclear reactions) or through direct ionization.

For the first mechanism, in addition to fitting with a Weibull function, there is also the possibility to fit the data with the Bendel model [171, 172], which will also influence the end calculation results.

For proton induced SEE there is another need, expressed in particular by the space industry, related to the possibility of using a model which predicts proton-induced SEE cross-sections from heavy ion experiment. The objective is to limit the SEE testing to heavy ion, even though heavy ion results would spot a potential sensitivity to proton induced SEE (i.e. threshold LET below 15 MeV.cm<sup>2</sup>.mg<sup>-1</sup>). There have been several models developed in order to achieve this goal, we can cite in particular SIMPA [173], PROFIT [174] and METIS [175], all integrated in the OMERE tool. These models, primarily developed for the SEU in low density memories, have limitations and shall be used in accordance with the applicable RHA specification [103]. This is also illustrated in Figure 50.

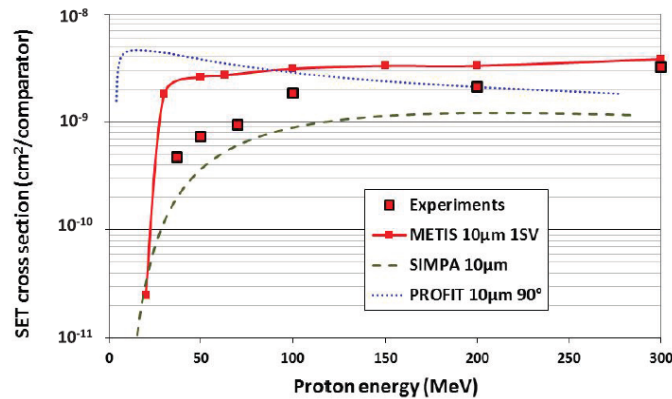


**Figure 50: LM139 - Proton experiments compared with METIS, SIMPA and PROFIT [175]**

Finally, a new topic was raised with the most recent technologies and their potential sensitivity to SEE induced by proton direct ionization. In this area, the prediction models are still under investigation (as the test procedure to implement) and determination of SEE rates linked to this mechanism are to be validated [176 to 180].

In-depth discussion of these topics can be found in the last part of this short course.

## 5.4 SEE – Radiation Hardness Assurance

The RHA process provides the top-level requirements to comply with. Airbus methodology for SEE management starts at device level by its categorization in compliance with ESCC-Q-ST-60-15C [103]. Parts are ranked in 3 main groups depending on their SEE sensitivities based upon the LET threshold ( $LET_{th}$ ) criteria. Those criteria define if an analysis has to be made, and if it is the case, what kind of analysis (considering just heavy ions constraints or both heavy ions and protons constraints).

The validity of the LET values (extracted from SEE tests) are part of the RHA requirements. Table 2 shows the SEE analysis requirements criteria used at Airbus Defence & Space.

SEE LET threshold in MeV.cm <sup>2</sup> /mg	Analysis Requirement	Environment to be assessed	Part category
$LET_{th} \geq 60^*$	<b>SEE risk negligible, no further analysis needed</b>	-	<b>A</b>
$15 < LET_{th} < 60$	<b>SEE risk, heavy ion induced SEE rates to be analyzed</b>	HI (GCR, solar flare ions)	<b>B</b>
$LET_{th} \leq 15$	<b>SEE risk high, heavy ion and proton induced SEE rates to be analyzed</b>	HI (GCR, solar flare ions) + Protons (trapped, solar flare protons)	<b>C</b>

(\* ) For Power MOSFETs, the  $LET_{th}$  is set @ 38 MeV.cm<sup>2</sup>/mg

**Table 2: SEE analysis requirements criteria based upon the  $LET_{th}$  of the single event effect**

According to Table 2:

- **Group A** devices are considered as not sensitive to SEE and can be used without any particular precaution (non-critical parts). No further analysis is necessary.
  - o Special case for MOSFETs being in their SOA at a LET of 38 MeV.cm<sup>2</sup>/mg
- **Group B** devices are sensitive to heavy ion-induced SEE.
- **Group C** devices are sensitive to heavy ion- and proton-induced SEE.

For devices that fall into Group B or Group C, the RHA methodology may rely

- on the SEE rate prediction and in that case, the event rates (under quiet and during flare period) are calculated and then compared to the acceptable error rates for the equipment,
- or, on application of derating rules (Power MOSFETs and possibly some diodes). The part acceptance criteria is then based upon the use within their SOA for SEB/SEGR and application of a 0.8 derating factor for the application condition (Drain-to-source voltage  $V_{DS}$  for MOSFETs and reverse voltage  $V_R$  for diodes).

Once the categorization is done, one shall separate destructive SEE from non-destructive SEE.

For non-destructive SEE the SEE tolerance will be the acceptable rate for which the equipment or subsystem or system is still meeting the reliability and availability requirements.

For destructive SEE the acceptable probability is very often set by reference to the device intrinsic reliability figure. In some cases it may be set according to equipment reliability and availability specifications. Finally, SEE acceptance is also a very variable notion!

The reader must bear in mind that the objective of the Airbus RHA is to achieve space systems which fulfil their mission without SEE impact. Without impact do not mean “without risk” but rather “with acceptable risks”. Therefore a proper SEE impact management from the part selection to the detailed design of the equipment, subsystem or system shall be implemented.

The Figure 51 shows an overview of the SEE management flow chart.

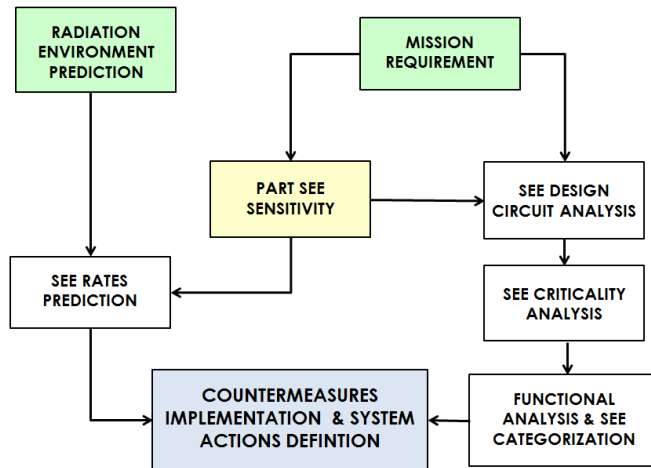


**Figure 51: Overview of the SEE management process flow chart [112, 181]**

## 5.5 SEE – LINK WITH DESIGN ENGINEERING

### 5.5.1 SEE Inputs

A SEE test report shall be written to present the SEE test results in a concise and exhaustive form to be suitable for use by design engineers. According to [182], the SEE test report shall contain:

- Component designation, e.g. integrated circuit, quad 2-input exclusive or gate, and commercial part number if necessary.
- Manufacturer/User Single Event Test specification number, revision and issue.
- Component Family, Component Group, Device package.
- Applicable ESCC Generic and Detail Specifications (numbers, issues, revisions).
- Test facility, name and address.
- Single Event Test Plan number, revision and issue.

- Manufacturer's name and address.
- Type of radiation: Heavy Ions or Protons.
- Manufacturing date code and mask set, Pictures of package, die and die marking.
- Device construction (technology): CMOS bulk, CMOS EPI, CMOS SOS, CMOS SOI, or other (specify). Enter also feature size/line-width in  $\mu\text{m}$ , Die size in mm.
- Type of test: (SEU, SEFI, SET, SEL, SEB, SEGR, Other).
- Test Conditions.
- Type of radiation source and dosimetry technique, ion species and charge state, energy in MeV or MeV/n, linear energy transfer, temperature of the device under test, tilt angle of device under test with respect to the beam axis, and effective linear energy transfer.
- Plots of SEE cross-section (per bit or per device) versus LET or energy, including error bars and confidence level.
- Additional remarks: the estimated total ionizing dose received during testing, reference to any special occurrences during the test, such as soft or hard latches, software crashes or effect of total ionizing dose (increased leakage etc.), should be made. Die markings may also appear in this section.
- ...

This is quite a lot of information, however, nothing which is directly usable by an electronic designer.

At Airbus DS, the link between radiation and design engineering is made through a “SEE sheet”. The SEE sheet will for example include the envelope of SET shapes recorded during testing (illustrated in Figure 52), the SEU rates of the tested device for some typical orbits, the SOA for the tested MOSFET (Figure 53), etc...

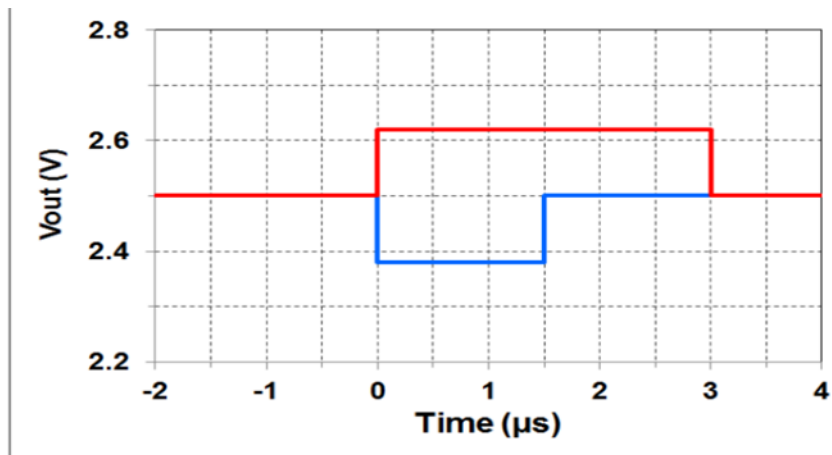


Figure 52: SET template for a given device in a given application condition

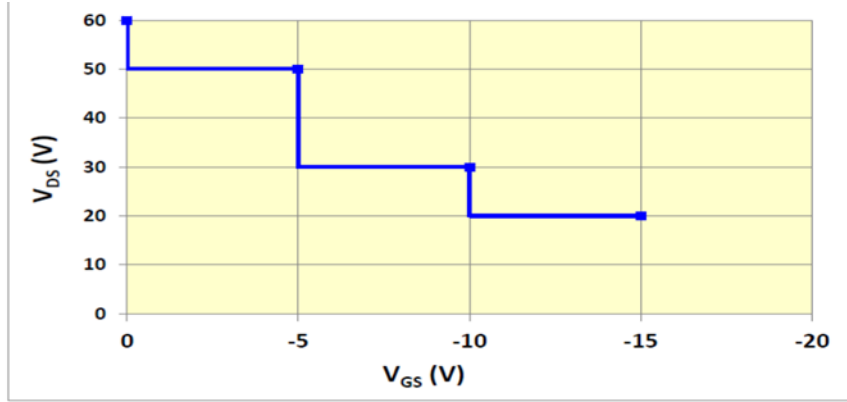


Figure 53: MOSFET Safe Operating Area

### 5.5.2 SEE Mitigation – Part/Equipment/Subsystem Level

There have been several courses dealing with SEE in general and with SEE mitigation in particular, for more detailed information the reader can for example refer to [183 to 186].

In a word:

- Unlike for TID, shielding is not an effective mitigation technique for SEEs because they are induced by very penetrating high energy particles (HI or protons).
- SET mitigation: to design circuits as robust as possible to worst-case transient envelopes recalled in Table 1. This is also clearly the most cost-effective approach since SEE testing is felt as costly. If not possible, to use actual SEE envelopes derived from the relevant test conditions
- Non-destructive SEE in general: the mitigation techniques take the form of, for example, scrubbing, Triple-Modular-Redundancy (TMR) with majority voter or triplication, Error-Detection and Correction Codes (EDAC), and filtering circuitry.

The mitigation technique to implement depends on the nature of the SEE and on the criticality level for the circuit and the system. For linear devices such as comparators (for example the well-known LM139) for which the SET sensitivity has been shown to increase for lower differential input voltages [187, 188, 189], design recommendations will first consist of limiting as much as possible the differential voltage above the sensitivity limit. In case of digital SEEs (SEU, MBU, row/column errors...), the analysis relies on the impact of the SEE rate in the application. For example, any single bit SEU can be detected and corrected by simple EDAC schemes. On the contrary, it is very important to characterize the occurrence of MBUs, row/column errors, SEFI,... etc, because those types of events may defeat the simplest EDAC schemes. In other words, it is from a good characterization of SEE signatures that a good EDAC scheme can be designed.

Destructive SEE may or may not be circumvented at circuit level depending on the individual device response and may require a mitigation action at system level. When possible, system hardening is very difficult to handle and in most cases not particularly effective. For destructive SEE the preferred

option is evidently to use non-sensitive parts, the most critical ones being the Single Event Latchup (SEL) which is possibly destructive, and Single Event Burn-out (SEB). When a SEL occurs the Latchup state can only be cleared by switching-OFF the power to the device (hard reset). A SEL protection circuitry (current detection and hardware shutdown) may be used in conjunction with the failure mode analysis. However, care is necessary when using SEL protection circuitry since SEL can damage a microcircuit and reduce its reliability even when it does not cause outright failure.

Many latch-up paths can occur in complex devices leading to a wide range of SEL currents. Micro latch-up may sometimes be observed necessitating the use of accurate current limiting circuits with the threshold currents set very close to the steady state consumption of the device [190]. It has been reported for example that CMOS devices after non-destructive SEL reveal structural changes in interconnects. Those changes were caused by localized ejection of part of the metallization due to metallization melting. Those structural damages, called latent damages, did not cause any electrically observable, parametric, or catastrophic device failure but were detected by surface analysis. Those latent damages represent a possible reliability hazard and they must be considered when testing devices for SEL as well as establishing limits for current detection and shutdown as a mean of SEL protection [191].

For SEB/SEGR in Power MOSFETs (and SEB in some diodes), mitigation relies on using the device within its SOA plus a derating factor.

Single Event Hard Errors (SHE) and Single Event Functional Interrupts (SEFI) represent special cases to be treated on a case by case basis.

SHE corresponds to the impossibility to write a bit at a different value, permanently or for a significant duration. So it will not only defeat correction schemes (the bit cannot be re-written), but it will also generate a permanent error flag from the detection code, which could saturate error messages, jeopardizing the mitigation strategy of the error correction code (ECC). In case of such events, the only way is to have spare memory space and design programs able to be re-routed to a safe memory zone.

SEFI is a functional interrupt. After the SEFI, the device may be restored using a reset or a power OFF/ON cycle. But it may be impossible to restore its functionality (modification of a hidden, non-accessible non-volatile cell, for example), in which case it can be assimilated to a destructive effect and treated using the methodology described for destructive effects.

### **5.5.3 SEE Mitigation – System Level**

This is the ultimate level of mitigation (scrubbing, management of soft/hard resets, ...). Its implementation is decided in the course of the design phase for the considered product/program, as a function of the identified needs in terms of system mitigation. The target is to insure that SEE effect cannot propagate in the system in a detrimental way, and that the SEE impacts at system level (if any) are identified and that the associated occurrence rate are in conformance with end-customer specified values for reliability and availability.

## **6. Conclusion**

This work is intended to provide an overview of the radiation engineering management from the industrial standpoint focusing on the variability at all steps of the Radiation Hardness Assurance process.

Space industry's keyword in this area is that RHA is based on risk management and not in risk avoidance. This is why Airbus Defence & Space developed its own RHA standard and process, at a time when the normative documents were not in an advanced state.

The task of the radiation engineering in support to a space industry is to fully account for both scientific and industrial contexts. Most of our products (equipment or systems) are now developed for multiple missions and customers: these are our product lines. This strategy implies developing these products based on a sometimes complex combination of worst case and pragmatic considerations, but in all cases on stable requirement sets.

The robustness and the efficiency of the RHA process within Airbus Defence & Space relies on a collaborative approach between a variety of engineering skills. The radiation engineer is working daily in a concurrent engineering scheme with other disciplines (electronic design, EEE part procurement and engineering, equipment procurement, system and electrical architects, etc..) for the full benefit of the internal customers (programs, product) and therefore, of the end customer.

## 7. References

- 1 "The space radiation environment", T.P. O'Brien and J.E. Mazur, NSREC short course, 2016
- 2 "Comparative Earth and Jovian Space Environment", Sébastien Bourdarie, NSREC short course, 2014
- 3 "Spacecraft Environment Interactions", Henry B. Garrett, NSREC short course, 2011
- 4 "The evolution of the radiation environments", J.L. Barth, RADECS short course, 2009
- 5 "The space radiation environment", M. Xapsos and Sébastien Bourdarie, RADECS short course, 2007
- 6 "Modeling Space Radiation environments", J. Barth, NSREC short course, 1997.
- 7 "Radiation Environment for Space", E.G. Stassinopoulos, NSREC short course, 1990.
- 8 "From space environment to specification", Sébastien Bourdarie, RADECS short course, 2011
- 9 "Environment (mission) analysis and specification", Renaud Mangeret, RADECS short course, 2003.
- 10 "Space engineering - Space environment", ECSS-E-ST-10-04C
- 11 "Last upgrades and development of the space environment information system (SPENVIS)", Michel Kruglanski et al, RADECS 2009
- 12 <https://www.spenvis.oma.be/>
- 13 "OMERE space radiation environment and effects tool: new developments and new interface", A. Varotsou et al, ESA-CNES RFP Days – March 7, 2017
- 14 <http://www.trad.fr/en/space/omere-software/>
- 15 "Long-term modulation of galactic cosmic radiation and its model for space exploration", G. D. Badhwar and P. M. O'Neill, Advances in Space Research, vol. 14, no. 10, pp. 749-757, 1994.
- 16 "Galactic cosmic radiation model and its applications", G. Badhwar and P. O'Neill, Advances in Space Research, vol. 17, no. 2, pp. 7-17, 1996.
- 17 "Badhwar-O'Neill 2010 Galactic Cosmic Ray Flux Model; Revised", P. O'Neill, Nuclear Science, IEEE Transactions on, vol. 57, pp. 3148-3153, Dec 2010.
- 18 "Badhwar-O'Neill 2011 Galactic Cosmic Ray Flux Model Description", P. M. O'Neill and C. C. Foster, Tech. Rep. NASA/TP-2013-217376, (2013).
- 19 "Badhwar - O'Neill 2014 Galactic Cosmic Ray Flux Model Description", P. M. O'Neill, S. Golgey and T. C. Slaba, Tech. Rep. NASA/TP-2015-218569, (2015).
- 20 "A Model of Galactic Cosmic Ray Fluxes", Nymmik, R.A., Panasyuk, M.I., Pervaja, T. I. and Suslov, A.A., Nucl. Tracks & Radiat. Meas, 20, 427-429 (1992).
- 21 "Galactic cosmic ray flux simulation and prediction", Nymmik, R.A., Panasyuk, M.I. and Suslov, A.A., Adv. Space Res., Vol. 17, No. 2, (1996).
- 22 "CREME96: A Revision of the Cosmic Ray Effects on Micro-Electronics Code", Tylka, A. J., et al., IEEE Trans. Nucl. Sci., 44, 2150-2160, 1997.
- 23 ISO Model 15390:2004, ISO/TC 20/SC 14 Space systems and operations, June 2004
- 24 "Cosmic Ray Effects on MicroElectronics, part IV," J.H. Adams, Jr, NRL Memorandum report 5901, Naval Research Laboratory, Washington, DC, December 31, 1987.
- 25 "Rate Prediction for Single Event Effects - A Critique", E.L. Petersen et al, IEEE Trans. On Nucl. Sci. NS-39, n°6, pp 1577-1599, December 1992.
- 26 "Probability Model for Cumulative Solar Proton Event Fluences", M.A. Xapsos et al, IEEE TRANSACTIONS ON NUCLEAR SCIENCE, VOL. 47, NO. 3, JUNE 2000
- 27 "Moyens d'évaluation de l'environnement radiatif des véhicules spatiaux", D. Boscher et al, Rapport ONERA RTS 2/05726 DESP, Octobre 2001
- 28 "Updated Model of the Solar Energetic Proton Environment in Space", P. Jiggens et al,
- 29 "The Solar Accumulated and Peak Proton and Heavy Ion Radiation Environment (SAPPHIRE) Model, P. Jiggens et al, IEEE Transactions on Nuclear Science, Year: 2018, Volume: 65, Issue: 2
- 30 "New interplanetary proton fluence model", J. Feynman et al, J. Spacecraft, vol. 27, n°4, p403, July 1990.
- 31 "Space Environment Effects: Model for Emission of Solar Protons (ESP) – Cumulative and Worst Case Event Fluences", M. Xapsos et al, <NASA/TP-1999-209763>, December 1999, pp. 30.
- 32 "The AE8 Trapped Electron Model Environment", J.I. Vette, NSSDC/WDC-A-R&S 91-24, NASA/Goddard Space Flight Center, Greenbelt, MD, November 1991
- 33 "Model for the geostationary electrons environment : POLE", D. Boscher et al, IEEE TRANSACTIONS ON NUCLEAR SCIENCE, VOL. 50, NO. 6, DECEMBER 2003

- 34 "A new international geostationary electron model: IGE2006, from 1 keV to 5.2 MeV", A. Sicard-Piet et al, SpaceWeather, 6, S07003, doi:10.1029/2007SW000368.2008
- 35 "Electron environment specification models for navigation orbits", S. Bourdarie et al, RADECS 2009 pp 364-368, 2009.
- 36 "Outer electron belt specification model", S. Bourdarie et al, IEEE TNS, vol 56, n°4, pp2251-2257, Aug. 2009
- 37 "AE9, AP9 and SPM: New Models for Specifying the Trapped Energetic Particle and Space Plasma Environment", G. P. Ginet et al, Space Sci Rev, p. 1-37, 2013
- 38 "AP8 Trapped Proton Environment for Solar Maximum and Solar Minimum", D. M. Sawyer and J.I. Vette, NSSDC/WDC-A-R&S, 76-06, NASA/Goddard Space Flight Center, Greenbelt, MD, December 1976.
- 39 "A new model for the low altitude trapped protons environment", S.L. Huston et al, IEEE Trans. On Nucl. Sci. NS-45, pp 2972-2978, December 1998.
- 40 "Probabilistic model for Low Altitude Trapped Protons fluxes", M.A. Xapsos et al, IEEE Trans. On Nucl. Sci. NS-49, n°6, pp 2776-2781, December 2002.
- 41 "Preliminary comparison of dose measurements on CRRES to NASA model predictions", M. S. Gussenhoven, et al, IEEE Trans. Nuc. Sci., vol. 38, pp. 1655-1662, 1991
- 42 "A New Proton Model for Low Altitude High Energy Specification", D. Boscher et al, IEEE Transactions on Nuclear Science ; Year: 2014, Volume: 61, Issue: 6, Pages: 3401 - 3407
- 43 "NOVICE, a Radiation Transport/Shielding Code", T.M. Jordan, E.M.P. Consultant's Report, 1982 -1996.
- 44 "The accuracy of NOVICE electron shielding calculations", Jordan, T.M., Radiation and its Effects on Devices and Systems, RADECS 91, pp 320 - 324, 1991.
- 45 SYSTEMA/DOSRAD, Airbus DS software package for system level analysis, Airbus internal document.
- 46 "Fastrand new tool for radiation prediction", T. Beutier et al, Proceedings of the 7th European Conference on Radiation and Its Effects on Components and Systems, 2003. RADECS 2003.
- 47 "Impact of material properties and shielding structures on dose level calculation", R. Mangeret, EADS ASTRUM SAS report, CNES funded study, 2001.
- 48 "Review of Deposited Dose Calculation Methods Using Ray Tracing Approximations", Philippe Calvel et al, IEEE Transactions on Nuclear Science Year: 2008, Volume: 55, Issue: 6, Pages: 3106 - 3113
- 49 "GEO Telecoms Radiation Tools Efficiency Improvement with Methods and Geometry Exchanges for Industrial Tools (GTREFF)", ESA contract 000111684/14/NL/LF, 2016
- 50 "Dose and Dose Rate Effects In Microelectronics: Pushing the Limits to Extreme Conditions", Philippe Adell - Jerome Boch, NSREC short course, 2014
- 51 "TID Through the Looking Glass", K.F. Galloway, NSREC short course, 2013.
- 52 "Evolution of Total Ionizing Dose Effects in MOS Devices with Moore's Law Scaling", D.M. Fleetwood, RADECS short course, 2017.
- 53 "Review of displacement damage effects in silicon devices", J. R. Srour, IEEE Trans. Nucl. Sci., vol. 50, no. 3, pp. 653-670, Jun. 2003.
- 54 "Displacement damage in optoelectronic devices for space applications", Olivier Gilard, Cedric Virmontois, RADECS short course, 2017.
- 55 "Displacement Damage Effects in Devices", J.R. Srour and J.W. Palko, NSREC short course, 2013.
- 56 "Geant4 - A Simulation Toolkit", S. Agostinelli et al., Nucl. Instrum. Meth. A 506, 2003, p. 250. URL: <http://cern.ch/geant4>
- 57 "Improved point kernels for electron and beta ray dosimetry", M. J. Berger, NBS Report NBSIR 73 107 (1973)
- 58 "MCNP - A General Monte Carlo N-Particle Transport Code, Version 4C," J F Briesmeister, Ed., LA-13709-M, 2000.
- 59 "Implementation of the reverse/adjoint Monte Carlo method into Geant4", Desorgher L. et al, Nuclear Inst. and Methods in Physics Research, A, Volume 621, issue 1-3 (September 1-21 2010), p.247-257
- 60 "Rapid Reverse Monte Carlo (RRMC) Project: Contract Final Report", ESA contract 21435/08/NL/AT, July 2012
- 61 "ITS Version 5.0: The Integrated TIGER Series of coupled electron/photon Monte Carlo transport codes with CAD geometry," Brian C Franke et al, Sandia National Laboratory report SAND2004-5172, 2005.
- 62 "MCNPX user's manual version 2.5.0," Los Alamos National Laboratory report, D. B. Pelowitz, ed., In press (February 2005).

- 63 "MCNP: Multigroup/Adjoint Capabilities", J. C. Wagner, et al, LA-12704, 1994
- 64 "Effects of material and/or structure on shielding of electronic devices", Mangeret, R. et al, ", IEEE Trans. On Nucl. Sci. vol. 43, pp 2665 – 2670, 1996.
- 65 "Impact des proprietes effectives des materiaux et structures de blindage sur le calcul de niveaux de dose", R. Mangeret, ASTRUM internal report AIN.RA.RM.705.102.01, Jan. 2001.
- 66 "Basic Mechanisms of Radiation Effects in Electronic Materials and Devices", F.B. McLean and T.R. Oldham, NSREC short course, 1987.
- 67 "Charge yield for cobalt-60 and 10-keV X-ray irradiations of MOS devices", M. R. Shaneyfelt, et al, IEEE Trans. Nucl. Sci. 38, 1187 (1991)
- 68 "Verification of Co-60 TID testing representativeness for EEE components flown in the Jupiter environment", M. Pinto et al, ESA Contract No: RFQ/3-13975/13/NL/PA, ESA/CNES final presentation days, March 2017
- 69 "Response of advanced bipolar processes to ionizing radiation", E.W. Enlow et al, IEEE Trans. On Nucl. Sci. vol. 38, pp 1342-1351, 1991.
- 70 "Hardness Assurance Issues for lateral PNP bipolar junction transistors", R.D. Schrimpf et al, , IEEE Trans. On Nucl. Sci. vol. 42, pp 1641-1649, 1995.
- 71 "Trends in the total dose response of modern bipolar transistors", R.N. Nowlin et al, , IEEE Trans. On Nucl. Sci. vol. 39, pp 2026-2035, 1996.
- 72 "Total dose effects in conventional bipolar transistors and linear integrated circuits", AH Johnston et al, IEEE Trans.on Nucl. Sci, vol. 41, N°6, 2427, 1994.
- 73 "Evaluation of accelerated total dose testing of linear bipolar circuits", Carrière T. et al, , IEEE Trans. On Nucl. Sci.vol.47 , pp 2350 - 2357, 2000.
- 74 "Hardness assurance testing of bipolar junction transistors at elevated irradiation temperature", S.C. Witczac et al, , IEEE Trans. On Nucl. Sci. vol.44 , pp 1989 - 2000, 1997.
- 75 "Impact of passivation layers on enhanced low-dose-rate sensitivity and pre-irradiation elevated-temperature stress effects in bipolar linear ICs", Shaneyfelt, M.R. et al, , IEEE Trans. On Nucl. Sci. vol. 49 , pp 3171 - 3179, 2002.
- 76 "Effect of switching from high to low dose rate on linear bipolar technology radiation response", J. Boch et al, IEEE Transactions on Nuclear Science Year: 2004, Volume: 51, Issue: 5, Pages: 2896 - 2902
- 77 "Applicability of the Accelerated Switching Test Method - A Comprehensive Survey", M. Wind et al, 2011 IEEE Radiation Effects Data Workshop Pages: 1 - 8 Year: 2011
- 78 "ENHANCED LOW-DOSE RATE SENSITIVITY ANALYSIS Summary Test Results and Analysis on Bipolar Devices.", G. Fernandez et al, ESA CONTRACT N°: 4000100717/2010/F/WE, CNES-ESA Final Presentation Days 2013
- 79 "Analysis in the frame of space radiation hardness assurance of low dose rate results obtained with MIL and ESCC test method", R. Marec et al, 14th European Conference on Radiation and Its Effects on Components and Systems (RADECS), 2013.
- 80 "Dose Rate Effect on Bipolar Circuits Degradation", J.-P. David et al, ESA Contract #11407/95/NL COO10, CNES-ESA Final Presentation Days 2013.
- 81 "Ionizing Dose and Neutron hardness assurance guidelines for microcircuits and semi-conductor devices", MIL-HDBK-814
- 82 "Total Ionizing and Non Ionizing Dose radiation hardness assurance", C. Poivey, NSREC short course, 2017.
- 83 "TOTAL DOSE STEADY-STATE IRRADIATION TEST METHOD", ESCC Basic Specification No. 22900, issue 5, June 2016
- 84 "DEPARTMENT OF DEFENSE - TEST METHOD STANDAMICROCIRCUITS: MIL-STD-883J 1019.9 Ionizing radiation (total dose) test procedure, June 2015
- 85 "TEST METHOD STANDA- ENVIRONMENTAL TEST METHODS FOR SEMICONDUCTOR DEVICES", MIL-STD-750-1A W/CHANGE 2, METHOD 1019.5, STEADY-STATE TOTAL DOSE IRRADIATION PROCEDURE, 12 August 2016
- 86 "Proton effects in charge-coupled devices", Hopkinson, G.R. et al, Nuclear Science, IEEE Transactions on, Volume 43, Issue 2, Page(s): 614-627, 1996
- 87 "Proton damage effects in linear integrated circuits", Rax, B.G. et al, Nuclear Science, IEEE Transactions on, Volume 45, Issue 6, Page(s): 2632-2637, 1998
- 88 "Radiation effects in a CMOS active pixel sensor", Hopkinson, G.R., Nuclear Science, IEEE Transactions on, Volume 47, Issue 6, Page(s): 2480-2484, 2000
- 89 "Testing and Qualifying Linear Integrated Circuits for Radiation Degradation in Space", Johnston, A.H. et al, , Nuclear Science, IEEE Transactions on, Volume 53, Issue 4, Page(s): 1779-1786, 2006

- 90 "Radiation Effects in InGaAs and Microbolometer Infrared Sensor Arrays for Space Applications", Hopkinson, G. et al., Nuclear Science, IEEE Transactions on, Volume 55, Issue 6, Page(s): 3483-3493, 2008
- 91 "Radiation characterization and test methodology study of optocouplers devices for space applications", Mangeret, R. et al., Radiation and Its Effects on Components and Systems (RADECS), Page(s): 166-171, 09/2001
- 92 "Proton Test Guideline Development - Lessons Learned", Stephen Buchner et al, NASA/Goddard Space Flight Center, 8/22/02
- 93 « Spécification générique pour le test d'irradiation des composants optoélectroniques », Olivier GILA et al, CNES report ref. DCT/AQ/EC -2008/06142, 2008
- 94 "Component Characterization and Testing, Displacement Damage.", Gordon Hopkinson, RADECS 2003 short course notes
- 95 "Correlation of proton radiation damage in InGaAs-GaAs quantum-well light-emitting diodes", R.J. Walters et al, IEEE Trans Nucl Sci, 48, No 6 pp1773-1777, 2001.
- 96 "Proton Testing of nVidia Jetson TX1", E.J. Wyrwas1, NASA Goddard Space Flight Center, October 2016
- 97 "Use and Benefits of COTS Board Level Testing for Radiation Hardness Assurance", M. Rousselet et al, Radiation and Its Effects on Components and Systems (RADECS), 2016.
- 98 "Board Level Proton Testing Book of Knowledge for NASA Electronic Parts and Packaging Program", S.M. Guertin et al, JPL Publication 17-7 NASA WBS: 724297.40.49.11 JPL Project Number: 104593, 2017
- 99 "Radiation evaluation method of commercial off-the-shelf (COTS) electronic printed circuit boards (PCBs)", K.A. LaBel et al, Fifth European Conference on Radiation and Its Effects on Components and Systems. Pages: 528 – 534, RADECS 1999
- 100 "Radiation testing of commercial-off-the-shelf GPS technology for use on low earth orbit satellites", C. Renaudie, 9th European Conference on Radiation and Its Effects on Components and Systems, Pages: 1 – 8, RADECS 2007
- 101 "Radiation effects and COTS parts in Smallsat", D. Sinclair, 27<sup>th</sup> annual AIAA/USU conference on small satellites, 2013
- 102 "Standards for Space Radiation Environments and Effects", E. Daly et al, , RADECS 2003 proceedings, p175
- 103 "Space product assurance: Radiation hardness assurance - EEE components", ECSS-Q-ST-60-15C, October 2012
- 104 "Space engineering: Methods for the calculation of radiation received and its effects, and a policy for design margins", ECSS-E-ST-10-12C, November 2008
- 105 "Radiation Hardness Assurance (RHA) requirements for NEOSAT", ref. NSAT.SP.GPMO.00000905, 2014, Airbus/TAS internal document.
- 106 "NEOSAT Space radiation environment specification", ref. NSAT.SP.GPMPO.00000924, 2015, Airbus/TAS internal document
- 107 "SINGLE EVENT UPSET MECHANISMS AND PREDICTIONS", JC Pickel, NSREC Short Course, Gatlinburg, 1983.
- 108 "Low-energy proton-induced single-event-upsets in 65 nm node, silicon-on-insulator, latches and memory cells", K. P. Rodbell et al, IEEE Trans. Nucl. Sci., vol. 54, no. 6, pp. 2474-2479, Dec. 2007
- 109 "Low energy proton single-event-upset test results on 65 nm SOI SRAM", D. F. Heidel et al, IEEE Trans. Nucl. Sci., vol. 55, no. 6, pp. 3394-3400, Dec. 2008.
- 110 "The Contribution of Low-Energy Protons to the Total On-Orbit SEU Rate", N. A. Dodds et all, IEEE TRANSACTIONS ON NUCLEAR SCIENCE, VOL. 62, NO. 6, DECEMBER 2015
- 111 "Strategies for SEE hardness assurance – from buy it and fly it to bullet proof", R. Ladbury, NSREC short course, 2017.
- 112 "INDUSTRIAL POINT OF VIEW FOR SPACE APPLICATIONS: BEST PRACTICES FROM PARTS SELECTION TO FLIGHT", A. Carvalho, RADECS short course, 2017.
- 113 "Single Event Effects testing", S. Duzellier, RADECS short course notes, 09/2003
- 114 "Single Event Effect (SEE) Test planning", K. LaBel RADECS short course notes, 09/2011
- 115 "SINGLE-EVENT AND TOTAL DOSE TESTING FOR ADVANCED ELECTRONICS", J.A. Pellish, " , NSREC short course notes, 07/2012
- 116 "Radiation Testing and the RHA Process", R. Mangeret, RADECS short course notes, 2013

- 117 "SEE on Advanced CMOS Bulk, FinFET and UTBB SOI Technologies", P. Roche and G. Gasiot, NSREC short course notes, 2014
- 118 Data Sheet BUY15CS23K-01, Infineon, Sep 2016
- 119 "Development of a test methodology for single-event transients (SETs) in linear devices", Poivey, C. et al., Nuclear Science, IEEE Transactions on Volume 48, Issue 6, Page(s): 2180-2186, 2001
- 120 "Assessing the impact of the space radiation environment on parametric degradation and single event transients in optocouplers", Reed, R.A. et al., Nuclear Science, IEEE Transactions on, Volume 48, Issue 6, Page(s): 2202-2209, 2001
- 121 "Single-event transients in high-speed comparators", Johnston, A.H. et al., Nuclear Science, IEEE Transactions on, Volume 49, Issue 6, Page(s): 3082-3089, 2002
- 122 "Single-event transients in bipolar linear integrated circuits", S. Buchner and D. McMorrow, IEEE Trans. Nucl. Sci., vol. 53, no. 6, pp. 3079–3102, Dec. 2006
- 123 "Development of a test methodology for single-event transients (SETs) in linear devices"
- 124 "Simulation of Proton Induced SET in Linear Devices and Assessment of Sensitive Thicknesses", C. Weulersse et al, 15th European Conference on Radiation and Its Effects on Components and Systems (RADECS), 2015
- 125 "Single-Event Transient Response of Comparator Pre-Amplifiers in a Complementary SiGe Technology", Adrian Ildefonso et al, IEEE Transactions on Nuclear Science, Year: 2017, Volume: 64, Issue: 1, Pages: 89 - 96
- 126 "Physically Based Predictive Model for Single Event Transients in CMOS Gates", Mehdi Saremi et al, IEEE Transactions on Electron Devices; Year: 2016, Volume: 63, Issue: 6 Pages: 2248 - 2254
- 127 "Single-event transients in digital CMOS—A review", V. Ferlet-Cavrois et al, IEEE Trans. Nucl. Sci., vol. 60, no. 3, pp. 1767–1790, Jun. 2013
- 128 "Pulsed-laser testing methodology for single event transients in linear devices", Buchner, S. et al, Nuclear Science, IEEE Transactions on, Volume 51, Issue 6, Page(s): 3716-3722, 2004
- 129 "Probing SET sensitive volumes in linear devices using focused laser beam at different wavelengths", Weulersse, C. et al., Radiation and Its Effects on Components and Systems, RADECS 2007. 9th European Conference on, Page(s): 1-7, 09/2007
- 130 "Comparison of Single Event Transients Generated at Four Pulsed-Laser Test Facilities-NRL, IMS, EADS, JPL", Buchner, S., Nuclear Science, IEEE Transactions on, Volume 59, Issue 4, Page(s): 988-998, 2012
- 131 "Analysis of Single-Event Effects in DDR3 and DDR3L SDRAMs Using Laser Testing and Monte-Carlo Simulations", P. Kohler et al, IEEE Transactions on Nuclear Science Year: 2018, Volume: 65, Issue: 1 Pages: 262 - 268
- 132 "IC and Component Selection for Space Systems", K.A. LaBel, L.M. Cohn, RADECS 2007 short course
- 133 "A novel method for SEE validation of complex SoCs using Low-Energy Proton beams", Gianluca Furano et al, IEEE International Symposium on Defect and Fault Tolerance in VLSI and Nanotechnology Systems (DFT) Year: 2016 Pages: 131 - 134
- 134 "TID and SEE Characterization of Microsemi's 4th Generation Radiation Tolerant RTG4 Flash-Based FPGA", Nadia Rezzak et al, IEEE Radiation Effects Data Workshop (REDW) Year: 2015 Pages: 1 - 6
- 135 "Using Benchmarks for Radiation Testing of Microprocessors and FPGAs", Heather Quinn et al, IEEE Transactions on Nuclear Science Year: 2015, Volume: 62, Issue: 6 Pages: 2547 - 2554
- 136 "Catastrophic Latchup in CMOS Analog-to-Digital Converters", T. F. Miyahira et al., IEEE Trans. Nuc. Sci., Vol 48, N° 6, pp 1833-1840, 2001.
- 137 "Single Event Upset in the PowerPC750 Microprocessor", G. Swift et al., IEEE Trans. Nucl. Sci., Vol 48, N° 6, pp 1822-2710, 2001
- 138 "Practical Aspects of Single-Event Testing: Experimental planning and Interpretation", G. Swift and A. H. Johnston, RADECS 2007 Short Course Notebook, September 10th 2007, Deauville, France
- 139 "Charge Collection in Power MOSFETs for SEB Characterization – Evidence of Energy Effects", V. Ferlet-Cavrois et al, IEEE Trans. Nucl. Sci., Vol. 57, No. 6 pp. 3515-3527, 2010.
- 140 "Influence of Beam Conditions and Energy for SEE Testing", Ferlet-Cavrois, V. et al., Nuclear Science, IEEE Transactions on, Volume 59, Issue 4, Page(s): 1149-1160, 2012
- 141 "SEGR characterization of power MOSFETs: A new insight on PIGST associated to a non-destructive charge collection measurement tool", Carvalho, A. et al, Radiation and Its Effects on Components and Systems (RADECS), Page(s): 649-655, 09/2011
- 142 "Sensitivity to LET and Test Conditions for SEE Testing of Power MOSFETs", Scheick, L et al, Radiation Effects Data Workshop, Page(s): 82-93, 2009

- 143 <https://www.jyu.fi/science/en/physics/research/infrastructures/accelerator-laboratory/radiation-effects-facility/heavy-ion-cocktail-1/available-cocktails-in-radef>
- 144 "Test Procedure for the Measurement of SEE in Semiconductor Devices from Heavy-Ion irradiation", JEDEC JESD57. Dated: 1996 (last draft version dated: 2017)
- 145 "Test Standard for the measurement of proton Radiation SEE in Electronic Devices" JEDEC JESD234. Dated: 2014 (last draft version dated: 2017).
- 146 "Environmental Test Methods for Semiconductor Devices (method TM1080)" MIL-STD-750-1, test method 1080. Dated: 2014.
- 147 "Standard Guide for the Measurement of Single Event Phenomena (SEP) Induced by Heavy Ion Irradiation of Semiconductor Devices", ASTM 1192. Dated: 2011
- 148 "JESD57 Test standard, "Procedures for the measurement of Single-event effects in Semiconductor Devices from Heavy-Ion Irradiation" Revision Update, J.-M. Lauenstein, Single Events Effects (SEE) Symposium and Military and Aerospace programmable Logic Devices (MAPLD), Workshop, La Jolla, CA, 2016
- 149 "MIL/JEDEC standards Update", S. Agarwa, 2016 Electronics Technology Workshop (ETW), NASA Electronic Parts and Packaging Program (NEPP), GSFC, Greenbelt, Maryland, June 2016.
- 150 "Testing guideline for Single-Event Gate Rupture (SEGR) of power MOSFETs", L. Scheick, NASA Electronic Parts and packaging (NEPP) Program Office of Safety and Mission assurance - Jet Propulsion Laboratory, California Institute of Technology Pasadena - CA, JPL Publication Ref: 08-10 2/08.
- 151 "An Updated Perspective of Single Event Gate Rupture (SEGR) and Single Event Burnout (SEB) in Power MOSFETs", J. L. Titus, IEEE Trans. Nucl. Sci., Vol. 60, No. 3, pp. 1912-1928, June 2013.
- 152 "Single Event Burnout Observed in Schottky Diodes", J. S. George et al., NSREC 2013 Radiation Effects Data Workshop (REDW), San Francisco, CA, USA
- 153 "Schottky Diode Derating For Survivability In A Heavy Ion Environment", M. Casey et al., IEEE Trans. Nuc. Sci., Vol 62, Nº 6, pp 2482-2489, 2015
- 154 "Single event burnout testing of high power Schottky Diodes", P. Garcia et al., ESA/CNES Final Presentation Days, Contract N° 4000118250, European Space Agency, Noordwijk, The Netherlands, March 2017.
- 155 "Single-Event Effects Ground Testing and On-Orbit Rate Prediction Methods: The Past, Present, and Future", R.A. Reed et al, IEEE TRANSACTIONS ON NUCLEAR SCIENCE, VOL. 50, NO. 3, JUNE 2003.
- 156 "Single-Event Effects Rate Prediction", James C. Pickel, BEE TRANSACTIONS ON NUCLEAR SCIENCE, VOL. 43, NO. 2, APRIL 1996.
- 157 "Calculation of LET-spectra of heavy cosmic ray nuclei at various absorber depths," W. Heinrich, Radiat. Eff., vol. 34, pp. 145-148, 1977
- 158 "Cosmic ray induced errors in MOS memory cells", J. C. Pickel and J. T. Blandford Jr., IEEE Trans. Nucl. Sci., vol. NS-25, p. 1166, 1978.
- 159 "Analytic SEU rate calculations compared to space data", D. Binder, IEEE Trans. Nucl. Sci., vol. 35, p. 1570, 1988.
- 160 "Suggested single event upset figure of merit", E. L. Petersen et al, IEEE Trans. Nucl. Sci., vol. NS-30, p. 4533, 1983.
- 161 "The SEU figure of merit and proton upset rate calculations", E. L. Petersen, IEEE Trans. Nucl. Sci., vol. 45, p. 2550, 1998.
- 162 "Predictions and observations of SEU rates in space", E. L. Petersen, IEEE Trans. Nucl. Sci., vol. 44, p. 2174, 1997.
- 163 "Detailed analysis of secondary ions effects for the calculation of neutron-induced SER in SRAMs", G. Hubert et al, IEEE Trans. Nucl. Sci., vol.48, 2001.
- 164 "Integrating circuit level simulation and Monte-Carlo radiation transport code for single event upset analysis in SEU hardened circuitry.", K. M. Warren et al, IEEE Trans. Nucl. Sci., vol. 55, pp. 2886-2894, 2008
- 165 "DASIE analytical version: A predictive tool for neutrons, protons and heavy ions induced SEU cross section", C. Weulersse et al, IEEE Trans. Nucl. Sci., vol. 53, no. 4, pt. 1, pp. 1876-1882, Aug. 2006.
- 166 "Compact Modelling and Simulation of Heavy Ion-Induced Soft Error Rate in Space Environment: Principles and Validation", Gennady I. Zebrev and Artur M. Galimov, IEEE TRANSACTIONS ON NUCLEAR SCIENCE, VOL. 64, NO. 8, AUGUST 2017.
- 167 "CRÈME-MC: A physics-based single event effects tool", Brian D. Sierawski et al, IEEE Nuclear Science Symposium & Medical Imaging Conference Year: 2010 Pages: 1258 - 1261
- 168 "Statistical estimation of uncertainty for single event effect rate in OMERE", Nicolas Sukhaseum et al, 12th European Conference on Radiation and Its Effects on Components and Systems, 2011

- 169 "CRÈME: The 2011 Revision of the Cosmic Ray Effects on Micro-Electronics Code, J. H. Adams et al, IEEE TRANSACTIONS ON NUCLEAR SCIENCE, VOL. 59, NO. 6, DECEMBER 2012
- 170 "Statistical Properties of SEE Rate Calculation in the Limits of Large and Small Event Counts", R. Ladbury, IEEE Transactions on Nuclear Science Year: 2007, Volume: 54, Issue: 6 Pages: 2113 - 2119
- 171 "PREDICTING SINGLE EVENT UPSETS IN THE EARTH'S PROTON BELTS", W.L. Bendel and E.L. Petersen, IEEE Transactions on Nuclear Science, Vol. NS-31, No. 6, December 1984
- 172 "Two parameter Bendel model calculations for predicting proton induced upset [ICs]", W. J. Stapor et al, IEEE Transactions on Nuclear Science Year: 1990, Volume: 37, Issue: 6 Pages: 1966 - 1973
- 173 "Model of single event upsets induced by space protons in electronic devices", B. Doucet et al, Proceedings of the Third European Conference on Radiation and its Effects on Components and Systems Year: 1995 Pages: 402 - 408
- 174 "An empirical model for predicting proton induced upset", P. Calvel et al, IEEE Transactions on Nuclear Science Year: 1996, Volume: 43, Issue: 6 Pages: 2827 - 2832
- 175 "Predictions of Proton Cross-Section and Sensitive Thickness for Analog Single-Event Transients" Cécile Weulersse et al, IEEE TRANSACTIONS ON NUCLEAR SCIENCE, VOL. 63, NO. 4, AUGUST 2016
- 176 "Assessment of the Direct Ionization Contribution to the Proton SEU Rate", N. Sukhaseum et al, ESA/CNES Presentation Days, 07/03/2017
- 177 "A calculation method for proton direct ionization induced SEU rate from experimental data: Application to a commercial 45 nm FPGA," N. Sukhaseum et al, presented at the IEEE Nuclear and Space Radiation Effects Conf., 2014
- 178 "Impact of Low-Energy Proton Induced Upsets on Test Methods and Rate Predictions", Brian D. Sierawski et al, IEEE Transactions on Nuclear Science Year: 2009, Volume: 56, Issue: 6 Pages: 3085 - 3092
- 179 "Hardness Assurance for Proton Direct Ionization-Induced SEEs Using a High-Energy Proton Beam", N. A. Dodds et al, IEEE Transactions on Nuclear Science Year: 2014, Volume: 61, Issue: 6 Pages: 2904 - 2914
- 180 "MUSCA SEP3 contributions to investigate the direct ionization proton upset in 65 nm technology for space, atmospheric and ground applications", G. Hubert et al, in Proc. Conf. Radiation and Its Effects on Components and Systems, 2009, pp.179–186.
- 181 "RADIATION HARDNESS ASSURANCE FOR SPACE SYSTEMS", Christian Poivey, 2002 IEEE NSREC Short Course Section V.
- 182 "SINGLE EVENT EFFECTS TEST METHOD AND GUIDELINES", ESCC Basic Specification No. 25100, Issue 2, October 2014.
- 183 "Design approaches for survivable space power systems", L.F. Scheick, NSREC short course notes, 2015.
- 184 "SYSTEM-LEVEL SINGLE-EVENT EFFECTS", S. Mitra, NSREC short course notes, 2012.
- 185 "Radiation Hardening at the System Level", R. Ladbury, NSREC short course notes, 2007.
- 186 "Space product assurance - techniques for radiation effects mitigation in ASICs and FPGAs handbook", ECSS-Q-HB-60-02A, 09/2016.
- 187 "Testing Guidelines for Single Event Transient (SET) Testing of Linear Devices", C. Poivey et al, NASA Electronic Parts and Packaging (NEPP) Program Electronics Radiation Characterization (ERC) Project And Defense Threat Reduction Agency (DTRA), 2003
- 188 "Radiation Effects Predicted, Observed, and Compared for Spacecraft Systems", B. E. Pritchard et al, IEEE NSREC 2002 Data Workshop Proceedings, pp. 7-17, 2002.
- 189 "Single Event Transients in LM139 comparators", C. Poivey, NASA-GSFC test report, Dec. 2000.
- 190 "Catastrophic Latchup in CMOS Analog-to-Digital Converters", T. F. Miyahira et al, IEEE Trans. Nuc. Sci., Vol 48, N° 6, pp 1833–1840, 2001.
- 191 "Radiation Hardness Assurance for Space Systems – Component Selection, System Hardening and Counter-Measures", C. Poivey, RADECS 2003 Short Course Notebook, September 15th 2003, Noordwijk, The Netherlands.

# **Process variations and radiation effects in advanced transistors**

Marc Gaillardin,  
CEA, DAM, DIF

## Table of Contents

1.	Introduction.....	3
2.	Microelectronic Technology: From Micro To Nanometer Scaled Transistors .....	5
2.1.	Transistors architectures .....	5
2.2.	Commercial market insights .....	6
2.3.	MOSFET devices: evolutions and major breakthroughs .....	7
2.4.	MOSFET function: basic static I-V characteristics.....	8
2.5.	MOSFETs evolution 1970's – 2000's.....	10
2.6.	2010's: depleted active layer technologies: FinFET and Ultra-Thin SOI .....	17
2.7.	Beyond the nanometer era: nanowires, 3D stacking and disruptive scaling.....	18
2.8.	Insights into process variability issues.....	19
2.9.	Microelectronic technologies: some keypoints.....	23
3.	Radiation Effects in Ultra-Scaled MOSFETs.....	24
3.1.	Basic radiation effects in devices and ICs .....	24
3.2.	TID effects in bulk silicon MOSFETs .....	26
3.3.	Insights into "high" TID – up to several MGy - effects in MOSFETs .....	28
3.4.	TID effects in SOI technologies.....	29
3.5.	TID effects in multiple-gate technologies: FinFET and nanowires .....	31
3.6.	Radiation response variability .....	35
3.7.	Radiation effects in ultra-scaled technologies: some keypoints .....	40
4.	Upcoming Issues and Conclusions .....	42
4.1.	Short terms perspectives: technology roadmap.....	42
4.2.	Radiation effects and variability issues .....	43
4.3.	Summary and conclusions .....	44
5.	References .....	46

## 1. Introduction

The original idea which has revolutionized computing, calculations, communications, and many other applications... dates back to 1925 when J.E. Lilienfield [1] proposed a device concept which aims at controlling actively electric current. This basic concept is the one of the "transistor" which is the elementary cell of microelectronic technology. Since then, the transistor was proposed with different structures such as the Bipolar Junction Transistor (BJT) [2,3], the Junction Field Effect Transistor (JFET) [4,5] or the Metal-Oxide-Semiconductor Field Effect Transistor (MOSFET) [6]. Each device structure features properties that lead to either high drive current, low consumption or fast switching from a logic state to another. Using such specific properties allows electronic designers to build analog or digital functions in order to generate, to transform, to send, to receive and to interpret information. Such information may be carried by an analog value such as a resistance, a voltage, a current or even a capacitor. But it could also be coded into a set of numbers usually made of binary digits. Applications are about infinite. They can be devoted to both simple activities like sensing temperature or to high complexity tasks such as decrypting human genome. To do so, the original transistor experienced several evolutions and revolutions to become the elementary device used in state-of-the-art digital technologies, the FinFET. It is a silicon-based MOSFET which features multiple gates, uses complex semi-conductor/dielectric/metal stacks, is 3D-patterned and reaches nanometric dimensions.

This was achieved thanks to about sixty years of technological research which was mainly driven by device scaling. There are several reasons to do so, the first one being an economical one, as described for the first time by G.E. Moore in 1965 [7]. In fact, reducing the transistor sizes allows semiconductor companies to fabricate more integrated circuits per wafer, for a cheaper production cost. There are also physical reasons since downscaling transistor dimensions improves electrical performances and energy efficiency, as described by Dennard *et al.* in 1974 [8]. The combination of both drivers has pushed the microelectronic industry to increase the number of transistors per unit surface by a factor of two every about two years since the 1960's (see Figure 1). The initial active volume of the first MOSFET had dimensions of about  $10 \mu\text{m} \times 10 \mu\text{m} \times 10 \mu\text{m}$  [6], whereas it is limited to few cubic nanometers in current leading edge technologies, to reach transistor densities as high as  $100.8 \times 10^6$  transistors/ $\text{mm}^2$  [9,10]. This corresponds to nine orders of magnitude reduction of the transistor volume. Such a huge technology evolution thus requires continuous innovations.

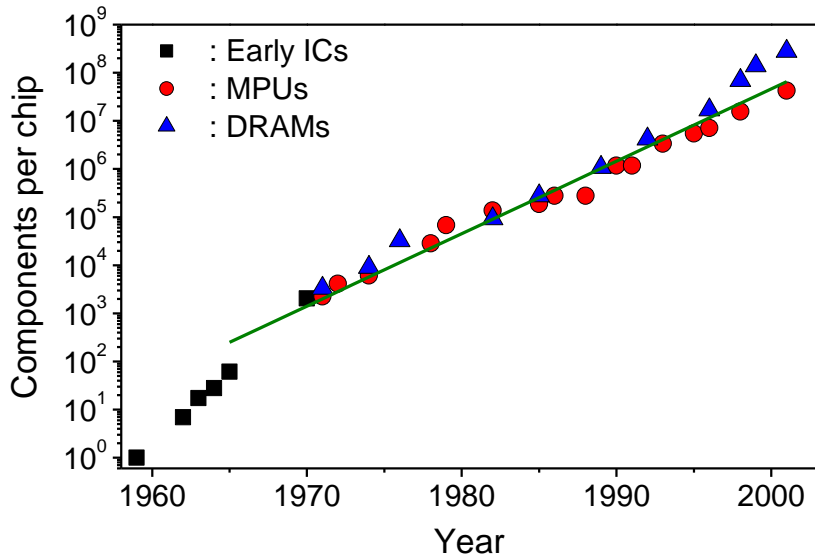


Figure 1: Moore's law economical driver. From [11]

In this context of fast and continuous evolution of microelectronic technologies, several challenges were faced such as dielectric processing, doping implantations, high resolution lithography, material etching, etc. Such fabrication steps use stochastic physical processes which lead to variations of the final transistor shape and then of its final electrical behavior. For these reasons, process variability has been identified since 1961 [12] as a critical aspect for microelectronic device fabrication. This induces part-to-part, wafer-to-wafer, lot-to-lot and foundry-to-foundry variations. Devices and Integrated Circuits (IC) are all similar but all different at the same time. This is a critical issue for production of millions of ICs which must operate with similar performance, electrical consumption and reliability. Actually, this is not a novel issue, but novel sources of variability arise with process technology enhancements required to meet requirements of device scaling.

Dealing with variability is an obvious challenge for process technology and a serious issue for radiation applications. Radiation effects are studied from the early times of microelectronic technology since they can be additional sources of device function modifications and/or fluctuations. Radiation effects are usually divided into four categories: Total Ionizing Dose (TID), Total Non-Ionizing Dose (TNID) also known as Displacement Damage Dose (DDD), Single-Event Effects (SEE) and Transient Radiation Effects in Electronics (TREE). All these contributions can change devices and ICs functions, and sometime can lead to IC destruction.

This short course is thus devoted to present the key issues of major microelectronic technology evolutions and their implications for radiation effects, particularly for TID- (and TNID-) induced effects. Variability sources are presented as well as the usual manner to measure them and their implications for radiation applications. The last part of the notes will focus on what could be envisioned in the near future about the impact of both radiation effects and variability on leading edge and innovative device structures.

## 2. Microelectronic Technology: From Micro To Nanometer Scaled Transistors

### 2.1. Transistors architectures

Various electronic devices have been invented from the early 1930's: the MOSFET, the BJT and the JFET (or MESFET). The first practical realization was achieved by the Bell labs in 1953 [5] which fabricated a Germanium-based Bipolar Junction Transistor using doping diffusion to form the emitter-base-collector structure. The conduction was made possible in the device volume thanks to the space charge regions modulation between the emitter, the base and the collector. Just a few years later the first Junction Field Effect transistor was invented and fabricated. Here, a gate made of polysilicon (or metal in MESFETs) modifies the depletion depth through a Schottky contact which modulates the current between the doped source and drain regions. The third major device is the MOSFET. Its original feature is the insulator between the gate electrode and the active semiconductor region. This structure includes a gate electrode on top of the insulator to change the semiconductor-insulator surface potential. This provides the ability to modify locally the semiconductor regime from accumulation to depletion and then inversion. MOSFET operations are achieved through a surface conduction path contrary to both the BJT and the JFET which use volume conduction. Actually, the idea of the MOSFET was invented in the 1930's while the other concepts were proposed later. But the process to fabricate a high quality gate-dielectric in the MOSFET was a great challenge to overcome. The first working MOSFET was fabricated in the early 1960's, about ten years later than the first BJT and the JFET [13].

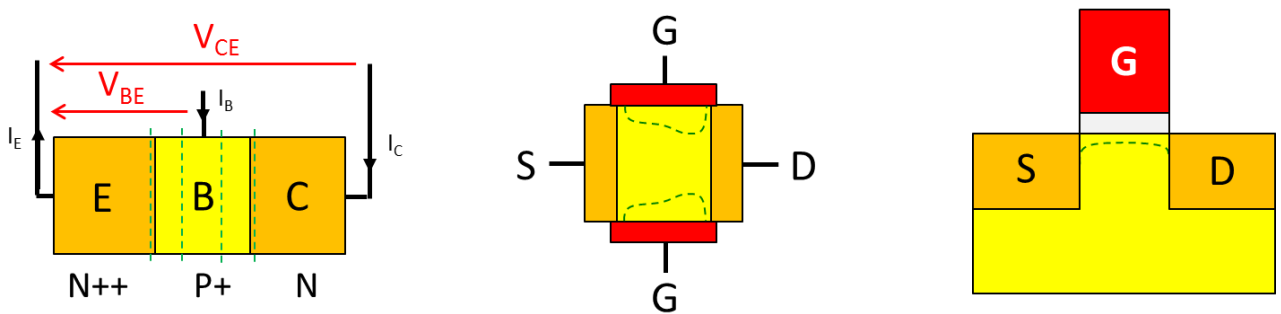


**Figure 2: Schematic description of three basic microelectronic devices structures: (a) the Bipolar Junction Transistor (BJT), (b) the Junction Field Effect Transistor (JFET) and (c) the Metal-Oxide-Semiconductor Field Effect Transistor (MOSFET).**

All these devices have strengths and weaknesses. But major MOSFET advantages over other device structures are both high scalability and easy complementary devices co-integration to fabricate basic Boolean functions.

Scalability allows higher complexity and a lower power cost per function. This is presented by Dennard *et al.* for MOSFETs [8] who shows the implications of applying a scaling factor  $\kappa$  on major device characteristics (doping, voltage, power dissipation...see Figure 3), while keeping the same electric field and power density.

Device or circuit parameter	Scaling factor
Device dimension $t_{ox}, L, W$	$1/\kappa$
Doping concentration $N_a$	$\kappa$
Voltage $V$	$1/\kappa$
Current $I$	$1/\kappa$
Capacitance $\varepsilon A/t$	$1/\kappa$
Delay time $VC/I$	$1/\kappa$
Power dissipation/circuit $VI$	$1/\kappa^2$
Power density $VI/A$	1

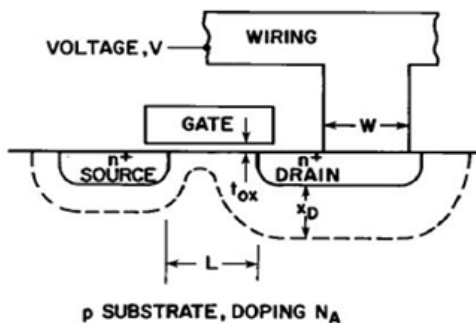


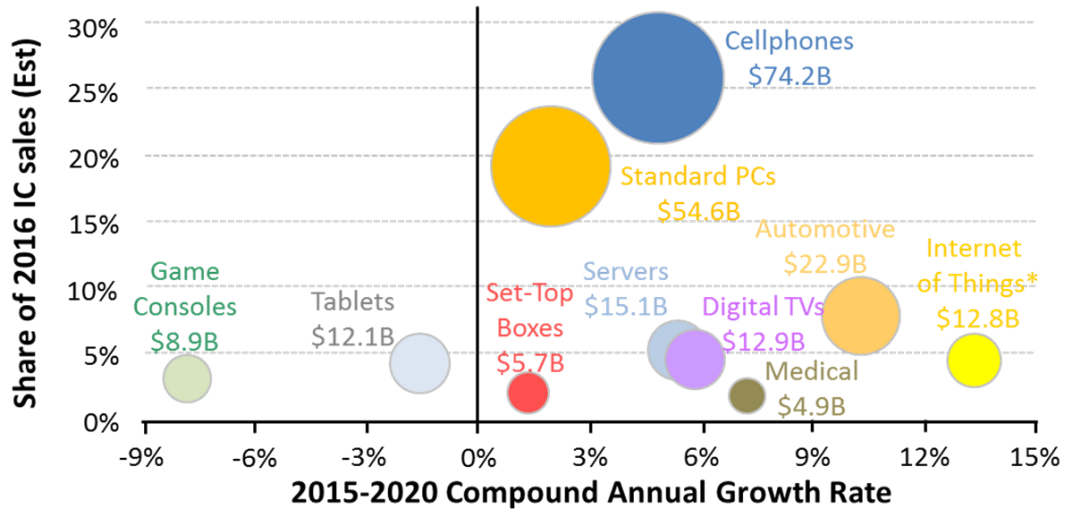
Figure 3: Dennard's law, i.e. the physics of scaling [8].

MOSFETs have the ability to be driven by either electron or hole conduction and to be easily co-integrated: this enables the Complementary Metal Oxide Semiconductor (CMOS) technology. This is a key factor since it allows one to build Boolean operators such as the OR, AND, NOR, NAND and XOR which are the bases of digital computing and thus of Arithmetic Logic Units (ALU) included in modern processors units. Furthermore, CMOS technology has the specific feature to have a theoretical “zero” static electrical power consumption. It makes CMOS technology efficient to design ICs to perform complex calculations.

The last (but not the least) driver for MOSFETs and CMOS development is its cost efficiency thanks to scaling. As mentioned previously, G.E. Moore early describes the microelectronic technology evolution from an economic standpoint, stating that “cramming more components” in a single chip makes them cheaper to produce (see Figure 1) for a given function. But to do so, CMOS technologies had to overcome a number of challenges to meet the requirements of the so-called “Moore’s law” up until today.

## 2.2. Commercial market insights

Figure 4 exhibits the major current end-user markets, their respective sales and the envisioned compound annual growth rate [14]. This is a “snapshot” of the major end-user market drivers for microelectronic industries. It is worth noting that cellphones and standard Personal Computers (PC) represent half of the global market. These two huge mainstream applications both continue to increase in proportion, while some like game consoles decrease. The same picture in the late 1990’s was strongly different. Particularly, cellphones were an emerging, but highly growing market while standard PC was the main driver which is now a consolidated market with a weak positive growth rate.



\*Covers only the internet connection portion of systems.

Source: IC Insights/electronicsweekly.com

**Figure 4: Overview of the Integrated Circuit (IC) end-use markets in 2016 and the envisioned growth rates (from [14]).**

The major issue revealed by Figure 4 is the need for Very Large Scale Integration (VLSI) technologies for almost all major end-user markets. CMOS technologies currently serve these various applications but they have required strong innovations from the original structure of the silicon-based MOSFET to remain in the roadmap.

### 2.3. MOSFET devices: evolutions and major breakthroughs

This section focuses on the basic element of modern CMOS technologies: the bulk silicon MOSFET. Its original structure is made of a vertical stack of bulk silicon,  $\text{SiO}_2$  dielectric and a poly-silicon gate electrode completed by two minority carrier tanks referred as the source and the drain regions (cf. Figure 5). Source and drain regions are formed by using acceptor or donor dopant atoms. Usual impurities are boron for acceptor-type dopants to fabricate P-type MOSFETs (referred as PMOSFET in the following) and either phosphorus or arsenic for donor-type dopants to fabricate N-type MOSFETs (referred to as NMOSFET in the following). Both MOSFET types are obtained by creating deep well regions (N or P-type) in which each transistor is formed. The gate dielectric made of  $\text{SiO}_2$  is grown and then the polysilicon gate is deposited and etched to form the gate stack. The gate is used as a mask for the drain/source self-alignment in the dopant implantation step. Each MOSFET is isolated from its neighbor either by the formation of a junction which is reverse biased during device operation or by a dielectric usually named field oxide in order to mitigate inter-device leakage. This makes it possible to fabricate N- and P-type transistor with symmetric operations, a key advantage of CMOS technology.

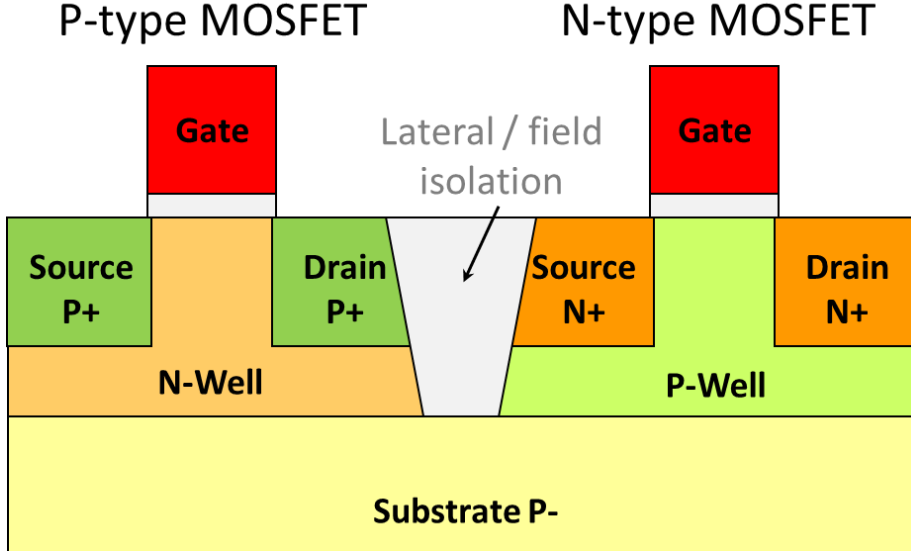


**Figure 5:** Schematic description of a P-type (left) and of a N-type (right) Metal-Oxide-Semiconductor Field Effect Transistor (MOSFET), the two transistors being dielectrically isolated by a field oxide. The combination of the two transistor types is the basis of the CMOS technology.

#### 2.4. MOSFET function: basic static I-V characteristics

The bulk MOSFET function is widely described in the literature [13]. The basic operations are recalled here to illustrate the major electrical parameters used to benchmark MOSFETs for their electrical performances, ionizing radiation sensitivity and to measure process variability. Figure 6 exhibits a static drain current  $I_D$  (in log scale) vs gate-to-source voltage  $V_{GS}$  of a NMOSFET (as schematically described on the right hand side in Figure 5). The electrical behavior of this NMOSFET can be separated into three main regimes: accumulation, depletion and inversion (weak and strong).

For  $V_{GS} < 0$  V, majority carriers of the P-well (holes) are accumulated at the silicon-gate oxide interface due to the vertical (also referred as transverse) electric field through the gate oxide that comes from the silicon and points to the gate electrode. This is the accumulation regime. No current flows from the source to the drain. It is only limited to a leakage current which is usually denoted  $I_{OFF}$  (in A) for  $V_{GS} = 0$  V.

For  $0 \text{ V} < V_{GS} < V_{TH}$ , where  $V_{TH}$  is named the threshold voltage, the electric field direction changes to come from the gate electrode and to point in the direction of the silicon substrate. Majority carriers, *i.e.* holes, are pushed away from the silicon-gate oxide interface. In other words, the silicon-gate oxide interface is more and more depleted from majority carriers as  $V_{GS}$  increases to higher positive values while minority carriers, *i.e.* electrons in NMOSFETs, are attracted from the source and drain regions. This is the depletion regime. The drain current increases exponentially with  $V_{GS}$ . The slope of the I-V characteristic is referred to as the subthreshold slope  $S$ , or more usually to the inverse of  $S$  called the subthreshold swing  $S^{-1}$  (in mV/decade).

For  $V_{GS} > V_{TH}$ , carriers from the source and the drain regions, *i.e.* electrons, are attracted to the silicon-gate oxide interface thanks to the transverse electric field. Their density becomes greater than that of majority carriers (*i.e.* holes). The carrier type is locally inverted to form a thin layer of minority carriers (N-type) in the P-well region usually named the conduction channel. This is the inversion regime. The drain current increases almost linearly with  $V_{GS}$ , to reach the drive current called  $I_{ON}$  for  $V_{GS} = V_{DD}$ , the nominal bias voltage of the transistor.

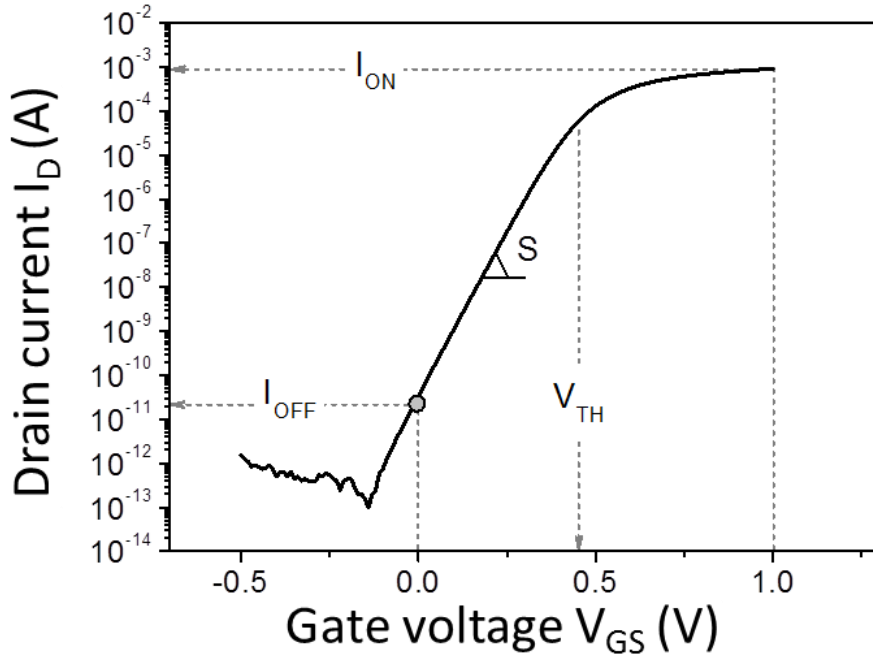
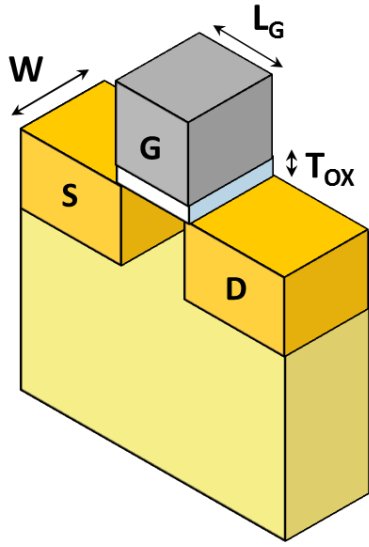


Figure 6: Static drain current  $I_D$  (in log scale) vs gate-to-source voltage  $V_{GS}$  of a NMOSFET.

The objective is to reach the highest  $I_{ON}/I_{OFF}$  ratio to optimize the electrical performance as well as the power consumption, since increasing the drain current  $I_D$  in the inversion regime leads to much faster devices. This can be improved by several manners. Equation 1 exhibits the proportional relationship between the drain current and several parameters including:

- The MOSFET dimensions with  $W$ ,  $L_G$  and  $T_{ox}$  which correspond to the transistor width, the gate length and the gate oxide thickness respectively (as described in Figure 7).
- The minority carrier mobility  $\mu$  in the semiconductor material, here made of silicon.
- The relative dielectric permittivity  $\epsilon_{ox}$  of the gate oxide.

The drain current also depends on electrical parameters such as the drain-to-source or the gate-to-source voltage depending on the conduction regime. However, Equation 1 highlights key aspects that have driven major technological evolutions from the original MOSFET to the one fabricated in current leading edge CMOS technologies.



**Figure 7: Schematic description of a bulk silicon MOSFET with its main geometrical characteristics.**

$$I_D \propto \mu \frac{W}{L_G} \frac{\epsilon_0 \epsilon_{ox}}{T_{ox}} \quad (\text{Eq. 1})$$

$\mu$  is the carrier mobility.

$W$ ,  $L_G$  and  $T_{ox}$  are the MOSFET width, gate length and gate oxide thickness (for  $\text{SiO}_2$ ) respectively as presented in the schematic description presented in Figure 7.

$\epsilon_0$  the vacuum permittivity.

\*  
 $\epsilon_{ox}$  is the relative permittivity of the gate dielectric.

## 2.5. MOSFETs evolution 1970's – 2000's

Equation 1 shows that altering the MOSFET dimensions modulates its drain current without changing other parameters like the gate oxide material (related to  $\epsilon_{ox}$ ) or the semiconductor material (related to  $\mu$ ). This is the key motivation for device scaling. Reducing  $L_G$ ,  $T_{ox}$  and  $W$  leads to a better electrical performance and decreased device dimensions, and thus fabrication cost per function. But downscaling the MOSFET size requires continuous evolutions and innovations to keep the  $I_{ON}/I_{OFF}$  ratio high enough for the MOSFET to function properly.

The fundamental milestone in micro-electronic process technology is the first fabrication of a working MOSFET presented by D. Kahng and M.M. Atalla in 1959 [15]. The general architecture of this first MOSFET became the basis for device scaling [7] but has experienced significant evolutions [16] to remain under the spotlights such as:

- Doped polysilicon gate material which is used to self-align the source/drain regions and as a hard mask for dopant diffusion and activation [17]. Doped polysilicon gates are also used to modify the gate-to-silicon workfunction difference which is a key factor in determining the MOSFET threshold voltage  $V_{TH}$ .
- Lightly doped drain region, processed using tilted implants through gate spacers while the supply voltage remained unchanged at 5 V during almost 20 years before decreasing down to less than 1 V in order to reduce hot carrier effects that became a major concern in the late 1970s [18].

- Nitrided gate oxides [19,20] and more recently the introduction of high-k dielectrics [21,22] to mitigate gate leakage current.
- Strain engineering [23,24] either through SiGe source-drain regions or introduced via stressed capping etch stop layers in order to improve carrier mobility.
- “Generalized scaling” concept [25] in order to mitigate short channel effects.

These are only few examples of the evolutions introduced in the MOSFET to be scaled from 10  $\mu\text{m}$  to reach the deep-submicron era. Since the end of 1990’s, *i.e.* 0.25  $\mu\text{m}$ /0.18  $\mu\text{m}$  technology nodes, two serious issues have emerged: Short Channel Effects (SCE) and gate leakage. They are both due to the continuous reduction of MOSFET dimensions, SCE being due to gate length decrease while gate leakage is induced by gate oxide thinning.

### 1.1.1.Two major issues: short channel effects and gate leakage currents

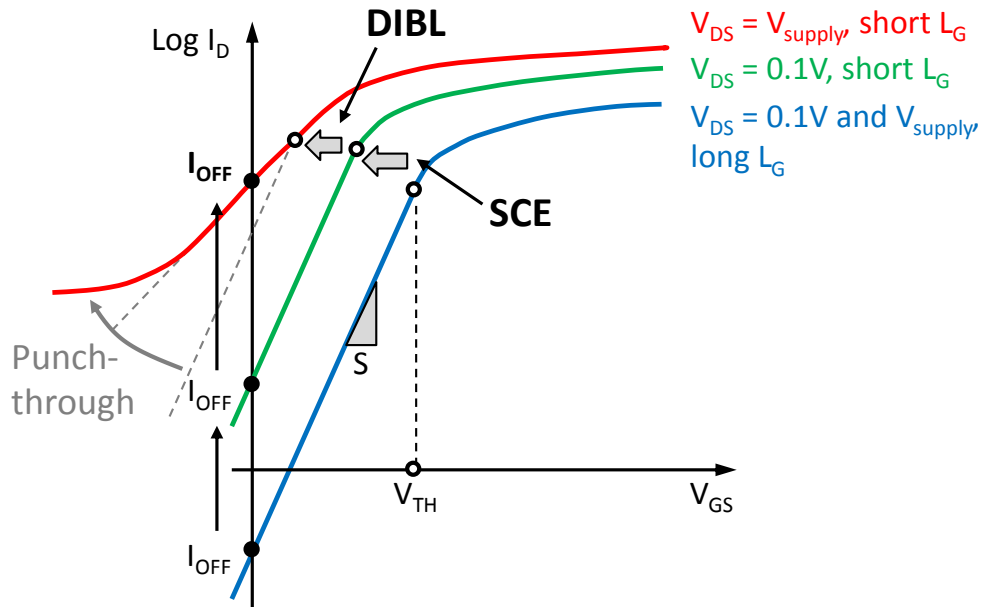


**Figure 8: Illustration of impact of Short Channel Effect (SCE) on static drain current  $I_D$  vs gate-to-source voltage  $V_{GS}$  characteristics (from [26]). Both Drain Induced Barrier Lowering (DIBL) and punch-through effects are also exhibited.**

Figure 8 summarizes the impact of short channel effects on MOSFET  $I_D$ - $V_{GS}$  curves. They can be separated into three major effects: the short channel effect itself, the drain induced barrier lowering and the punch through effect, all inducing drain leakage currents.

The starting point is to consider a long channel MOSFET (for instance  $L_G = 10 \mu\text{m}$ ) with a low drain-to-source bias (for instance  $V_{DS} = 0.1 \text{V}$ , Figure 8 blue curve). The  $I_D$ - $V_{GS}$  curve exhibits both low  $I_{OFF}$  and  $I_{ON}$  currents. Reducing  $L_G$  down to deep-submicron length such as 0.18  $\mu\text{m}$  leads to increases in both the drive current  $I_{ON}$  and the leakage current  $I_{OFF}$  by shifting the threshold voltage  $V_{TH}$ . This improves the device speed but also its static power consumption. This is due to the effective

reduction of the body-to-source potential barrier height  $\phi_{BS}$  as depicted in Figure 9 which eases the passage of a carrier from the source to the drain.

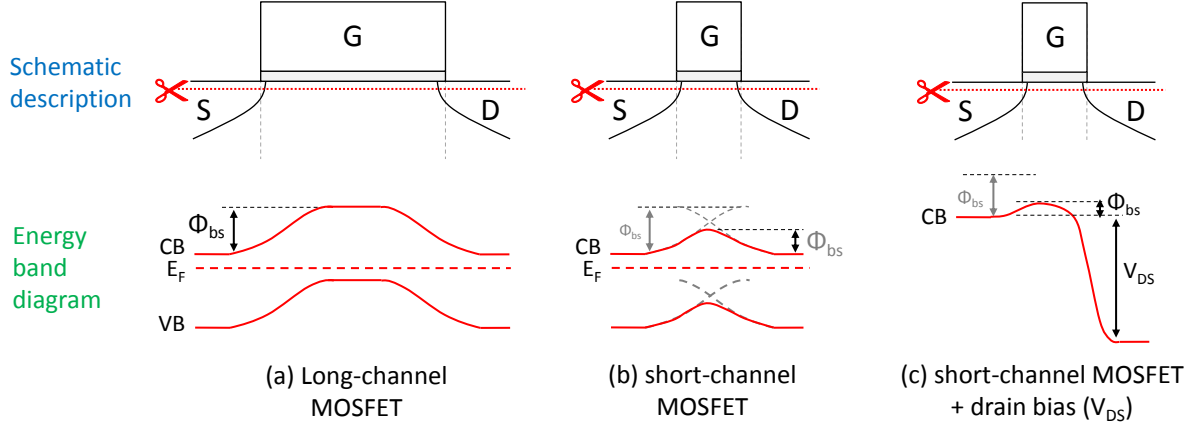


**Figure 9: Schematic description of short channel effects on band diagram at the silicon-gate oxide interface (at the scissors location) of a long-channel MOSFET (a), a short-channel MOSFET (b) and a drain-biased short channel MOSFET (c) to illustrate the Drain Induced Barrier Lowering (DIBL). The valence band, conduction band, Fermi level and source junction barrier height are indicated as VB, CB, EF and  $\phi_{BS}$  respectively.**

DIBL occurs in short channel devices with a large drain bias. The drain bias  $V_{DS}$  stretches the conduction band energy shape which minimizes  $\phi_{BS}$  as described in Figure 9 (c).  $V_{TH}$  is shifted to lower  $V_{GS}$  on the  $I_D-V_{GS}$  curves (see Figure 8). Drain bias can also trigger punch through effects which depend on carriers going from the source to the drain much deeper in the silicon, which usually increases the subthreshold swing  $S^{-1}$  of the  $I_D-V_{GS}$  curve. Both DIBL and punch through increase the drain leakage current  $I_{OFF}$ . Despite the  $I_{ON}$  improvement obtained thanks to gate length reduction, short channel effects have to be mitigated to maintain a sufficiently high  $I_{ON}/I_{OFF}$  ratio for proper MOSFET operations. This is usually achieved by doping engineering such as introducing channel or pockets implants [27] but a compromise must be found since it has a direct incidence on the threshold voltage and then on the  $I_{ON}/I_{OFF}$  characteristics.

Gate leakage is the second great issue caused by device scaling. It becomes a critical issue in MOSFETs processed with a gate oxide thinner than 2-2.5 nm, *i.e.* below the 90 nm node. Using such extremely thin dielectric layers enhances tunneling currents that pass through the gate dielectric [27]. Figure 10 shows a schematic description of the mechanism for a MOSFET with bias applied on both the drain and the gate. Some of the carriers which leave the source can reach the gate electrode instead of the drain. This gate current dramatically increases with oxide thinning, weakening the drain current at the same time. In other words, part of the  $I_{ON}$  improvement obtained thanks to gate length downscaling is lost due to gate leakage. Furthermore, two other effects appear when thinning the gate oxide: the poly-depletion and the darkspace. Poly-depletion is due to the carrier repulsion from the gate oxide-polyilicon gate material interface while the darkspace is induced by a carrier confinement effect close to the silicon-gate oxide interface. Both have the same consequence: an apparent increase of the gate oxide thickness that lowers the current delivered on the drain electrode. For these reasons, the Equivalent Oxide Thickness (EOT) is used in Equation 1. EOT takes

into account both the poly-depletion and darkspace in addition to the physical gate oxide thickness. Here again, these two mechanisms reduce the performance gain brought by scaling.

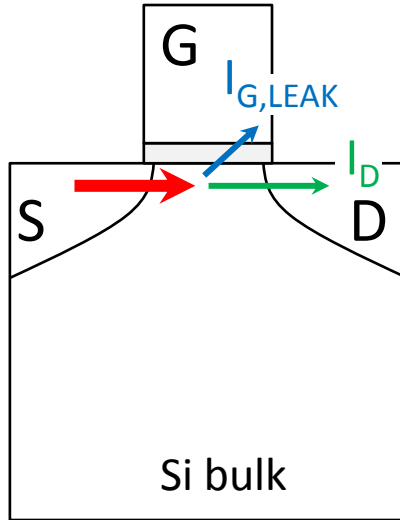


**Figure 10: Schematic description of the gate leakage current mechanism. The drain current  $I_D$  is lowered because of carriers which pass through the thin gate dielectric, i.e.  $I_{G,LEAK}$ .**

To go further into device scaling, the only solution to mitigate gate leakage currents (and darkspace) is to get thicker dielectrics without degrading the total gate capacitance, i.e.  $C_{ox} = \epsilon_0 \cdot \epsilon_{ox} / T_{ox}$ , while mitigating poly depletion requires to modify the gate material.

#### 1.1.2. Technologies to push silicon-based MOSFETs down to the 30 nm node

Nitrided oxides were first used instead of silica, but a dielectric with a higher relative dielectric permittivity  $\epsilon_{ox}$  is required to meet requirements of technology nodes below the 45 nm node. They are called high- $k$  dielectric in the following. Hafnium-based dielectrics have emerged as an appropriate solution since they are a compromise between a high  $\epsilon_{ox}$  value ( $\epsilon_{HfO_2} \approx 25$  instead of  $\epsilon_{SiO_2} = 3.9$  in  $SiO_2$ ) and a “moderate” bandgap (about 5.8 eV in  $HfO_2$  instead of 9 eV in  $SiO_2$ ) [28]. However, such hafnium-based dielectrics have worse chemical compatibility with silicon compared to  $SiO_2$ . A thin buffer of  $SiO_2$  is usually grown before the high- $k$  dielectric deposition process to achieve a high quality silicon-gate dielectric interface. In that case, EOT is used to get an “equivalent  $SiO_2$ ” thickness. It can be expressed using equation 2.

$$EOT = \frac{\epsilon_{SiO_2}}{\epsilon_{high-k}} T_{high-k} \quad (\text{Eq. 2})$$

Not only the gate capacitance is improved but also the electric field across the dielectric is lowered which mitigates hot carrier effects. Beside the replacement of the usual  $SiO_2$  as gate dielectric, metal

gates were introduced instead of polysilicon gates in order to suppress poly-depletion. A description of such complex gate stacks is presented in Figure 11.

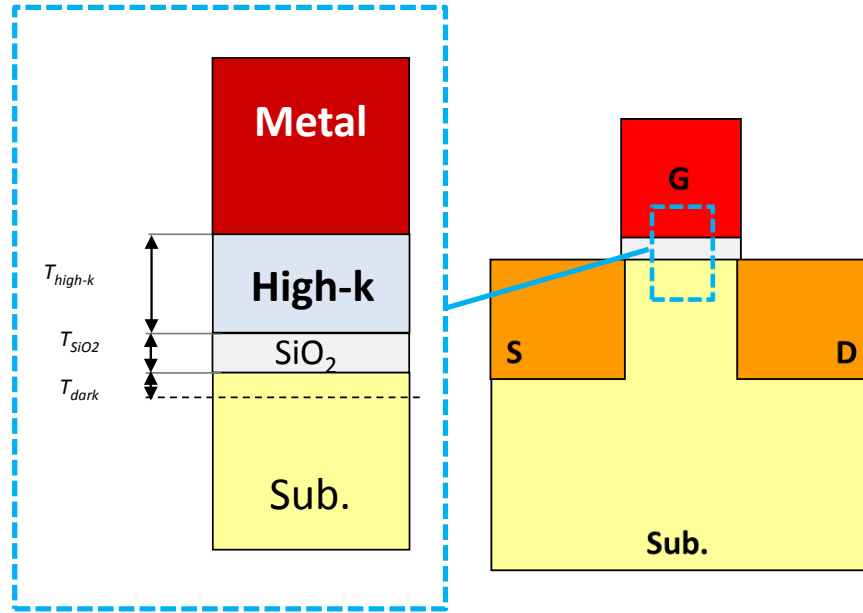


**Figure 11: Description of complex gate stack which involves a thin pedestal SiO<sub>2</sub> topped by a high-k dielectric and a metal-gate material.**

The major drawback of metal gates is the loss of one degree of freedom to modulate the MOSFET threshold voltage which was available with polysilicon gates. The metal gate workfunction is fixed so the metal must be chosen in order to work with both N- and PMOSFETs with symmetric operations. TiN material is identified as a good candidate since its workfunction makes it close to silicon mid-gap. This leads to almost symmetric threshold voltages for N- and PMOSFETs with the assumption of low-doped channels.

High-k/metal gate associated with small dimensions are two of three drivers to push planar bulk silicon MOSFETs to deep submicron technologies, the last one being to improve the carrier transport properties in the semiconductor material. They are described by the carrier mobility  $\mu$  in Equation 1. The carrier mobility depends on the silicon electronic band structure, and thus on its crystal lattice and particularly on its periodicity. A first manner to improve it is to change the channel material, for instance using Germanium or III-V materials for which either the hole or the electron mobility is higher than in bulk silicon. Changing the intrinsic electronic properties of silicon is an alternative way to get better carrier mobility. The basic idea is to modify the silicon crystal lattice itself by applying a mechanical stress. This can be induced by several methods:

- Process-induced strain which transfers part of the stress from the capping layers or from the STI to the silicon channel [29].
- Using the crystal lattice mismatch between two materials such as in SiGe-Si heterostructures [27].

In both cases, the strain applied to the channel material changes the electronic band structure and can induce energy levels splitting [30]. The tricky aspect is that both compressive and tensile strain on various space directions can be achieved in the GPa order of magnitudes. Such strains may be additive [31] and some can improve electron mobility but degrade that of holes. The first MOSFET which uses strain engineering was demonstrated in 2002 for 90 nm node transistors [32,33]. Such MOSFETs include Germanium source/drain regions that induce a compressive strain in the channel axis of PMOSFETs which enhances the holes mobility. The scanning electron microscopy image of such a transistor is shown in Figure 12 (left) as well as an example of the  $I_{ON}/I_{OFF}$  improvement that can be achieved using strain engineering (right, from [27]).

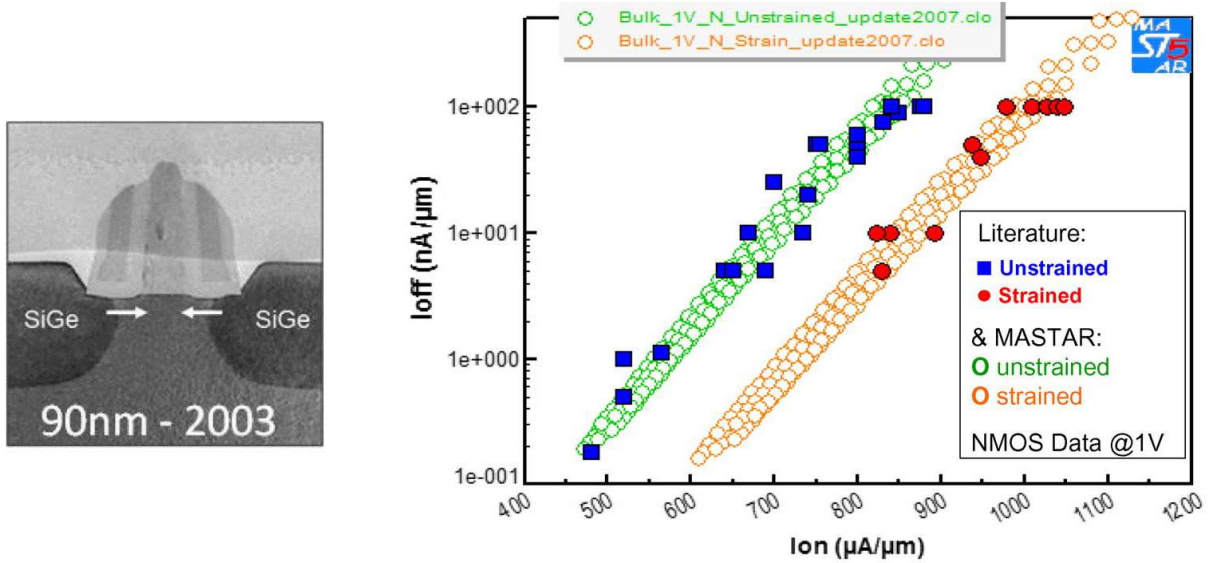


**Figure 12:** Scanning electron microscopy image of a 90 nm MOSFET with SiGe source/drain [32] (left) and  $I_{ON}/I_{OFF}$  graph for MOSFETs fabricated without (blue squares) and with (red circles) strain electrical performance booster [27].

The combination of strain, high-k dielectric and metal gate electrodes give to bulk silicon MOSFETs the ability to meet the requirements of the 32/28 nm technology nodes without modifying the overall architecture of the first planar bulk silicon MOSFET fabricated in 1960.

#### 1.1.3.The Silicon-On-Insulator (SOI) alternative

In parallel to the bulk silicon MOSFET progress, the Silicon-On-Insulator (SOI) technology has been developed since the mid-1960's. The first SOI MOSFET was fabricated on a Silicon-On-Sapphire (SOS) wafer [34]. This was primarily motivated by radiation hardness purposes, particularly the need to mitigate the destructive radiation-induced effect called Single-Event Latch-up (SEL) [35]. This phenomenon is triggered when an incident ionizing particle strikes a region between two MOSFETs. Generated charges can forward bias the PN junction which is usually reverse-biased between two transistors depending on the incident particle strike location and the energy transferred to silicon. Then, a thyristor between the two neighboring MOSFETs can be triggered and the process can be self-sustained. The current delivered by this parasitic thyristor continuously increases up to destroy the involved transistors and the IC function.

The major objective of the SOI technology is to dielectrically isolate the active area of the MOSFET from the bulk silicon substrate thanks to a buried dielectric named Buried OXide (BOX) as schematically described in Figure 13. In SOI technologies, the active area of MOSFETs is made of a silicon island which stands on the BOX.

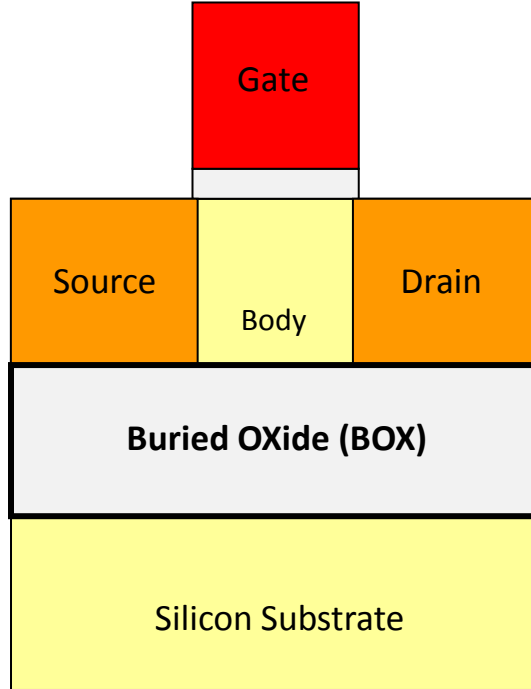


**Figure 13: Schematic description of a SOI transistor. The active MOSFET area is made of a silicon island above the Buried OXide (BOX).**

The MOSFET active area is strictly limited to the surface of the MOSFET. This is located at the silicon-gate dielectric interface while the rest of the bulk silicon substrate is not actively involved in current conduction. It may even slow down the MOSFET operations because of parasitic depletion capacitances between the source/drain regions and the silicon substrate. Introducing a BOX intrinsically prevents any charge collection from the silicon substrate to reach the MOSFET active areas. Using a BOX combined with field isolations, such as LOCAl Oxidation of Silicon (LOCOS) [36] or Shallow Trench Isolation (STI) [37,38], makes SOI ICs immune to SEL. This specific feature makes SOI technologies interesting for a wide range of radiation-tolerant/hard applications. But its development was limited for a long time to niche markets because of its high cost compared to bulk silicon. Furthermore, the active silicon-BOX interface usually has a poor electrical quality. A considerable effort was devoted to improving the SOI fabrication process, with techniques such as the Zone Melt Recrystallization (ZMR) [39], the Separation by IMplantation of OXYgen (SIMOX) [40,41] or the wafer Bonding and Etch back SOI (BESOI) [42,43]. Early SOI technologies were explored in various versions: thick SOI [44,45], Partially Depleted SOI [46,47] and Fully Depleted SOI [48,49], but a major turning point for SOI technology was the Smartcut® process to fabricate Unibond® SOI wafers [50,51]. This process developed in the late 1980's and early 1990's uses two

initial bulk silicon wafers to fabricate a high quality SOI wafer. At the end of the process, one SOI wafer is obtained and one another bulk silicon wafer can be reemployed to be reused to fabricate an additional SOI wafer. This significantly reduces the initial SOI wafer cost which was slowing down the SOI technology advancement. Since then, SOI technology has been widely used for a number of mainstream applications, especially for those which require low power operations [52]. SOI technology has strong interest for device scaling thanks to reduced parasitic depletion capacitances. Furthermore, PDSOI and FDSOI MOSFETs provide a natural punch through effect mitigation due to the BOX which cuts parasitic carrier conduction paths in the active SOI layer depth. The BOX of SOI technologies is a fundamental device structure modification which can help mitigating parasitic effects introduced by device scaling.

## 2.6. 2010's: depleted active layer technologies: FinFET and Ultra-Thin SOI

Below 28 nm, improvements brought to planar bulk and SOI MOSFETs with strain or high-k/metal gate stacks were not sufficient to ensure proper MOSFET operations. The capacitive control provided by the gate in the active layer is not enough to well control the carrier transport between source and drain regions. Stronger electrostatic potential control of the gate over the conduction channel was required to improve it. Using extremely thin depleted silicon layers has enabled such an electrostatic control improvement in order to improve both electrical performances and power efficiency. To do so, two device structures are introduced in current leading edge technologies: the Ultra-Thin SOI (UTSOI) and the FinFET technologies. Pioneering studies began in the early 1980's for FDSOI technologies [53,54] before becoming UTSOI technologies [55,56], while multiple-gate transistors [57,58,59,60,61,62,63,64,65] and FinFETs [66,67,68] were actively investigated since the early 1990's. They are used in production since 2012 for the 22 nm technology node [69] with a bulk FinFET structure.

Both device structures provide a confined channel in a fully depleted active silicon layer. The one of UTSOI remains horizontal in a 2D single-gate planar architecture between the gate stack and the BOX while the one of FinFETs, usually named fin, is vertical and surrounded by the gate electrode in a "2.5D" architecture as presented in Figure 14. The specific FinFET shape leads to a double- or a triple-gate transistor where conduction channels can be formed along all the silicon-gate dielectric interfaces. The conduction channel is not limited to the top interface. Silicon finger sidewalls are also involved in the carrier conduction, enhancing the drive current vs device surface ratio. In other words, FinFETs provide a wider effective transistor width W (see Equation 1 and Figure 7) than in 2D planar devices. The FinFET effective width  $W = 2 \times H_{FIN} + W_{FIN}$  where  $H_{FIN}$  is the fin height and  $W_{FIN}$  the physical fin width.

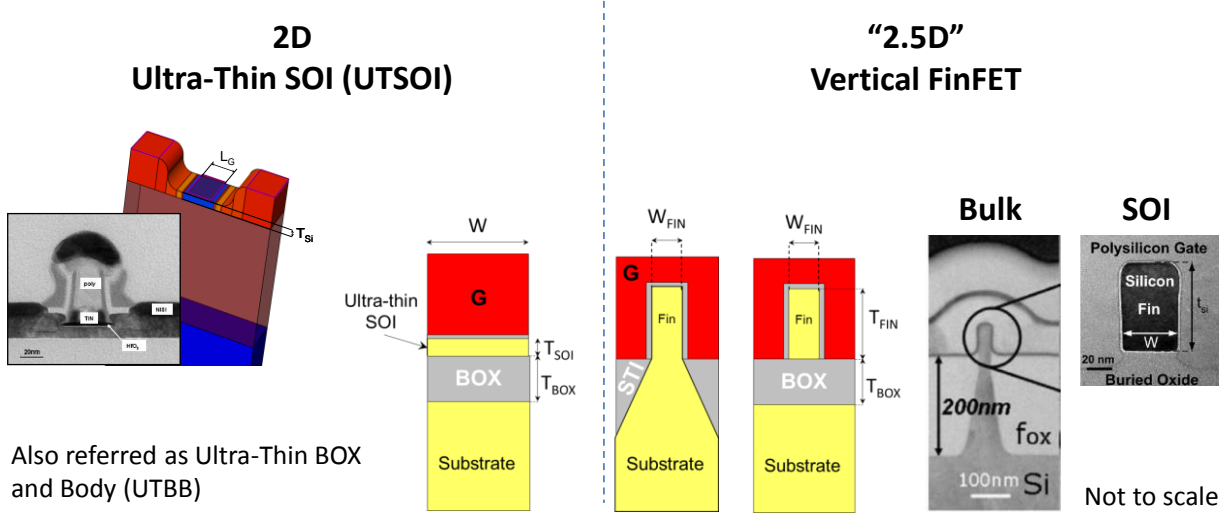


**Figure 14: Scanning Electron Microscopy (SEM) images and schematic descriptions of UTSOI [70] (left) and FinFET [71] (right) device structures.**

UTSOI and FinFETs have several advantages over standard planar technologies: reduced drain leakage currents for a strong SCE mitigation, well controlled electric fields, and reduced junction parasitic capacitances for faster devices. The main advantage of UTSOI is its enhanced energy efficiency which is ideal for low power applications, while FinFETs provide a high drive current vs density which is ideal for high performances.

### 2.7. Beyond the nanometer era: nanowires, 3D stacking and disruptive scaling

UTSOI technologies are used for technologies down to the 12 nm node [72] while the FinFET technology is currently developed for technologies down to the 10 nm [10,73] and even the 7 nm node [74], and technology roadmaps expect to push the FinFET architecture down to the 5 nm, and even to the 3 nm node [75]. Combining advantages of both UTSOI and FinFETs appears promising as demonstrated by multiple-gate nanowires [76,77,78], as well as using 3D stacking techniques capabilities [79] to increase the device density. It is worth noting that in such scenario the silicon-based MOSFET remain the basic device, even if it strongly differs from the initial one.

Other pathways are also envisioned for future electronics. Several concepts have been proposed such as the Tunnel FET [80,81] or quantum computation with qubits [82,83]. Beside basic device evolution, new memory concepts take part of such evolutions [84,85,86,87], particularly Non-Volatile Memories (NVM) of different natures, for instance Phase Change Random Access Memory (PCRAM), Conductive Bridge RAM (CBRAM) or Oxide-base RAM (OxRAM). No clear winner has been determined yet, but all these new NVM concepts can lead to significantly lower energy consumption with a strong co-integration. Doing this, neuromorphic computation architectures that can take inspiration from brain behavior are now envisioned using Resistive RAMs as synapses [88] to improve ICs computing capabilities. Silicon is finally a “magical” material for computing even if the active silicon area of elementary devices is now reduced to nanometer dimensions.

## 2.8. Insights into process variability issues

Integrating on one chip millions or billions of MOSFETs that all have the same electrical properties is a great challenge. This is hardly possible since almost all fabrication process steps used in microelectronics involve stochastic mechanisms which lead to variations. Process variability has several root causes but it is not a novel issue. It was already identified as a critical issue for microelectronic manufacturing in 1961 by W. Shockley [89]. It is even more challenging in leading edge technologies since new process variability sources arise with technology evolution.

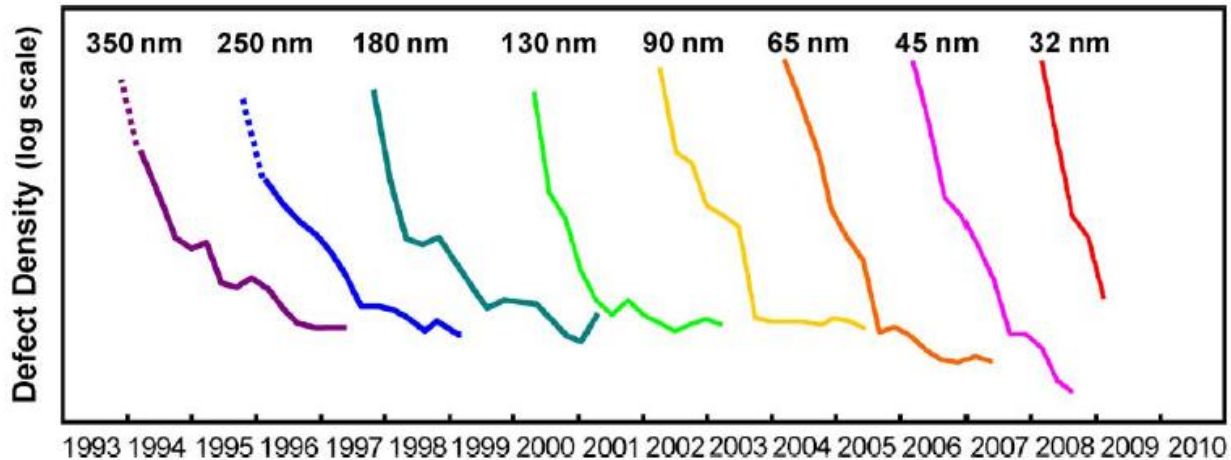


**Figure 15: Improvement in yield on process generations from 0.35 μm to 32 nm [90].**

Figure 15 (from [90]) represents the process yield evolutions on several process generations from 0.35 μm to 32 nm technologies. The yield improvement observed on each generation is achieved through innovations and continuous improvement strategies to mitigate process variations.

Systematic and random process variability sources are usually considered: systematic sources refer to the variation of the mean of a given parameter distribution with respect to its target value, while random sources can be defined as the statistical distribution around the mean target parameter as schematically presented in Figure 16.

Process variation sources are early identified during the microelectronic history such as patterning proximity effects [91], Line Edge/Width Roughness (LER/LWR) [92], polish variations or process variations from the gate dielectric due to Oxide Thickness Fluctuation (OTF) [93,94], fixed charges or traps. They are usually denominated as process variation "historical sources". They still exist in current fabrication processes but other sources of variations appear. They are considered as "emerging sources" of variations and include for instance Random Dopant Fluctuations (RDF) or Random Discrete Dopants [95], implant/anneal variations, strain induced fluctuations or Gate Material Granularity [96].

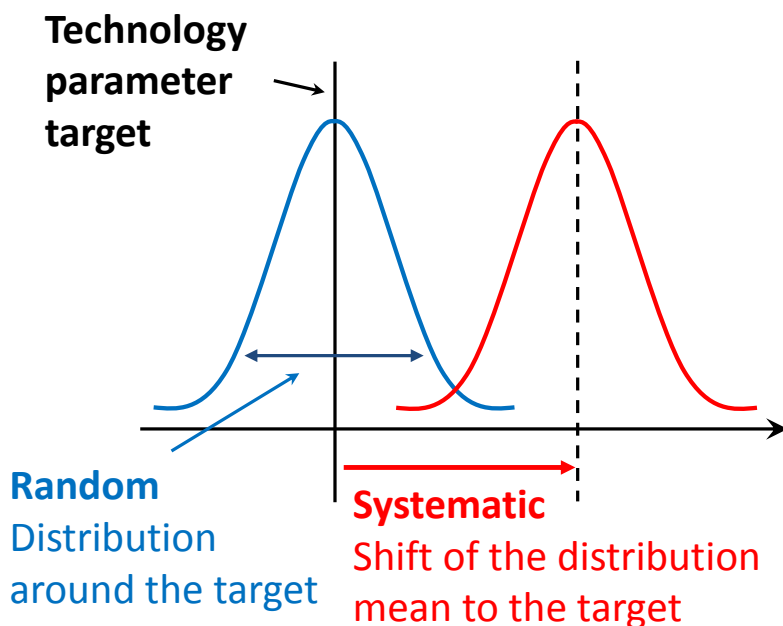


Figure 16: Description of systematic and random process variation sources.

For instance, RDF is induced by various doping implantation/anneal steps. Ion implantation is a highly probabilistic process on which the ion implantation profile into the silicon strongly depends. This is an emerging source of variation since mature technologies with long channels are weakly sensitive to “single” dopant atoms diffusing into the channel region or to small variations of the source/drain doping profiles. Such an assumption becomes more and more erroneous with technology scaling. In technologies with large feature sizes, doping profiles look like smooth Gaussian or exponential shapes while they seem much more discretized in deep submicron technologies.

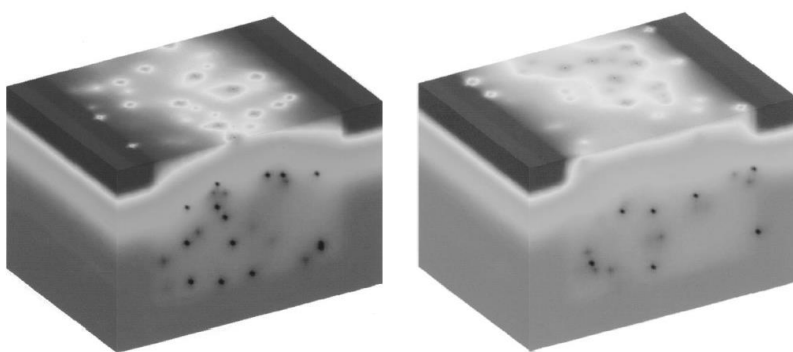
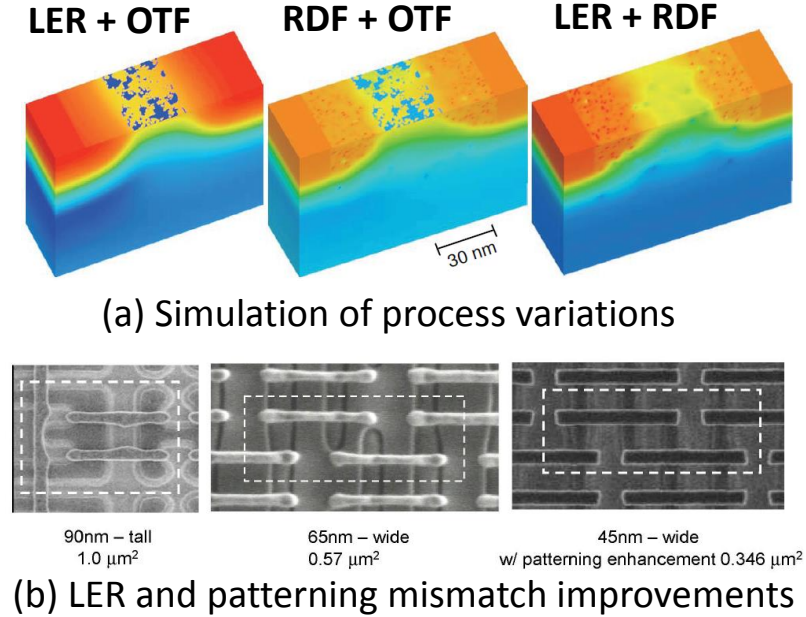


Figure 17: Potential distribution at the Si/SiO<sub>2</sub> interface of two microscopically different MOSFET's. Both have 170 dopant atoms in the channel depletion region but leads to threshold voltages V<sub>TH</sub> of either (left) 0.78 V or (right) 0.56 V (from [97]).

Figure 17 gives an example of 3D calculations of the electrostatic potential in a 50 nm x 50 nm MOSFET [97]. It includes 170 dopant atoms in the depletion channel region. They are differently distributed which results in large MOSFET threshold voltage differences.



**Figure 18: (a) Simulations of different sources of variations implications (Line Edge Roughness LER, Oxide Thickness Fluctuations OTF and Random Dopant Fluctuations RDF) on the electrostatic potential in a 35 nm x 35 nm MOSFET (from [98]), and (b) examples of LER and patterning mismatch improvements in 90 nm, 65 nm and 45 nm technologies (from [99]).**

Figure 18 shows (a) simulations of different combinations of process variations implications induced by LER, OTF and RDF on the electrostatic potential inside a MOSFET [98] while (b) exhibits examples of LER improvements from the 90 nm to the 45 nm technology [99] thanks to lithography tools enhancements.

Process variations have various implications on device electrical characteristics. As previously mentioned, they usually modify the MOSFET electrostatic behavior which leads to  $V_{TH}$  variations. This is why  $V_{TH}$  is often used as the main electrical parameter to benchmark process variations. This is also a key parameter because some others derive from  $V_{TH}$  such as  $I_{ON}$  or  $I_{OFF}$  of MOSFETs, but also the minimum operating voltage  $V_{CCmin}$  or the Static Noise Margin (SNM) of Static Random Access Memory (SRAM) cells.  $V_{TH}$  (or  $V_{CCmin}$ ) can be extracted from various devices such as MOSFET arrays [100], SRAM cells matrices [101], or Ring Oscillators (RO) [102] as exhibited in Figure 19.  $V_{TH}$  standard deviation measurements performed in ring oscillators (cf; Figure 19(c)) of various technologies from 0.13  $\mu\text{m}$  to 32 nm highlight an almost constant systematic process variation while the random sources increases from 0.13  $\mu\text{m}$  to reach a maximum at the 65 nm node before dropping since the 45 nm node. The 65 nm node is the last which uses extremely thin SiON gate dielectrics with doped polysilicon gate material, which are highly sensitive to Oxide Thickness Fluctuations. By contrast, the 45 nm node uses much thicker high- $k$  dielectrics along with novel lithography tools

which mitigate LER. These innovations strongly improve the random variations that would otherwise increase with technology scaling if no additional solution is introduced in the fabrication process of more integrated technologies.

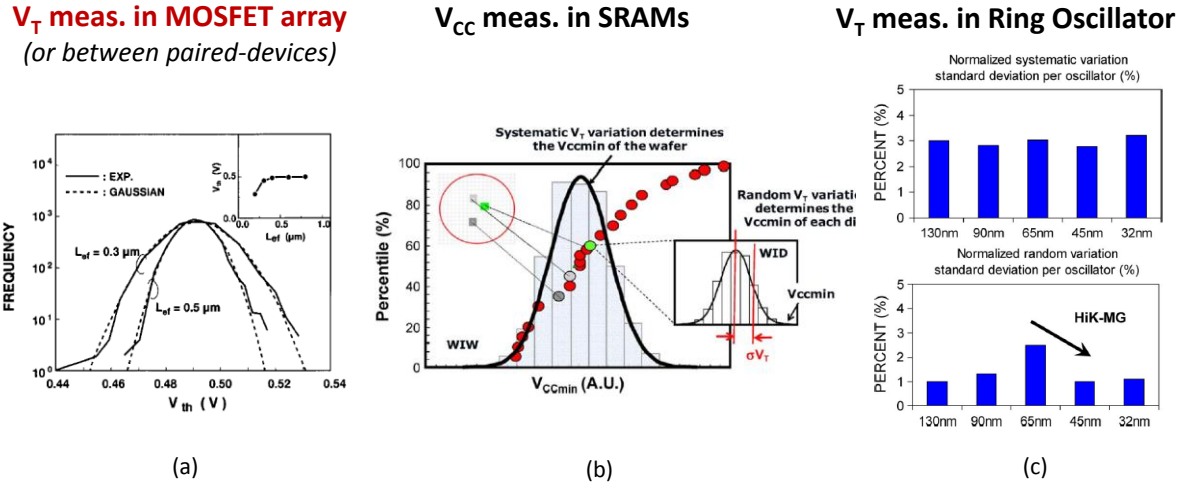


**Figure 19: Examples of (a) measured  $V_{th}$  distributions in MOSFET arrays [100], (b)  $V_{CCmin}$  in SRAMs [101], and (c)  $V_{th}$  in ring oscillators [102].**

Consequently, the random threshold voltage variation expressed by its standard deviation  $\sigma_{V_T}$  (or  $\sigma_{\Delta V_T}$ ) appears as an appropriate metric to estimate process variability. Analytical expressions are required to take into account major process parameters such as the dopant density, their position, the gate oxide thickness, etc. This is first proposed by Pelgrom in 1989 [103] where  $\sigma_{V_T}$  is expressed as function of the inverse square root of the MOSFET width and length product.

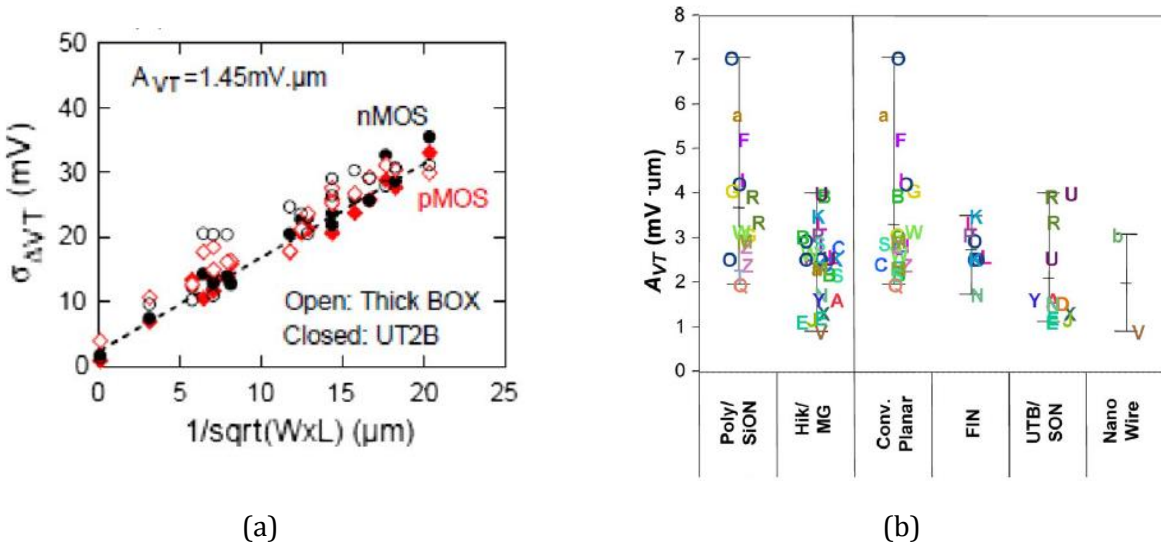


**Figure 20: (a) AVT plot obtained for UTSOI transistors (from [104]) and (b) a compilation of AVT parameters for different technologies (from [90]).**

The resulting  $\sigma_{V_T}$  vs  $1/\sqrt{W \cdot L}$  is usually named a “Pelgrom plot” or “Avt” plot since its slope is called  $A_{VT}$ : the higher the  $A_{VT}$ , the higher are the process variations. An  $A_{VT}$  plot (from [104]) is

shown on the Figure 20(a) as well as a compilation of  $A_{VT}$  parameters as a function of technology in Figure 20(b) (from [90]). It highlights that technologies with most advanced processes, such as UTSoI, FinFETs or nanowires, exhibit lower variability than conventional planar technologies. Their low process variability is also the result of using depleted channel without doping implants. This is highlighted by UTSoI transistors while FinFETs show slightly higher  $A_{VT}$  which could be attributed to fin edge roughness in these first FinFETs. Variability is still a hot topic for leading edge and future technologies manufacturing. A lot of modeling and simulation efforts are performed to predict the process variability of different options such as bulk or SOI-based FinFETs or nanowires.

## 2.9. Microelectronic technologies: some keypoints

More than 50 years of technology innovations have turned the bulk silicon MOSFET of several micrometers dimensions into nanometer scaled devices made of multiple-gates and extremely thin depleted layers. Billions of MOSFETs are integrated in typical ICs which are the computing cores of mobile phones or laptops. The silicon-based MOSFET is still the basis but numerous aspects have changed:

- Materials: metal gates, high-k dielectrics, SiGe source/drain regions, strained semiconductors instead of doped polysilicon,  $\text{SiO}_2$ , Si source/drain and relaxed silicon respectively.
- Geometry and architecture: Ultra-thin SOI and “2.5D” FinFETs are now leading edge technologies but they probably represent just a temporary step before more 3D integration.
- Variability is always a major issue for micro- and nano-electronic manufacturing since the first developed MOSFET technology. Novel sources of variability can emerge each time changes are brought to fabrication processes. On the one hand, technologies can become sensitive to variability sources due to device scaling as demonstrated for Random Dopant Fluctuations or Random Discrete Dopants. But on the other hand, innovations may mitigate the impact of variability sources as already observed with the introduction of high-k dielectrics that are thicker, and so less sensitive to oxide thickness fluctuations, than former extremely thin  $\text{SiON}$  or  $\text{SiO}_2$  gate dielectrics.

Such MOSFET evolutions define reliability challenges which can be of different natures: electrically driven [105,,106,107,108], induced by elevated or low temperatures [109,110], dependent on the moisture environment [111] or induced by radiation environment [112] which is detailed in the following sections.

### 3. Radiation Effects in Ultra-Scaled MOSFETs

#### 3.1. Basic radiation effects in devices and ICs

Microelectronic devices and ICs which operate in radiation environments are exposed to ionizing particles that can include neutrons, protons, electrons, heavy ions, photons... , radiation effects in electronics occur when such particles strike a target medium where they can lose part (or all) of their energy [108]. They can lose energy either through ionizing or non-ionizing processes. Basically, ionizing processes produce electron-hole pairs while non-ionizing processes displace atoms. Ionizing energy loss creates free charges while non-ionizing energy creates displacement damages, both altering material and device properties. These basic mechanisms lead to several major radiation effects in electronics presented in Figure 21 (Transient Radiation in Electronics Effects (TREE) is also a major concern for radiation effects in electronic but it is not addressed in these short course notes).

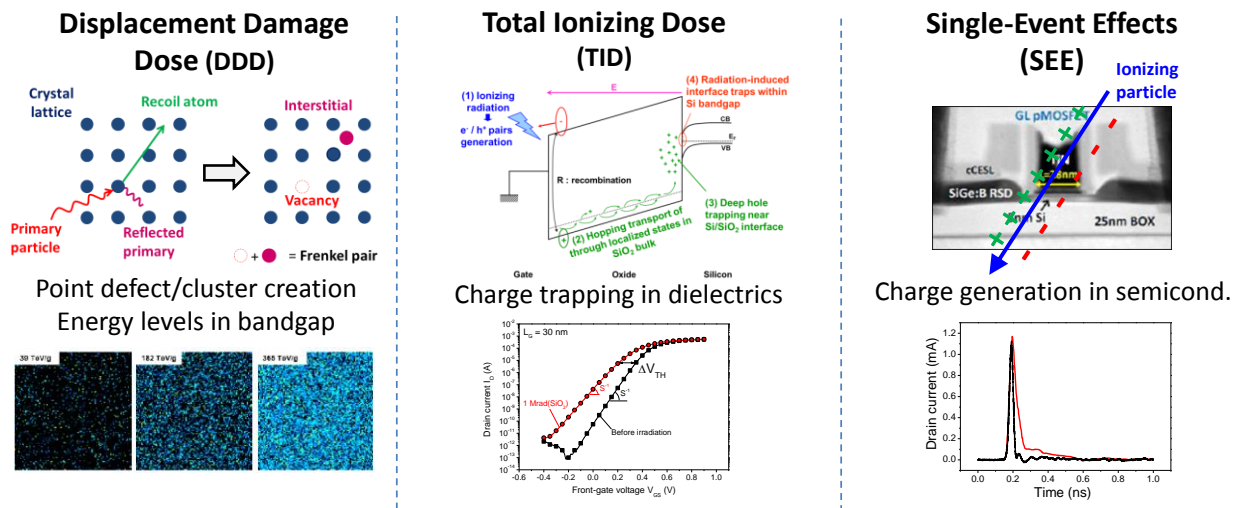
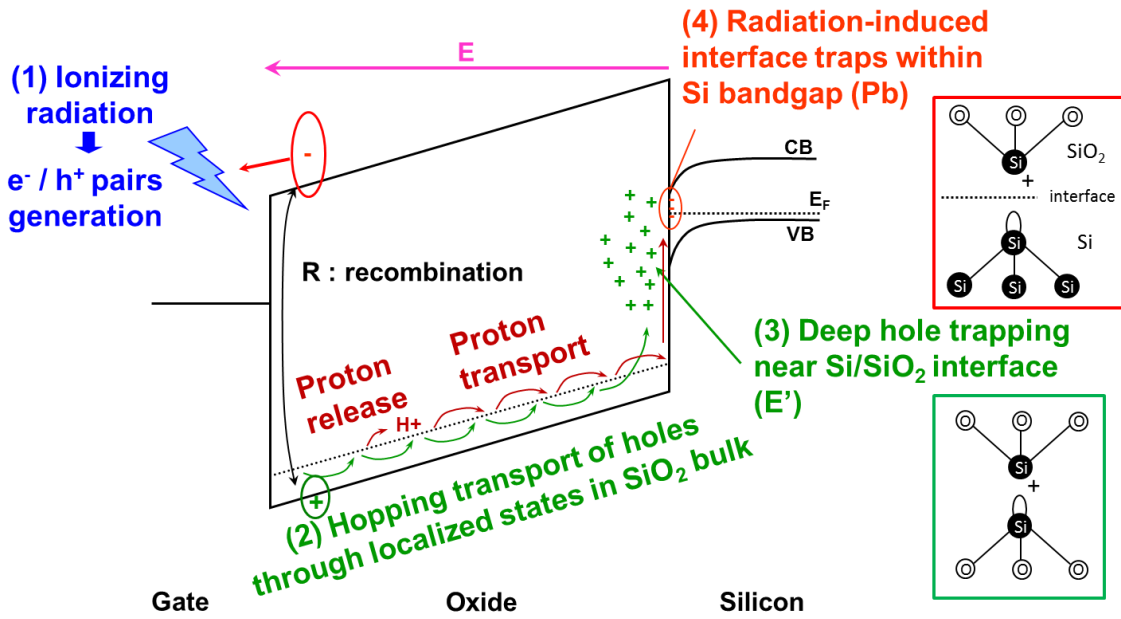


Figure 21: Summary of major radiation effects induced in electronic devices and ICs (images after [113,114,115,116,117,118,119]).

Displacement Damage Dose (DDD), also referred to as Total Non-Ionizing Dose (TNID), effects occur when a primary particle strikes an atom from the target material which is displaced from its initial location. Recoil and reflected atoms are generated leading to the formation of a vacancy and of an interstitial in the silicon crystal lattice, a combination known as Frenkel pair. This is a major issue in electronic devices governed by volume carrier conduction such as PN diodes, PiN diodes, BJT or Active Pixel Sensors (APS). They can create generation/recombination currents which can modify electrical characteristics. For instance, neutron-irradiated BJTs usually suffer from generation currents in the base region which can dramatically decrease their current gain [120]. The same root cause in APS may lead to a dramatic increase of their dark current, the onset of bright pixels or unstable pixels due to Random Telegraph Signal phenomenon [121]. CMOS technologies are usually considered weakly impacted by DDD since they are driven by surface carrier conduction [120].

Single-Event Effects (SEE) are triggered when single ionizing particles randomly strike the active area of an electronic device. Electron-hole pairs are created in the semiconductor active region and then collected by biased electrodes. This leads to current transients which may induce destructive events, such as the aforementioned latch-up or the Single-Event Burnout (SEB) in power MOSFETs [122], or non-destructive events such as Single Event Upsets (SEU) in SRAMs [123]. SEE are thoroughly detailed in part II of this short course.

Total Ionizing Dose (TID) effects are induced by ionizing particles which create electron-hole pairs in dielectrics of electronic devices. A band diagram of a biased Metal-Oxide-Semiconductor is presented in Figure 22 to highlight the successive phenomena which occur during a TID irradiation.



**Figure 22: Total ionizing dose effect described in the band diagram of biased Metal-Oxide-Semiconductor structure (after [115,116]).**

(1) Electron-hole pairs are generated depending on the incident particle energy. Some of them quickly recombine. Electron-hole pairs are separated thanks to the electric field which stands into the oxide. Electrons are evacuated from the oxide thanks to their high mobility while (2) the fraction of unrec combined holes are transported along the electric field lines through localized states in  $\text{SiO}_2$  bulk. At the same time, protons are released and transported to the  $\text{SiO}_2$ -Si interface. (3) Holes are finally trapped at pre-existing oxygen vacancies, which relax after hole capture to form  $E'$  centers [124,125] while hydrogen transport is involved in (4) interface traps buildup in the silicon bandgap at the  $\text{SiO}_2$ -Si interface. In  $\text{SiO}_2$ , net oxide trapped charge is positive while interface traps can be either filled with electrons or holes depending on the MOSFET type. Despite the important literature available on interface traps [126,127,128], some open questions still remain particularly for interface traps buildup modeling [129,130,131,132,133]. Border traps buildup may also be generated [126]. These are oxide traps which can exchange charges in the time frame of an electrical measurement, so acting as interface traps. MOSFETs may be highly sensitive to TID effects

since their active area is totally surrounded by dielectrics made of the gate oxide, field oxides, spacers, capping layers or the BOX in SOI technologies.

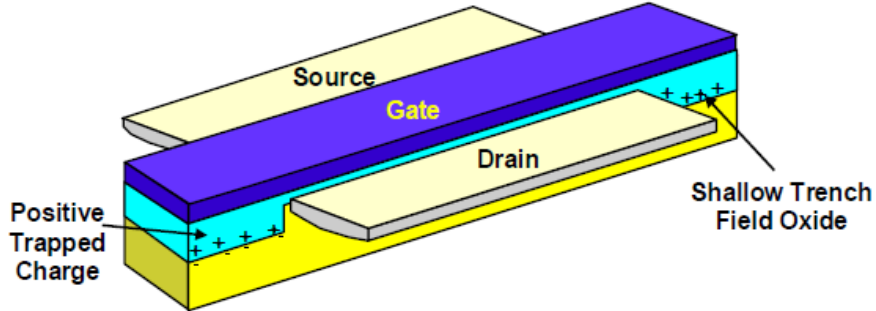


Figure 23: Cross-section view of a STI isolated bulk silicon MOSFET (after [134])

### 3.2. TID effects in bulk silicon MOSFETs

As described in section 3.1, TID effects in MOS devices are governed by both bulk positive charge trapping in oxides and buildup of interface traps at Si-SiO<sub>2</sub> interfaces. The MOSFET TID response is thus governed by the electrostatic impact of such phenomena on the carrier conduction.

Figure 23 shows a cross-section view of a bulk silicon MOSFET which uses Shallow Trench Isolation field oxides. In highly integrated MOSFETs, radiation-induced charge trapping in such thick field oxides is the major contributor to the bulk MOSFET TID response while the thin gate oxide is not a major issue anymore [134,135].

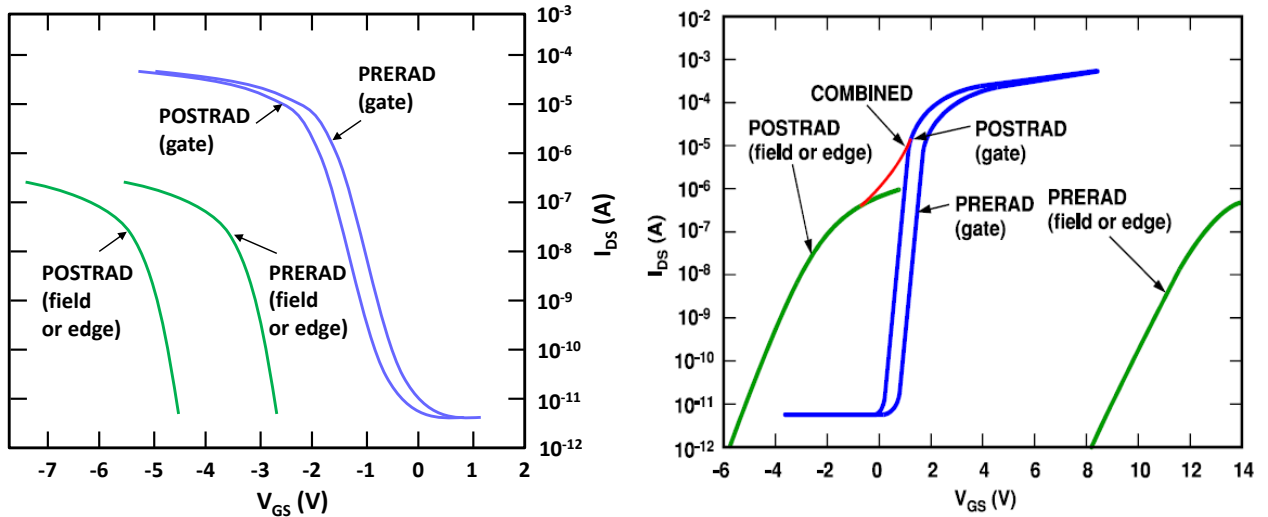
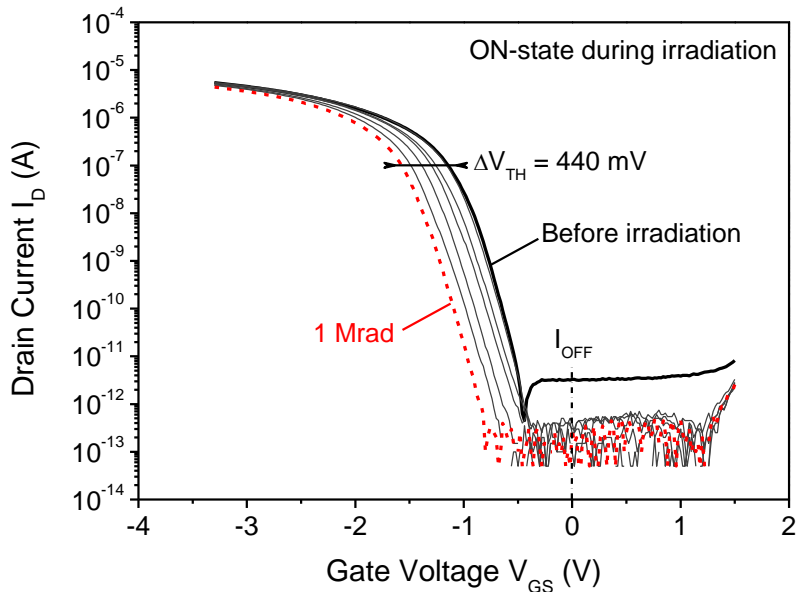


Figure 24: Illustration of TID induced effects on bulk silicon (a) PMOSFET and (b) NMOSFET ID-VGS curves. A parasitic lateral transistor (green curve) in the NMOSFET appears in addition to the I-V shift (blue curves) induced by charge trapping in the gate oxide (after [112]). The PMOSFET does not suffer from parasitic edge transistor.

Charge trapping in thin gate oxides ( $T_{GATEOX} < 2 \text{ nm}$ ) is not high enough to modify significantly the surface potential into the conduction channel, and then to induce a large electrical characteristics

shift. In contrast, charge trapping into the STI can trigger parasitic conduction paths at the MOSFET edges [136]. I-V characteristics of parasitic edge (or lateral) transistors are shifted with TID faster than those of the main MOSFET leading to the onset of a “shoulder” on the MOSFET  $I_D$ - $V_{GS}$  curves as exhibited in Figure 24. The drain leakage current increases sharply which strongly degrades the  $I_{ON}/I_{OFF}$  ratio. These phenomena have been reported in several types of field oxide isolated MOSFET, such as those used in LOCOS isolation [137]. Such phenomena are observed only in NMOSFET. PMOSFETs cannot be impacted since the parasitic edge transistor is shifted farther from its main I-V curve, because net trapped charges in  $\text{SiO}_2$  isolation oxides are nearly always net positive.

Since mid-2000's [138,139], enhanced susceptibility to TID is observed in deep-submicron technologies. Radiation-Induced Narrow Channel Effects (RINCE) [138] has been observed in narrow MOSFETs [140]. RINCE has the same root origin as parasitic edge transistors, *i.e.* positive charge trapping in field oxides, but different consequences. In narrow bulk silicon MOSFETs, charge trapping in field oxides not only modifies the electrostatic potential at the transistor's edges, but also into the whole width of the conduction channel. This leads to significant voltage shifts  $\Delta V_{TH}$  of  $I_D$ - $V_{GS}$  curves. Both PMOSFETs and NMOSFETs can be sensitive to RINCE, contrary to the onset of parasitic edge transistors, since it impacts the surface potential in the whole conduction channel region. An example of  $I_D$ - $V_{GS}$  curves exhibiting RINCE in a PMOSFET is presented in Figure 25.



**Figure 25: ID-VGS curves obtained on a bulk silicon PMOSFET at several total dose steps. ID-VGS curves are presented for a narrow transistor with  $W = 0.24 \mu\text{m}$  (after [140]).**

The aforementioned voltage shifts induced by TID on I-V curves are due to the net positive charge trapping in dielectrics. Furthermore, interface traps buildup can also occur in addition to the radiation-induced oxide trapped charge contribution.

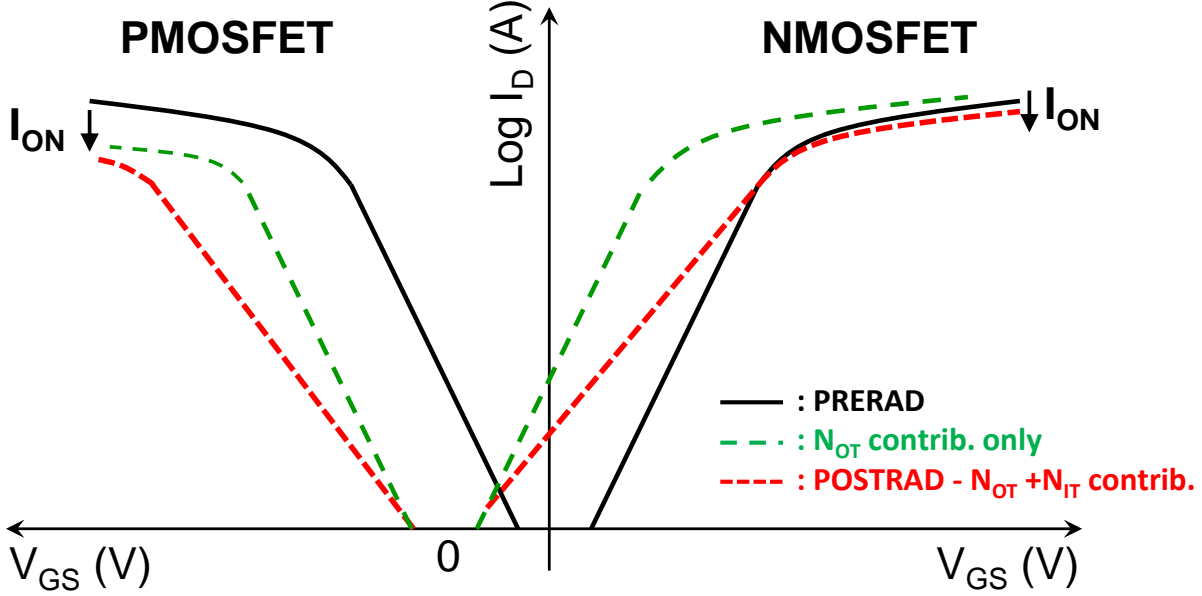


**Figure 26: Radiation-induced oxide trapped charge (green dash) and interface traps (red short dash) contributions on I-V curves in PMOSFET and NMOSFETs.**

Figure 26 shows the contribution of interface trap buildup at the gate oxide-silicon interface on the  $I_D$ - $V_{GS}$  curves of bulk silicon MOSFETs in addition to the one of oxide trapped charges. Interface traps buildup acts as a parasitic to the main conduction channel increasing the subthreshold swing  $S^{-1}$ . Interface traps are either positively or negatively charged in PMOSFET and NMOSFET respectively which increases the TID induced threshold voltage shift in PMOSFETs while it apparently mitigates it in NMOSFETs. Interface trap buildup is a slow process. Its evolution across time is widely investigated [141,142] and requires to test devices in appropriate conditions [143] to get their impact on device response.

### 3.3. Insights into “high” TID – up to several MGy - effects in MOSFETs

Besides usual TID effects presented in 3.3, some applications require huge TID assessments for devices. This may be encountered for high energy physics, fusion experiments, nuclear waste management or incidental conditions in nuclear power plants. In those conditions, several MGy can be reached which requires testing devices under highly aggressive TID environments. Some studies are done in the late 1980's for high energy physics applications [144,145]. Such data are updated since the 2000's for the Large Hadron Collider application [138] or after the Fukushima power plant incident [146]. Since then, several efforts have been performed to determine whether or not electronic devices, ICs and systems may operate in such MGy dose environments [147]. Novel effects are observed in such high TID environments that were referred to as Radiation Induced Short Channel Effects (RISCE) [148]. An explanation of mechanisms governing the high-TID response of a 65 nm technology is proposed recently by F. Faccio et al. [149]. It relies on possible enhanced charge trapping in the spacer region which plays a strong role in the conduction channel buildup, particularly close to the Lightly Doped Drain (LDD) regions, as already primarily observed

by. S. Gerardin et al. [150]. These effects still need investigations with dedicated test structures to fully understand the basic mechanisms triggered at high TID.

### 3.4. TID effects in SOI technologies

The additional dielectric, *i.e.* the BOX, in SOI technologies compared to bulk silicon technologies, may be a source of TID induced effects. Positive oxide charge trapping in the BOX of SOI technologies has various consequences depending on the SOI technology type.

In PDSOI technology, charges trapped in the BOX can trigger a parasitic conduction path at the back side of the active silicon layer as described in Figure 27(a). This phenomenon is usually named parasitic back transistor. The back transistor is constituted by the SOI layer as the active area and its gate stack is made of the BOX and of the silicon substrate as “gate” dielectric and gate material respectively. An example I-V characteristic is presented in Figure 27(b) (left). It is shifted to negative back gate voltages due to positive charge trapping into the BOX.

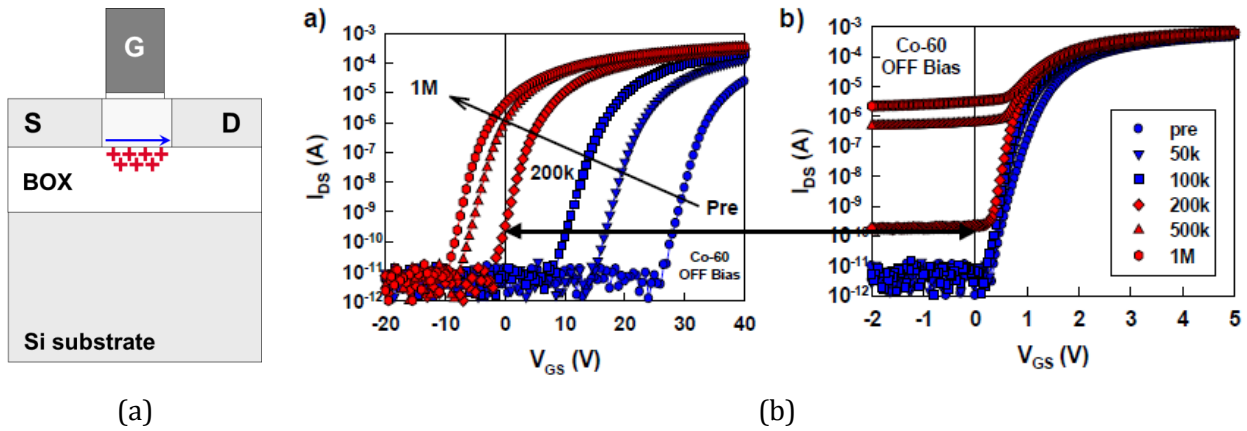


**Figure 27:** (a) schematic description of positive charge trapping into the BOX which induces a parasitic conduction path at the back-side of the SOI active layer and (b) back (left) and front-gate (right) I-V curves at several TID steps in a PDSOI NMOSFET (after [151]).

Its impact on the front-gate characteristic can be extracted for 0 V applied to the back-gate voltage. This is highlighted by the arrow between the front- and the back-gate I-V curves in Figure 27(b) where the leakage current of the back-gate transistor is identical to that in the front-gate I-V curve. The parasitic back transistor appears as a drain leakage current plateau which increases with TID [152,153,154] (cf. Figure 27(b) right) [151].

In FDSOI technologies, the consequences of charge trapping into the BOX on I-V curves differ from the one described in PDSOI transistors because of capacitive coupling effects [53] between the front- and the back interfaces of the FDSOI layer. This is highlighted in Figure 28 as well as its consequence on the front-gate  $I_D$ - $V_{GS}$  curve of FDSOI NMOSFET. In FDSOI transistors, positive charge trapping in the BOX are coupled to the front surface potential since the transistor’s “body” is fully depleted from free carriers. The front-gate surface potential at the SOI-gate oxide interface directly depends on the one at the SOI-BOX interface [155,156,157].

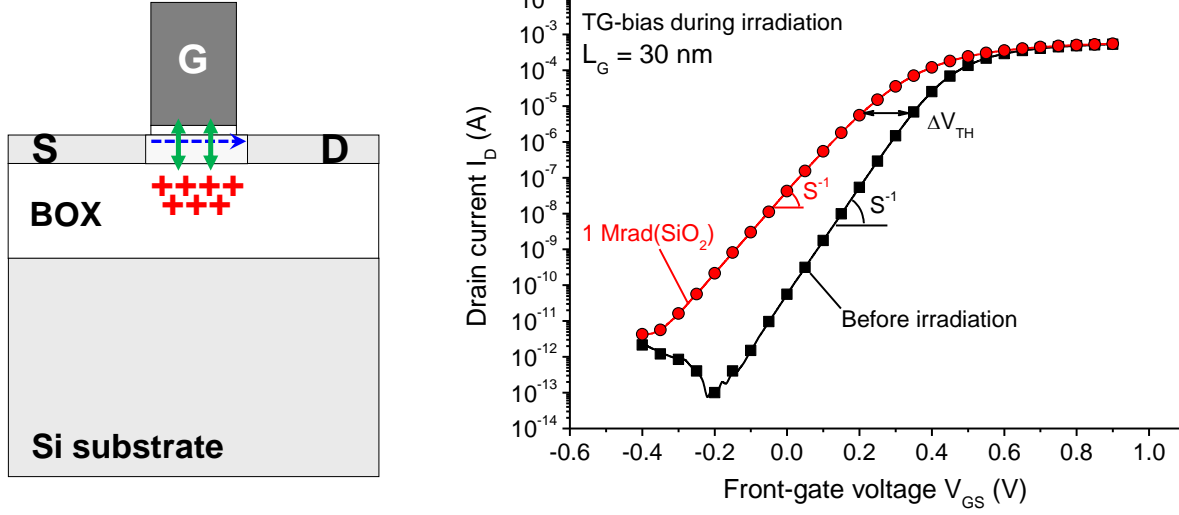


**Figure 28:** (a) Schematic description of positive charge trapping in the BOX of a FDSOI MOSFET, green arrows highlighting capacitive coupling effects between the front- and back interfaces. (b) Consequence of positive charge trapping into the BOX on front-gate ID-VGS curves of a FDSOI transistor (after [118]).

In other words, any modification of the surface potential at one SOI interface has an impact on the one at the opposite side of the SOI layer. For instance, biasing the substrate leads to shift the front-gate  $I_D$ - $V_{GS}$  curves either to negative  $V_{GS}$ , for positive back-gate bias, or to positive  $V_{GS}$ , for negative back-gate bias. Positive charge trapping into the BOX has similar consequences as back-gate biasing: it shifts the front-gate I-V curves through electrostatic coupling effects. This is shown in Figure 28(b) where front-gate I-V characteristics of a NMOS FDSOI transistor are plotted. They exhibit both a significant negative  $\Delta V_{TH}$  induced by coupling effects previously mentioned and also a slight degradation of the subthreshold swing  $S^{-1}$  that is attributed to interface trap buildup. TID-induced voltage shifts can reach relatively high values, about 100 mV, related to the nominal voltage used for such highly integrated technologies (between 0.8 V and 1.1 V for UTSoI technologies below 30 nm).

Mitigating such effects is not an easy task in FDSOI technologies since doping the active layer is avoided to improve electrical performances. Thinning the BOX could be effective to achieve reduced TID-induced shifts [158] in FDSOI transistors even if using a thinner BOX theoretically enhances coupling effects. This is investigated in [118] where a  $\Delta V_{TH}$  trend versus MOSFET gate length for three BOX thicknesses is given (see Figure 29). The TID tolerance is improved with BOX thinning but it is not as large as it could be expected. The BOX is thinned from  $T_{BOX} = 145$  nm down to  $T_{BOX} = 11$  nm while the maximum  $\Delta V_{TH}$  is only reduced by less than a factor of two.

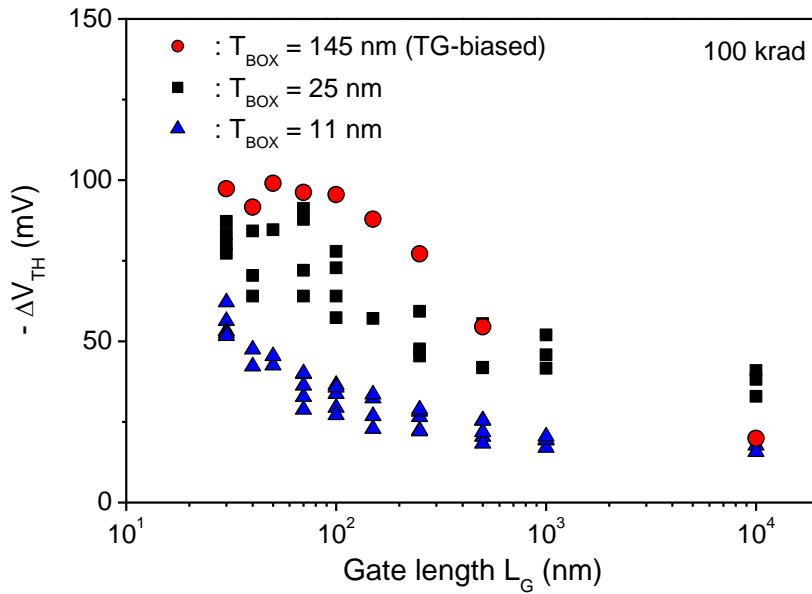


**Figure 29: Negative threshold voltage shift vs gate length measured on FDSOI transistors with three BOX thicknesses TBOX = 145 nm (red circles), TBOX = 25 nm (black squares) and TBOX = 11 nm (blue triangles).**

Additional TID mitigation strategies should be investigated to ensure reliable operations of FDSOI technologies in order to optimize their entire features to withstand radiation environments since they exhibit high SEE tolerance due to small sensitive volumes to incident ionizing particles [159]. Planar FDSOI technologies have other interests since bonding processes developed for SOI technologies have been demonstrated to be suitable for 3D integration. One TID effect study performed in a 3-tier FDSOI IC has demonstrated that TID effects are similar whatever the considered tier [160] which makes 3D integrated devices promising for both radiation effects and to increase IC integration density.

### 3.5. TID effects in multiple-gate technologies: FinFET and nanowires

#### 3.5.1.SOI multiple-gate FETs

Multiple-gate transistors are now widely used in leading edge technologies. Bulk FinFETs are currently the major MOSFET structure to meet requirements of future technology nodes down to 7 nm-5 nm. Even more 3D scaled device structures are envisioned to go further into device scaling, nanowires being promising candidates. Before that, TID-effects investigations in multiple-gate transistors began in the early 1990's, in the so-called Gate-All Around (GAA) transistor [161,162,163]. These first TID effect studies are followed more than one decade later by a succession of dedicated studies [164,165,166,167,168,169,170,171,172] with the growing interest of multiple-gate technologies for process technologies, most of them being based on SOI technologies.

Figure 30 summarizes results obtained by several research groups in various SOI multiple-gate MOSFET designs exposed to ionizing radiation. All studies report a strong geometrical dependence of the TID sensitivity. The fin width plays a major role in the TID response: the narrower is the fin, the higher is the TID tolerance.

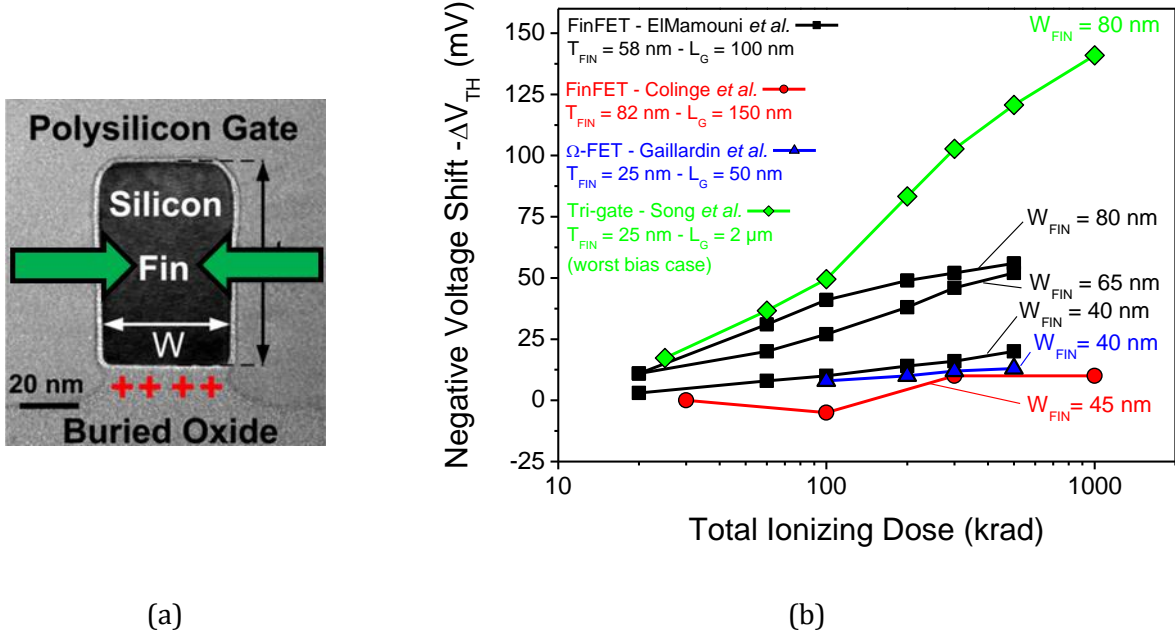


Figure 30: (a) Scanning electron microscopy image of a SOI FinFET gate cross-section and (b) summary of TID induced threshold voltage shifts extracted in different multiple-gate NMOSFETs (after [165,166,168,170]).

In narrow SOI multiple-gate FETs, lateral gates efficiently control the electrostatic potential into the fin which mainly screens any external sources of potential modifications such as those induced by trapped charges into the BOX. I-V characteristics are weakly impacted by TID which demonstrate the intrinsic TID tolerance of such narrow multiple gate devices.

In contrast, lateral gates do not play a significant role in wide SOI multiple-gate FETs. They behave as planar FDSOI transistors after TID exposure: coupling effects between the front- and the back-interface of the SOI layer dominate the transistor's TID response which exhibits a significant threshold voltage shift.

### 3.5.2.Bulk FinFETs

Besides SOI multiple-gate MOSFET investigations, the bulk FinFET advent [173] since the early 2010's has motivated radiation effects studies in such technologies [174,175]. Here again, the TID response is mainly driven by the fin width. No significant threshold voltage shift is observed in bulk FinFETs. TID mainly impacts their I-V characteristic by increasing the OFF-state leakage current (see Figure 31(b)). Charge trapping in field oxides made of STI (see Figure 31(a)) leads to a effect similar to that observed in planar bulk MOSFETs (see section 3.2): a parasitic lateral transistor is triggered. However, no RINCE seems to occur despite the extreme fin narrowness which means that

the surrounding gate has enough electrostatic potential control over the conduction channel to avoid such TID-induced effect compared to planar MOSFETs.

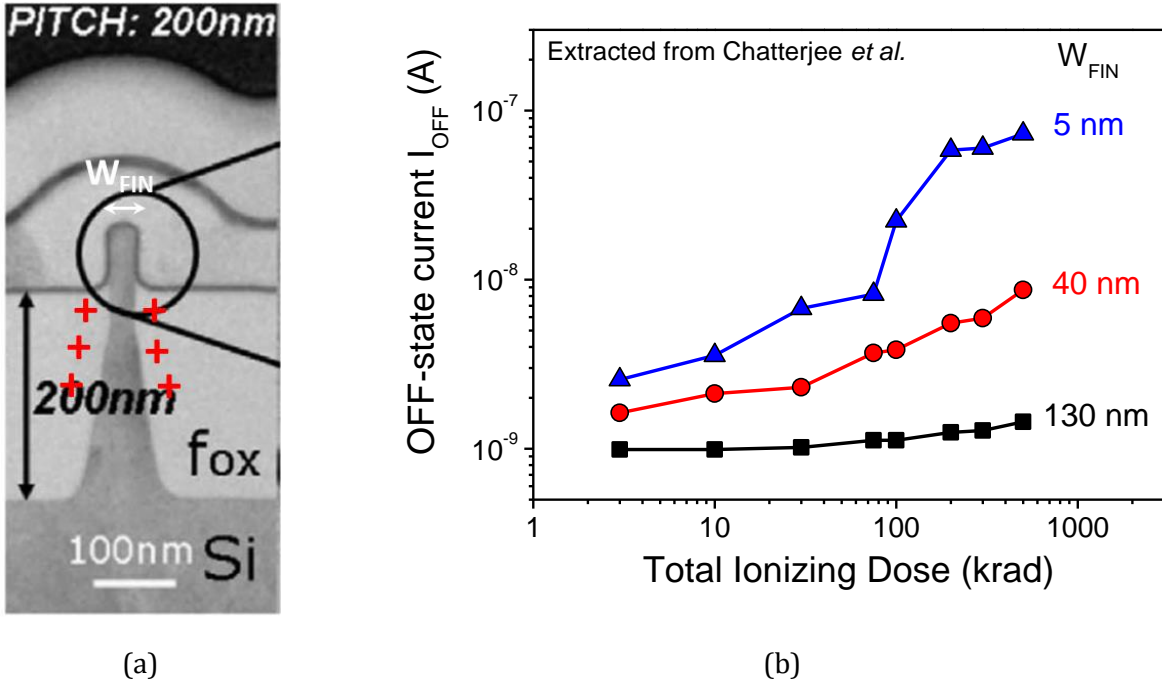


Figure 31: (a) Scanning electron microscopy image of a bulk FinFET in a gate cross-section and (b) TID induced OFF-state drain leakage vs TID in bulk NMOS FinFET (after [175]).

One should note that the TID sensitivity has an opposite geometrical behavior in bulk FinFETs than in SOI multiple-gate FETs. Narrow bulk FinFETs are more TID sensitive than their wide counterparts while narrow SOI multiple-gate MOSFETs exhibit high tolerance to TID.

### 3.5.3.Nanowires (on SOI)

Shrinking device dimensions to several nanometers in all space dimensions makes MOSFETs nanowire-shaped. As for multiple-gate MOSFET, such research devices are currently fabricated on SOI. Their objectives are to combine in one device design advantages of both UTSoI and FinFET structures: a reduced active depleted silicon area wrapped in the gate stack. Their TID behavior has been investigated for about a decade. Their TID response has strongly evolved with improvements in fabrication processes. Most recent GAA nanowire FETs present high TID tolerance while pioneering works report significant threshold voltage shifts as shown in Figure 32 (after [176,177,178] and summarized in [179]).

Nanowires should exhibit weak TID sensitivity since active NanoWire-FET (NWFET) parts should have interfaces only with extremely thin dielectrics which may not trap large amount of charges. Such an expected TID response is highlighted for instance in [177] which demonstrates an almost "0 V" threshold voltage shift even after a 1 Mrad( $\text{SiO}_2$ ) irradiation. But despite their nanowire structures, such studies always focus on NMOS NWFETs, and sometimes not nanometer scaled in all the three dimensions.

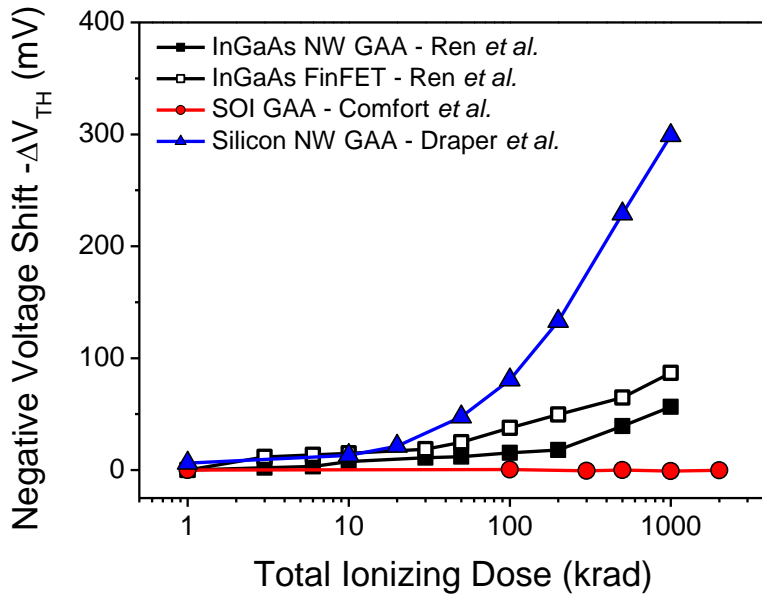


**Figure 32: Summary of TID induced threshold voltage shifts extracted in GAA nanowire FETs (after [176,177,178]).**

In recent years, some papers dealt with TID effects in SOI multiple-gate NWFETs [180,181,182]. Both NMOS and PMOS NWFET are investigated using systematic I-V studies to get the TID properties of such devices. Such NWFETs have extremely reduced dimensions:  $T_{SOI} = 12 \text{ nm}$ ,  $W_{NW} = 15 \text{ nm}$  and  $L_G = 24 \text{ nm}$  as described in Figure 33. NMOS NWFET exhibit usual TID behavior of SOI multiple-gate FETs with a strong dependence on the silicon nanowire width and gate length. Narrow NWFETs are still weakly sensitive to TID effects.

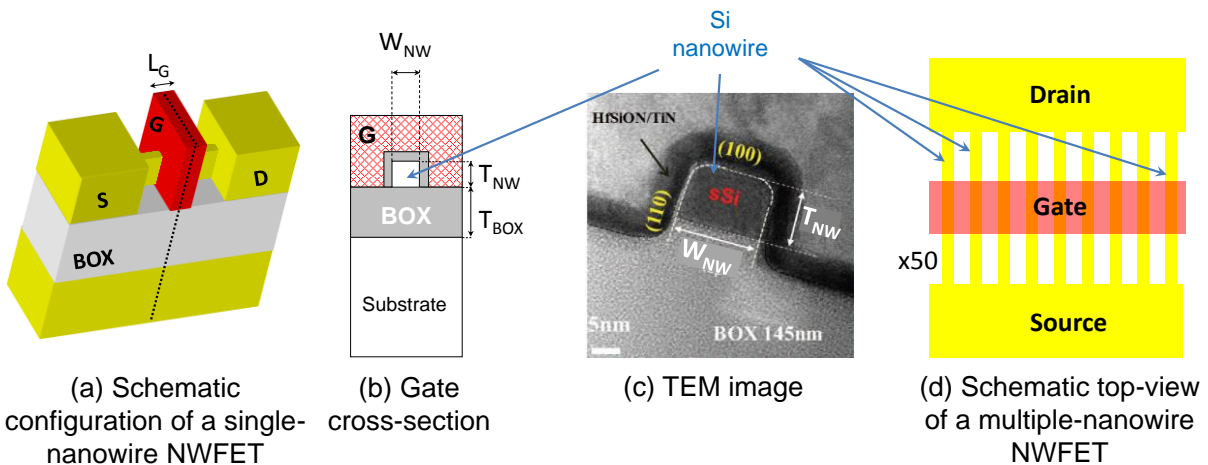


**Figure 33: Schematic description of NanoWire Field-Effect Transistors (NWFET): (a) a schematic configuration of a single-nanowire NWFET, (b) a schematic gate cross-section, (c) a TEM image, (d) a top-view of a 50-parallel nanowires NWFET [78].**

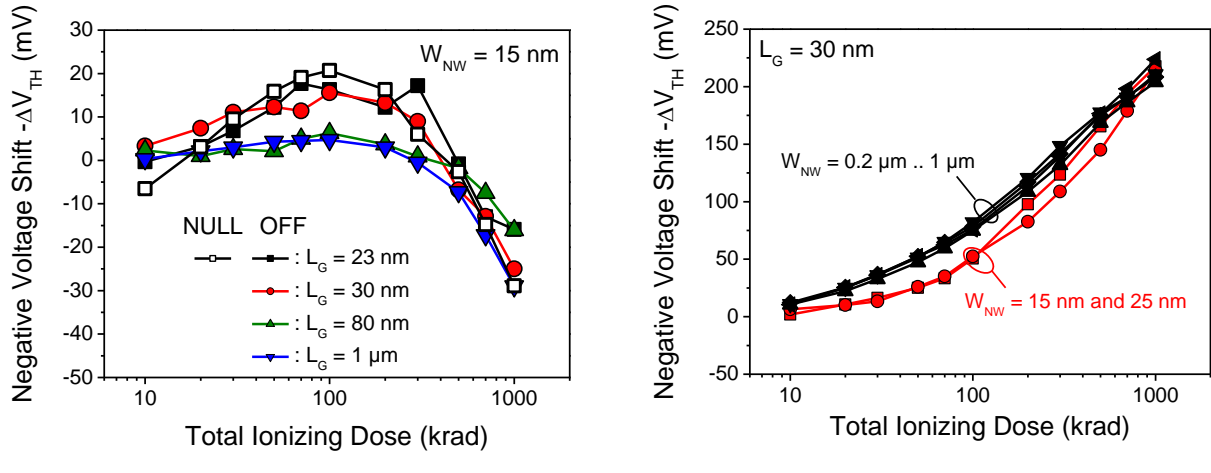


**Figure 34: TID induced threshold voltage shift in (a) NMOS and (b) PMOS SOI NWFET. NWFET dimensions can reach  $TSOI = 12\text{ nm}$ ,  $WNW = 15\text{ nm}$  and  $LG = 24\text{ nm}$  (after [180]).**

The major issue is shown by PMOS NWFETs which exhibit large TID-induced threshold voltage shifts even in narrow devices contrary to NMOS NWFETs. Furthermore, the geometrical dependence observed in NMOS NWFETs is strongly lowered. It still governs the TID response of PMOS NWFETs fabricated with a long gate length ( $L_G > 80$  nm) [182] while short gate lengths NWFETs do not follow the same behavior. In PMOS NWFET with short gate length, only a few mVs separate  $\Delta V_{TH}$  extracted in narrow devices compared to wide ones. The PMOS NWFET shape has no clear impact on their TID response which is governed by a different root cause than in NMOS devices. The contribution of oxide trap charges drives the PMOS NWFET TID response. The one of interface traps is unexpectedly weak in PMOS devices which would otherwise further enhance the extracted  $\Delta V_{TH}$  if it had the same contribution as in their NMOS counterparts. Such studies demonstrate the need for continuous investigations of novel device structures which foreshadow upcoming or emerging technologies.

### 3.6. Radiation response variability

### 3.6.1.Radiation source and electric field dependence

The first origin of TID effects variations induced in electronics is the radiation source itself. As already presented in section 3.1, incident ionizing particles interact with materials of the irradiated devices through various mechanisms. Energetic photons mainly interact through the photoelectric effects for low photon energies ( $\ll 1$  MeV) such as 10 keV x-rays while Compton scattering governs interaction mechanisms for high energy photons like  $\gamma$  generated either by  $^{60}\text{Co}$  (1.25 MeV) or  $^{137}\text{Cs}$  (0.66 MeV) sources. Charged particles such as electrons or protons can interact with matter through different processes which include for instance the ionization process. These various particle-matter interaction processes are first sources of TID response variation in electronic devices and ICs. In all cases, electron-hole pairs are created in dielectric materials. But only part of generated holes escapes from initial recombination which depends on both the ionizing particle and the electric field

which stands into the irradiated dielectric. This fraction of unrecombined holes is named charge yield. It is plotted in Figure 35 vs the applied electric field in the dielectric.

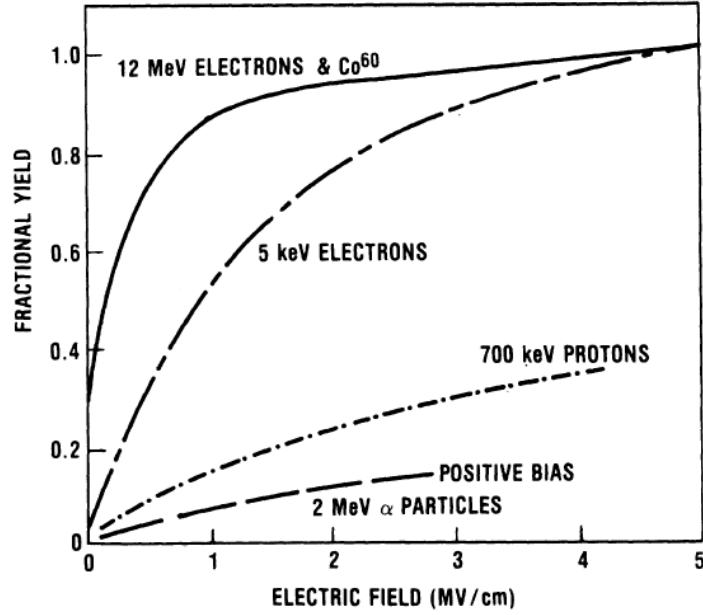


**Figure 35:** The fraction of holes that escape initial recombination (charge yield) for x rays, low-energy protons, gamma rays, and alpha particles (after [115,183,184]).

The electric field strongly increases charge yield, since it improves electron-hole pair separation and reduces recombination. One implication is that the electronic device TID response usually depends on the bias configuration used during irradiation.

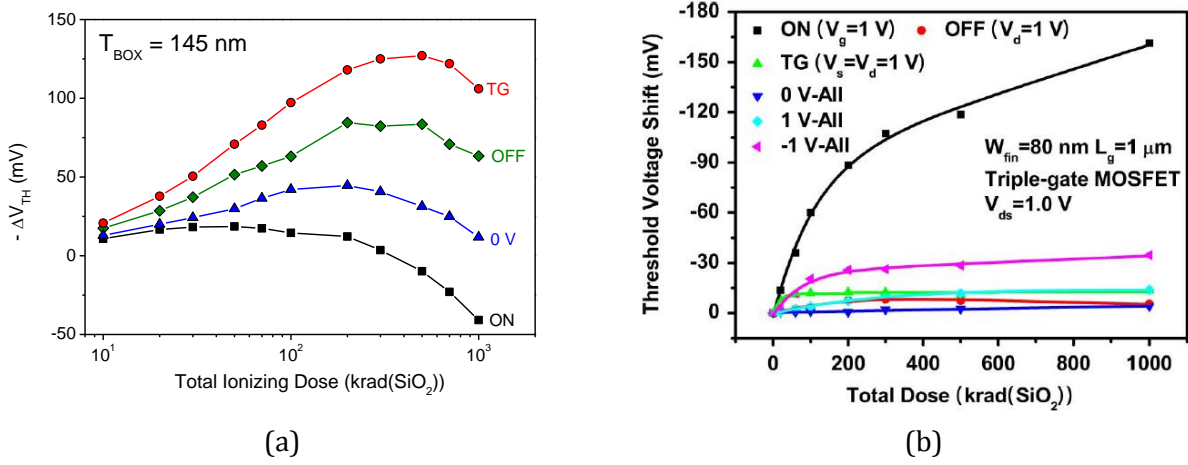


**Figure 36:** (a)  $\Delta V_{TH}$  vs TID extracted in NMOS UTSOI transistors biased in four configurations during irradiations (after [147]), (b) impact of bias configuration during irradiation on radiation-induced threshold-voltage shift in SOI tri-gate MOSFETs (after [170]).

Several papers have investigated such an issue in order to determine worst case bias during TID irradiations [185,186,147]. The MOSFET bias configuration used during irradiation governs the electric field shape in dielectrics. This determines the location where radiation-generated charges are trapped in dielectrics. An example of calculated trapped-charge distributions in the BOX of a PDSOI transistor is presented in Figure 37 for two bias configurations during irradiation (after [185]).

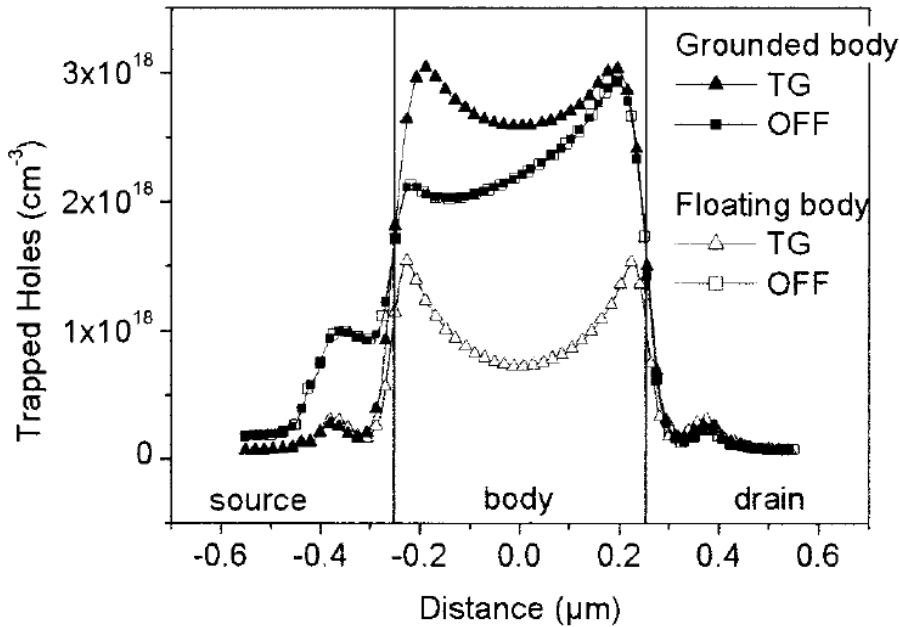


**Figure 37:** Technology Computer Aided Design simulations of radiation-induced trapped charge distributions in the BOX of a PDSOI technology. Results are presented in a source-drain cut along the SOI-BOX interface for various bias configurations used during irradiation referred as OFF and TG (after [185]).

This leads to different trapped charge distributions which have various impacts on MOSFETs electrical response. Such a distribution can also be reduced to a trapped-charge centroid, its electrostatic impact being dependent on its location in the dielectric. Its effect on MOSFET electrostatics is more and more significant when it comes closer to the active silicon region, particularly if it is close to the conduction channel area. All microelectronic technologies, bulk silicon, SOI, FinFETs, are subject to such effects which mainly depends on the transistor geometry and structure, its design and to process parameters like doping levels in active area. Variations of fabrication processes and charge lateral nonuniformities [187,188] could thus have implications on electronic devices and ICs radiation hardness.

### 3.6.2. Process variability and TID effects

Process variability is a critical issue for hardness assurance since part selection in a lot of wafers must guarantee high survivability of selected devices in radiation environments [189]. This requires sampling strategies for part selection and radiation testing in order to get high confidence levels for selected parts [190]. Such strategies should also be a compromise between “generality” and cost

since all parts cannot be tested to assess their radiation hardness. To do so, statistical methods for high reliability applications are proposed and regularly updated to evaluate random and systematic errors for high reliability applications [191]. As described in [191] the most general strategy consists in getting large samples to achieve high confidence of high success probability. Such an approach assumes small variations in Radiation Response Distributions (RRD). This well behaves for many probability distribution shapes to determine the probability of success with a high confidence level for a fixed TID, but it cannot be used to predict the number of parts which would pass at other TID levels.

In contrast, other strategies make assumptions on a consistent part-to-part radiation response within a wafer and a specific form for the RRD [192]. This allows reaching a high confidence level and high probability of success with smaller samples. However, if the assumptions made to use such a strategy are erroneous or violated, such a strategy may not be efficient to detect parts with pathological behaviors which can jeopardize radiation hardness assurance. Adapting the methodology is needed. It depends on lot-to-lot vs wafer lot, and to inter-lot vs intra-lot variability. Statistical models to estimate radiation-induced degradation should thus be carefully chosen as described in [193] which suggests guidelines for TID radiation hardness assurance methodologies allowing qualification based on “historical” data.

Such methodologies are applied to mitigate risks of failure during device operations. Managing RRD can be a difficult challenge since, the radiation response for one unique IC design, using only one technology, with a unique manufacturer, may strongly differs depending on the foundry where the ICs are fabricated as demonstrated by [194] and presented in Figure 38.

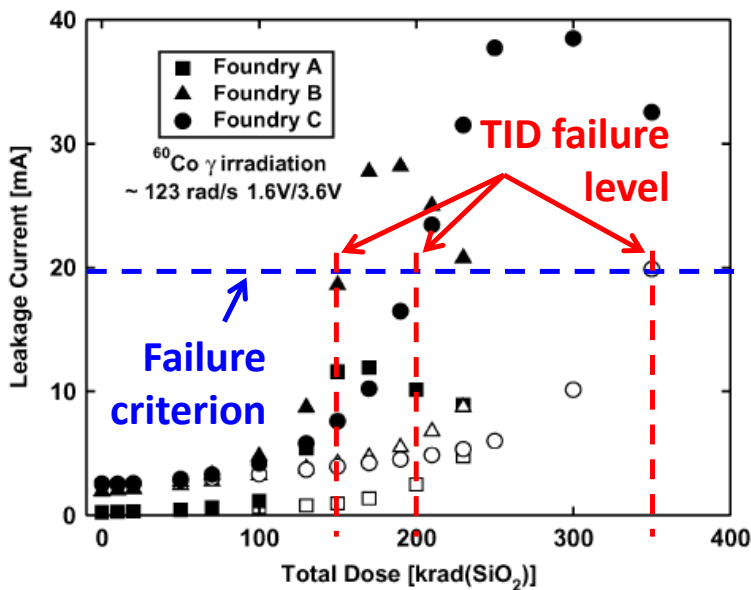
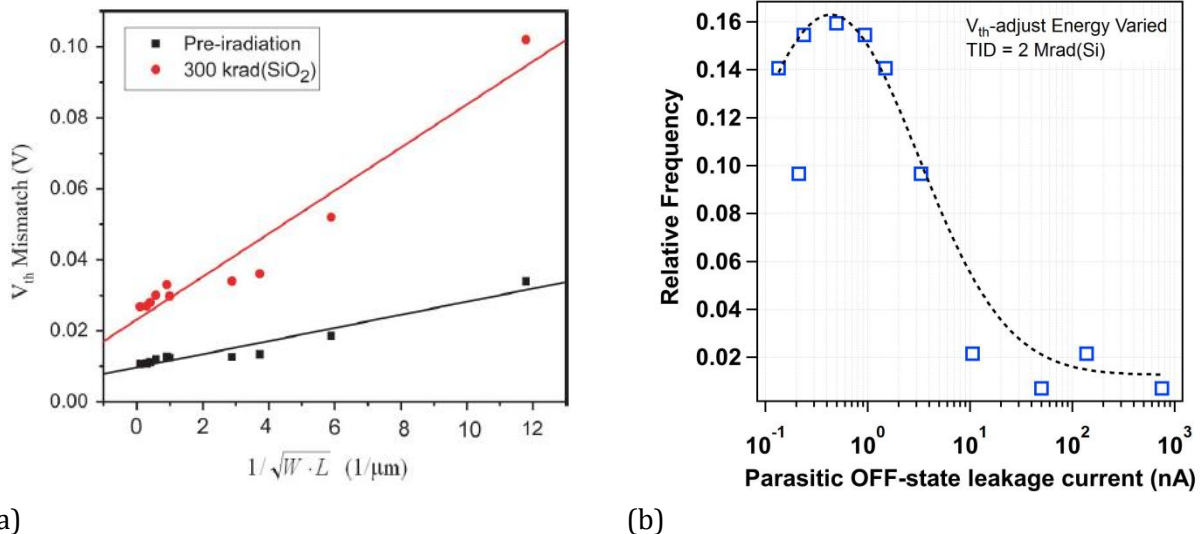


Figure 38: Leakage current vs TID curves of one IC fabricated using three different foundries (after [194]).

Results presented in Figure 38 are obtained for the same custom design, manufacturer, technology, design kit and layout with only one difference: the foundry where the IC is processed. Results highlight considerable radiation response variations despite the same radiation conditions including the radiation source and the operating conditions during tests. For a chosen TID failure criterion on the leakage current, ICs from one foundry have a TID failure level that can be two times greater than the same ICs but fabricated in another foundry from the same manufacturer. It is worth noting that similar results are also obtained for latch-up [194]. This is a serious issue for radiation hardness assurance that aforementioned part selection methodologies can manage to mitigate risk of failure.

Finding a correlation between process variability and TID response is rarely obvious, particularly when looking at the impact of only one process parameter. But in recent years, studying the impact of process variability on radiation response is the subject of increasing research efforts [195,196,197] since introducing it in electrical models can help IC designers in identifying “radiation design corners” [198,195].



**Figure 39: (a) TID impact on V<sub>th</sub> mismatch in a AVT plot (after [195]), and (b) influence of VT implant on the OFF-state leakage current in bulk NMOSFETs after 2 Mrad irradiation. (after [197]).**

Figure 39(a) (after [195]) shows the influence of a TID irradiation on the A<sub>VT</sub> plot (cf. Figure 20(a), section 2.8) which increases the initial statistical variability measured before irradiation in 90 nm and 65 nm technologies. The influence of V<sub>T</sub> doping implant variations is investigated in 90 nm bulk technologies [197] (see Figure 39(b)). It is concluded that channel implant parameters can significantly impact the doping profile along the field oxide interfaces made of STI and thus on the radiation-induced edge leakage currents. Statistical variations involved in doping implants can have direct implications for device radiation hardening.

However, such correlations are not always as straightforward as these two examples. [199] demonstrates that statistical variability of bulk 65 nm devices is not significantly affected by 1 Mrad

irradiation. However, MOSFETs drive current variability sharply increases for TID in the MGy range, as exhibited in Figure 40, but no clear correlation with the pre-irradiation variability is found.

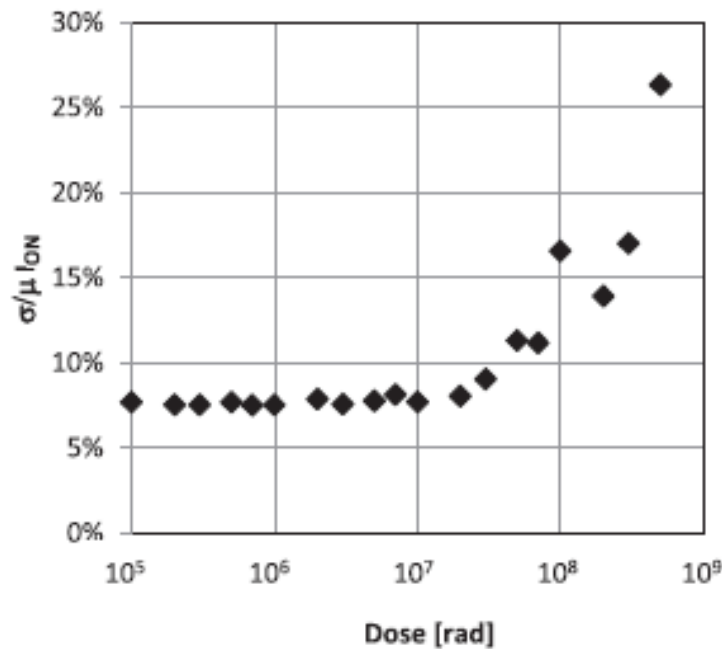


**Figure 40: Standard deviation over mean for the on-current of six pMOSFETs with W/LG = 120 nm / 60 nm vs TID (after [199]).**

Variability vs radiation effects in more advanced technologies is still an open question that will require significant research efforts in the upcoming years since novel sources of variability are involved by both new fabrication processes and radiation effects in highly scaled devices.

### 3.7. Radiation effects in ultra-scaled technologies: some keypoints

MOSFET evolutions are continuously required by technology downscaling. Innovations brought to the overall MOSFET structure have often implications for radiation hardening. Depleted channel devices, such as planar UTSOI MOSFETs and bulk FinFETs, are currently the major device structures of leading edge technologies. Their TID responses are both governed by the same basic mechanisms which include charge trapping in dielectrics and interface traps buildup. However, their degradation does not have the same origin. Radiation-induced charge trapping in the BOX is responsible for most of the electrical characteristic changes observed in UTSOI technologies (planar and multiple-gate) while the one occurring in STI drives the TID response of bulk FinFETs.

Novel TID effects are identified for TID in the MGy range in 65 nm technologies. They are still under investigation but such phenomena may be triggered for lower TID in more integrated technologies.

PMOSFETs appear to become increasingly sensitive to TID with device scaling compared to older technologies. They are shown to be potentially impacted by Radiation Induced Narrow Channel Effects in planar bulk devices. Going further into device scaling, nanometer-scaled PMOS nanowire FETs exhibit unexpected TID sensitivity compared to their NMOS counterparts. Such an assymmetry

between NMOS and PMOS already exist because of the opposite interface traps contribution in NMOS and PMOS devices. But in the present case, the asymmetry is much more attributed to the oxide trap charge contribution. Thus, again, radiation effects implications continuously change with device structures, novel materials and fabrication process innovations.

Variability is not a novel issue but process variations have an impact on electronic devices radiation response. Correlations can be found between a process parameter and its implications for device hardening, such as the impact of channel doping and its variation on radiation-induced edge leakage current. But it is not always so straightforward since several sources of process variability, for instance oxide thickness fluctuations or line edge roughness, could also play a role in the radiation response and its variability. Until now, only few studies have been devoted to investigating process variability implications on radiation-hardening in ultra-scaled devices. It opens new fields of investigations both for leading edge and upcoming technologies.

## 4. Upcoming Issues and Conclusions

### 4.1. Short terms perspectives: technology roadmap

Technology roadmaps still envision device scaling down to the 3 nm technology node and below. Figure 41 presents the IMEC roadmap [200] which foresees the FinFET structure to be scaled down to the 5 nm node, and even the 3 nm node for high performances applications. It also highlights the first appearance of nanowires which offer a better performance-area tradeoff starting from this integration level.

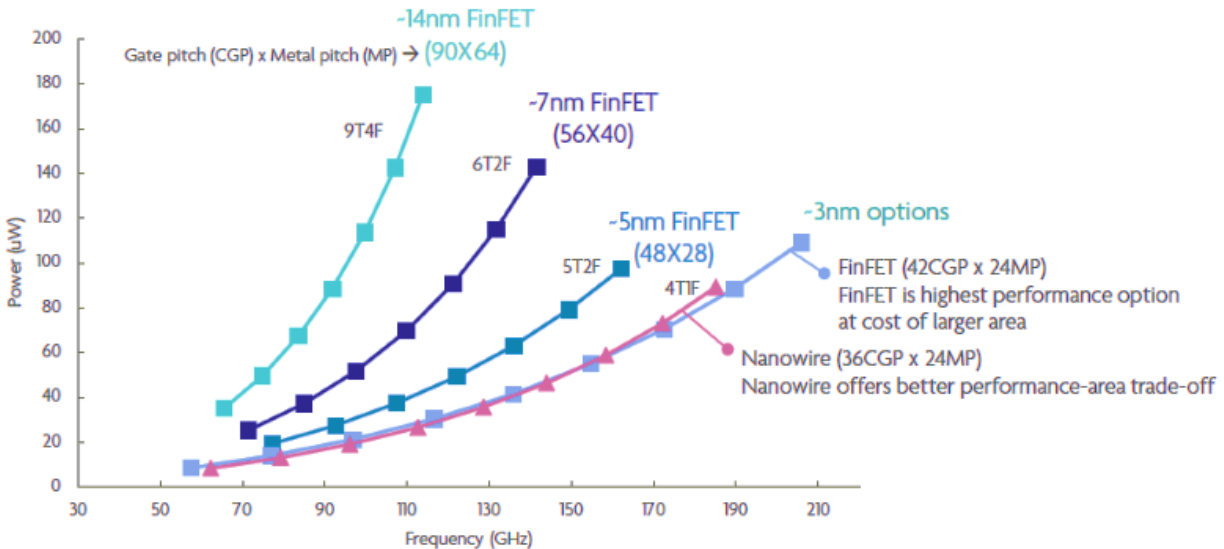
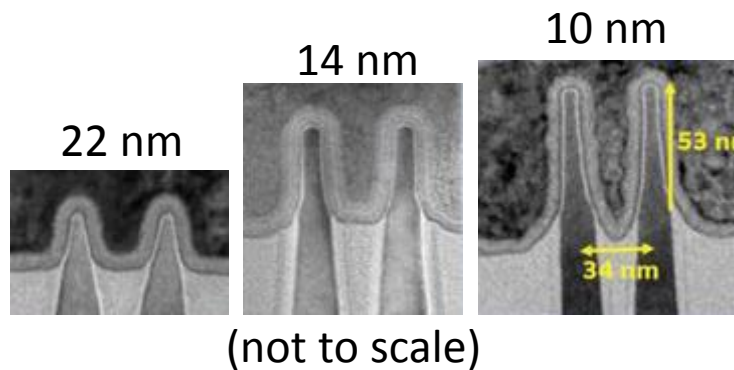


Figure 41: IMEC roadmap down to the 3 nm technology node (after [200]).

Before that, FinFET are demonstrated to be scalable down to the 5 nm node by changing the FinFET shape. The original “tri-gate” shape used in the first bulk FinFET technology [69] has evolved to a more vertical shape and “double-gate” structure for the 10 nm technology [10] (cf. Figure 42). Such a device structure improves both the device electrostatics and the performance-area-consumption tradeoff. However, process challenges must be overcome to achieve such vertical shapes with high fin uniformity with well controlled variability. Fin Edge Roughness is becoming a major source of FinFET technologies variations. The tools to fabricate these device structures currently are at their limits, particularly optical lithography tools which now must turn to lower wavelengths to continue device scaling with cost effectiveness. Extreme Ultra-Violet (EUV) lithography is currently under integration in fabrication processes for next technology nodes [201] but it requires huge technical developments and financial investments to meet the availability requirements of mass production. However, it could be a major asset to continue device scaling since it reduces the lithography steps number to pattern well-shaped tall and narrow FinFETs.



**Figure 42: Evolution of the bulk FinFETs shape with device scaling (after [10,69]).**

Silicon-based MOSFETs are still in the technology roadmap for semiconductors 60 years after the first MOSFET demonstration. This is achieved thanks to constant evolution of their device structure, to step-by-step introduction of novel materials to gain better electrostatic performances such as high-k materials, metal gates and strained materials. Next steps will probably even reduce silicon to the smallest part of future MOSFET generations, silicon-germanium, germanium and III-V materials being good candidates to further improve carrier transport mechanisms in MOSFET-based devices. Other materials or device structures are currently under investigations, such as graphene [202,203], carbon nanotube FET [204], or tunnel FETs [80,81,205], but until now, none of them has reached the performance-cost tradeoff of silicon based technologies.

#### 4.2. Radiation effects and variability issues

Narrow/vertical FinFETs and nanowires are the best candidates for next technology generations. Their structures are based on depleted nanometer scaled active area which are surrounded by large “defect rich” dielectric volumes made of spaces, field oxides, capping layers or BOX. Both small dimensions and low doping could make them highly sensitive to single- or discrete-defects.

On the one hand, the number of doping atoms regularly decreases with technology generation as shown in Figure 43. Less than 10 dopant atoms are implanted in active regions of 10-nm technologies, explaining the potential influence of Random-Dopant Fluctuations or Random-Discrete Dopants on MOSFET electrical characteristics variability. Using depleted channels, *i.e.* undoped channels, helps reducing variability in channel implants. But it makes devices more sensitive to statistical variations of doping implants and to potential dopant diffusion during annealing steps. Following the same idea, introducing a single-defect (also called discrete-defect), such as those generated by displacement damage, into the active region should have strong implications on device function. Generation/recombination currents could modify both leakage and drive currents delivered by MOSFETs as it is usually observed in photodiodes [206], BJTs [120] or active pixel sensors [114]. This could be emphasized despite the reduced MOSFET active volume but which is offset by the huge number of potentially sensitive devices on a chip. To sum up, displacement damage dose effects could become an increased contributor to the ultra-scaled MOSFETs radiation response. If so, such devices may also be sensitive to effects like Random Telegraph Noise which may also be induced by defects in the active semiconductor region [207].

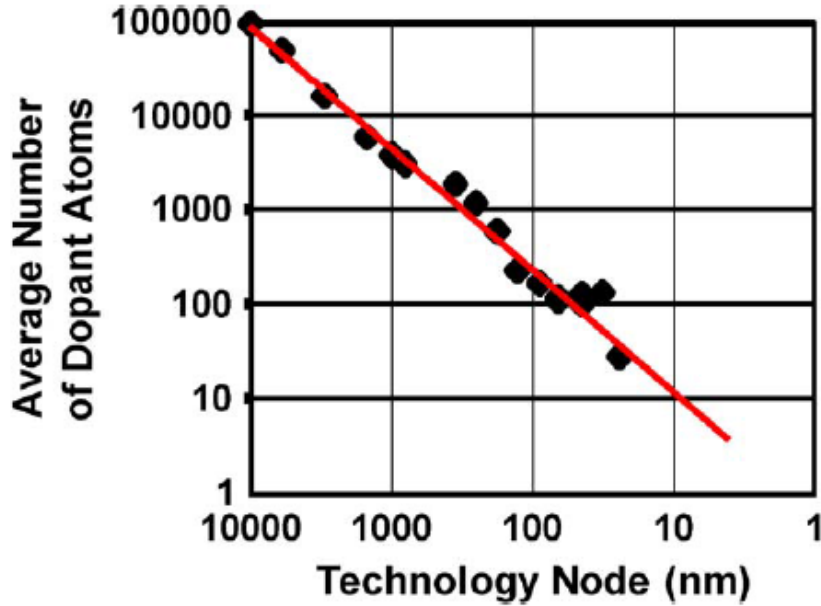


Figure 43: Reduction in the number of dopant atoms per generation (after [208] and [99])

On the other hand, in nano devices surrounded by dielectrics, TID effects will certainly be strengthened despite the systematic multiple-gate usage in device structures which ensures high control of the gate over the electrostatic potential in the channel region. Discrete trapped charges and their location in dielectrics could also play an important role in the variability of the TID response, since they strongly modify the local trapped charge density and then its electrostatic impact on device electrical characteristics. Finally, combining fin/nanowire uniformity and roughness (as presented in section 4.1) with TID effects will probably reveal an additional source of radiation sensitivity and variability.

#### 4.3. Summary and conclusions

New challenges and opportunities emerge with the advent of ultra-scaled devices. They inherited more than six decades of innovations incorporated into microelectronic process technology. The silicon-based MOSFET structure is still used even after extreme device scaling, with 7-nm technologies currently under development.

These notes give an overview of major technological innovations introduced to push the MOSFET limits in order to achieve nanometer scaled depleted MOSFETs with multiple-gates envisioned for future generations. Sources of process variability are presented as well as their implications for device functions and examples of innovations brought to fabrication processes to mitigate them.

The impact of radiation effects, particularly total ionizing dose effects, induced in MOSFETs from mature to emerging technologies are reviewed to guide device radiation hardening. Here again, sources of TID response variability are presented including both process-induced and radiation mechanisms-induced sources.

Finally, upcoming issues related to recent technology evolutions are discussed to predict the foreseeable future for radiation effects in ultra-scaled devices. The current trend is to fabricate even smaller transistors and low (no) doping. Potential sources of radiation sensitivities could arise such as electronic implications induced by single-defects in semiconductor materials or discrete-trapped charges in dielectrics. Novel sources of radiation sensitivities at the boundary between TID, DDD and SEE may arise since nanometer scaled devices could be sensitive to each single- or discrete-event/defects which may occur in its neighborhood.

## 5. References

- 1 J.E. Lilienfeld, "Method and apparatus for controlling electric current," Canadian application Oct. 22nd 1925, Filed Oct. 8, 1926
- 2 J. Bardeen and W.H. Brattain, "The transistor, a semi-conductor triode", Phys. Rev., vol. 74, pp. 230-231, June 1948.
- 3 W. Shockley, "The theory of p-n junctions in semiconductors and p-n junction transistors", The Bell Syst. Tech. J., vol. 28, no. 3, pp. 435-489, July 1949.
- 4 W. Shockley, "A unipolar "feld-effect" transistor", Proceedings of the IRE, vol. 40, no. 11, pp. 1365-1376, Nov. 1952.
- 5 G.C. Dacey and I.M. Ross, "Unipolar "Field-Effect" transistor", Proceedings of the IRE, vol. 41, no. 8, pp. 970-979, Aug. 1953.
- 6 D. Kahng and M.M. Atalla, "Silicon-silicon dioxide field induced surface device," IRE-AIEE Solid-State Device Research Conference, MIT, 1960.
- 7 G.E. Moore, "Cramming more components onto integrated circuits," Electronics Magazine, vol. 38, no. 8, 1965
- 8 R.H. Dennard, F.H. Gaenslen, H.-N. Yu, V.L. Rideout, E. Bassous, and A.R. LeBlanc, "Design of ion-implanted MOSFET's with very small physical dimensions", IEEE Jour. Solid-State Circ., vol. 9, no. 5, pp. 256-268, Oct. 1974.
- 9 Intel website, <https://newsroom.intel.com/newsroom/wp-content/uploads/sites/11/2017/09/10-nm-ifc-factsheet.pdf> 2017.
- 10 C. Auth et al, « A 10nm high performance and low-power CMOS technology featuring 3rd generation FinFET transistors, self-aligned quad patterning, contact over active gate and cobalt interconnects », 2017 IEEE Electron Devices Meeting (IEDM), p. 29, Dec. 2017, DOI: 10.1109/IEDM.2017.8268472.
- 11 G.D. Hutcheson, "Moore's law: the history and economics of an observation that changed the world", The Electro-Chemical Society Interface, pp.17-21, 2005.
- 12 W. Shockley, "Problems related to p-n junctions in silicon", Solid-State electronics, vol. 2, pp. 35-67, Jan. 1961.
- 13 S.M. Sze, "Physics of semiconductor devices – 2<sup>nd</sup> edition", John Wiley & Sons edition, 30 sept. 1981.
- 14 IC Insights web site, from "IC Market Drivers 2017 – A study of emerging and major End-Use applications fueling demand for Integrated Circuits", available at <http://www.icinsights.com/news/bulletins/IoT-and-Automotive-to-Trive-IC-Market-Growth-Through-2020>.
- 15 D. Kahng and M.M. Atalla, "Silicon-silicon dioxide field induced surface device," in IRE-AIEE Solid-State Device Research Conference, 1960.
- 16 C.T. Sah, "Evolution of the MOS transistor – From conception to VLSI", Proc. IEEE, vol. 76, no. 10, pp. 1280 – 1285, 1988
- 17 F. Faggin, T. Klein, and L. Vadasz, "Insulated gate field effect transistor integrated circuits with silicon gates," IEEE Trans. Electron. Dev., vol. 16, no. 2, p. 236, 1969.
- 18 S. Ogura, P.J. Tsang, W.W. Walker, D.L. Critchlow, and J.F. Shepard, "Design and characteristics of the lightly doped drain-source (LDD) insulated gate field-effect transistor," IEEE Trans. Electron. Dev., vol. 27, no. 8, pp. 1359 – 1367, 1980.
- 19 T. Hori and H. Iwasaki, "Improved hot-carrier immunity in submicrometer MOSFET's with reoxidized nitrided oxides prepared by rapid thermal processing," IEEE Electron Device Lett., vol. 10, no. 2, pp. 64 – 66, 1989.
- 20 H.S. Momose, S. Kitagawa, K. Yamabe, and H. Iwai, "Hot carrier related phenomena for n- and p-channel MOSFETs with nitride gate oxide by RTA," in IEDM Tech. Dig., 1989, pp. 267 – 270.
- 21 Y. Ma, Y. Ono, L. Stecker, D.R. Evans, and S.T. Hsu, "Zirconium oxide based gate dielectrics with equivalent oxide thickness of less than 1.0 nm and performance of submicron MOSFET using nitride gate replacement process," in IEDM Tech. Dig., 1999, pp. 149 – 151.
- 22 B.H. Lee, L. Kang, W.J. Qi, R. Nieh, Y. Jeon, K. Onishi, and J.C. Lee, "Ultrathin hafnium oxide with low leakage and excellent reliability for alternative gate dielectric application," in IEDM Tech. Dig., 1999, p. 133 – 136.
- 23 K. Ismail, S.F. Nelson, J.O. Chu and B.S. Meyerson, "Electron transport properties of Si/SiGe heterostructures: Measurements and device implications," Appl. Phys. Lett., vol. 63, no. 5, pp. 660 – 662, 1993.
- 24 K. Mistry, C. Allen, C. Auth, B. Beattie, D. Bergstrom, M. Bost, M. Brazier, M. Buehler, A. Cappellani, R. Chau, C.-H. Choi, G. Ding, K. Fischer, T. Ghani, R. Grover, W. Han, D. Hanken, M. Hattendorf, J. He, J. Hicks, R. Huessner, D. Ingerly, P. Jain, R. James, L. Jong, S. Joshi, C. Kenyon, K. Kuhn, K. Lee, H. Liu, J. Maiz, B. McIntyre, P. Moon, J. Neirynck, S. Pae, C. Parker, D. Parson, C. Prasad, L. Pipes, M. Prince, P. Rarade, T. Reynolds, J. Sandford, L. Shifren, J. Sebastian, J. Seiple, D. Simon, S. Sivakumar, P. Smith, C. Thomas, T. Troeger, P. Vandervoorn, S. Williams, and K. Zawadzki, "A 45 nm logic

- technology with high-k+metal gate transistors, strained silicon, 9 Cu interconnect layers, 193 nm dry patterning, and 100 % Pb-free packaging," in IEDM Tech. Dig., 2007, pp. 247 – 250.
- 25 D.L. Critchlow, "MOSFET scaling – The driver of VLSI technology," Proceedings of the IEEE, vol. 87, no. 4, pp. 659-667, Apr. 1999.
- 26 T. Skotnicki, "Transistor MOS et sa technologie de fabrication", Techniques de l'ingénieur, article E2430 v2, pp. 1-37, feb. 2000, available at : <https://www.techniques-ingeneur.fr/base-documentaire/electronique-photonique-th13/technologies-des-dispositifs-actifs-41186210/transistor-mos-et-sa-technologie-de-fabrication-e2430/>
- 27 T. Skotnicki, C. Fenouillet-Beranger, C. Gallon, F. Boeuf, S. Monfray, A. Pouydebasque, M. Szczap, A. Farcy, F; Arnaud, S. Clerc, M. Sellier, A. Cathignol, J.-P. Schoellkopf, E. Perea, R. Ferrant and H. Mingam, "Innovative materials, devices, and CMOS technologies for low-power mobile multimedia," IEEE Trans. Electron Dev., vol. 55, no. 1, pp. 96 – 130, 2008.
- 28 J. Robertson, "Band offsets of wide-band-gap oxides and implications for future electronic devices," J. Vac. Sci. Technol. B, vol. 18, no. 3, pp. 1785-1791, 2000.
- 29 F. Bœuf, F. Arnaud, B. Duriez, M. Bidaud, P. Gouraud, C. Chaton, P. Morin, J. Todeschini, M. Jurdit, L. Pain, V. De-Jonghe, M.T. Basso, D. Sotta, F. Wacquant, J. Rosa, R. El-Farhane, S. Jullian, N. Bicais-Lepinay, H. Bernard, J. Bustos, S. Manakli, M. Gaillardin, J. Grant, and T. Skotnicki, "A conventional 45 nm CMOS node low-cost general platform for general purpose and low power applications," in IEDM Tech Dig., pp. 425-428, Dec. 2004.
- 30 F. Payet, N. Cavassilas, and J.L. Autran, "Theoretical investigation of hole phonon-velocity in strained Si/SiGe MOSFET's," J. Appl. Phys. Vol. 95, pp. 713-717, 2004.
- 31 F. Andrieu, F. Allain, C. Buj-Dufournet, O. Faynot, F. Rochette, M. Cassé, V. Delaye, F. Aussenac, L. Tosti, P. Maury, L. Vandroux, N. Daval, I. Cayrefourcq, and S. Deleonibus, "Additivity between sSOI- and CESL-induced nMOSFETs performance boosts," Int. Conf. on Solid State Dev. And Mat. (SSDM), pp. 888-889, 2007.
- 32 S. Thompson, N. Anand, M. Armstrong, C. Auth, B. Cot, M. Alavi, P. Bai, I. Bielefeld, R. Bigwood, J. Brandenburg, M. Buehler, S. Cea, V. Chikarmane, C. Choi, R. Frankovic, T. Ghani, G. Glass, W. Han, T. Hoffmann, M. Hussein, P. Jacob, A. Jain, C. Jan, S. Joshi, C. Kenyon, I. Klaus, S. Klopccic, I. Luce, Z. Ma, B. McIntyre, K. Misty, A. Munhy, P. Nguyen, H. Pearson, T. Sandford, R. Schweinfuh, R. Shah, S. Sivkumar, M. Taylor, B. Tufts, C. Wallace, P. Wang, C. Weber, and M. Bohr, "A 90 nm Logic Technology Featuring 50nm Strained Silicon Channel Transistors, 7 layers of.Cu Interconnects, Low k ILD, and 1  $\mu\text{m}^2$  SRAM Cell," in IEDM Tech. Dig. pp. 61-64, 2002.
- 33 T. Ghani, M. Armstrong, C. Auth, M. Bost, P. Charvat, G. Glass, T. Hoffmann, K. Johnson, C. Kenyon, J. Klaus, B. McIntyre, K. Mistry, A. Murthy, J. Sandford, M. Silberstein, S. Sivakumar, P. Smith, K. Zawadzki, S. Thompson, and M. Bohr, "A 90 nm high volume manufacturing logic technology featuring novel 45 nm gate length strained silicon CMOS transistors," in IEDM Tech. Dig., pp. 978–980, 2003.
- 34 H.M. Manasevit and W.I. Simpson, "Single-crystal silicon on a Sapphire substrate," J. Appl. Phys., vol. 35, pp. 1349-1351, 1964.
- 35 W.A. Kolasinski, J.B. Blake, J.K. Anthony, W.E. Price, and E.C. Smith, "Simulation of cosmic-ray induced soft errors and latch-up in integrated-circuit computer memories," IEEE Trans. Nucl. Sci., vol. NS-26, no. 6, pp. 5087-5091, Dec. 1979.
- 36 E. Kooi, B. Brandt, J. Shappir, and W. Steinmayer, "Processes for compact LOCOS integrated circuits," in IEDM Tech. Dig., pp. 4-5, 1971.
- 37 T. Yamaguchi, S. Morimoto, and G. Kawamoto, "Process and device performance of 1- $\mu\text{m}$ -channel N-Well CMOS using deep-trench isolation technology," Symp. On VLSI Tech., pp. 26-27, 1983.
- 38 Y. Niitsu, S. Taguchi, K. Shibata, H. Fuji, Y. Shimamune, H. Iwai, and K. Kanzaki, , "Latch-up free CMOS structure using shallow trench isolation," in IEDM Tech. Dig., pp. 509-512, 1985.
- 39 Y. Kobayashi and A. Fukami, "Improvement of SOI/MOSFET characteristics by recrystallizing connected silicon islands on fused silica," IEEE Electron. Dev. Lett., vol. 5, no. 11, pp. 485-460, 1984.
- 40 M. Akiya, K. Ohwada, and S. Nakashima, "High-voltage buried-channel MOS fabricated by implantation into silicon," IEEE Electron. Lett., vol. 17, no. 18, pp. 640-641, 1981.
- 41 K. Izumi, Y. Omura, M. Ishikawa, and E. Sano, "SIMOX technology for CMOS LSIs," Symp. On VLSI tech. pp. 10-11, 1982.
- 42 C.E. Hunt, "Film uniformly in bond and etch-back silicon on insulator (BESOI)," SOS/SOI technology workshop proceedings, p. 57, 1988.
- 43 L.J. Palkuti, P. Ling, P. Leonov, H. Kawayoshi, R. Ormond, and J. Yuan, "Radiation response of CMOS/SOI devices formed by wafer bond and etchback," IEEE Trans. Nucl. Sci., vol. 35, no. 6, pp. 1653-1656, 1988.
- 44 H.W. Lam, "Laser-recrystallized silicon-on-oxide – The ideal silicon-on-insulator structure for VLSI?," in IEDM Tech. Dig., pp. 556-558, 1980.
- 45 A.F. Tasch, T.C. Holloway, K.F. Lee, and J.F. Gibbons, "Silicon-on-insulator MOSFETs fabricated on laser-annealed polysilicon on SiO<sub>2</sub>," Electron. Lett., vol. 15, no. 14, pp. 435-437, 1979.

- 46 A.J. Auberton-Hervé, M. Bruel, C. Jaussaud, J. Margail, W. D'Hespel, J.F. Péré, A; Vitez, and A. Tissot, "A CMOS SOI 1.4  $\mu$ m technology on 1300°C substrates without epitaxy," E-SOI workshop, 1988.
- 47 J.L. Leray, E. Dupont-Nivet, O. Musseau, Y.M. Coïc, A. Umbert, P. Lalande, J.F. Péré, A.J. Auberton-Hervé, M. Bruel, C. Jaussaud, J. Margail, B. Giffard, R. Truche, and F. Martin, "From substrate to VLSI: investigation of hardened SIMOX without epitaxy, for dose, dose rate and SEU phenomena," IEEE Trans. Nucl. Sci., vol. 35, no. 6, pp. 1355-1360, 1988.
- 48 J.P. Colinge, K. Hashimoto, T. Kamins, S.-Y. Chiang, E.-D. Liu, S. Peng, and P. Rissman, "High-speed, low power, implanted-buried oxide CMOS circuits," IEEE Electron Device Lett. Vol. EDL-7, no. 5, pp. 279-281, 1986.
- 49 H.-K. Lim and J.G. Fossum, "Current-voltage characteristics of thin-film SOI MOSFET's in strong inversion," IEEE Trans. Electron Dev., vol. ED-31, no. 4, pp. 401-408, 1984.
- 50 M. Bruel, "Silicon on insulator material technology," Electronic Lett., vol. 31, no. 14, pp. 1201-1202, 1995.
- 51 M. Bruel, B. Aspar, B. Charlet, C. Maleville, T. Poumeyrol, A. Soubie, A.J. Auberton-Hervé, J.M. Lamure, T. Barge, F. Metral, and S. Trucchi, "Smart-cut: a promising new SOI material technology," IEEE Int. SOI Conf. Proc., pp. 178-179, 1995.
- 52 J.-P. Noel, O. Thomas, M.-A. Jaud, C. Fenouillet-Beranger, P. Rivallin, P. Scheiblin, T. Poiroux, F. Boeuf, F. Andrieu, O. Weber, O. Faynot, and A. Amara, "UT2B-FDSOI device architecture dedicated to low power design techniques," in ESSDERC proc., pp. 210-213, 2010.
- 53 H.K. Lim and J.G. Fossum, H.K. Lim and J.G. Fossum, "Threshold voltage of thin film Silicon-on-Insulator (SOI) MOSFET's," IEEE Trans. Electron Dev., vol. ED-30, no. 10, pp. 1244-1251, Oct. 1983.
- 54 G.K. Celler and S. Cristoloveanu, "Frontiers of silicon on insulator," Journal of Appl. Phys. vol. 93, no. 3, pp. 4955 - 4978, 2003.
- 55 R. Ranica, N. Planes, O. Weber, O. Thomas, S. Haendler, D. Noblet, D. Croain, C. Gardin, F. Arnaud, "FDSOI process/design full solutions for ultra-low leakage, high speed and low voltage SRAMs", in Symp. on VLSI Tech., 2013, pp. 210-211.
- 56 N. Planes, O. Weber, V. Barral, S. Haendler, D. Noblet, D. Croain, M. Bocat, P.-O. Sassoulas, X. Federspiel, A. Cros, A. Bajolet, E. Richard, B. Dumont, P. Perreau, D. Petit, D. Golanski, C. Fenouillet-Béranger, N. Guillot, M. Rafik, V. Huard, S. Puget, X. Montagner, M.-A. Jaud, O. Rozeau, O. Saxod, F. Wacquant, F. Monsieur, D. Barge, L. Pinzelli, M. Mellier, F. Boeuf, F. Arnaud, M. Haond, "28nm FDSOI Technology Platform for High-Speed Low-Voltage Digital Applications", in Symp. on VLSI Tech., 2012, pp. 133-134.
- 57 F. Balestra, S. Cristoloveanu, M. Benachir, J. Brini, and T. Elewa, "Double-gate Silicon-on-Insulator transistor with volume inversion: A new device with greatly enhanced performance," IEEE Electron Device Lett., vol. 8, no. 9, pp. 410-412, Sep. 1987.
- 58 J.P. Colinge, M.H. Gao, A. Romano-Rodriguez, H. Maes, and C. Claeys, "Silicon-on-Insulator 'Gate-All-Around device," in IEDM Tech. Dig., The IEEE, New York, p. 595, Dec. 1990.
- 59 B.J. Blalock, S. Cristoloveanu, B.M. Dufrene, F; Allibert, and M. Mojarradi, "The multiple-gate MOS-JFET transistor," Int. Journal of High Speed Electronics and Systems, vol. 12, no. 2, pp. 511 - 520, 2002.
- 60 M. Vinet, T. Poiroux, J. Widiez, J. Lolivier, B. Previtali, C. Vizioz, B. Guillaumot, Y. Le Tiec, P. Besson, B. Biasse, F. Allain, M. Cassé, D. Lafond, J. M. Hartmann, Y. Morand, J. Chiaroni, and S. Deleonibus, "Bonded planar double-metal-gate NMOS transistors down to 10 nm," IEEE Electron Device Lett., vol. 26, no. 5, p. 317, 2005.
- 61 G.K. Celler and S. Cristoloveanu, "Frontiers of silicon on insulator," Journal of Appl. Phys. vol. 93, no. 3, pp. 4955 - 4978, 2003.
- 62 B. Doyle, B. Boyanov, S. Datta, M. Doczy, S. Hareland, B. Jin, J. Kavalieros, T. Linton, R. Rios, and R. Chau, "Tri-gate fully-depleted CMOS transistors: fabrication, design and layout," in Symp. on VLSI Tech., 2003, pp. 133-134.
- 63 B.J. Blalock, S. Cristoloveanu, B.M. Dufrene, F; Allibert, and M. Mojarradi, "The multiple-gate MOS-JFET transistor," Int. Journal of High Speed Electronics and Systems, vol. 12, no. 2, pp. 511 - 520, 2002.
- 64 S. Harrison, P. Coronel, F. Leverd, R. Cerutti, R. Palla, D. Delille, S. Borel, S. Jullian, R. Pantel, S. Descombes, D. Dutartre, Y. Morand, M.P. Samson, D. Lenoble, A. Talbot, A. Villaret, S. Monfray, P. Mazoyer, J. Bustos, H. Brut, A. Cros, D. Munteanu, J.L. Autran, and T. Skotnicki, "Highly performant double-gate MOSFET realized with SON process", in IEDM Tech. Dig, 2003, pp. 449-451.
- 65 J.P. Colinge, "Multiple-gate SOI MOSFETs," Solid State Electron., vol. 48, no. 6, pp. 897 - 905, 2004.
- 66 D. Hisamoto, T. Kaga, and E. Takeda, "Impact of the vertical SOI 'DELTA' structure on planar device technology," IEEE Trans. Electron Devices, vol. 38, no. 6, pp. 1419-1424, Jun. 1991.
- 67 X. Huang, W.-C. Lee, C. Kuo, D. Hisamoto, L. Chang, J. Kedzierski, E. H. Anderson, H. Takeuchi, Y.-K. Choi, K. Asano, V. Subramanian, T.-J. King, J. Bokor, and C. Hu, "Sub-50 nm P-channel FinFET," IEEE Trans. Electron Dev., vol. 48, no. 5, p. 880, 2001.

- 68 J. Kedzierski, D.M. Fried, E.J. Nowak, T. Kanarsky, J.H. Rankin, H. Hanafi, W. Natzle, D. Boyd, Y. Zhang, R.A. Roy, J. Newbury, C. Yu, Q. Yang, P. Saunders, C.P. Willets, A. Johnson, S.P. Cole, H.E. Young, N. Carpenter, D. Rakowski, B.A. Rainey, P.E. Cottrell, M. Ieong, and H.-S.P. Wong, "High-performance symmetric-gate and CMOS-compatible VT asymmetric-gate FinFET devices," in IEDM Tech. Dig, The IEEE, New York, p. 437, Dec. 2001.
- 69 C.-H. Jan, U. Bhattacharya, and R. Brain et al., "A 22 nm SoC platform technology featuring 3-D tri-gate and high-k/metal gate, optimized for ultra low power, high performance and high density SoC applications," in IEDM Tech. Dig, pp. 4476–4482, Dec. 2012.
- 70 C. Fenouillet-Beranger, S. Denorme, P. Perreau, C. Buj, O. Faynot, F. Andrieu, L. Tosti, S. Barnola, T. Salvetat, X. Garros, M. Cassé, F. Allain, N. Loubet, L. Pham-Nguyen, E. Deloffre, M. Gros-Jean, R. Beneyton, C. Laviron, M. Marin, C. Leyris, S. Haendler, F. Leverd, P. Gouraud, P. Scheiblin, L. Clement, R. Pantel, S. Deleonibus, T. Skotnicki, "FDSOI devices with thin BOX and ground plane integration for 32 nm node and below," in Proc. ESSDERC, pp. 206-209, 2008, DOI: 10.1109/ESSDERC.2008.4681734.
- 71 C.C. Wu, et al., "High performance 22/20 nm FinFET CMOS devices with advanced high-k/metal gate scheme," in IEDM Tech. Dig, pp. 600-603, Dec. 2010.
- 72 Global foundries website: <https://www.globalfoundries.com/technology-solutions/cmos/fdx/12fdx>.
- 73 Samsung website: <https://news.samsung.com/global/samsung/samsung-starts-mass-production-of-its-2nd-generation-10nm-finfil-process-technology>, nov. 2017.
- 74 Global foundries website: <https://www.globalfoundries.com/technology-solutions/cmos/performance/7nm-finfil>
- 75 R. Merritt, "4 views of the silicon roadmap," EETimes, available at: [https://www.eetimes.com/document.asp?doc\\_id=1331766](https://www.eetimes.com/document.asp?doc_id=1331766), may 19<sup>th</sup>, 2017.
- 76 H. Iwai, "Roadmap for 22 nm and beyond," Microelectron. Engineer., vol. 86, no. 7-9 , pp. 1520 – 1528, 2009.
- 77 S. Barraud, M. Cassé, L. Gaben, P. Nguyen, J.M. Hartmann, M.P. Samson, V. Maffini-Alvaro, C. Tabone, C. Vizioz, C. Arvet, P. Pimenta-Barros, F. Glowacki, N. Bernier, O. Rozeau, M.A. Jaud, S. Martinie, J. Laccord, F. Allain, B. De Salvo and M. Vinet, "Opportunities and challenges of nanowire-based CMOS technologies", SOI-3D-Subthreshold Microelectronics Technology Unified Conference (S3S), DOI: 10.1109/S3S.2015.7333520, 2015.
- 78 S. Barraud, J.-M. Hartmann, V. Maffini-Alvaro, L. Tosti, V. Delaye, and D. Lafond, "Top-down fabrication of epitaxial SiGe/Si multi-(core/shell) p-FET nanowire transistors," IEEE Trans. Electron. Dev., vol. 61, no. 4, pp. 953-956, 2014.
- 79 P. Batude, C. Fenouillet-Beranger, L. Pasini, V. Lu, F. Deprat, L. Brunet, B. Sklenard, F. Piegas-Luce, M. Cassé, B. Mathieu, O. Billoint, G. Cibrario, O. Turkyilmaz, H. Sarhan, S. Thuries, L. Hutin, S. Sollier, J. Widiez, L. Hortemel, C. Tabone, M.-P Samson, B. Previtali, N. Rambal, F. Ponthenier, J. Mazurier, R. Beneyton, M. Bidaud, E. Josse, E. Petitprez, O. Rozeau, M. Rivoire, C. Euvard-Colnat, A. Seignard, F. Fournel, L. Benaissa, P. Coudrain, P. Leduc, J-M. Hartmann, P. Besson, S. Kerdiles, C. Bout, F. Nemouchi, A. Royer, C. Agrafieil, G. Ghibaudo, T. Signamarcheix, M. Haond, F. Clermidy, O. Faynot, and M. Vinet, "3D VLSI with CoolCube process: an alternative path to scaling", Symposium on VLSI-Technology, paper 5-2, 2015.
- 80 T. Nirschl, P.-F. Wang, W. Hansch, and D. Schmitt-Landsiedel, "The tunneling field effect transistors (TFET): the temperature dependence, the simulation model, and its applications," IEEE Int. Symp. On Circuits and Syst, vol. 3, pp. III-713-III-716, 2004.
- 81 W.M. Reddick, and G.A.J. Amaralunga, "Silicon surface transistor," Appl. Phys. Lett., vol. 67, no. 4, pp. 494-496, July 1995.
- 82 I.L. Chuang, L.M.K. Vandersypen, and J.S. Harris, "Bulk spin quantum computation: toward large-scale quantum computation," IEEE Int. Solid-State Circ. Conf. (ISSCC), pp. 96-97, 1998.
- 83 S. De Franceschi, L. Hutin, R. Maurand, L. Bourdet, H. Bohuslavskyi, A. Corna, D. Kotekar-Patil, S. Barraud, X. Jehl, Y.-M. Niquet, M. Sanquer, and M. Vinet, " SOI technology for quantum information processing," in IEDM Tech. Dig, pp. 13.4.1-13.4.4, 2016.
- 84 M. Suri, O. Bichler, D. Querlioz, O. Cueto, L. Perniola, V. Sousa, D. Vuillaume, C. Gamrat, and B. De Salvo, "Phase change memory as synapse for ultra-dense neuromorphic systems : application to complex visual pattern extraction," in IEDM Tech. Dig, pp. 4.4.1-4.4.4, 2011.
- 85 M. Suri, O. Bichler, D. Querlioz, B. Traoré, O. Cueto, L. Perniola, V. Sousa, D. Vuillaume, C. Gamrat, and B. De Salvo, "Physical aspects of low power synapses based on phase change memory devices," J. Appl. Phys., vol. 112, pp. 054904-1 – 054904-10, 2012.
- 86 O. Bichler, M. Suri, D. Querlioz, D. Vuillaume, B. De Salvo, and C. Gamrat, "Visual pattern extraction using energy-efficient "2-PCM synapse" neuromorphic architecture," IEEE Trans. Electron. Dev., vol. 59, no. 8, pp. 2206–2214, 2012.

- 87 D. Garbin, M. Suri, O. Bichler, D. Querlioz, C. Gamrat, B. De Salvo, "Probabilistic neuromorphic system using binary phase change memory (PCM) synapses: detailed power consumption analysis," IEEE. Int. Conf. on Nanotechnology, pp. 91-94, 2013.
- 88 T. Werner, E. Vianello, O. Bichler, A. Grossi, E. Nowak, J.-F. Nodin, B. Yvert, B. De Salvo, and L. Perniola, "Experimental demonstration of short and long term synaptic plasticity using OxRAM multi k-bit arrays for reliable detection in highly noisy input data," in IEDM Tech. Dig, pp. 16.6.1-16.6.4, 2016.
- 89 W. Shockley, "Problems related to p-n junctions in silicon," Solid-State Electron., vol. 2, no. 1, pp. 35-67, 1961.
- 90 K.J. Kuhn, M.D. Giles, D. Becher, P. Kolar, A. Kornfeld, R. Kotlyar, S.T. Ma, A. Maheshwari, and S. Mudanai, "Process technology variations", IEEE Trans. Electron. Dev., vol. 58, no. 8, pp. 2197-2208, 2011.
- 91 L.-T. Pang, K. Qian, C.J. Spanos, and B. Nikolic, "Measurements and analysis of variability in 45 nm strained-Si CMOS technology", IEEE J. of Solid-state Circ., vol. 44, no. 8, pp. 2233-2243, Aug. 2009.
- 92 K. Nagase, S.-I. Ohkawa, M. Aoki, and H. Masuda, "Variation status in 100nm CMOS process and below," in. Int. Conf. on Microelectron. Test Structures Proc., vol. 17, p. 257-261, 2004.
- 93 Y.X. Liu, K. endo, S. O'uchi, T. Kamei, J. Tsukada, H. Yamauchi, Y. Ishikawa, T. Hayashida, K. Sakamoto, T. Matsukawa, A. Ogura, and M. Masahara, "On the gate-stack origin threshold voltage variability in scaled FinFETs and multi-FinFETs," in Symp. On VLSI Tech. pp. 101-102, 2010.
- 94 H.-W. Cheng, M.-H. Han, Y. Li, K.-F Lee, C.-Y. Yiu, and T.-T. Khaing, "Electrical characteristics fluctuation and suppression in emerging CMOS device and circuit," Silicon nanoelectronics workshop, pp. 1-2, 2010, DOI: 10.1109/SNW.2010.5562560.
- 95 A. Asenov, "Simulation of statistical variability in nano MOSFETs," Symposium on VLSI-Technology, pp. 86-87, 2007.
- 96 A. Chatignol, B. Cheng, D. Chanemougane, A.R. Brown, K. Rochereau, G. Ghibaudo, and A. Asenov, "Quantitative evaluation of statistical variability sources in a 45-nm technological node LP -NMOSFET," IEEE Electron. Dev. Lett., vol. 29, no. 6, pp. 609-611, June 2008.
- 97 A. Asenov, "Random dopant induced threshold voltage lowering and fluctuations in sub-0.1  $\mu$ m MOSFET's: a 3-D "atomistic" simulation study", IEEE Trans. Electron Devi., vol. 45, no. 12, 1998.
- 98 A. Asenov, "Simulation of statistical variability in nano MOSFETs", Symp. On VLSI technology, paper 6A-1, pp. 86-87, 2007.
- 99 K. J. Kuhn, "Reducing variation in advanced logic technologies: Approaches to process and design for manufacturability of nanoscale CMOS," in IEDM Tech. Dig., pp. 471-474, Dec. 2007.
- 100 T. Mizuno, J.-I. Okamura, and A. Toriumi, "Experimental study of threshold voltage fluctuation due to statistical variation of channel dopant number in MOSFETs," IEEE Trans. Electron Devices, vol. 41, no. 11, pp. 2216-2221, Nov. 1994.
- 101 Y. Wang, U. Bhattacharya, F. Hamzaoglu, P. Kolar, Y. Ng, L. Wei, Y. Zhang, K. Zhang, and M. Bohr, "A 4.0-GHz 291-Mb voltage-scalable SRAM design in 32-nm high-k metal-gate CMOS with integrated power management," in Proc. IEEE Int. Solid-State Circuits Conf, Dig. Tech. Papers, pp. 456-457, 2009.
- 102 P. Packan, S. Akbar, M. Armstrong, M. Brazier, H. Deshpande, K. Dev, G. Ding, T. Ghani, O. Golonzka, W. Han, J. He, R. Heussner, R. James, J. Jopling, C. Kenyon, S.-H. Lee, M. Liu, S. Lodha, B. Mattis, A. Murthy, L. Neiberg, J. Neirynck, S. Pae, C. Parker, L. Pipes, J. Sebastian, J. Seiple, B. Sell, S. Sivakumar, B. Song, A. St. Amour, K. Tone, T. Troeger, C. Weber, and K. Zhang, "High performance 32-nm logic technology featuring 2nd-generation high-k+ metal gate transistors," in IEDM Tech. Dig., pp. 659-662, Dec. 2009.
- 103 M. J. M. Pelgrom, A. C. J. Duinmaijer, and A. P. G. Welbers, "Matching properties of MOS transistors," IEEE J. Solid-State Circuits, vol. 24, no. 5, pp. 1433-1439, Oct. 1989.
- 104 F. Andrieu, O. Weber, J. Mazurier, O. Thomas, J.-P. Noel, C. Fenouillet-Beranger, J.-P. Mazellier, P. Perreau, T. Poiroux, Y. Morand, T. Morel, S. Allegret, V. Loup, S. Barnola, F. Martin, J.-F. Damencourt, I. Servin, M. Casse, X. Garros, O. Rozeau, M.-A. Jaud, G. Cibrario, J. Cluzel, A. Toffoli, F. Allain, R. Kies, D. Lafond, V. Delaye, C. Tabone, L. Tosti, L. Brevard, P. Gaud, V. Paruchuri, K. K. Bourdelle, W. Schwarzenbach, O. Bonnin, B.-Y. Nguyen, B. Doris, F. Boeuf, T. Skotnicki, and O. Faynot, "Low-leakage and low-variability ultrathin body and buried oxide (UT2B) SOI technology for 20-nm low-power CMOS and beyond," in VLSI Symp. Tech. Dig., pp. 57-58, Jun. 2010.
- 105 S. Ogura, P.J. Tsang, W.W. Walker, D.L. Critchlow, and J.F. Shepard, "Design and characteristics of the lightly doped drain-source (LDD) insulated gate field effect transistors," IEEE Trans. Electron. Dev., vol. ED-27, no. 8, pp. 1359-1367, Aug. 1980.
- 106 B.S. Doyle, B.J. Fishbein, and K.R. Mistry, "NBTI-enhanced hot carrier damage in p-channel MOSFETs," in IEDM Tech. Dig, pp. 529-532A, 1991.
- 107 B.E. Deal, M. Sklar, A.S. Grove, and E.H. Snow, "Characteristics of the surface-state charge (QSS) of thermally oxidized silicon," J. Electrochemical Soc., vol. 114, no. 3, pp. 266-274, 1967.

- 108 S.A. Abbas and R.C. Dockerty, "Hot carrier instability in IGFET's," *Appl. Phys. Lett.*, vol. 27, pp. 147-148, 1975.
- 109 B. Kurz, "Degradation phenomena of planar Si devices due to surface and bulk effects," in 6<sup>th</sup> annual IEEE Reliability Phys. Symp., pp. 47-65, 1967.
- 110 D.M. Fleetwood, F.V. Thome, S.S. Tsao, P.V. Dressendorfer, V.J. Dandini, and J.R. Schwank, "High-temperature Silicon-On-Insulator electronics for space nuclear power systems: requirements and feasibility," *IEEE Trans. Nucl. Sci.* vol. 35, no. 5, pp. 1099-1112, Oct. 1988.
- 111 E.D. Metz, "Metal problems in plastic encapsulated integrated circuits," *Proc. IEEE*, vol. 57, no. 9, pp. 1606-1609, Sept. 1969.
- 112 J.R. Schwank, "Total ionizing dose effects in MOS devices", NSREC short course, 2002.
- 113 A.R. knudson, A.B. Campbell, W.J. Stapor, P. Shapiro, G.P. Mueller, and R. Zuleeg, "Radiation damage effects of electrons and H, He, O, Cl and Cu ions on GaAs JFETs," *IEEE Trans. Nucl. Sci.*, vol. 32, no. 6, pp. 4388-4392, 1985.
- 114 C. Virmontois, V. Goiffon, P. Magnan, S. Girard, C. Inguimbert, S. Petit, G. Rolland, and O. Saint-Pe, "Displacement damage effects due to neutron and proton irradiations on CMOS image sensors manufactured in deep submicron technology," *IEEE Trans. Nucl. Sci.*, vol. 57, no. 6, pp. 3101-3108, Dec. 2010.
- 115 F. B. McLean and T. R. Oldham, "Basic Mechanisms of Radiation Effects in Electronic Materials and Devices," Harry Diamond Laboratories Technical Report, No. HDL-TR-2129, September 1987.
- 116 M.R. Shaneyfelt, J.R. Schwank, D.M. Fleetwood, P.S. Winokur, K.L. Hughes, G.L. Hash, and M.P. Connor, "Interface-trap buildup rates in wet and dry oxides," *IEEE Trans. Nucl. Sci.*, vol. 39, no. 6, pp. 2244-2251, 1992.
- 117 O. Weber et al., "14 nm FDSOI technology for high speed and energy efficient applications," *Symp. on VLSI Tech.*, pp. 1-2, 2014, DOI: 10.1109/VLSIT.2014.6894343.
- 118 M. Gaillardin, M. Martinez, P. Paillet, F. Andrieu, S. Girard, M. Raine, C. Marcandella, O. Duhamel, N. Richard, O. Faynot, "Impact of SOI substrate on the radiation response of ultra-thin transistors down to the 20 nm node", *IEEE Trans. Nucl. Sci.*, Vol. 60, pp. 2583 – 2589, 2013.
- 119 V. Ferlet-Cavrois, P. Paillet, D. McMorrow, A. Torres, M. Gaillardin, J.S. Melinger, A.R. Knudson, A.B. Campbell, J.R. Schwank, G. Vizkelethy, M.R. Shaneyfelt, K. Hirose, O. Faynot, C. Jahan, and L. Tosti, "Direct measurement of transient pulses induced by laser and heavy ion irradiation in deca-nanometer devices," *IEEE Trans. Nucl. Sci.*, vol. 52, no. 6, pp. 2104-2113, 2005.
- 120 Holmes Siedle and Len Adams, "Handbook of radiation effects," Oxford Science Publications, 1993.
- 121 G.R. Hopkinson, V. Goiffon, and A. Mohammadzadeh, "Random telegraph signals in proton irradiated CCDs and APS," *IEEE Trans. Nucl. Sci.*, vol. 55, no. 8, pp. 2197-2204, 2007.
- 122 A.E. Waskiewicz, J.W. Groninger, V.H. Strahan, and D.M. Long, "Burnout of power MOS transistors with heavy ions of californium-252," *IEEE Trans. Nucl. Sci.*, vol. 33, no. 6, pp. 1710-1713, 1986.
- 123 S.E. Diehl-Nagle, "A new class of Single-Even soft errors," *IEEE Trans. Nucl. Sci.*, vol. 31, no. 6, pp. 1145-1148, 1984.
- 124 D.L. Griscom, "Characterization of three E' center variants in X- and  $\gamma$ -irradiated high purity a-SiO<sub>2</sub>," *Nucl. Inst. Meth. In Phys. Res. B (NIMB)*, pp. 481-488, 1984.
- 125 D.L. Griscom and E.J. Friebel, "Fundamental radiation-induced defect centers in synthetic fused silicas: atomic chlorine, delocalized E' centers, and a triplet state," *Phys. Rev. B*, vol. 34, pp. 7524-7533, Dec. 1986.
- 126 D.M. Fleetwood, P.S. Winokur, R.A. Reber, T.L. Meisenheimer, J.R. Schwank, M.R. Shaneyfelt, and L.C. Riewe, "Effects of oxide traps, interface traps, and border traps on metal-oxide-semiconductor devices," *J. Appl. Phys.*, vol. 73, pp. 5058-5074, May 1993.
- 127 E.H. Nicollian and J.R. Brews, "MOS (Metal Oxide Semiconductor) physics and technology," Wiley Ed., New York, 1982.
- 128 T.P. Ma and P.V. Dressendorfer, "Ionizing radiation effects in MOS devices and circuits," Wiley Ed. New York, 1989.
- 129 F.B. McLean, "A framework for understanding radiation-induced interface states in SiO<sub>2</sub> MOS structures," *IEEE Trans. Nucl. Sci.*, vol. 27, no. 6, pp. 1651-1657, 1980.
- 130 P.S. Winokur, H.E. Boesch, J.M. McGarrity, and F.B. McLean, "Field- and time-dependent radiation effects at the SiO<sub>2</sub>/Si interface of hardened MOS capacitors," *IEEE Trans. Nucl. Sci.*, vol. 24, no. 6, pp. 2113-2118, 1977.
- 131 N.S. Saks, M.G. Ancona, and J.A. Modolo, "Generation of interface states by ionizing radiation in very thin MOS oxides," *IEEE Trans. Nucl. Sci.*, vol. 33, no. 6, pp. 1185-1190, 1986.
- 132 S.N. Rashkeev, D.M. Fleetwood, R.D. Schrimpf, and S.T. Pantelides, "Effects of hydrogen motion on interface trap formation and annealing," *IEEE Trans. Nucl. Sci.*, vol. 51, no. 6, pp. 3158-3165, 2004.
- 133 N.S. Saks and D.B. Brown, "Interface trap formation via the two-stage H+ process," *IEEE Trans. Nucl. Sci.* vol. 36, no. 6, pp. 1848-1857, 1989.

- 134 M.R. Shaneyfelt, P.E. Dodd, B.L. Draper, and J.R. Schwank, "Challenges in hardening technologies using shallow trench isolation," IEEE Trans. Nucl. Sci., vol. 45, no. 6, pp. 2584-2592, 1998.
- 135 H.J. Barnaby, "Total-ionizing dose effects in modern CMOS technologies," IEEE Trans. Nucl. Sci., vol. 53, no. 6, pp. 3103-3121, 2006.
- 136 M. Turowski, A. Raman, and R.D. Schrimpf, "Nonuniform total-dose-induced charge distribution in shallow trench isolation oxides," IEEE Trans. Nucl. Sci., vol. 51, no. 6, pp. 3166-3171, 2004.
- 137 C. Brisset, V. Ferlet-Cavrois, O. Flament, O. Musseau, J. L. Leray, J.L. Pelloie, R. Escoffier, A. Michez, C. Cirba, and G. Bordure, "Twodimensional simulation of total dose effect on NMOSFET with lateral parasitic transistor," IEEE Trans. Nucl. Sci., vol. 43, p. 2651, Dec. 1996.
- 138 F. Faccio, and G. Cervelli, "Radiation-Induced Edge Effects in Deep Submicron CMOS Transistors" IEEE Transactions on Nuclear Science, vol. 52 (6), p. 2413, 2005.
- 139 M. McLain, H.J. Barnaby, K.E. Holbert, R.D. Schrimpf, H. Shah, A. Amort, M. Baze, and J. Wert, "Enhanced TID susceptibility in sub-100 nm bulk CMOS I/O transistors and circuits," IEEE Trans. Nucl. Sci., vol. 54, no. 6, pp. 2210-2217, 2007.
- 140 M. Gaillardin, V. Goiffon, S. Girard, M. Martinez, P. Magnan and P. Paillet, "Enhanced radiation-induced narrow channel effects in commercial 0.18  $\mu$ m bulk technology," IEEE Trans. Nucl. Sci., vol. 58, no. 6, pp. 2807-2815, Dec. 2011.
- 141 H.E. Boesch, "Time dependent interface trap effects in MOS devices," IEEE Trans. Nucl. Sci., vol. 35, pp. 1160-1167, Dec. 1988.
- 142 D.B. Brown, "The time dependence of interface state production," IEEE Trans. Nucl. Sci., vol. NS-32, no. 6, pp. 3900-3904, Dec. 1985.
- 143 ASTM F1892 - 12, "Standard guide for ionizing radiation (total dose) effects testing of semiconductor devices," ASTM international, 2018.
- 144 J.L. Leray, E. Dupont-Nivet, J.F. Pere, O. Musseau, P. Lalande, A. Umbert, "Limiting factors for SOI VLSI high-level hardness : modeling and improving", SOS/SOI technology conference, pp. 114-115, 1989.
- 145 J.L. Leray, E. Dupont-Nivet, J.F. Pere, Y/M. Coic, M. Raffaelli, A.J. Auberton-Hervé, M. Bruel, B. Giffard, J. Margail, "CMOS / SOI hardening at 100 Mrad(SiO<sub>2</sub>)", IEEE Trans. Nucl. Sci., vol. 37, n°6, pp. 2013-2019, 1990.
- 146 M. Gaillardin, S. Girard, P. Paillet, J.L. Leray, V. Goiffon, P. Magnan, C. Marcandella, M. Martinez, M. Raine, O. Duhamel, N. Richard, F. Andrieu, S. Barraud and O. Faynot, "Investigations on the vulnerability of advanced CMOS technologies to MGy dose environments," IEEE Trans. Nucl. Sci., vol. 60, no. 4, pp. 2590-2597, 2013.
- 147 M. Gaillardin, M. Martinez, S. Girard, V. Goiffon, P. Paillet, J.L. Leray, P. Magnan, Y. Ouerdane, A. Boukenter, C. Marcandella, O. Duhamel, M. Raine, N. Richard, F. Andrieu, S. Barraud, and O. Faynot, "High total ionizing dose and temperature effects on micro- and nano-electronic devices," IEEE Trans. Nucl. Sci., vol. 62, no. 3, pp. 1226-1232, 2015.
- 148 F. Faccio, S. Michelis, D. Cornale, A. Paccagnella, and S. Gerardin, "Radiation-induced short channel (RISCE) and narrow channel (RINCE) effects in 65 and 130 nm MOSFETs," IEEE Trans. Nucl. Sci. Vol. 62, no. 6, pp. 2398-2403, 2015.
- 149 F. Faccio, G. Borghello; E. Lerario, D.M. Fleetwood, R.D. Schrimpf, H. Gong, E.X. Zhang, P. Wang, S. Michelis, S. Gerardin, A. Paccagnella, and S. Bonaldo, "Influence of LDD spacers and H<sup>+</sup> transport on the total-ionizing-dose response of 65-nm MOSFETs irradiated to ultrahigh doses," IEEE Trans. Nucl. Sci., vol. 65, no. 1, pp. 164-174, Jan. 2018.
- 150 S. Gerardin, A. Gasperin, A. Cester, A. Paccagnella, G. Ghidini, A. Candelori, N. Bacchetta, D. Bisello and M. Glaser, "Impact of 24-GeV proton irradiation on 0.13  $\mu$ m CMOS devices," IEEE Trans. Nucl. Sci., vol. 53, no. 4, pp. 1917-1922, Aug. 2006.
- 151 J.R. Schwank, V. Ferlet-Cavrois, M.R. Shaneyfelt, P. Paillet and P.E. Dodd, "Radiation effects in SOI technologies," IEEE Trans. Nucl. Sci. Vol. 50, no. 3, pp. 522-538, 2003.
- 152 J.R. Schwank, M.R. Shaneyfelt, B.L. Draper, and P.E. Dodd, "BUSFET- a radiation-hardened SOI transistor," IEEE Trans. Nucl. Sci., vo. 46, no. 6, pp. 1809-1816, 1999.
- 153 N. Rezzak, E.X. Zhang, M.L. Alles, R.D. Schrimpf, and H.L. Hughes, "Total ionizing dose radiation response of partially-depleted SOI devices," in IEEE Int. SOI conf. Proc., pp. 1-2., 2010, DOI: 10.1109/SOI.2010.5641057.
- 154 M.L. Alles, H.L. Hughes, D.R. Ball, P.J. McMarr, and R.D. Schrimpf, "Total-ionizing-dose response of narrow, long channel 45 nm PDSOI transistors," IEEE Trans. Nucl. Sci., vol. 61, no. 6, pp. 2945-2950, 2014.
- 155 W.C. Jenkins and S.T. Liu, "Radiation response of fully-depleted MOS transistors fabricated in SIMOX," IEEE Trans. Nucl. Sci. vol. 41, no. 6, pp. 2317-2321, 1994.
- 156 J.R. Schwank, M.R. Shaneyfelt, P.E. Dodd, J.A. Burns, C.L. Keast, and P.W. Wyatt, "New insights into fully-depleted SOI transistor response after total-dose irradiation," IEEE Trans. Nucl. Sci., vol. 47, no. 3, pp. 604-612, 2000.

- 157 P. Paillet, M. Gaillardin, V. Ferlet-Cavrois, A. Torres, O. Faynot, C. Jahan, L. Tosti, and S. Cristoloveanu, « Total ionizing dose effects on deca-nanometer fully depleted SOI devices,” IEEE Trans. Nucl. Sci., vol. 52, no. 6, pp. 2345-2352, 2005.
- 158 P. Gouker, J. Burns, P. Wyatt, K. Warren, E. Austin, R. Milanowski, “Substrate Removal and BOX Thinning Effects on Total Dose Response of FDSOI NMOSFET”, IEEE Trans. Nucl. Sci., Vol. 50, n°6, p. 1776, 2003.
- 159 P. Roche, J.-L. Autran, G. Gasiot, and D. Munteanu, “Technology downscaling worsening radiation effects in bulk: SOI to the rescue,” in IEDM Tech. Dig., pp. 31.1.1-31.1.4, 2013, DOI: 10.1109/IEDM.2013.6724728.
- 160 P.M. Gouker, B. Tyrrell, R. D’Onofrio, P. Wyatt, T. Soares, C. Chen, J.R. Schwank, M.R. Shaneyfelt, E.W. Blackmore, K. Delikat, M. Nelson, P. McMarr, H. Hughes, J. Ahlbin, S. Weeden-Wright, and R. Schrimpf, “Radiation effects in 3D integrated SOI SRAM circuits”, IEEE Trans. Nucl. Sci., vol. 58, no. 6, pp. 2845 – 2854, 2011.
- 161 R.K. Lawrence, J.P. Colinge, and H.L. Hughes, “Radiation effects in gate-all-around structures”, in Proc. of the 1991 IEEE Int. SOI Conf., The IEEE, New York, p. 80, Oct. 1991.
- 162 J.P. Colinge and A. Terao, “Effects of total-dose irradiation on Gate-All-Around (GAA) devices,” IEEE Trans. Nucl. Sci., vol. 40, no. 2, pp. 78-82, Apr. 1993.
- 163 E. Simoen, C. Claeys, S. Coenen, and M. Decreton, “D.C. and low frequency noise characteristics of  $\gamma$ -irradiated gate-all-around silicon-on-insulator MOS transistors,” Solid-State Electron., vol. 38, no. 1, pp. 1-8, Jan. 1995.
- 164 M. Gaillardin, P. Paillet, V. Ferlet-Cavrois, S. Cristoloveanu, O. Faynot, and C. Jahan, “High tolerance to total ionizing dose of  $\Omega$ -shaped gate field effect transistors,” Appl. Phys. Lett., vol. 88, p. 223511, 2006.
- 165 M. Gaillardin, P. Paillet, V. Ferlet-Cavrois, O. Faynot, C. Jahan, and S. Cristoloveanu, “Total ionizing dose effects on triple-gate FETs,” IEEE Trans. Nucl. Sci., vol. 53, no. 6, pp. 3158-3165, Dec. 2006
- 166 J.P. Colinge, A. Orozco, J. Rudee, W. Xiong, C. Rinn Cleavelin, T. Schulz, K. Schrüfer, G. Knoblinger, and P. Patruno, “Radiation dose effects in trigate SOI MOS transistors,” IEEE Trans. Nucl. Sci., vol. 53, no. 6, pp. 3237-3241, Dec. 2006.
- 167 S. Put, E. Simoen, C. Collaert, C. Claeys, M. Van Uffelen, and P. Leroux, “Geometry and strain dependence of the proton radiation behavior of MugFET devices,” IEEE Trans. Nucl. Sci., vol. 54, no. 6, pp. 2227-2232, Dec. 2007.
- 168 F. ElMamouni, E.X. Zhang, R.D. Schrimpf, D.M. Fleetwood, R.A. Reed, S. Cristoloveanu, and W. Xiong, “Fin-width dependence of ionizing radiation-induced subthreshold-swing degradation in 100 nm-gate-length FinFETs,” IEEE Trans. Nucl. Sci., vol. 56, no. 6, pp. 3250-3255, Dec. 2009.
- 169 P.G.D. Agopian, J.A. Martino, D. Kobayashi, E. Simoen, and C. Claeys, “Impact of proton irradiation on strained triple-gate SOI p- and n-MOSFET,s” Proc. RADECS Conf., p. 7, 2011.
- 170 J.-J. Song, B.K. Choi, E.X. Zhang, R.D. Schrimpf, D. M. Fleetwood, C.-H Park, Y.-H Jeong, and O. Kim, “Fin width and bias dependence of the response of triple-gate MOSFETs to total dose irradiation,” IEEE Trans. Nucl. Sci., vol. 58, no. 6, pp. 2871-2875, Dec. 2011.
- 171 V. Kilchytska, J. Alvarado, N. Collaert, R. Rooyakers, O. Militaru, G. Berger, and D. Flandre, “Total-Dose Effects Caused by High-Energy Neutrons and  $\gamma$ -Rays in Multiple-Gate FETs,” IEEE Trans. Nucl. Sci, vol. 57, no. 4, pp. 1764-1770, Aug. 2010.
- 172 S. Put, E. Simoen, M. Jurczak, M. Van Uffelen, P. Leroux, and C. Claeys, “Influence of fin width on the total dose behavior of p-channel bulk MugFETs,” IEEE Electron Dev. Lett., vol. 31, no. 3, pp. 243-245, Mar. 2010.
- 173 C.-H. Jan, U. Bhattacharya, and R. Brain et al., “A22 nm SoC platform technology featuring 3-D tri-gate and high-k/metal gate, optimized for ultra low power, high performance and high density SoC applications,” in IEDM Tech. Dig., Dec. 2012, pp. 4476-4482.
- 174 I. Chatterjee, E. X. Zhang, and B. L. Bhuva et al., “Bias dependence of total ionizing dose response in bulk FinFETs,” IEEE Trans. Nucl. Sci., vol. 60, no. 6, pp. 4476-4482, Dec. 2013
- 175 I. Chatterjee, E. X. Zhang, B. L. Bhuva, R. A. Reed, M. L. Alles, N. N. Mahatme, D. R. Ball, R. D.Schrimpf, D.M. Fleetwood, D. Linten, E. Simôen, J. Mitard, and C. Claeys, “Geometry Dependence of Total-Dose Effects in Bulk FinFETs,” IEEE Trans. Nucl. Sci., vol. 61, no. 6, pp. 2951-2958, Dec. 2014.
- 176 B. Draper, M. Okandan, and M. Shaneyfelt, “Radiation response of a gate-all-around nano-wire transistor,” IEEE Trans. Nucl. Sci., vol. 56, no. 6, pp. 3274-3279, Dec. 2009.
- 177 E.S. Comfort, M.P. Rodgers, W. Allen, S.C. Gausepohl, E.X. Zhang, M.L. Alles, H.L. Hughes, P.J. McMarr, and J.U. Lee, “Intrinsic tolerance to total ionizing dose radiation in Gate-All-Around MOSFETs,” IEEE Trans. Nucl. Sci., vol. 60, no. 6, pp. 4483-4487, Dec. 2013.
- 178 S. Ren, M. Si, K. Ni, X. Wan, J. Chen, S. Chang, X. Sun, E.X. Zhang, R.A. Reed, D.M. Fleetwood, P. Ye, S. Cui, and T.P. Ma, “Total ionizing dose (TID) effects in extremely scaled ultra-thin channel nanowire (NW) Gate-All-Around (GAA) InGaAs MOSFET,” IEEE Trans. Nucl. Sci., vol. 62, no. 6, pp. 2888-2893, Dec. 2015.
- 179 M. Gaillardin, C. Marcandella, M. Martinez, M. Raine, P. Paillet, O. Duhamel, and N. Richard, “Total ionizing dose effects in multiple-gate field-effect transistors”, Semiconductor Science and Technology, vol. 32, no. 8, art. no. 083003, DOI: 10.1088/1361-6641/aa6c02.

- 180 M. Gaillardin, C. Marcandella, M. Martinez, O. Duhamel, T. Lagutere, P. Paillet, M. Raine, N. Richard, F. Andrieu, S. Barraud, and M. Vinet, "Total Ionizing Dose Response of Multiple-Gate Nanowire Field Effect Transistors", IEEE Trans. Nucl. Sci., vol. 64, no. 8, pp. 2061-2068, Aug. 2017.
- 181 J. Riffaud, M. Gaillardin, C. Marcandella, M. Martinez, P. Paillet, O. Duhamel, T. Lagutere, M. Raine, N. Richard, F. Andrieu, S. Barraud, M. Vinet, and O. Faynot, "Investigations on the geometry effects and bias configuration on the TID response of nMOS SOI tri-gate nanowire field effect transistors," IEEE Trans. Nucl. Sci., vol. 65, no. 1, pp. 39-45, 2018.
- 182 J. Riffaud, M. Gaillardin, C. Marcandella, N. Richard, O. Duhamel, M. Martinez, M. Raine, P. Paillet, T. Lagutere, F. Andrieu, S. Barraud, M. Vinet and O. Faynot, "TID response of PMOS nanowire field-effect transistors: geometry and bias dependence," IEEE Trans. Nucl. Sci., (accepted), 2018.
- 183 M. R. Shaneyfelt, D. M. Fleetwood, J. R. Schwank, and K. L. Hughes, "Charge Yield for Cobalt-60 and 10-keV X-Ray Irradiations," IEEE Trans. Nucl. Sci. vol. 38, no. 6, pp. 1187-1194, Dec. 1991.
- 184 T.R. Oldham and J.M. McGarrity, "Comparison of 60Co and 10 keV X-ray response in MOS capacitors," IEEE Trans. Nucl. Sci., vol. NS-30, no. 6, pp. 4377-4381, Dec. 1983.
- 185 S. T. Liu, S. Balster, S. Sinha, and W. C. Jenkins, "Worst case total dose radiation response of 0.35 \_m SOI CMOSFETs," IEEE Trans. Nucl. Sci., vol. 46, p. 1817, Dec. 1999.
- 186 V. Ferlet-Cavrois, T. Colladant, P. Paillet, J.L. Leray, O. Musseau, J.R. Schwank, M.R. Shaneyfelt, J.L. Pelloie, J. du Port de Pontcharra, "Worst Case Bias During Total Dose Irradiation of SOI Transistors", IEEE Trans. Nucl. Sci., Vol. 47, n°6, p. 2183, 2000.
- 187 R.K. Freitag, E.A. Burke, C.M. Dozier and D.B. Brown, "The development of non-uniform deposition of holes in gate oxides," IEEE Trans. Nucl. Sci. vol. 35, no. 6, pp. 1203-1207, Dec. 1988.
- 188 E. A. Burke, "Ionizing Events in Small Device Structures", IEEE Trans. Nuc. Sci., vol. NS-22, pp. 2543-2548, 1975.
- 189 A. Namenson, "Lot uniformity and sample sizes in hardness assurance", IEEE Trans. Nucl. Sci., vol. 35; no. 6, pp. 1506-1511, Dec. 1988.
- 190 R.L. Pease, "Microelectronic Piece Part Radiation Hardness Assurance for Space Systems", NSREC short course, 2004.
- 191 R. Ladbury and J.L. Gorelick, "Statistical method for large flight lots and ultra-high reliability applications", IEEE Trans. Nucl. Sci., vol. 52, no. 6, pp. 2630-2637, Dec. 2005.
- 192 Ionizing dose and neutron hardness assurance guidelines for microcircuits and semiconductor devices, 2005. MIL-HDBK-814
- 193 R. Ladbury, J.L. Gorelick and S.S. McClure, "Statistical model selection for TID hardness assurance", IEEE Trans. Nucl. Sci., vol. 56, no. 6, pp. 3354-3360, Dec. 2009.
- 194 J.A. Felix, P.E. Dodd, M.R. Shaneyfelt, J.R. Schwank, and G.L. Hash, "Radiation Response and Variability of Advanced Commercial Foundry Technologies", IEEE Trans. Nucl. Sci., vol. 53, no. 6, pp. 3187-3194, Dec. 2006.
- 195 P.J. McNulty, K.F. Poole, L.Z. Scheick, and S. Yow, "Role of Process Variation in the Radiation Response of FGMOS Devices", IEEE Trans. Nucl. Sci., vol. 58, no. 6, pp. 2673-2679, Dec. 2011.
- 196 Y. Li, N. Rezzak, E. X. Zhang, R.D. Schrimpf, D.M. Fleetwood, J. Wang, D. Wang, Y. Wu, and S. Cai, "Including the Effects of Process-Related Variability on Radiation Response in Advanced Foundry Process Design Kits", IEEE Trans. Nucl. Sci., vol. 57, no. 6, pp. 3570-3574, Dec. 2010.
- 197 M.L. McLain, H.J. Barnaby, and G.Schlenvogt, "Effects of Channel Implant Variation on Radiation-Induced Edge Leakage Currents in n-Channel MOSFETs", IEEE Trans. Nucl. Sci., vol. 64, no. 8, pp. 2235-2241, Aug. 2017.
- 198 Y. Li, N. Rezzak, R.D. Schrimpf, D.M. Fleetwood, E. X. Zhang, Y. Wu, J. Wang, and D. Wang, " Including the Effects of Process-Related Variability on Radiation Response Using a New Test Chip", Int. Solid State Circuit Conf., 2010.
- 199 S. Gerardin, M. Bagatin, D. Cornale, L. Ding, S. Mattiazzo, A. Paccagnella, F. Faccio, and S. Michelis, "Enhancement of Transistor-to-Transistor Variability Due to Total Dose Effects in 65-nm MOSFETs", IEEE Trans. Nucl. Sci., vol. 62, no. 6, pp. 2398-2403, Dec. 2015.
- 200 R. Merritt, "4 views of the silicon roadmap. Distant hope for a 14-angstrom node," EETimes, available at: [https://www.eetimes.com/document.asp?doc\\_id=1331766](https://www.eetimes.com/document.asp?doc_id=1331766), May 19<sup>th</sup>, 2017.
- 201 S.K. Moore, "EUV lithography finally ready for chip manufacturing. This long awaited technology will extend the life of Moore's law," IEEE Spectrum, available at: <https://spectrum.ieee.org/semiconductors/nanotechnology/euv-lithography-finally-ready-for-chip-manufacturing>, Jan. 5th, 2018.
- 202 P.R. Wallace, "The band theory of graphite," Phys. Rev., vol. 71, no. 9, pp. 622-633, 1947.
- 203 K.S. Novoselov, A.K. Geim, S.V. Morozov, D. Jiang, Y. Zhang, S.V. Dubonos, I.V. Grigorieva, and A.A. Firsov, "Electric field effect in atomically thin carbon films," Sciences, vol. 306, no. 5696, pp. 666-669, 2004.

- 204 S.J. Wing, J. Appenzeller, R. Martel, V. Derycke, and Ph. Avouris, "Vertical scaling of carbon nanotube field-effect transistors using top-gate electrodes," *Appl. Phys. Lett.*, vol. 80, pp. 3817-3819, 2002.
- 205 D. M. Fleetwood, "The evolution of MOS total-ionizing-dose response with Moore's Law scaling," *IEEE Trans. Nucl. Sci.*, vol. 65, no. 8, Aug. 2018 (to be published).
- 206 E.C. Auden, R.A. Weller, M.H. Mendenhall, R.A. Reed, R.D. Schrimpf, N.C. Hooten, and M.P. King, "Single-particle displacement damage in silicon," *IEEE Trans. Nucl. Sci.* vol. 59, no. 6, pp. 3054-3061, Dec. 2012.
- 207 T. Grasser, K. Rott, H. Reisinger, M. Waltl, J. Franco, and B. Kaczer, "A Unified Perspective of RTN and BTI," in *Int. Rel. Phys. Symp. Proc.*, pp. 4A.5.1-4A.5.7, 2014.
- 208 K. Kuhn, C. Kenyon, A. Kornfeld, M. Liu, A. Maheshwari, W.-K. Shih, S. Sivakumar, G. Taylor, P. VanDerVoorn, and K. Zawadzki, "Managing process variation in Intel's 45-nm CMOS technology," *Intel Tech. J.*, vol. 12, no. 2, pp. 93-110, Jun. 2008.

# **Addressing device and environment variations in single event rate predictions**

Brian Sierawski,  
Vanderbilt University,  
Institute for Space and Defense Electronics

## Table of Contents

1 Introduction.....	3
2 Single Event Effects .....	4
2.1 Single Event Upsets.....	4
2.2 Destructive Single Event Effects.....	5
2.3 Random Nature of Single Event Effects.....	5
2.4 Rate Prediction Overview .....	6
2.5 Mechanisms of Energy Loss .....	7
2.6 Proton SEE Cross Sections and Rate Prediction.....	9
2.7 Heavy Ion SEE Cross Sections and Rate Prediction.....	10
2.8 Energy Deposition .....	13
3 Monte Carlo Simulations .....	15
3.1 Energy Deposition.....	15
3.2 Considerations for Radiation Hardened Devices.....	16
3.3 Considerations for Small Volumes.....	18
3.4 Energy Deposition Fluctuations .....	19
3.5 Localized Energy Deposition .....	22
4 Environments .....	24
4.1 Solar Particle Events.....	25
4.2 Geomagnetic Shielding.....	25
4.3 Trapped Particle Environment .....	26
5 Observed On-Orbit Error Rates.....	27
5.1 On-Orbit Single Event Upsets .....	28
6 Summary.....	30
References.....	31

## 1 Introduction

Microelectronics for spacecraft systems are expected to reliably operate in the natural radiation environment, but ionizing radiation limits the useful lifetime of components through permanent failures and reduces availability through transient faults. Even individual energetic particles in these environments present "single event" hazards to electronics. The ability of a component to survive and operate with minimal contribution to a system's error budget are both factors for the part selection process and anomaly reviews. The random nature of particle arrival times and subsequent effects mean that this hazard can affect a system throughout its lifetime. The practice of predicting the "single event" hazard focuses on obtaining the rate of occurrence over a specified mission segment. Worst case analysis addresses the low probability, high radiation levels that a spacecraft might encounter, however, the single event effect (SEE) rates in nominal environments are in most cases treated as static threats. The dynamic environment, orbit, and variation in energy deposition and device response mean that the predicted rate may differ from observed rates. In some cases, this difference is systematic as opposed to variable around the predicted value.

The goal of this course is to increase awareness of the environmental factors and processes that are included in single event models and their impact on the fidelity of rate predictions. Addressing the impact of variation in the environment and device response can be handled if recognized in ground test, modeling, and prediction. In some cases, device variability has long been a part of traditional rate prediction methods. In other cases, the potential for variations in the response to radiation must be considered during ground test. We note that probabilistic environment models have been recently developed to predict environments to a given confidence level. When we calculate or receive an error rate predict, it is an average of many factors. This review will attempt to help the reader answer the questions: How much do changes in the environment influence on-orbit single event effect (SEE) rates? Further, are there circumstances of accelerated test that are not faithful reproductions of the space environment? When should we be concerned or spend additional resources characterizing SEEs?

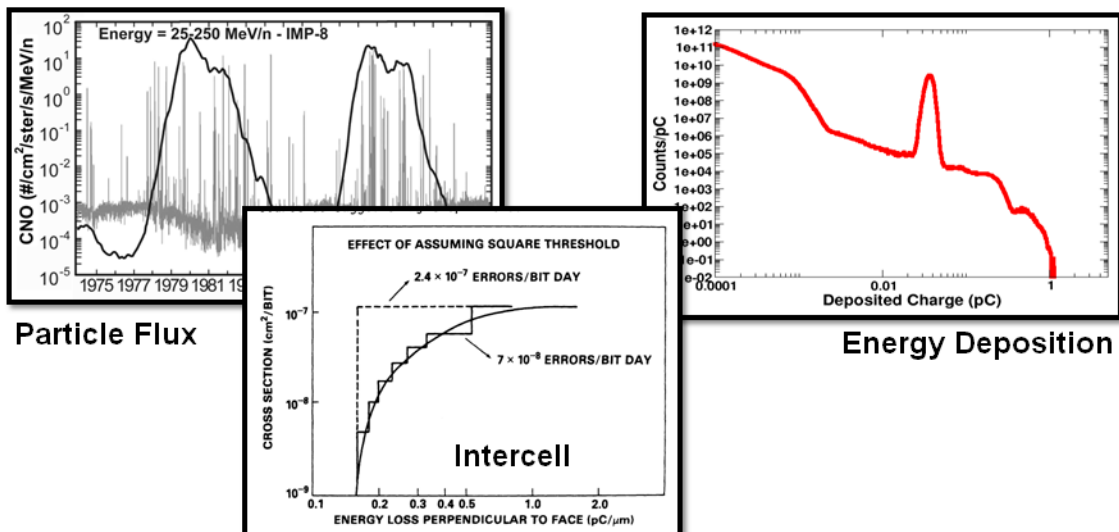


**Figure 1:** Considerations influencing SEE rates include dynamics of the environment, intercell device sensitivity, and probabilistic energy deposition.

In the following sections, basics of single event effects and error rate predictions are reviewed. As illustrated in Figure 1, the dynamic behavior of the space environment, intercell differences in radiation sensitivity, and probabilistic energy deposition should be considered when relating ground test data to on-orbit SEE rates. Specifically, a spacecraft's environment can change over its orbit as well as encounter both long term variation in background radiation and short term events that increase particle flux by orders of magnitude. Also, the distribution of individual cells with in a population of microelectronic devices produces effects at varying thresholds. Finally, individual ion interactions deposit a wide range of energies and rare events can determine the reliability of a part. We show how Monte Carlo methods have been introduced to address and evaluate stochastic energy deposition and provide examples of on-orbit data compared with predicted rates.

## 2 Single Event Effects

Single event effects are unwanted or erroneous electronic responses triggered when an ionizing particle causes an electrical perturbation within a circuit that was designed to control the flow of current and the establishment of electric fields. This typically applies to carrier generation with active portions of semiconductors, although this is not universally true. The result of carrier generation can have either a transient or catastrophic effect on the semiconductor device [1].

Figure 2 illustrates a physical cross-section of a simple complementary-metal-oxide-semiconductor (CMOS) circuit. The pull-up and pull-down transistors implement a simple logic inverter similar to what would be found in a static random access memory (SRAM) bit. In this construction, only one transistor is conducting at a time. When a LOW bias is applied to Q, the n-type transistor is OFF and the drain is biased HIGH through the p-type transistor. This produces a depletion region and electric field across the drain-body junction. When electron-hole generation occurs within a depletion region, carriers are separated by the electric field instead of recombining. The collection of the carriers at the junction produces a spurious current known as a single event transient (SET).

If a single event can cause an effect in a circuit node, it is termed a sensitive node and the region of charge collection around this node is termed the sensitive volume (SV) (Figure 3). A circuit may have multiple sensitive nodes and volumes. In some cases a circuit effect requires disturbance of two or more nodes. Although sensitive volumes are related to physical device geometries, the specifics are often unknown and the circuit response is an aggregate behavior.

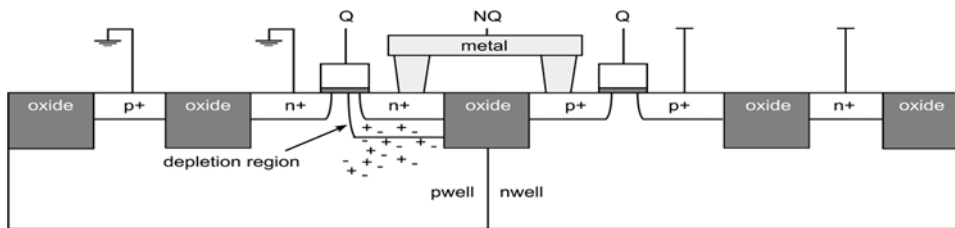


**Figure 2: Example CMOS inverter cross section following generation of charge carriers.**

### 2.1 Single Event Upsets

If this circuit-level effect manifests within a bistable circuit such as the (SRAM) bit (Figure 3), it can feedback and reinforce a state change. The minimum amount of charge generated within a sensitive

volume that is capable of initiating a single event upset is defined as the critical charge  $Q_{\text{crit}}$ . The single event upset (SEU) represents a change in a control or data state and can be attributed to one or more sensitive volumes within the cell (Figure 4). The sensitive node in this example is state dependent and will change according to the value stored in the cell. For this reason, memory cells may have different  $Q_{\text{crit}}$  thresholds for SEU in the '0' and '1' states.

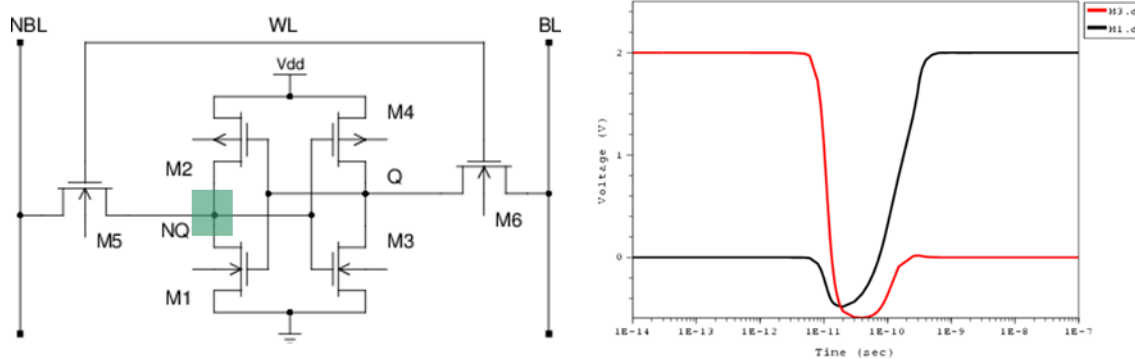


**Figure 3:** Schematic illustration of single a SRAM bit cell and sensitive area (left) with simulated result of circuit node bias following a particle strike (right).

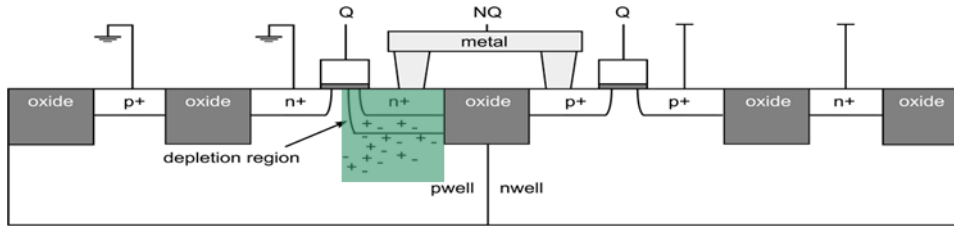


**Figure 4:** Sensitive volume associated with single event upset in SRAM bit cell.

## 2.2 Destructive Single Event Effects

Alternatively, the modulation of electrostatic potentials within the circuit may cause a feedback of electrical current by triggering a parasitic thyristor. This effect, known as single event latchup (SEL), can be physically damaging to the victim if the run-away current is uncontrolled. Other destructive effects such as single event gate rupture (SEGR) and burnout (SEB) can occur when the modulated electric fields exceed critical levels particularly in high voltage applications. Such effects are unrecoverable and therefore present an existential threat to an application. This category of SEE is commonly handled by avoiding parts with the potential for destructive effects, by derating the operational parameters of the part to a safe level, or by demonstrating that the part presents minimal risk to its application. Computing an error rate, or probability of failure in this case, is only meaningful if used in an argument that the part is so unlikely to experience a destructive event that it presents an acceptable risk. Therefore this short course addresses issues pertaining to transient effects, although implications for ground test and modeling should be considered when evaluating catastrophic effects [2][3].

## 2.3 Random Nature of Single Event Effects

Whether subjected to a natural or accelerated environment, we assume that particles incident on a device arrive randomly in space and time. The passage of particles through a unit area is described

as a particle flux and therefore measured in particles/cm<sup>2</sup>-s. The time integrated flux yields fluence measured in particles/cm<sup>2</sup>. A random process where events, such as particle arrival times, occur independently is known as a Poisson process. Mathematically, the probability of k events within t time units can be described by a Poisson distribution. The distribution is parameterized by  $\lambda$ , an assumed constant rate derived from the mean number of events observed in a time interval. For single event effects, this is the familiar errors/second or errors/day.

$$P(k; t) = e^{-\lambda t} \frac{(\lambda t)^k}{k!}$$

The rate parameter  $\lambda$  is typically the object of analysis and is a prediction from accelerated ground tests combined with models of the space environment. This form is most appropriate for predicting single event transients and upsets where it is assumed that a previous effect does not influence the occurrence of another. As we will see in the following sections, in practice, the rate parameter is estimated from average events over some finite time frame, often mission, orbit averaged, or occasionally for a given time window (e.g. 5 minutes). These time scales work nicely with classical rate prediction tools, but may not be what is sought for the probabilistic analysis. For instance, rather than seeking an error rate, one might actually be interested in the probability of an error within a given time window or critical operation. Perhaps one is interested in the probability of multiple bit upsets which are strongly dependent on the rate  $\lambda$ . In these cases, typical orbit averaged predictions can be insufficient.

## 2.4 Rate Prediction Overview

The rate parameter is generally not measurable and must be predicted through a process involving experimental characterization and modeling (Figure 5). Prediction is a necessary activity because we cannot fully reproduce the energetic particle environment on the ground. Various methods have developed over time but each relies on integrating the probability that a particle will cause an event over the population of the same particle in the environment. In operation spacecraft will be subject to ionizing radiation from the background of space, solar particle events, and trapped particles near-Earth or bodies with a significant magnetosphere (Jupiter) [4]. The galactic cosmic ray (GCR) background includes highly energetic particles beyond the ability to artificially reproduce. Particularly true for the highly energetic environment minimally affected by spacecraft shielding, the particle flux is nearly isotropic. Environment models generate particle flux spectra for worst case (peak), orbit-averaged, and orbit segments.

In the absence of a simulated environment, ground-based accelerators are used to sample from the natural particle distribution in order to characterize a device. The most common practice is to subject a device to a mono-energetic broadbeam in a series of exposures. With limited samples, simple models are used to substitute probabilities as well as interpolate and extrapolate data. A reduced dataset is necessitated by the inability to reproduce environmental factors, time constraints, both from projects and accelerator availability, and cost constraints.

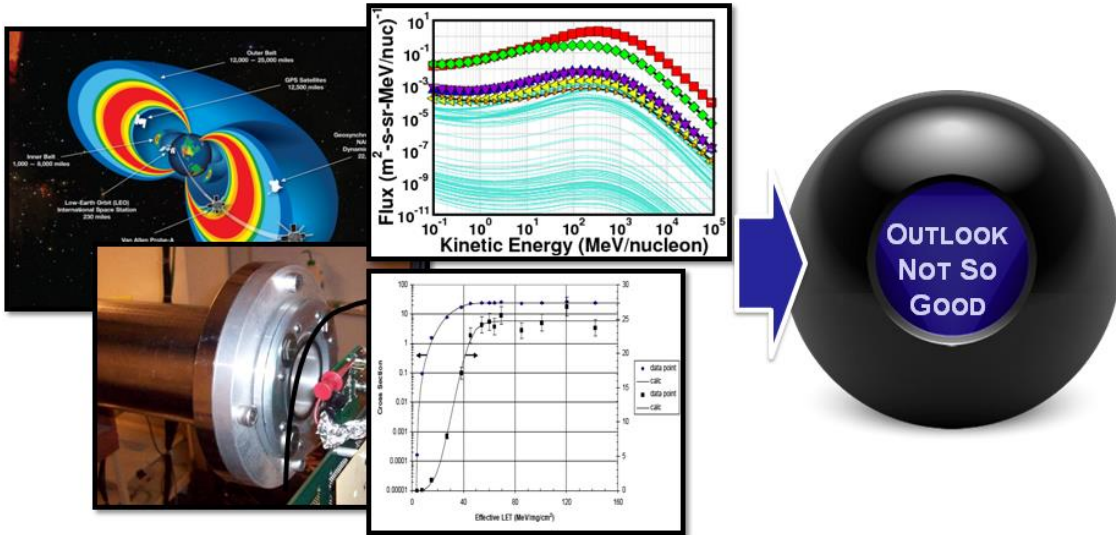


Figure 5: Inputs into general rate prediction tools.

## 2.5 Mechanisms of Energy Loss

As energetic particles move through material structures, they transfer energy to the structure through electronic and nuclear interactions [5]. Figure 6 illustrates an ion losing energy through electronic stopping. In this process, the particle undergoes multiple inelastic interactions with electrons in the target. In a semiconductor, the energy excites electrons into the conduction band creating electron-hole pairs along the projectiles trajectory. Over the entirety of the trajectory, this appears as a continuous process of energy loss and particle stopping and can be represented as a rate of energy loss  $dE/dx$  (MeV/cm). For a given material normalized to the target density, this yields the familiar particle linear energy transfer or LET (MeV-cm<sup>2</sup>/mg). This representation makes energy deposition a predictable process that can be characterized by tables indexed by atomic number, energy, and target material. SRIM is one such useful application to obtain the energy loss values [5].

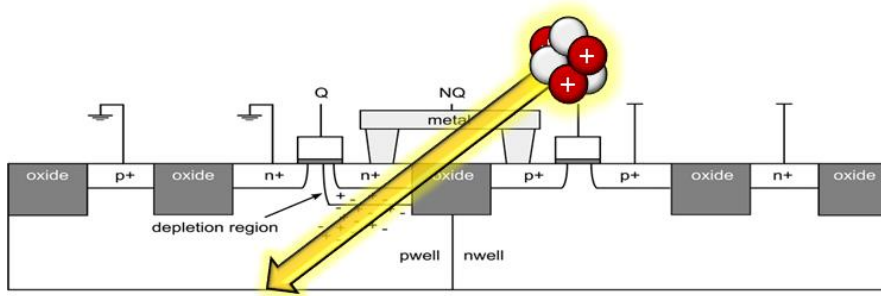
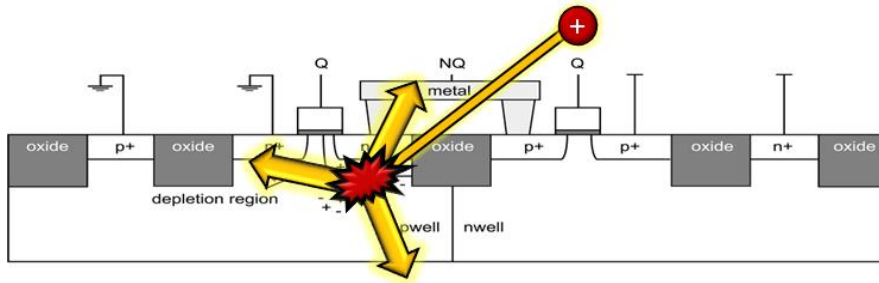


Figure 6: Electronic stopping of an ionized particle in a semiconductor device.

Occasionally, an energetic particle (ion, proton, or neutron) interacts with atomic nuclei in the semiconductor device (Figure 7). When this happens, the collision may be elastic or inelastic. The primary particle may transfer some of its energy to a recoiling nucleus which in turn moves through the device producing charge carriers. Alternatively, the reaction may be inelastic in which case the nucleus may fragment into two or more particles. The break up may follow any of a number of

channels producing secondaries with atomic numbers as high as the sum of the struck nucleus and projectile. The secondaries move away from the reaction site and produce charge carriers along multiple tracks. In any of these cases, the secondary particles are capable of ionizing the surrounding material with potentially larger  $dE/dx$  values than the primary particle. This has historically been the mechanism by which energetic protons cause ionization effects.



**Figure 7: Nuclear stopping of a particle in a semiconductor device.**

Experimentally, an interaction cross section is the probability of a projectile interacting with a target. This is measured by accelerating a beam of projectiles at a target and counting the resulting interactions. The probability of interaction is the number of events for a given beam fluence ( $\text{cm}^{-2}$ ) and therefore yields cross section units of  $\text{cm}^2$ . This concept has been extended to single event effects where an interaction is a proton or ion event that results in an upset, latchup, burnout, etc. Through counting observable effects, SEE cross sections can be measured. Cross section is commonly represented as  $\sigma$ , however, being a measurement, it is also subject to uncertainty frequently reported in terms of the standard deviation. Herein,  $\sigma$  will be used exclusively to represent a cross section. Proton cross sections are measured as a function of energy and heavy ion cross sections are commonly measured as a function of LET. When a measured cross section is the result of many targets such as memory array, the reported value can be normalized to the number of repetitions providing a normalized value ( $\text{cm}^2/\text{bit}$ ).

While it is easy to imagine that this method can measure a geometric area (i.e. sensitive area), one should take care to remember the value is in fact a probability. Energetic proton SEE cross sections are an appropriate example. In this case an incident proton must strike a target nucleus in order to generate sufficient charge and also do so in a location that leads to an SEE. An interaction may also be defined as simultaneous events such as one primary particle striking two circuit nodes simultaneously. It may even require that a digital circuit be in a particular operational state for the effect to be observed therefore the measured probability of an interaction is conditional to the circuit being in the required state. Clearly, an interaction cross section is not necessarily a geometric cross section.

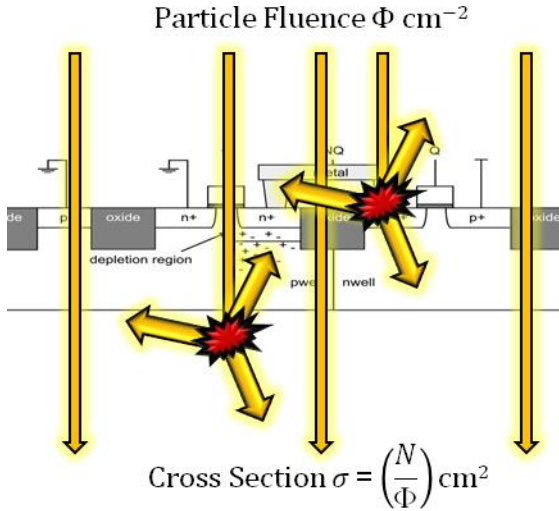


**Figure 8: Experimental measurement of interaction cross section.**

## 2.6 Proton SEE Cross Sections and Rate Prediction

Proton-induced SEE cross sections can be measured experimentally at an accelerator by tuning or degrading a beam to various energies. In the case of protons, one typically measures up to hundreds of MeV. At these energies protons are so weakly ionizing that they primarily initiate SEE through nuclear reactions. Additionally, the angular distribution of secondaries is mostly isotropic. Together, this means that the proton SEE cross section is often independent of the beam direction. For many devices, this reduces the number of test conditions. At each energy step, events are observed for a measured beam fluence. The cross-section is calculated at several energies with the intention to determine a proton energy threshold and cross section saturation value. Proton SEE cross sections will increase with energy in accordance with the increase in interaction cross sections.

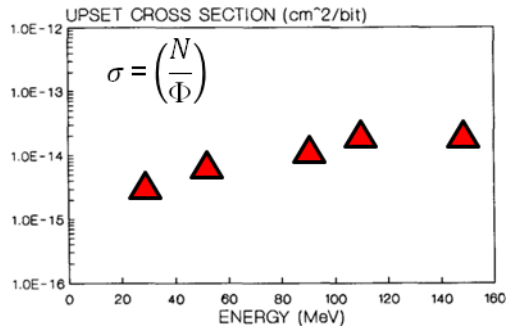


**Figure 9: Example proton single event upset cross sections from [8].**

Protons are so weakly ionizing, they primarily initiate SEE through nuclear reactions and the angle of the incoming beam does not matter. This simplification permits one to assume that the cross-section is independent of angle. In modern devices, protons are capable of causing single event upset through direct ionization and will be addressed in Section 3.3.

Each device may have different saturation cross-sections because of the size of the sensitive volume and different energy thresholds because of the type of secondary particles and associated kinetic energy required to initiate an event.  $\sigma(E)$  is in practice the continuous function fit to experimental

measurements to allow for interpolation and extrapolation across the energy domain. Bendel proposed a function to characterize the cross section over energy easily parameterized by a single threshold parameter A [7]. Later, this function was modified to the present two-parameter form (Figure 10 left) by including the fitting parameter B [8]. In the current form, the threshold and saturated cross section can be fit independently.

Given the proton SEE cross section is constant over angle of incidence for a device under test, measurements from broadbeam irradiation can be combined with an environment flux to yield an error rate (Figure 10 right). This takes the form of the integral of the product of the proton SEE cross section and flux over energy. The rate calculated in this fashion is appropriate for all manner of SEE applied to both devices and systems. Dependence of the proton cross section on angle has been observed for some devices and may require a more general form of integration for the predicted rate [9-11].

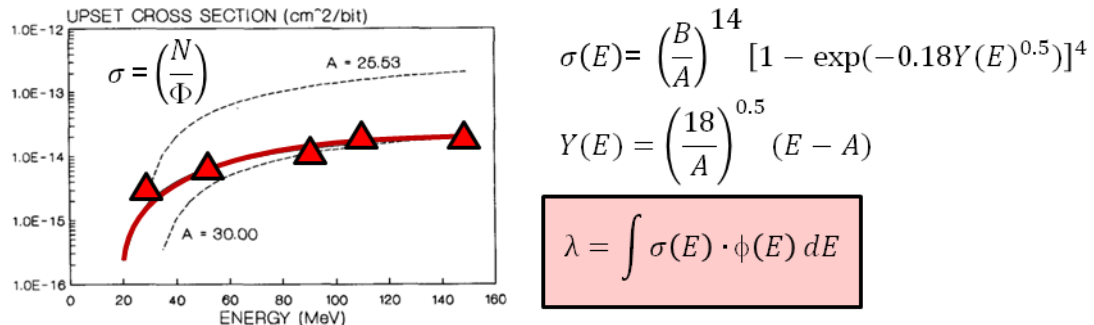
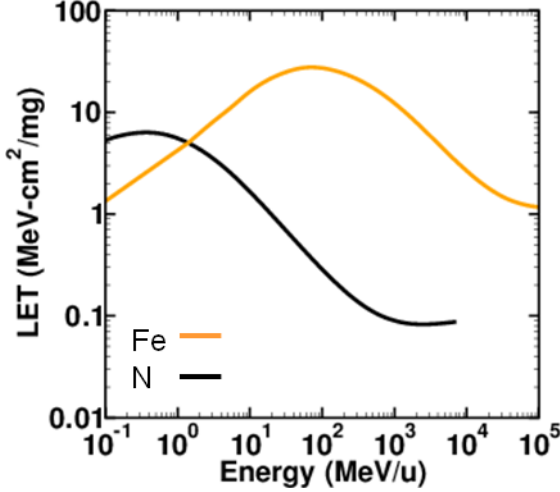


Figure 10: Traditional proton single event rate prediction from [8].

## 2.7 Heavy Ion SEE Cross Sections and Rate Prediction

LET finds application to prediction for two reasons. First, we cannot reproduce the full space environment over energy on the ground. In many cases of ion-induced single event effects, the kinetic energy and mass of the initiating particle is inconsequential. The effect for these cases is a function of the amount of charge generated in a region or sensitive volume within the device.

Although the ion kinetic energy is not directly connected to SEE, the energy loss is a function of particle energy (MeV/u) and ionization state (commonly particle Z). This is described by LET curves for a given target material. LET curves for iron and nitrogen in silicon are shown in Figure 11. The particle LET is not monotonic with energy. The rate of ionization increases at low energies up to the Bragg peak and then falls off at higher energies. The particle then reaches a minimum ionization until it is corrected by relativistic effects at even higher energies. In this plot, it is apparent that different ion species can have the same LET (e.g. 2 MeV-cm<sup>2</sup>/mg). Therefore, LET does not uniquely describe an incident particle. In fact, there are often multiple combinations of ion species and energy that can be folded into a single LET value.



**Figure 11:** Linear energy transfer curves for iron and nitrogen in silicon.

The natural space environment consists of all ion species and is available from tools like CREME96 [12]. Light ions tend to be the highest in abundance with a large flux of protons, helium, carbon, nitrogen, and oxygen (Figure 12 left). Additionally, iron is one of the most abundant species in space, and thus plays a prominent role in single event effects. The differential particle flux over energy spectra are reduced to a single flux over LET spectrum through application of the stopping power curves. Shown in integral form (Figure 12 right), the spectrum yields a convenient form for heavy ion analysis.

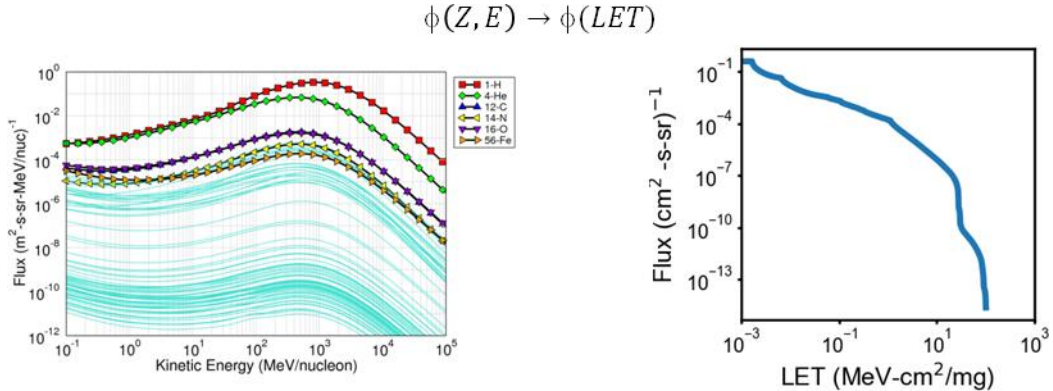


**Figure 12:** CREME96 generated particle environments.

Heavy ion energy deposition is dominated by ionization and therefore depends on its path through a sensitive volume. Assuming the LET is unchanging over short distances, the charge generated in the sensitive volume  $Q_{\text{dep}}$  is the product of the LET and pathlength  $p$ . If an incident particle deposits sufficient energy to exceed the critical charge value associated with the sensitive volume, a single event will follow.

The idea of a rectangular parallelepiped (RPP) shaped sensitive volume (Figure 13 left) with a single critical charge threshold can be used to explain cross sections and on-orbit error rates [13-15]. Informing the model requires an estimate of the critical charge and sensitive volume dimensions. As the latter is informed by experimental measurement, it is an inherent assumption that a circuit only

has a single sensitive volume, or repetition of that volume. Contributions from additional volumes contribute to inaccuracy of the rate calculation. Experimentally, one measures the SEE cross section as a function of LET, assuming this is unique. Using a broadbeam incident to the normal direction of the die, these data (Figure 13 right) should resemble a Heaviside function (also assuming all incident particles have identical LET values). Since only a single pathlength exists, runs below a threshold  $LET_{th}$  do not deposit sufficient energy to result in an SEE and therefore yield a null cross section. Runs above  $LET_{th}$  will result in SEE with a cross section (probability) related to the projected area of the sensitive volume. In practice, however, the cross section curve does not resemble a Heaviside function even at normal incidence. These curves tend to have a soft turn-on or threshold.

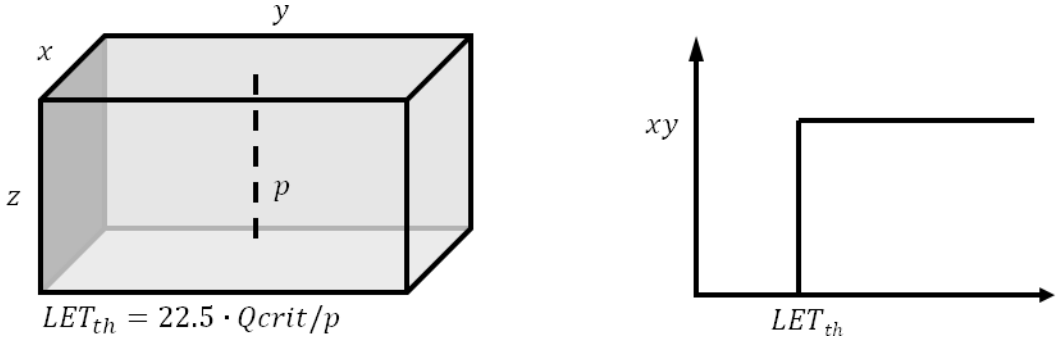


**Figure 13:** Assumptions of the rectangular parallelepiped (RPP) model and projected cross section.

At angle, there is a distribution of pathlengths through the sensitive volume. For a given LET, there will result a distribution of deposited charge associated with cross sections from 0 to the projected area. In practice, an SEE cross section / device is measured at normal incident, normalized to the number of volumes or bits, and applied to the RPP lateral dimensions. The depth dimension is difficult to obtain experimentally and as such is assumed to be 1  $\mu\text{m}$ .

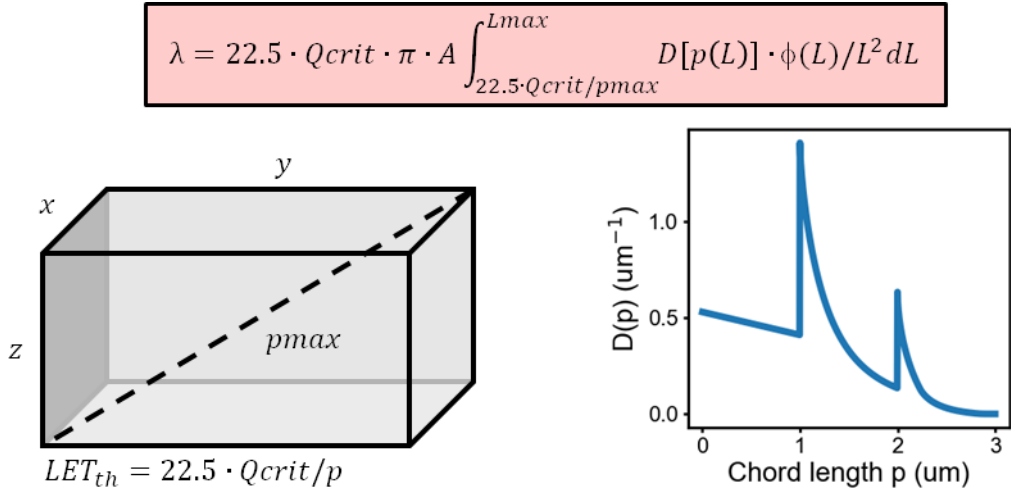


**Figure 14:** RPP method of SEE rate prediction.

The integral RPP (IRPP) method was proposed to account for apparent device to device variations. Petersen suggested that an array of devices have a distribution of critical charge values rather than

a single well-defined threshold [17]. This results in ground based test data having a softer threshold (Figure 15 right). The aggregate per bit cross section is an average of individual cell responses. Whether the process variation here is in critical charge, sensitive volume collection depth, or a gain parameter [18], the result is the same. The integration is over a series of RPP volumes with identical dimensions but varied LET thresholds and not a distribution of sensitive areas within a cell. One could calculate this, however, it is not implemented in the traditional IRPP.

Data exhibiting this trend are fit to a continuous function for interpolation and extrapolation. Most commonly, a Weibull form or lognormal form is used. The Weibull curve therefore captures the die-level process variation. Additional variation of critical charge values or  $LET_{th}$  should not be applied to the curve as it is already present. However, die-to-die process variations could still alter the threshold parameter. Intracell variation of sensitive volume dimensions are not captured in this method. Such variations would result in a distribution of what is considered the saturated cross section. The population of cells with a given  $Q_{crit}$  is obtained by interpreting the normalized Weibull as a cumulative distribution function [19]. Later interpretation attributed the shape of the cross section curve to intracell variation in charge collection and amplification [20]. The IRPP is, however, expressed as the integral of the probability a volume has a critical charge value  $Q_{crit}$  times the RPP-calculated error rate for the sensitive volume.

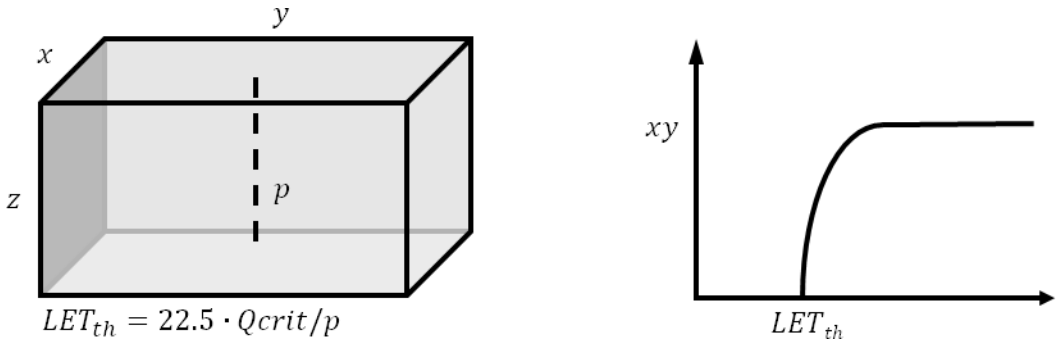


Figure 15: Typical shape of measured SEE cross section curves.

## 2.8 Energy Deposition

Although the heavy ion rate predictions previously described performed over LET space, LET does not uniquely describe an incident particle. The reduction of the space environment into an LET distribution loses information about the particle energy and mass. Again, using iron and nitrogen as examples, the two ions overlap in LET space but over different energy ranges. The overlapping region for nitrogen is below 10 MeV/u. Iron can have LET values that range from 1 to 26 MeV-cm<sup>2</sup>/mg in silicon. Comparable LET values to nitrogen are achieved only at very high energies rather than near stopping.

If species in the space environment is plotted as its percent composition over LET (Figure 16), it is plain to see that iron dominates the majority of the spectrum easily compromising 50% of the galactic cosmic ray flux for its full LET range. The species constitutes nearly all of the environment around 26 MeV-cm<sup>2</sup>/mg making it a goal for radiation-hardened electronics. However, iron also comprises nearly 80% of ~ 1 MeV-cm<sup>2</sup>/mg particles making it major contributor to SEE in soft

electronics as well. Unfortunately, accelerated tests at these energies can present significant logistical and cost barriers [21].

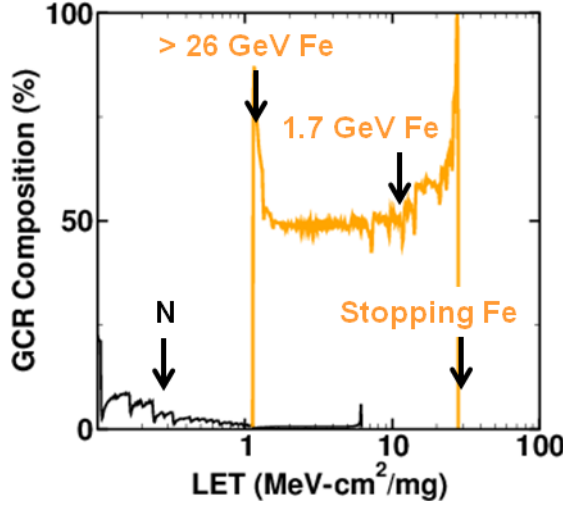


**Figure 16:** LET composition of the GCR environment computed by CREME96.

Most single event rate predictions assume that particle LET defines a unique cross section. This allows us to test with particles available at accelerator facilities as substitutes for constituents of the entire space environment. These facilities accelerate particles to 10s of MeV/u and only cover a small portion of the energies found in space. Texas A&M for example, offers 40 MeV/u beams. Even using 15 MeV/u beams, the majority of the LET space is covered. However, Figure 17 highlights the portion of corresponding energy space covered in the natural environment. This can amount to a deficiency in test. For example, the majority of particles in space with  $\text{LET} = 1.2 \text{ MeV/cm}^2\text{-mg}$  are 78 GeV Fe ions. As a substitute in ground tests, a device can be exposed to 210 MeV N at TAMU. A second desirable data point for characterization exists at 27 MeV/cm<sup>2</sup>-mg. In space, stopping Fe ions constitute a large flux at this LET, but would be a difficult test on the ground because of limited range and straggling. Instead, 1.3 GeV Kr could be used as a substitute with a similar LET. In both of these examples, there is a large disparity between the test energy and that experienced in space. Experimental characterization and implications of ion energy for SEE test have been reported in [22-25].

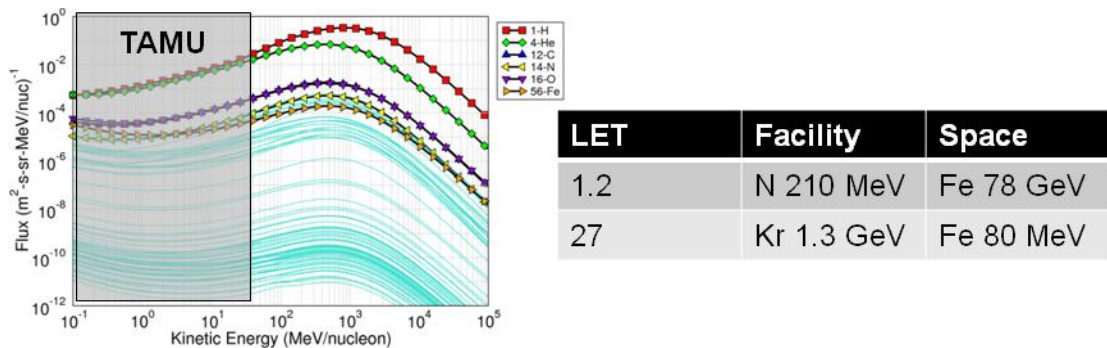


**Figure 17:** Comparison between accelerated test energies and the space environment.

### 3 Monte Carlo Simulations

Complete consideration of the particle environment and the mechanisms for energy loss is really only practical through Monte Carlo simulations. This is particularly true for complex materials systems and circuits. A number of groups have developed Monte Carlo tools capable of assessing total ionizing dose and single event effects for microelectronics. Some of these include CUPID, MCNPX, PHITS, and Geant4 derivatives such as MRED. An anthology of Monte Carlo tools along with brief descriptions and references for the aforementioned tools can be found in Reed [26]. The codes attempt to include electronic and nuclear stopping of protons and ions with the probability of interactions based off of physical models and empirical cross sections. Simulations can reproduce broadbeam or isotropic environments and track individual particles in microelectronic structures (Figure 18). The following discussions will use MRED as a simulation tool, but are not specific to the tool alone [27-29].

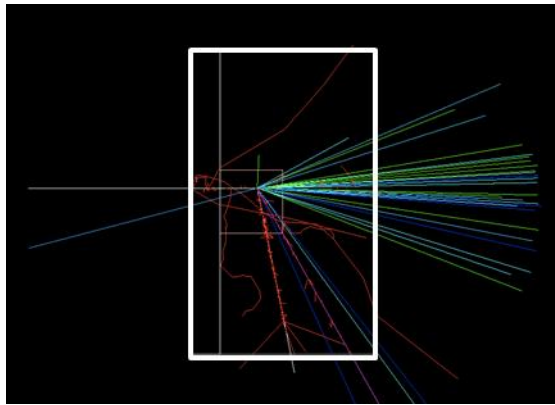


Figure 18: Example radiation transport simulation illustrating particle trajectories.

#### 3.1 Energy Deposition

Monte Carlo tools in general integrate a value of complex probabilities by randomly sampling from an input distribution. Fundamental to this technique is the sampling of large numbers of events. A common treatment of the simulated result is to summarize by means of a histogram. For radiation effects this process samples incident particles contributing to a distribution of energy deposition within a sensitive volume. The total energy lost is tabulated and scored within a histogram. Figure 19 is the output of a simulation where each bin contains the number of incident particles that resulted in the respective generated charge (22.5 MeV/pC in silicon). In this example, the counts have been normalized to the bin width to plot a differential spectrum. The outcome counts associated with any bin conveys the probability of the outcome occurring.

Simulations of a mono-energetic ion beam on a sensitive volume will have energy (charge) distributions with similar shapes. The pronounced peak in the middle of the plot indicates the large probability of outcomes associated with electronic stopping. The energy value where the peak occurs will be associated with the product of the particle LET and the distance traveled through the volume. The peak has some width as well characteristic of energy straggling as each ion will have slightly different energy loss. However, not all incident particles result in energy deposition directly related to the particle LET. In the lowest bins, simulated particles with trajectories that miss the

sensitive volume scatter secondary electrons into the volume. The higher energy bins are populated by events that caused recoils and particle reactions. These events are much less common than direct ionization but can deposit much more charge. The inclusion of multiple physical processes allows a single simulation to fully reproduce energy deposition distributions.

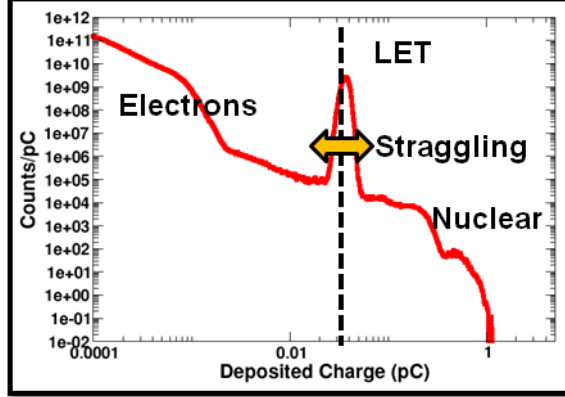


Figure 19: Example output of radiation transport simulation.

### 3.2 Considerations for Radiation Hardened Devices

Figure 20 presents a representative dataset where more than one energy loss mechanism was involved in the measurement of experimental single event cross sections. The data were collected at TAMU on an SEU-hardened SRAM array. Circuit and TCAD simulations showed the device to be immune to SEU up to 50 MeV-cm<sup>2</sup>/mg. However, upsets below the LET threshold were measured at the beam. Troublesome datasets like this exhibit cross sections that vary over several orders of magnitude from low to high-LET [30][31]. The saturation cross section appears characteristic of direct ionization but does not fall to zero below the threshold. While the IRPP method was proposed to address non-ideal, rolling steps between threshold and saturated cross sections, measurable cross sections down to LET = 1.79 MeV-cm<sup>2</sup>/mg (523 MeV Ne) are hard to justify through critical charge variations. The shape of this cross section curve suggests separate mechanisms at work in the low LET and high LET regions [32].

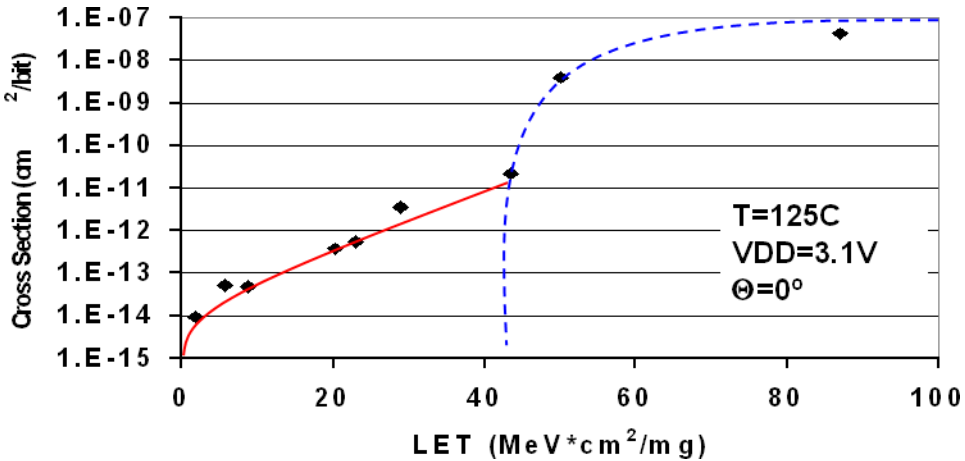
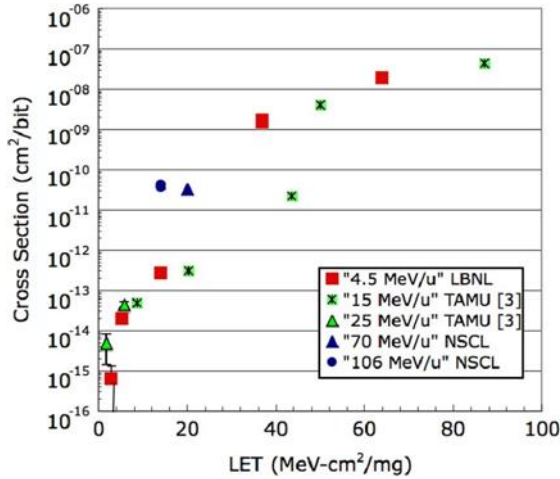


Figure 20: Single event upset cross sections for an SEU hardened SRAM from [31].

In 2007, a set of publications addressed the issue of the energy dependent single event cross section [34][35]. In these datasets, Figure 21 for example, distinct cross section values were measured with high and low-energy beams. In this case, cross sections below an  $\text{LET} = 50 \text{ MeV}\cdot\text{cm}^2/\text{mg}$  are in question. Multiple dataset were presented that exhibit the same lack of correlation for single event upsets and single event latchup in a variety of SRAMs. Monte Carlo simulations of single event cross sections across energy corroborated this conclusion. In addition to undermining the application of LET-based rate predictions based off of routinely collected datasets, these works presented hardness assurance implications. Dodd recommends testing for energy dependence if possible, but recognized that schedule and cost restrictions could preclude such an activity. In addition, caution is given to datasets with LET threshold between 2 and 40  $\text{MeV}\cdot\text{cm}^2/\text{mg}$ . Further guidance can be found in [35]. When cross sections are driven by heavy ion nuclear reactions, the application of LET-based models does not appropriately calculate the contribution to the overall error rate. For this, a separate, detailed calculation is required.



**Figure 21: Energy dependent cross sections measured on a high-reliability, radiation-hardened SRAM from [34].**

The broad application of LET-based rate prediction methods to the radiation hardened SRAM previously presented will result in inaccuracies. The cross-section curve contains both upsets due to ionization, which are pathlength dependent, and nuclear reactions, which are pathlength independent. An IRPP method was applied to the low-LET and high-LET regions separately assuming that the two regions were the result of two distinct upset mechanisms. One population of sensitive volumes must have a small cross section and low-LET threshold and the other population must have a larger cross section and high-LET threshold. This resulted in underprediction of the observed error rate on the NASA MESSENGER spacecraft by nearly a factor of 500 [34]. Monte Carlo analysis after the discrepancy was identified produced an error rate that was in good agreement to data. This dataset has been cited as an example of the importance of identifying and treating the ion-induced nuclear reaction mechanism appropriately.

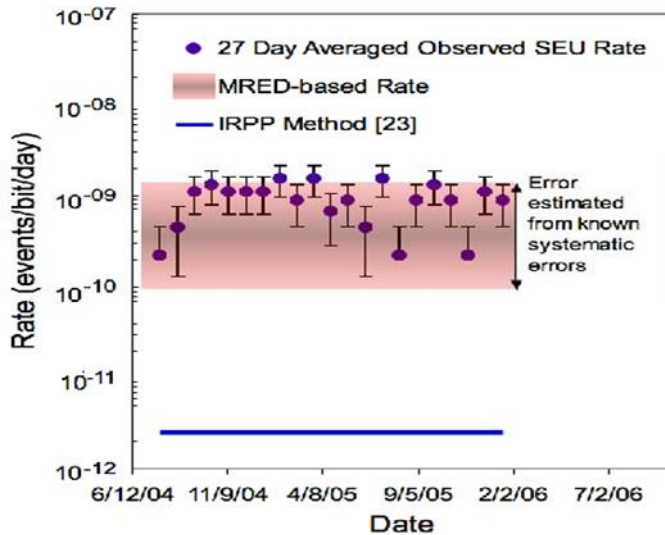


**Figure 22:** Predicted event rates for a radiation hardened SRAM using IRPP method and Monte Carlo simulation from [34].

### 3.3 Considerations for Small Volumes

As observed in the previous section, to understand single event sensitivity of radiation hardened devices, information about how much charge is generated within devices and where the charge is generated is necessary. Similarly, for small volumes, which tend to imply soft devices, detailed modeling of energy loss and charge generation can become important in ways not anticipated with LET models. Unless considering circuit or system level protection schemes like triple modular redundancy, ion-induced nuclear reaction induced events will not significantly contribute to the overall error rate. This is because the flux of low-LET particles that are capable of causing single event effects far exceeds the rare events. However, for small volumes, details of electronic stopping can lead to variation in effects. Investigations have suggested that measured effects at a facility may not represent the events observed on-orbit for these devices. Xapsos asserts that differences between energy deposited in volumes and the LET is only accurate in restricted conditions [36]. Differences arise because LET represents the average energy loss of the ion rather than energy deposited in a volume and simultaneously does not represent statistical variations.

Small feature sizes are often accompanied with low critical charge values. Over the last 10 years, a number of experiments have been conducted which conclude that singly-charged particles including protons, muons, and x-ray-induced electrons (Figure 23) are sufficiently ionizing to cause single event upsets in modern technology nodes [37-45]. These upsets have been demonstrated on both bulk and SOI CMOS devices at and below the 65 nm technology node. This is a significant conclusion for radiation-soft electronics in space are subject to a high flux of protons and electrons. Protons have a peak LET of approximately 0.5 MeV-cm<sup>2</sup>/mg. The plot in the upper left corner reports the dramatic increase in the SEU cross section comparing data collected at a low-energy mono-energetic proton beam to traditional many-MeV beams. Although results appear to jump around 1 MeV, this is just due to the energy required to penetrate into the device overlayers. In reality, the greatest cross section for a sensitive device will be due to proton stopping. In the GCR spectrum, the iron peak establishes a recognizable knee in the LET environment at 26 MeV-cm<sup>2</sup>/mg. Devices with

SEE thresholds near or below this knee can experience greatly increased error rates. Similarly, devices with SEE thresholds near or below the proton component will be vulnerable to a much larger component of the environment. The concern is that environments rich in protons may induce an overwhelming error rate in such devices and negate any sort of mitigation or error correction.

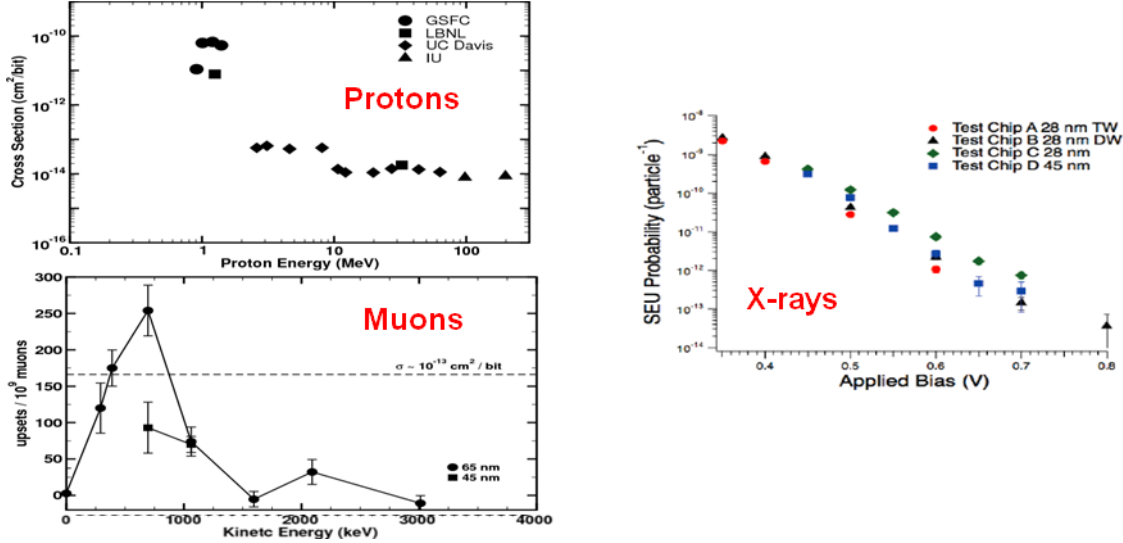


Figure 23: Experimental datasets demonstrating single event upsets from lightly ionizing particles (protons, muons, electrons) from [40][42][45].

### 3.4 Energy Deposition Fluctuations

LET is a measure of average energy loss over a pathlength resulting from the sum of individual interactions. Variation from the average occurs as a result of probabilistic interactions with the target material. It is important to remember that the stopping power curve is a characteristic model of the energy loss of a particle with a given kinetic energy. It tells nothing directly of the consequence for films of various thicknesses. Thickness of the target contributes to straggling observed as the broadening of the distribution of energy deposition around the LET value [46]. Additionally straggling is energy dependent. The distribution of energy loss along the length of the track is increased for thin absorbers and minimally ionizing particles [47].

In Figure 24 from [48], two particles passing through 1 μm silicon sensitive volume were simulated in MRED. The track on the left illustrates the path of a 50 MeV proton (blue) and the few electron interactions (red). The track on the right illustrates the result of a 280 MeV oxygen ion passing through the same structure. This simulation with a larger stopping power produced many more electron interactions spanning all along the projectiles path. In both simulations, each of the secondary electrons carries away part of the energy lost through electronic stopping. For additional protons, the few interactions in the target mean that event-by-event variability of energy deposition will be greater as occasionally one or more secondary electrons will be produced or stop within the sensitive volume. This process is efficiently averaged out in the case of the oxygen ion therefore less variability is observed.

The plot on the right captures the probability density of energy deposition events also known as the Landau distribution [49][50]. The distribution expresses the probability of a 50 MeV proton

depositing a given amount of energy in the 1  $\mu\text{m}$  thick silicon volume (i.e. eV/ $\mu\text{m}$ ). Although the particle LET is reported as  $9.84 \times 10^{-3} \text{ MeV}\cdot\text{cm}^2/\text{mg}$  (2 keV/ $\mu\text{m}$ ) by SRIM, it is clear that the most probable events are not represented by the average. For a given proton, the greatest probability is that the event results in less energy than predicted by the LET calculation. The plot also indicates that there is a large variance in the distribution.

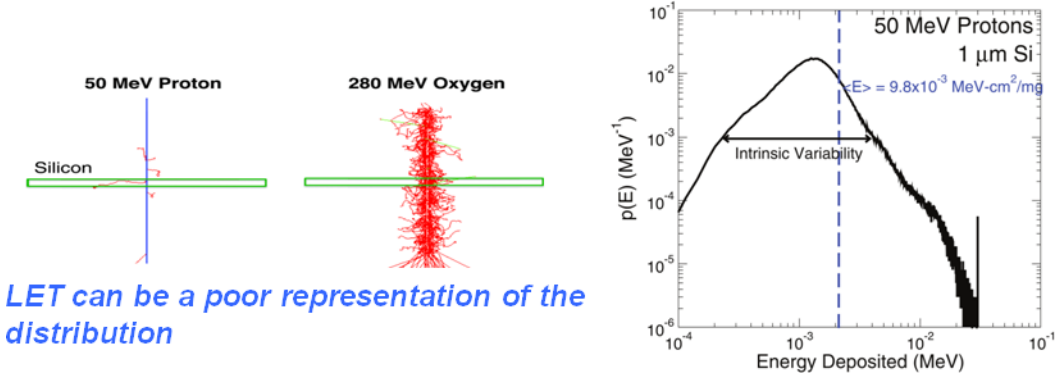


**Figure 24:** Simulated distribution of events as a result of energy deposition fluctuation in electronic stopping (50 MeV proton) from [48].

Simulations were constructed to tabulate the energy deposition from an 80 MeV iron beam of particles incident on layers of varying thicknesses. Distributions in Figure 25 are evaluated against the expected energy loss consistent with the particle LET of 27 MeV $\cdot\text{cm}^2/\text{mg}$ . In this case, each distribution should be identical except scaled along the energy axis in proportion to the layer depth. Each of the distributions is the result of numerous electronic interactions with peaks occurring on the mean value or LET. The 1  $\mu\text{m}$  thick layer therefore appears in the higher energy bins of the histogram with a very well-defined peak. The 100 nm thick volume produces the distribution in the middle. The energy of the peak should decrease by a factor of 10 consistent with the reduction of the particle pathlength. While this happens, the relative variance of this distribution has also increased. Decreasing the layer thickness to 10 nm, the variance in the distribution becomes wider spanning more than an order of magnitude in energy. Rare events even exceed the LET by a factor of 5. While application to modern devices depend on specific collection volumes (not planar layers) these thicknesses are representative of transistor feature sizes. Simulating 78 GeV iron on the same three layer thicknesses further increases the energy straggling in Figure 26. Differences in SEE occurrence depending on ion energy may be a consideration for these very small feature sizes.

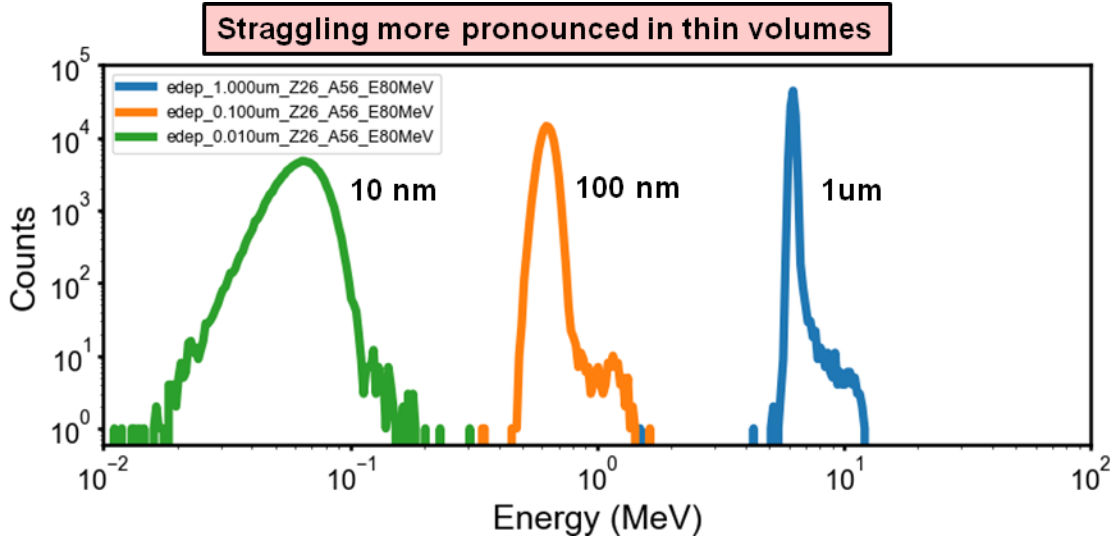


Figure 25: Simulated distribution of events as a result of energy deposition fluctuation (80 MeV iron).

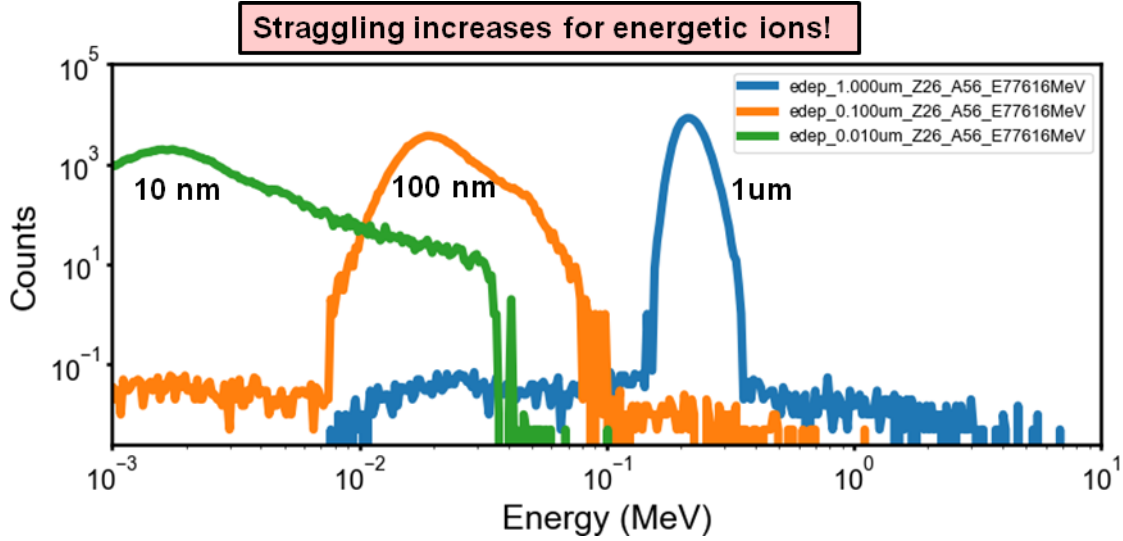
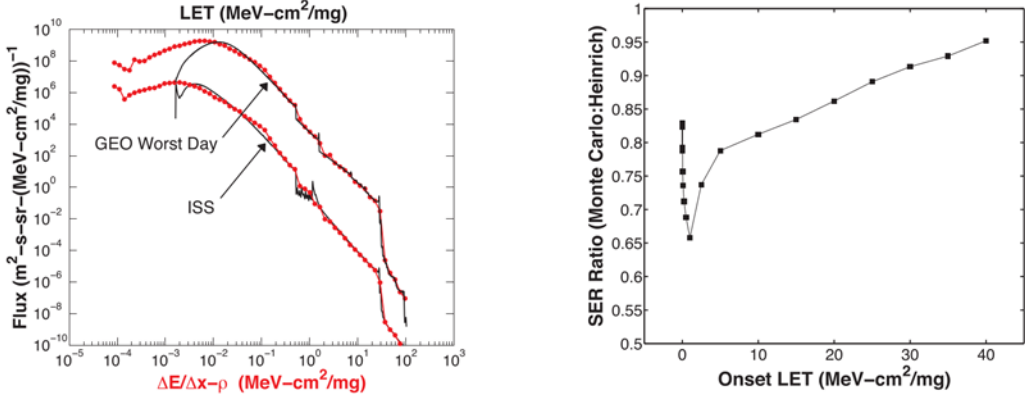


Figure 26: Simulated distribution of events as a result of energy deposition fluctuation (78 GeV iron).

Additional simulations evaluated the effect of straggling on the SEE rates. In this study, a 500 nm thick layer was placed within a silicon structure. The GEO worst day and ISS environments were generated with CREME96 and used as the environment. Particles were sampled by atomic number and energy. The energy deposited in the volume was recorded for each event and using the volume depth converted into an equivalent LET value. The aggregate behaviors of the simulations were replotted with the original spectra in Figure 27 (left). In essence the simulated output more accurately represents the distribution of energy deposition. The shape of the input and transported environments are very similar, but the LET peaks are missing. These peaks in the input spectrum exist because of the direct conversion from minimally ionizing particles to a LET value. Whereas in the simulation, the value varies and smooths out these portions of the spectrum. The authors concluded that the effect on an RPP calculated error rate (Figure 27 right) would be the greatest for parts with LET thresholds near one of these peaks in the spectrum.



Environment models for ISS and GEO worst day as simulated by MRED, and compared to the traditional LET spectrum from CREME96

The relative percent change in SER for the GEO solar minimum spectra simulated in this work and the traditional spectra used in CREME96.

**Figure 27: Impact on rate prediction for a 500 nm deep volume including energy straggling of the LET environment from [48].**

### 3.5 Localized Energy Deposition

Figure 28 illustrates the secondary electrons (red) produced by 280 MeV Fe (LET = 22 MeV-cm<sup>2</sup>/mg) and 28 GeV Fe (LET = 1.2 MeV-cm<sup>2</sup>/mg) ions. Within the material structure, small sensitive volumes are drawn representing a 22 nm SRAM technology. The few tracks on the right predict that each electron will be more energetic and have a larger range than the secondaries from the lower energy ion. Electrons in this simulation had as much as 10 keV and traveled well away from the primary particle path. This work proposed that individual electrons were capable of causing an upset in the 22 nm technology under consideration. Although these examples have different LET, one can imagine the implication for measured cross sections using particles with the same LET but vastly different energies.

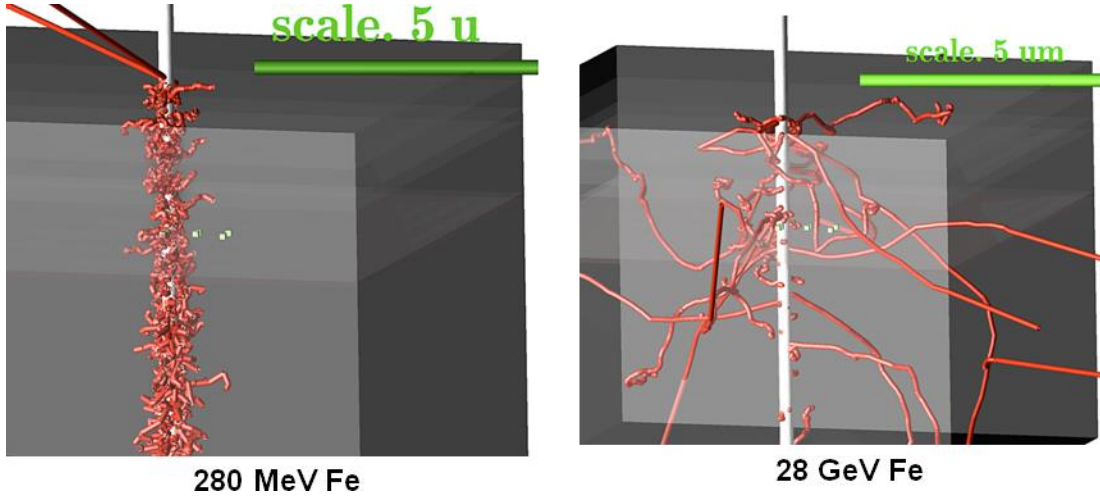


**Figure 28: Secondary electron tracks simulated in MRED for low and high energy ions from [51].**

When the electrons pass through the sensitive volume (left column, Figure 29 right), insufficient energy (charge) is recorded to result in an upset assuming a critical charge value of 0.09 fC in a 50 nm cube. However, some of the events generate delta electrons that stop within the sensitive volume. In this figure, the primary electron is drawn in blue, secondary or delta electrons are drawn

in red. These scattering events can deposit 10s of keV. When a short range delta electron is produced within close proximity to the sensitive volume (right column), charge is introduced locally and may be sufficient to initiate an SEE. The effect was evaluated for 40 and 100 keV primary electron beams to elucidate effects observed at the Arnold Engineering Development Complex (AEDC) [52].

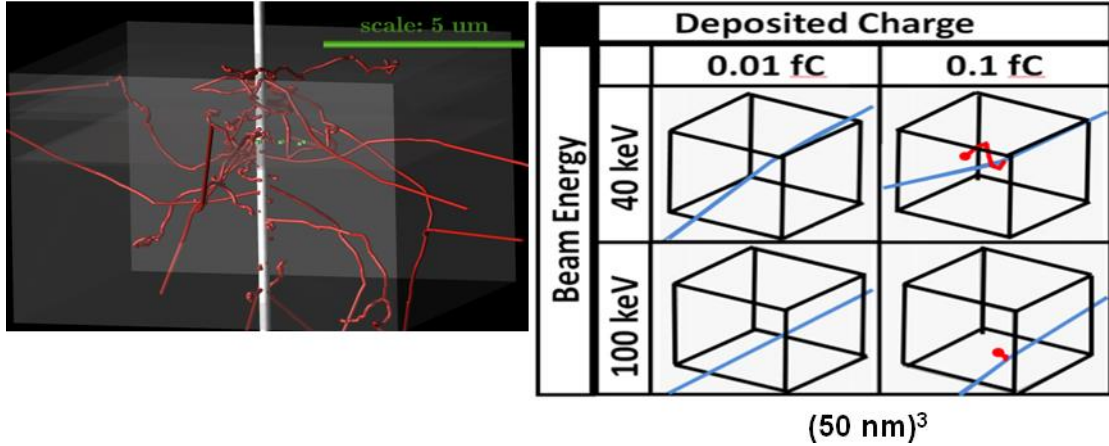


Figure 29: Simulated electron-induced single event effects from [52].

In a series of experiments, 28 and 45 nm SRAMs were exposed to 40 keV and 100 keV electron sources (Figure 30). The memories were held at reduced bias to intentionally increase the susceptibility to single event upset through lowering the critical charge and provide an indication of susceptibility of smaller technology nodes. Each device was demonstrated functional at the reduced bias. The measured electron induce SEU cross sections are larger for the 28 nm SRAM compared to the 45 nm and lower voltage 0.45V compared to 0.55 V.

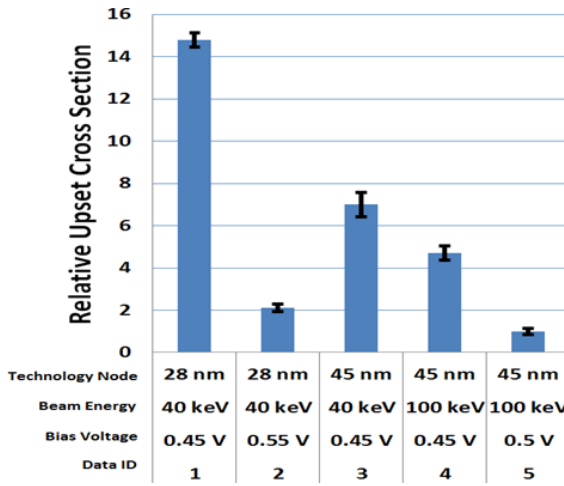


Figure 30: Measured electron-induced single event upsets from [52].

Monte Carlo simulations of various space environments evaluated the contribution of electron-induced events to the overall error rate. In Figure 31 charge generated in a sensitive volume was tabulated as the result of the galactic cosmic rays and electrons in the outer Van Allen belt. For most devices, consideration of the GCR environment alone is sufficient to predict the error rate. If the

device is sufficiently sensitive though, much like the 28 nm and 45 nm results, electron-induced SEE threshold can be observed. In this simulation, the threshold was observed at 0.2 fC. A very sensitive device would experience many times more frequent events. Also notable were simulations of the Jovian environment where a similar part could experience more electron-induced events than protons under particular shielding situations.

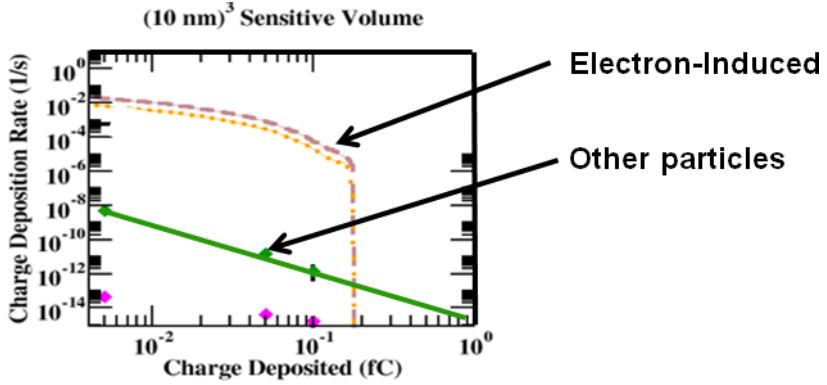


Figure 31: Simulated electron-induced single event effects in GEO from [52].

## 4 Environments

The space environment can present a large dynamic variation in particle flux and therefore single event error rates. In this section, the various components of the environment are examined and briefly discussed. The galactic cosmic ray background affects electronics both near-Earth and throughout the solar system. Satellites exposed to this environment will be subject to high-LET particles. The cosmic rays enter the solar system with a constant flux and consist of a wide range of ion species and energies. Observations of the near-Earth particle flux have recorded changes in the particle flux over time (Figure 32). Short-term jumps in the particle flux are due to solar particle events, however, the long-term background exhibits variations over many years. Solar activity, measured by the number of sunspots, modulates the GCR flux. Periods of high solar activity impede the extra-solar particles from reaching the inner solar system therefore creating an anti-correlation of the GCR flux with the 11 year solar cycle. Practically, this represents approximately a 30% change across the LET spectrum. The implication for single event rates will be relevant for both soft and radiation hard devices similarly.

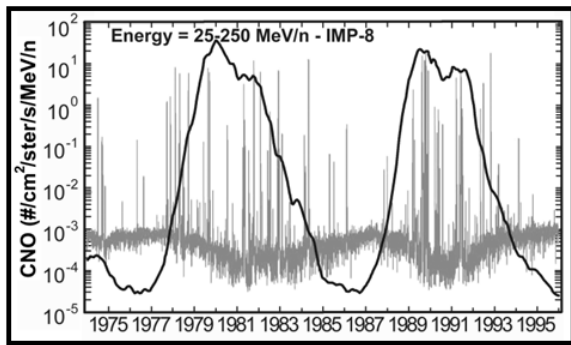


Figure 32: Particle flux variation over solar cycle from [4].

## 4.1 Solar Particle Events

Solar activity is associated with solar particle events that can greatly exceed the GCR background for several days at a time. Figure 33 contains measured proton fluence by the GOES-13 proton monitor [53]. Three energy ranges are plotted for greater than 1, 10, and 100 MeV. Spikes in the plot indicate solar radiation storms. Focusing on the greater than 1 MeV proton data, it is clear that the low energies are highly variable with swings nearly two orders of magnitude. For parts with similar SEE threshold energies, error rates could experience comparable swings.

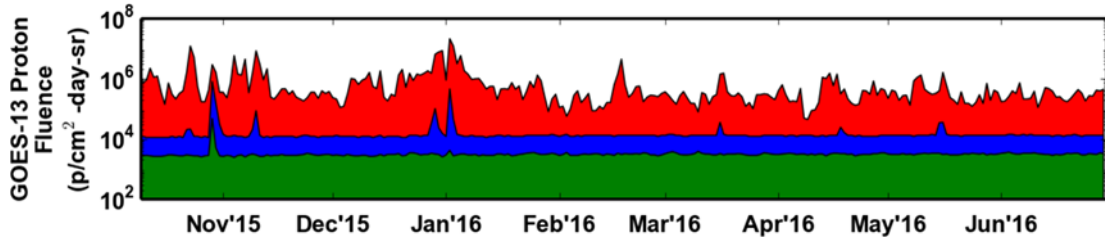


Figure 33: Solar particle events and increase in particle flux from [53].

A worst case LET environment presented in [54] (Figure 35) increases the particle flux by six orders of magnitude. More recent probabilistic models such as ESP [55] and PSYCHIC [56] are capable of predicting the solar fluences for radiation effects analyses.

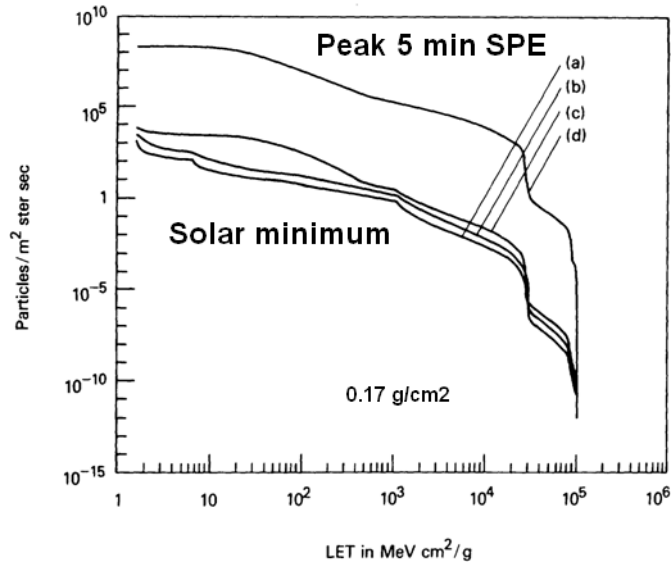
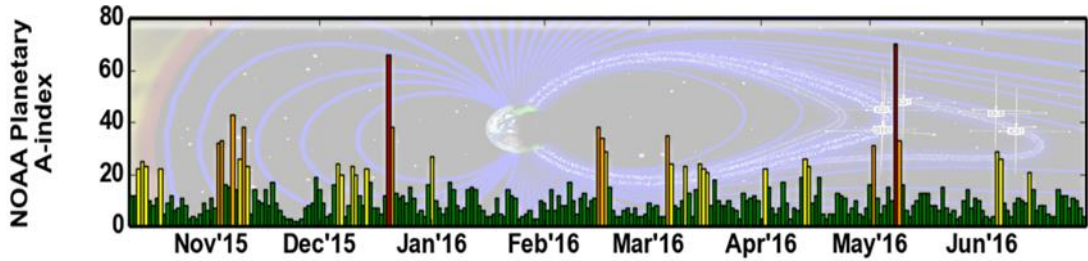


Figure 34: Increase in particle flux versus LET during peak five minute solar particle event compared to GEO solar minimum conditions from [54].

## 4.2 Geomagnetic Shielding

Satellites in low-Earth orbits will benefit from the protection provided by the Earth's magnetosphere. The magnetic field provides a shield against galactic cosmic rays by deflecting their trajectories. The resistance to deflection is measured by a particles magnetic rigidity. Orbits at low altitudes and inclination will benefit the most as particles must cross field lines in order to reach the satellite. Particles below a given rigidity cannot reach the satellite in a given position. This rigidity cutoff varies over time especially for eccentric or high inclination orbits. Note this is a cutoff based

on the particle momentum (energy) and not directly applied to a given LET range. The magnetosphere also exhibits dynamic behavior during geomagnetic storms due to solar activity. These disturbances can cause the rigidity cutoff to move to lower latitudes and rigidity values to change over altitude. The K-index is used to characterize disturbances in the magnetosphere as measured by individual ground-based observatories. Large values in this index indicate the effect of a geomagnetic storm. The A-index provided by NOAA (Figure 35) averages these measurements providing a metric of planetary disturbance [57]. The daily record provides an idea of the frequency of these events. Environment generators like the one found in CREME96 often provide either stormy or quiet magnetosphere conditions.



**Figure 35:** Historical planetary A-index recording recent geomagnetic storms from [57].

In the case of polar orbits, a satellite will experience a large change in the geomagnetic rigidity along its trajectory (Figure 36). The Earth's rigidity is strongest near the equator and allows ions to penetrate deep into the atmosphere near the poles. Therefore the ion flux is higher for that portion of the orbit compared to the remainder. When an orbit averaged particle flux spectrum is generated, this time dependence is removed; rather one assumes that the particle flux is uniform over the entire orbit. In reality, the error rate may vary across the orbit. This is also true of very elliptical orbits where the majority of time is spent at low cutoff (apogee).

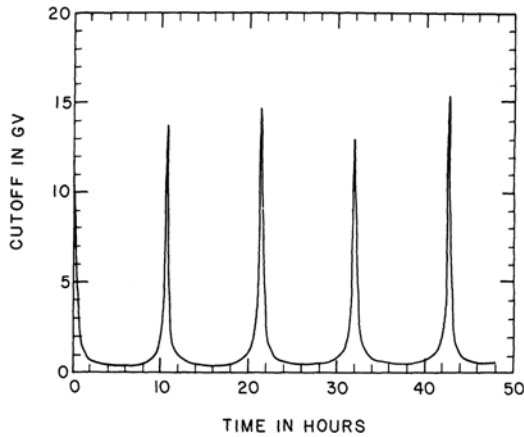


**Figure 36:** Variation in geomagnetic cutoff along satellite orbit from [54].

### 4.3 Trapped Particle Environment

Finally, the radiation belts provide a significant source of protons and electrons that can impact spacecraft in low and medium Earth orbits. Orbits with large eccentricity or high inclinations can produce temporal changes in particle flux as a spacecraft moves through the inner and outer belts.

Additionally, passes through the South Atlantic Anomaly will momentarily produce an increase in proton flux. For these reasons, trapped proton models often provide orbit-averaged particle flux and peak flux spectra (Figure 37). As the spacecraft may experience the majority of SEE in these high flux regions, the peak spectra are most appropriate for proton error rate predictions when the mission segment of interest is short (e.g. 5 minutes). Like the magnetosphere, the belts also fluctuate. New models of the trapped particle environment allow users to generate spectra for a given confidence level [58].

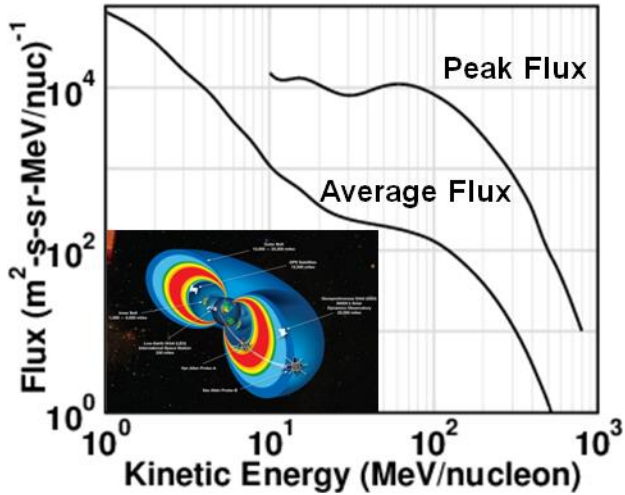
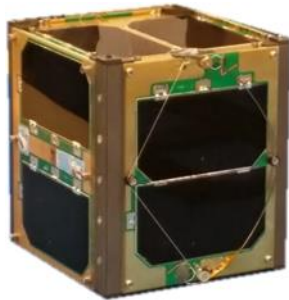


Figure 37: Comparison of peak and average trapped particle flux.

## 5 Observed On-Orbit Error Rates

The popularity of CubeSats in recent years has presented the opportunity to provide on-orbit data for comparison to predicted radiation effects in devices under test with relatively short development times. Typical delivery schedules are one to two years after the launch award. The Vanderbilt RadFxSat payload was designed to monitor single event effects in a device under test [59]. The objective is to collect data regarding mechanisms to improve modeling and prediction capabilities rather than fielding one specific part. For example, our objective is to improve our understanding of the relationship between ground test results and on-orbit errors for parts that exhibit proton direct-ionization sensitivity.

The payload has been integrated and flown on two AMSAT satellites to date (Figure 38). The first mission, AO-85, was launched in October 2015. The satellite currently operates in a low-Earth orbit primarily exposed to trapped protons. The experiment carries eight 4Mb SRAM (ISSIIS64WV25616B) and monitors the memories for single event upsets every five minutes. The telemetry report the aggregate number of single event upsets and experiment livetime.



**Figure 38: AO-85 CubeSat recording on-orbit single event upsets in SRAM.**

The science objective of AO-85 was to report on upsets in a memory that exhibited a low-energy proton sensitivity. SEU experiments were performed at Vanderbilt and the Indiana University Cyclotron Facility [60][61]. These memories do not exhibit a clear proton energy threshold for single event upset. The data in Figure 39 show SEU cross sections measurable down to 1.1 MeV and a peak value at 1.3 MeV. The apparent combination of energy loss mechanisms, electronic and nuclear, makes fitting the SEU cross section curve difficult. Both the Bendel 1 and 2 parameter fits were applied for illustration. Traditional CREME96 proton upset rates were calculated using the Bendel 2 parameter fit for an orbit-averaged flux and peak flux environment. The peak flux represents the passage of the satellite through the South Atlantic Anomaly.

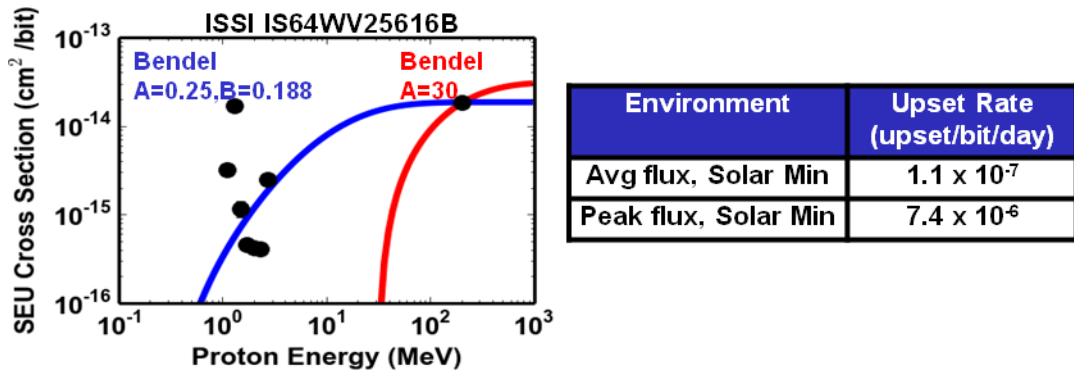


**Figure 39: Single event upset rate prediction for AO-85 SRAM from [59].**

### 5.1 On-Orbit Single Event Upsets

Telemetry from the spacecraft has recorded thousands of upsets in the memories. A portion of the data is shown in Figure 40. Although the data record time-tagged aggregate values, analyzing the data by day is instructive. Each day, the experiment reports an average of 4 upsets with some days reporting 0, other days as many as 12. This is to be expected for a random process. Plotting the number of days yielding a given number of upsets (bottom left) produces a histogram with a similar shape to the Poisson distribution with a mean value of 4.1. Perhaps more interesting, while the traditional calculation of proton upset rate was in good agreement with the observed values ( $1.1 \times 10^{-7}$  upsets/bit/day), the weekly averaged rates do not appear completely random around this value. Most notably, they appear to trend together and increase in the March - July time frame (bottom right).

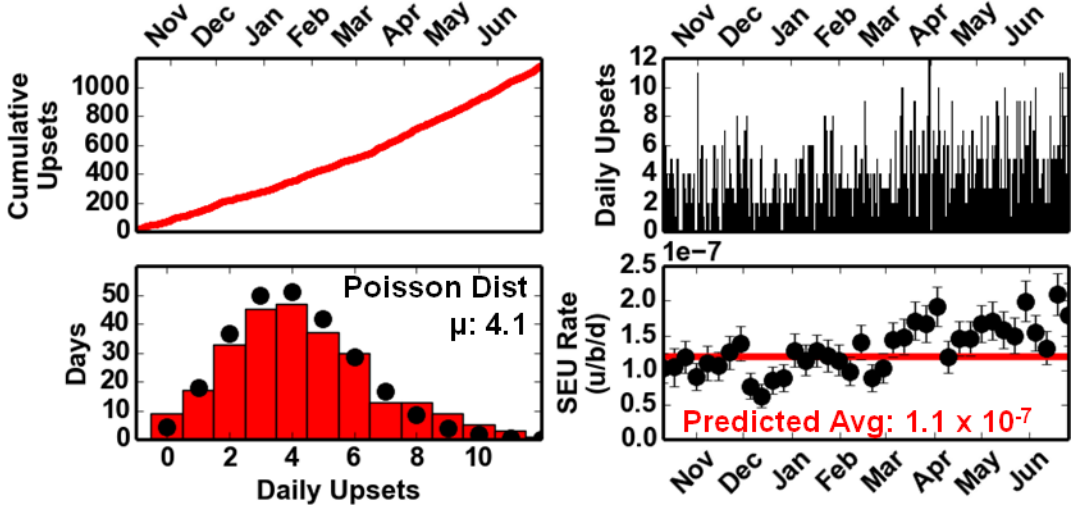


Figure 40: On-orbit telemetry reported by AO-85.

Although the environment analysis included the contribution of increase proton flux in the South Atlantic Anomaly, variation in the orbital parameters was not initially considered. The correlation of upset occurrence with satellite position confirms that the majority of events are due to the SAA (Figure 41 left). Each pass through this region presents the greatest probability of a single event upset. Although the satellite apogee, perigee, and inclination have remained nearly constant, the satellite does not always pass through the SAA at the same altitude. A pass through the SAA can be as low as perigee or as high as apogee if the orbit is properly aligned with the region. An orbit analysis recorded the minimum and maximum altitudes through the SAA from October 2015 to July 2016 (Figure 41 right). The minimum and maximum altitudes change over time as the orbit precesses around the Earth. In addition, the average altitude increased over this time period. The location of apogee appears to be a contributing factor to the increase in the observed error rate. This variation would likely be more pronounced for a larger orbital eccentricity.

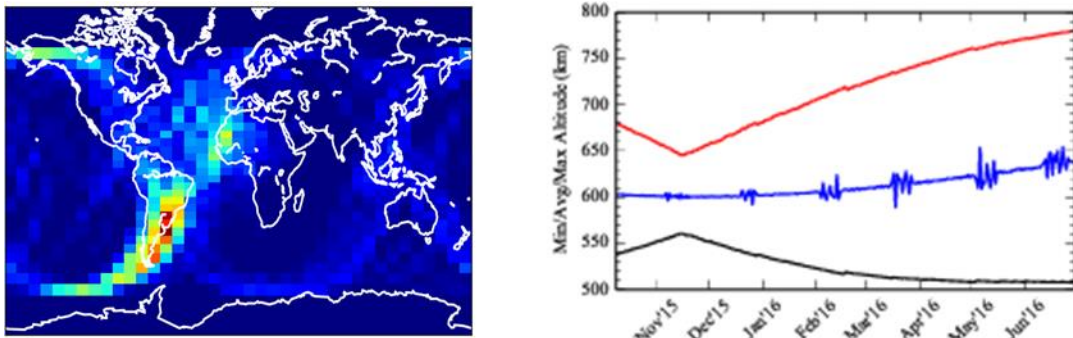


Figure 41: Single event upsets occurring in passes through the South Atlantic Anomaly (left). Minimum, average, and maximum altitude through SAA over time (right) from [59].

## **6 Summary**

The state of single event effect rate prediction tools for modern devices is at the doorstep of interesting new capabilities. The traditional and current state of the tool flow has been well-suited for worst case analysis and average event rate predictions for most cases. Event-by-event energy deposition analysis has been shown to be of utmost importance in other cases. The development of Monte Carlo analysis have enabled researchers to identify designs and accelerated test conditions that may not be suitable for classical analysis. In some cases, understanding how variations in part response might manifest at an accelerator facility can drive test campaigns and data collection. New technologies offering smaller and smaller devices will likely continue to contribute to variability in cell to cell and part to part radiation response. Fortunately, these variations are largely already a native part of the rate prediction process. The environment, as it always has been, is a large source of variation but new models incorporating confidence levels are improving our analyses. The development of each of these pieces, together with increasing interest in risk-tolerant missions such as CubeSats leading the way, has the potential to quantify risk as opposed to effectively eliminating it. Perhaps one day such an analysis will be possible, but until then, understanding the factors that drive single events can improve our ability to predict them.

## References

1. P. E. Dodd and L. W. Massengill, "Basic mechanisms and modeling of single-event upset in digital microelectronics," *IEEE Trans. Nucl. Sci.*, vol. 50, no. 3, pp. 583-602, June 2003.
2. G. H. Johnson and K. F. Galloway, "Single-event effects in the natural space radiation environment," *Part IV of the Short Course presented at the 1996 Nuclear and Space Radiation Effects Conference*, Indian Wells, CA, 15 July 1996.
3. J. L. Titus, "An updated perspective of single event gate rupture and single event burnout in power MOSFETs," *IEEE Trans. Nucl. Sci.*, vol. 60, no. 3, pp. 1912-1928, June 2013.
4. J. L. Barth, C. S. Dyer and E. G. Stassinopoulos, "Space, atmospheric, and terrestrial radiation environments," *IEEE Trans. Nucl. Sci.*, vol. 50, no. 3, pp. 466-482, June 2003.
5. R. A. Reed, "Fundamental mechanisms for single particle-induced soft errors," *Part I of the Short Course presented at the 2008 Nuclear and Space Radiation Effects Conference*, Tucson, AZ, 14 July 2008.
6. J. F. Ziegler, "Stopping and range of ions in matter," [Online]. Available: <http://www.srim.org/>
7. W. L. Bendl and E. L. Petersen, "Proton upsets in orbit," *IEEE Trans. Nucl. Sci.*, vol. 30, no. 6, pp. 4481-4485, Dec. 1983.
8. W. J. Stapor, J. P. Meyers, J. B. Langworthy, and E. L. Petersen, "Two parameter bendel model calculations for predicting proton induced upset," *IEEE Trans. Nucl. Sci.*, vol. 37, no. 6, pp. 1966-1973, Dec. 1990.
9. R. A. Reed, P. W. Marshall, H. S. Kim, P. J. McNulty, B. Fodness, T. A. Jordan, R. Reedy, C. Tabbert, M. S. T. Liu, W. Heikkila, S. Buchner, R. Ladbury, K. A. LaBel, "Evidence for angular effects in proton-induced single-event upsets," *IEEE Trans. Nucl. Sci.*, vol. 49, no. 6, pp. 3038-3044, 2002.
10. R. A. Reed, P. J. McNulty, and W. G. Abdel-Kader, "Implications of angle of incidence in SEU testing of modern circuits," *IEEE Trans. Nucl. Sci.*, vol. 41, no. 6, pp. 2049-2054, Dec. 1994.
11. R. A. Reed and P. J. McNulty, "Effects of geometry on the proton SEU dependence on the angle of incidence," *IEEE Trans. Nucl. Sci.*, vol. 42, no. 6, pp. 1803-1808, Dec. 1995.
12. A. J. Tylka, J. H. Adams, P. R. Boberg, B. Brownstein, W. F. Dietrich, E. O. Flueckiger, E. L. Petersen, M. A. Shea, D. F. Smart, and E. C. Smith, "CREME96: A revision of the cosmic ray effects on micro-electronics code," *IEEE Trans. Nucl. Sci.*, vol. 44, no. 6, pp. 2150-2160, Dec. 1997.
13. J. C. Pickel and J. T. Blandford, Jr., "Cosmic ray induced errors in MOS memory cells," *IEEE Trans. Nucl. Sci.*, vol. 25, no. 6, pp. 1166-1171, 1978.
14. J. N. Bradford, "A distribution function for ion track lengths in rectangular volumes," *J. Appl. Phys.*, vol. 50, no. 6, pp. 3799-3801, 1979.
15. J. N. Bradford, "Geometrical analysis of soft errors and oxide damage produced by heavy cosmic rays and alpha particles," *IEEE Trans. Nucl. Sci.*, vol. 27, no. 1, pp. 942-947, 1980.
16. W. L. Bendl, "Length distribution of chords through a rectangular volume," NRL Memorandum Report 5369, Jul. 3, 1984 [Online]. Available: [www.dtic.mil/cgi-bin/GetTRDoc?Location=U2&docName=a143302.pdf](http://www.dtic.mil/cgi-bin/GetTRDoc?Location=U2&docName=a143302.pdf).
17. E. L. Petersen, J. C. Pickel, J. H. Adams, Jr., and E. C. Smith, "Rate prediction for single event effects - a critique," *IEEE Trans. Nucl. Sci.*, vol. 39, no. 6, pp. 1577-1599, 1992.
18. L. W. Massengill, M. L. Alles, S. E. Kerns, and K. L. Jones, "Effects of process parameter distributions and ion strike locations on SEU cross-section data CMOS SRAMs," *IEEE Trans. Nucl. Sci.*, vol. 40, no. 6, pp. 1804-1811, Dec. 1993.
19. E. L. Petersen, "Single-event analysis and prediction," *Part III of the Short Course presented at the 1997 Nuclear and Space Radiation Effects Conference*, Snowmass Village, CO, 21 July 1997.
20. E. L. Petersen, "Soft error results analysis and error rate prediction," *Part III of the Short Course presented at the 2008 Nuclear and Space Radiation Effects Conference*, Tucson, AZ, 14 July 2008.
21. J. A. Pellish, M. A. Xapsos, K. A. LaBel, P. W. Marshall, D. F. Heidel, K. P. Rodbell, M. C. Hakey, P. E. Dodd, M. R. Shaneyfelt, J. R. Schwank, R. C. Baumann, X. Deng, A. Marshall, B. D. Sierawski, J. D. Black, R. A. Reed, R. D. Schrimpf, H. S. Kim, M. D. Berg, M. J. Campola, M. R. Friendlich, C. E. Perez, A. M. Phan, and C. M. Seidleck, "Heavy ion testing with iron at 1 GeV/amu," *IEEE Trans. Nucl. Sci.*, vol. 57, no. 5, pp. 2948-2954, Oct. 2010.
22. W. J. Stapor, P. T. McDonald, A. R. Knudson, A. B. Campbell, and B. G. Glagola, "Charge collection in silicon for ions of different energy but same linear energy transfer (LET)," *IEEE Trans. Nucl. Sci.*, vol. 35, no. 6, pp. 1585-1590, Dec. 1988.
23. T. L. Criswell, P. R. Measel, and K. L. Wahlin, "Single event upset testing with relativistic heavy ions," *IEEE Trans. Nucl. Sci.*, vol. 31, no. 6, pp. 1559-1561, Dec. 1984.
24. S. Duzellier, D. Falguere, L. Mouliere, R. Ecoffet, and J. Buisson, "SEE results using high energy ions," *IEEE Trans. Nucl. Sci.*, vol. 42, no. 6, pp. 1797-1802, Dec. 1995.
25. P. E. Dodd, J. R. Schwank, M. R. Shaneyfelt, V. Ferlet-Cavrois, P. Paillet, J. Baggio, G. L. Hash, J. A. Felix, K. Hirose, and H. Saito, "Heavy ion energy effects in CMOS SRAMs," *IEEE Trans. Nucl. Sci.*, vol. 54, no. 4, pp. 889-893, Aug. 2007.
26. R. A. Reed, R. A. Weller, A. Akkerman, J. Barak, W. Culpepper, S. Duzellier, C. Foster, M. Gaillardin, G. Hubert, T. Jordan, I. Jun, S. Koontz, F. Lei, P. McNulty, M. H. Mendenhall, M. Murat, P. Nieminen, P. O'Neill, M. Raine, B. Reddell, F. Saigne, G. Santin, L. Sihver, H. H. K. Tang, P. R. Truscott, and F. Wrobel, "Anthology of the development of radiation transport tools as applied to single event effects," *IEEE Trans. Nucl. Sci.*, vol. 60, no. 3, pp. 1876-1911, June 2013.
27. R. A. Weller, R. A. Reed, K. M. Warren, M. H. Mendenhall, B. D. Sierawski, R. D. Schrimpf, and L. W. Massengill, "General framework for single event effects rate prediction in microelectronics," *IEEE Trans. Nucl. Sci.*, vol. 56, no. 6, pp. 3098-3108, Dec. 2009.

28. R.A. Weller, M.H. Mendenhall, R.A.Reed, R.D. Schrimpf, K.M. Warren, B.D. Sierawski, and L.W. Massengill, "Monte carlo simulation of single event effects," *IEEE Trans. Nucl. Sci.*, vol.57, no.4, pp. 1726-1746, Aug. 2010.
29. R. A. Reed, R. A. Weller, M. H. Mendenhall, D. M. Fleetwood, K. M. Warren, B. D. Sierawski, M. P. King, R. D. Schrimpf, and E. C. Auden, "Physical processes and applications of the monte carlo radiative energy deposition (MRED) code," *IEEE Trans. Nucl. Sci.*, vol.62, no.4, pp. 1441-1461, Aug. 2015.
30. R. Ecoffet, S. Duzellier, D. Falguere, L. Guibert, and C. Inguimbert, "Low LET cross-section measurements using high energy carbon beam DRAMs/SRAMs," *IEEE Trans. Nucl. Sci.*, vol. 44, no. 6, pp. 2230-2236, Dec. 1997.
31. K. M. Warren, R. A. Weller, M. H. Mendenhall, R. A. Reed, D. R. Ball, C. L. Howe, B. D. Olson, M. L. Alles, L. W. Massengill, R. D. Schrimpf, N. F. Haddad, S. E. Doyle, D. McMorrow, J. S. Melinger, and W. T. Lotshaw, "The contribution of nuclear reactions to heavy ion single event upset cross-section measurements in a high-density SEU hardened SRAM," *IEEE Trans. Nucl. Sci.*, vol. 52, no. 6, pp. 2125-2131, Dec. 2005.
32. R. A. Reed, R. A. Weller, R. D. Schrimpf, M. H. Mendenhall, K. M. Warren and L. W. Massengill, "Implications of nuclear reactions for single event effects test methods and analysis," *IEEE Trans. Nucl. Sci.*, vol. 53, no. 6, pp. 3356-3362, Dec. 2006.
33. A. S. Kobayashi, D. R. Ball, K. M. Warren, R. A. Reed, N. Haddad, M. H. Mendenhall, R. D. Schrimpf, R. A. Weller, "The effect of metallization layers on single event susceptibility," *IEEE Trans. Nucl. Sci.*, vol. 52, no. 6, pp. 2189-2193, Dec. 2005.
34. R. A. Reed, R. A. Weller, M. H. Mendenhall, J.-M. Lauenstein, K. M. Warren, J. A. Pellish, R. D. Schrimpf, B. D. Sierawski, L. W. Massengill, P. E. Dodd, M. R. Shaneyfelt, J. A. Felix, J. Schwank, N. F. Haddad, R. K. Lawrence, J. H. Bowman, and R. Conde, "Impact of ion energy and species on single event effects analysis," *IEEE Trans. Nucl. Sci.*, vol.54, no.6, pp. 2312-2321, Dec. 2007.
35. P. E. Dodd, J. R. Schwank, M. R. Shaneyfelt, J. A. Felix, P. Paillet, V. Ferlet-Cavrois, J. Baggio, R. A. Reed, K. M. Warren, R. A. Weller, R. D. Schrimpf, G. L. Hash, S. M. Dalton, K. Hirose, and H. Saito, "Impact of heavy ion energy and nuclear interactions on single-event upset and latchup in integrated circuits," *IEEE Trans. Nucl. Sci.*, vol. 54, no. 6, pp. 2303-2311, Dec. 2007.
36. M. A. Xapsos, "Applicability of LET to single events in microelectronic structures," *IEEE Trans. Nucl. Sci.*, vol. 39, no. 6, pp. 1613-1621, Dec. 1992.
37. D. F. Heidel, K. P. Rodbell, P. Oldiges, M. S. Gordon, H. H. K. Tang, E. H. Cannon, and C. Plettner, Single-event-upset critical charge measurements and modeling of 65 nm silicon-on-insulator latches and memory cells," *IEEE Trans. Nucl. Sci.*, vol. 53, pp. 3512-3517, Dec. 2006.
38. K. P. Rodbell, D. F. Heidel, H. H. K. Tang, M. S. Gordon, P. Oldiges, and C. E. Murray, "Low-energy proton-induced single-event-upsets in 65 nm node, silicon-on-insulator, latches and memory cells," *IEEE Trans. Nucl. Sci.*, vol. 54, pp. 2474-2479, Dec. 2007.
39. D. F. Heidel, P. W. Marshall, K. A. LaBel, J. R. Schwank, K. P. Rodbell, M. C. Hakey, M. D. Berg, P. E. Dodd, M. R. Friendlich, A. D. Phan, C. M. Seidleck, M. R. Shaneyfelt, and M. A. Xapsos, Low energy proton single-event-upset test results on 65 nm SOI SRAM," *IEEE Trans. Nucl. Sci.*, vol. 55, pp. 3394-3400, Dec. 2008.
40. B. D. Sierawski, J. A. Pellish, R. A. Reed, R. D. Schrimpf, R. A. Weller, M. H. Mendenhall, J. D. Black, A. D. Tipton, M. A. Xapsos, R. C. Baumann, X. Deng, M. R. Friendlich, H. S. Kim, A. M. Phan, and C. M. Seidleck, "Impact of low-energy proton induced upsets on test methods and rate predictions," *IEEE Trans. Nucl. Sci.*, vol.56, no.6, pp. 3085-3092, Dec. 2009.
41. N. A. Dodds, M. J. Martinez, P. E. Dodd, M. R. Shaneyfelt, F. W. Sexton, J. D. Black, D. S. Lee, S. E. Swanson, B. L. Bhuva, K. M. Warren, R. A. Reed, J. Trippe, B. D. Sierawski, R. A. Weller, N. Mahatme, N. J. Gaspard, T. Assis, R. Austin, S. L. Weeden-Wright, L. W. Massengill, G. Swift, M. Wirthlin, M. Cannon, R. Liu, L. Chen, A. T. Kelly, P. W. Marshall, M. Trinczek, E. W. Blackmore, S. J. Wen, R. Wong, B. Narasimham, J. A. Pellish, and H. Puchner, "The contribution of low-energy protons to the total on-orbit SEU rate," *IEEE Trans. Nucl. Sci.*, vol.62, no.6, pp. 2440-2451, Dec. 2015.
42. B. D. Sierawski, M. H. Mendenhall, R. A. Reed, M. A. Clemens, R. A. Weller, R. D. Schrimpf, E. W. Blackmore, M. Trinczek, B. Hitti, J. A. Pellish, R. C. Baumann, S.-J. Wen, R. Wong, and N. Tam, "Muon-induced single event upsets in deep-submicron technology," *IEEE Trans. Nucl. Sci.*, vol.57, no.6, pp. 3273-3278, Dec. 2010.
43. B. D. Sierawski, B. Bhuva, R. Reed, N. Tam, B. Narasimham, K. Ishida, A. Hillier, M. Trinczek, E. Blackmore, S.-J. Wen, and R. Wong, "Bias dependence of muon-induced single event upsets in 28 nm static random access memories," in *Proc. of the Int. Rel. Physics Symp.*, Jun. 2014, pp. 2B.2.12B.2.5.
44. J. M. Trippe, R. A. Reed, B. D. Sierawski, R. A. Weller, R. A. Austin, L. W. Massengill, B. L. Bhuva, K. M. Warren, and B. Narasimham, "Predicting the vulnerability of memories to muon-induced SEUs with low-energy proton tests informed by monte carlo simulations," in *Proc. of the Int. Rel. Physics Symp.*, Apr. 2016, pp. SE61SE66.
45. M. P. King, R. A. Reed, R. A. Weller, M. H. Mendenhall, R. D. Schrimpf, B. D. Sierawski, A. L. Sternberg, B. Narasimham, J. K. Wang, E. Pitta, B. Bartz, D. Reed, C. Monzel, R. C. Baumann, X. Deng, J. A. Pellish, M. D. Berg, C. M. Seidleck, E. C. Auden, S. L. Weeden-Wright, N. J. Gaspard, C. Zhang, and D. M. Fleetwood, "Electron-induced single-event upsets in static random access memory," *IEEE Trans. Nucl. Sci.*, vol.60, no.6, pp. 41224129, Dec. 2013.
46. M. Raine, M. Gaillardin, P. Paillet, O. Duhamel, S. Girard, and A. Bourrel, "Experimental evidence of large dispersion of deposited energy in thin active layer devices," *IEEE Trans. Nucl. Sci.*, vol. 58, no. 6, pp. 2664-2672, Dec. 2011.

47. H. Bichsel, "A method to improve tracking and particle identification in TPCs and silicon detectors," *Nucl. Instrum. Methods Phys. Res. A*, vol. 562, pp. 157-197, Mar. 2006.
48. S. L. Weeden-Wright, M. P. King, N. C. Hooten, W. G. Bennett, B. D. Sierawski, R. D. Schrimpf, R. A. Weller, R. A. Reed, M. H. Mendenhall, D. M. Fleetwood, M. L. Alles, and R. C. Baumann, "Effects of energy-deposition variability on soft error rate prediction," *IEEE Trans. Nucl. Sci.*, vol.62, no.5, pp. 2181-2186, Oct. 2015.
49. L. J. Landau, "On the energy loss of fast particles by ionization," *J. Phys. (USSR)*, vol. 8, no. 4, pp. 201-205, 1944.
50. P. V. Vavilov, "Ionization losses of high-energy heavy particles," *Soviet Phys. JETP*, vol. 32, no. 4, pp. 749-751, 1957.
51. M. P. King, R. A. Reed, R. A. Weller, M. H. Mendenhall, R. D. Schrimpf, M. L. Alles, E. C. Auden, S. E. Armstrong, M. Asai, "The impact of delta-rays on single-event upsets in highly scaled SOI SRAMs," *IEEE Trans. Nucl. Sci.*, vol. 57, no. 6, pp. 3169-3175, Dec. 2010.
52. J. M. Trippe, R. A. Reed, R. A. Austin, B. D. Sierawski, R. A. Weller, E. D. Funkhouser, M. P. King, B. Narasimham, B. Bartz, R. Baumann, J. Labello, J. Nichols, R. D. Schrimpf, and S. L. Weeden-Wright, "Electron-induced single event upsets in 28nm and 45nm bulk SRAMs," *IEEE Trans. Nucl. Sci.*, vol.62, no.6, pp. 2709-2716, Dec. 2015.
53. Space Weather Prediction Center. (Jun. 2016). GOES proton flux. [Online]. Available: <http://www.swpc.noaa.gov/products/goes-proton-flux>.
54. J. H. Adams, "The variability of single event upset rates in the natural environment," *IEEE Trans. Nucl. Sci.*, vol. 30, no. 6, pp. 4475-4480, Dec. 1983.
55. M. A. Xapsos, G. P. Summers, J. L. Barth, E. G. Stassinopoulos, and E. A. Burke, "Probability model for cumulative solar proton event fluences," *IEEE Trans. Nucl. Sci.*, vol. 47, no. 3, pp. 486-490, Jun. 2000.
56. M. A. Xapsos, C. Stauffer, T. Jordan, J. L. Barth, and R. A. Mewaldt, "Model for cumulative solar heavy ion energy and linear energy transfer spectra," *IEEE Trans. Nucl. Sci.*, vol. 54, no. 6, pp. 1985-1989, Dec. 2007.
57. (Jun. 2016). Planetary K-Index. [Online]. Available: <http://www.swpc.noaa.gov/products/planetary-k-index>
58. G. Ginet, T. P. O'Brien, S. L. Huston, W. R. Johnston, T. B. Guild, R. Friedel, C. D. Lindstrom, C. J. Roth, P. Whelan, R. A. Quinn, D. Madden, S. Morley, and Yi-Jiun Su, "The AE9, AP9 and SPM: new models for specifying the trapped energetic particle and space plasma environment," *Space Sci. Rev.*, vol. 179, nos. 1-4, pp. 579-615, Nov. 2013.
59. B. D. Sierawski, K. M. Warren, A. L. Sternberg, R. A. Austin, J. M. Trippe, M. W. McCurdy, R. A. Reed, R. A. Weller, M. L. Alles, R. D. Schrimpf, L. W. Massengill, D. M. Fleetwood, A. Monteiro, G. W. Buxton, J. C. Brandenburg, W. B. Fisher, and R. Davis, "Cubesats and crowd-sourced monitoring for single event effects hardness assurance," *IEEE Trans. Nucl. Sci.*, vol. 64, no. 1, pp. 293-300, Jan. 2017.
60. M. W. McCurdy, M. H. Mendenhall, R. A. Reed, B. R. Rogers, R. A. Weller, and R. D. Schrimpf, "Vanderbilt pelletronLow energy protons and other ions for radiation effects on electronics," in *Proc. IEEE Rad. Effects Data Workshop (REDW)*, Jul. 2015, pp. 146-151.
61. B. von Przewoski, T. Rinckel, W. Manwaring, G. Broxton, M. Chipara, T. Ellis, E. R. Hall, A. Kinser, and C. C. Foster, "Beam properties of the new radiation effects research stations at Indiana University Cyclotron Facility," in *Proc. IEEE Rad. Effects Data Workshop (REDW)*, Jul. 2004, pp. 145-150.